Synthetic strategies to improve the performance of manganese oxide based layered and spinel materials for electrochemical energy storage

by

Charl Jeremy Jafta

Thesis submitted in fulfilment of the requirements for the degree of

Doctor of Philosophy

In the Faculty of Natural and Agricultural Sciences

Department of Physics

University of Pretoria

March 2014

Supervisor: Professor K. I. Ozoemena
Co-Supervisor: Professor N. Manyala

Declaration

I, Charl Jeremy Jafta, hereby declare that:

I understand what plagiarism is and I am aware of the University's policy in this regard;

The work contained in this thesis is my own original work;

I did not refer to work of current or previous students, lecture notes, handbooks or any other study material without proper referencing;

Where other people's work has been used this has been properly acknowledged and referenced;

I have not allowed anyone to copy any part of my thesis; I have not previously in its entirety or in part submitted this thesis at any university for a degree.

Signature of student:

Name of student: Charl Jeremy Jafta

Student number: 12384012

Date:

Dedication

To my beautiful and loving wife

Lizette

"So they are no longer two but one flesh. Therefore what God has joined together, no human being must separate." (Matthew 19:6)

Acknowledgements

First of all I would like to express my sincere gratitude to the Lord Jesus Christ by whose grace I had begun and completed this study.

The following people I would like to thank who supported and assisted me during the completion of this degree:

- My supervisor, mentor and friend, Prof. Kenneth Ozoemena who has absorbed me into his research and gave me countless opportunities for which I am very grateful.
- Dr. Mkhulu Mathe, my manager at CSIR, for his continual advice and support.
- Prof. Ncholu Manyala, for taking me on as his student and making me part of his research group.
- Prof. Wiets Roos, from the University of the Free State, for always making me feel welcome in Bloemfontein and allowing me to use the XPS.
- Funeka Nkosi, for all her help and scientific discussions.
- All my colleges at Energy Materials.
- A fellow student and friend Katlego Makgopa, for all the long relaxing talks and sometimes not so relaxing scientific discussions.
- My wife Lizette, for her support and sacrifices during this period.
- My mother Phoebe, my brother Malcolm and my sisters Debbie, Lorenda and Deidré.
- My in-laws for taking interest in my work.
- The CSIR for the Doctoral studentship.

TABLE OF CONTENTS

List of Tables

List of Figures

List of Abbreviations and Symbols

AFM	Atomic Force Microscopy
BTU	British Thermal Units
CA	Citric Acid
CSAFM	Current Sensing Atomic Force Microscopy
CV	Cyclic Voltammetry
DEC	Diethyl Carbonate
DMC	Dimethyl Carbonate
EC	Electrochemical Capacitor
EC	Ethyl Carbonate
EDLC	Electrical Double Layer Capacitor
EEC	Equivalent Electric Circuit
EG	Ethylene Glycol
EIS	Electrochemical Impedance Spectroscopy
EMC	Ethylene Methyl Carbonate
EMD	Electrolytic Manganese Dioxide
EV	Electric Vehicle
FESEM	Field Emission Scanning Electron Microscopy
HEV	Hybrid Electric Vehicle
IEA	International Energy Agency
IEO2013	International Energy Outlook 2013
LIB	Lithium Ion Battery
LMN	$LiMn_{1.5}Ni_{0.5}O_4$
LMNC	$Li_{1.2}Mn_{0.54}Ni_{0.13}Co_{0.13}O_2$
LMNCA	$Li_{1.2}Mn_{0.52}Ni_{0.13}Co_{0.13}Al_{0.02}O_2$
LMNCA-mic	Microwave treated $Li_{1.2}Mn_{0.52}Ni_{0.13}Co_{0.13}Al_{0.02}O_2$

LMNC-mic	Microwave treated $Li_{1.2}Mn_{0.54}Ni_{0.13}Co_{0.13}O_2$
LMN-mic	Microwave treated $LiMn_{1.5}Ni_{0.5}O_4$
MWCNT	Multi-Walled Carbon Nanotubes
NMP	N-Methyl-2-Pyrolidone
PVDF	Polyvinylidene Fluoride
Redox	Reduction-Oxidation
SDS	Sodium Dodecyl Sulphate
SEM	Scanning Electron Microscopy
SHE	Standard Hydrogen Electrode
SPM	Scanning Probe Microscopy
T	Temperature
V	Volt
XPS	X-ray Photoelectron Spectroscopy
XRD	X-ray Diffraction
φ	Phase shift
°C	Degree Celsius
C	Charge or Discharge Rate
C_{Li}	Concentration of the Lithium
C_{ox}	Concentration of the Oxidised Species
C_{red}	Concentration of the Reduced Species
C_s	Specific Capacity
D_{Li}	Diffusion Coefficient of the Lithium
D_{ox}	Diffusion Coefficient of the Oxidised Species
D_{red}	Diffusion Coefficient of the Reduced Species
E	Energy Density
E_0	Standard Potential
E_-^0	Negative Electrode Potential

E_{+}^{0}	Positive Electrode Potential
E_{cell}^{0}	Standard Cell Potential
E_{cell}	Cell Potential
E_{th}	Theoretical Energy Density
F	Faraday Constant
i	Current
j	Current Density
m	Mass
M	Molar Mass
M_w	Molecular Weight
n	Number of Electrons
P	Power Density
R	Gas Constant
U_0	Cell Potential
V_{oc}	Open Circuit Potential
ω	Radial Frequency
ΔE_0	Difference in the Electrode Potentials
ΔG_0	Gibbs Free Energy
ε_0	Dielectric Constant
ε_r	Electrolyte Dielectric Constant
σ	Warburg Factor

Abstract

This work studied the manganese oxide based nanostructures for enhanced performance (power and energy densities) as electrode materials in lithium ion batteries (LIBs) and electrochemical capacitors (ECs). The high energy $LiMn_{1.5}Ni_{0.5}O_4$ (LMN), the solid solution layered $Li_{1.2}Mn_{0.54}Ni_{0.13}Co_{0.13}O_2$ (LMNC) and Al doped $Li_{1.2}Mn_{0.52}Ni_{0.13}Co_{0.13}Al_{0.02}O_2$ counterpart (LMNCA) cathode materials for LIB were synthesized by a modified Pechini one-step powder forming, microwave-assisted method. This novel synthesis route also included an intermediate step where samples were treated with microwave irradiation for a short period (~ 20 min) prior to the extended period (~ 8 hr) of annealing (~ 700 – 800 °C). It is proved, for the first time, that microwave irradiation is capable of tuning the Mn^{3+} content of the LMN spinel for enhanced electrochemical performance (i.e., high capacity, high capacity retention, excellent rate capability, and fast Li^+ insertion/extraction kinetics).

For the first time, this work investigated the impact of doping LMNC with a very small amount of Al (LMNCA) with a view to improving its cycling stability and rate capability. Like the LMN above, the intermediate precursors were also subjected to microwave irradiation prior to high temperature annealing (abbreviated herein as LMNC-mic and LMNCA-mic). It was found that by substituting the Mn with Al, the Mn^{4+} concentration in the cathode material decreases. When these cathode materials are treated with microwave irradiation prior to annealing, the oxidation state of the Mn increases, therefore the Mn^{4+} concentration increases with microwave irradiation. The Mn oxidation state can be controlled via Al doping and microwave irradiation. By controlling the Mn

oxidation state, the electrochemical performance can thus be engineered. In summary, the electrochemical performance of the layered materials decreased as follows: LMNCA-mic > LMNCA > LMNC-mic > LMNC.

The South African abundant EMD was converted to a single-phased nanoparticulate material ideal for EC electrodes. The EMD was treated with NH_4OH for the conversion of the multi-phases to a single α phase MnO_2. The micron sized particles were converted to nanoparticles via the hydrothermal reaction in the presence and absence of the surfactant Sodium Dodecylsulphate (SDS). The surfactant is used for the dispersion of the nanoparticles and improvement of the electrochemical performance. These materials were then coated with Carbon nanotubes (CNT) or Graphene oxide and compared as to find the EC with the best electrochemical properties. A high-energy aqueous asymmetric electrochemical capacitor was developed using manganese dioxide (α-MnO_2)/graphene oxide (GO) nanocomposites. Unlike the as-prepared α-MnO_2, the presence of SDS during the hydrothermal reaction conferred different morphologies on the intermediate precursors for the α-$MnO_{2(SDS)}$. Also, the XRD patterns showed that the α-$MnO_{2(SDS)}$ are more crystalline than the as-prepared α-MnO_2. The superior electrochemical performance of the α-$MnO_{2(SDS)}$/GO composite (280 F g^{-1}, 35 Wh kg^{-1}, and 7.5 kW kg^{-1} at 0.5 A g^{-1}) coupled with excellent cycle life clearly indicates that this electrode system has the potential of being developed as an efficient aqueous asymmetric electrochemical capacitor. Interestingly, the electrochemical performance is comparable to or even better than those reported for the more conductive graphene/MnO_2 composites.

Chapter 1

Introduction

1.1 Renewable Energy and Society

There are several definitions of renewable energy. The International Energy Agency (IEA), for example, defines renewable energy as follows [1]: "*Renewable energy is derived from natural processes that are replenished constantly. In its various forms, it derives directly or indirectly from the sun, or from heat generated deep within the earth. Included in the definition is energy generated from solar, wind, biomass, geothermal, hydropower and ocean resources, and biofuels and hydrogen derived from renewable resources*".

The International Energy Outlook 2013 (IEO2013) projects that the world energy consumption will grow by 56 % between the years 2010 and 2040 [2]. Total world energy use rises from 524 quadrillion British thermal units (BTU), or 5.554×10^{17} kJ, in 2010 to 630 quadrillion Btu, or 6.678×10^{17} kJ, in 2020 and to 820 quadrillion Btu, or 8.692×10^{17} kJ, in 2040 (see **Figure 1.1**).

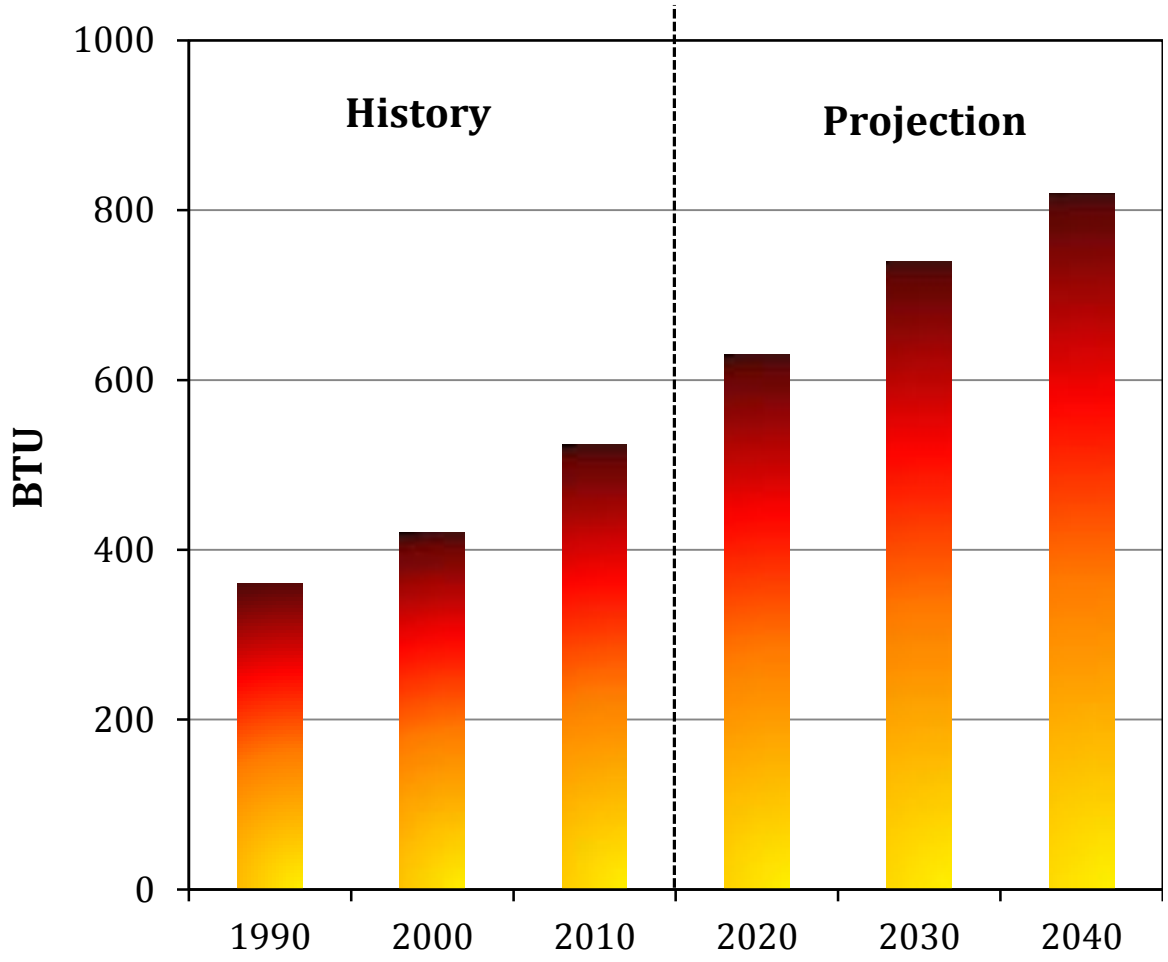

Figure 1.1: The world energy consumption from the year 1990 to the projected year 2040 (Data for the plot obtained from [2]).

Renewable energy and nuclear power are the world's fastest growing energy sources with each increasing by 2.5 % per year. However, fossil fuels continue to supply almost 80 % of world energy use through 2040 [2]. As capacity continues to grow and prices for renewable energy and its equipment continue to fall (due to the technological advancements), the share of renewable energy use is likely to further increase. Along with measures to promote energy efficiency, the increase in renewable energy will provide many benefits to both the global economy and individual countries. The adoption of

renewable energy technologies can help reduce the emission of CO_2 in the atmosphere. Today, in developed nations, the supply and availability of energy are taken for granted. The simple turn of a switch produces light or heat, electronic communication is instantaneous, and an assumed supply of gasoline enables mass transport on a global scale. Despite this, there are numerous people and groups that are tirelesly working on solving the world's energy crisses.

The burgeoning growth of the world's population and the expectation from underdeveloped countries for an equal stake in the earth's resources and quality of life are unsustainable without dramatic improvements in the control and efficiency of energy production, storage and use. Life's comforts over the past two centuries have been derived largely from the discovery and exploitation of fossil fuels, and the result of profound scientific and technological innovations. Whereas the creation of oil, coal, and natural gas reserves, the primary fuels for transportation, occurred over several hundred millions of years. We are on course to consume these non-renewable energy sources within several hundreds of years. Notwithstanding the unknown medium-to-long term implications of burning carbonaceous fuels and CO_2 emissions on a warming planet, it is abundantly clear that scientific and technological solutions are urgently required to avert a looming energy crisis of epic proportions [3].

1.1.1 Energy Storage

A key stumbling block in renewable energy is the technical difficulties of electricity storage and transmission. Thus, electrical energy storage in the form of batteries and ECs can be used not only as a back-up energy supply for national electric grids and smart grids

for localized communities, but also as the power source for transportation such as electric vehicles (EV) (see **Figure 1.2**), defence, or aerospace applications, as well as for smaller devices such as consumer electronics such as laptops and cell phones, medical implants such as pacemakers, defibrillators, and pumps, power tools, and toys. Batteries and ECs are now a commodity of national and strategic significance in a highly competitive international arena [4].

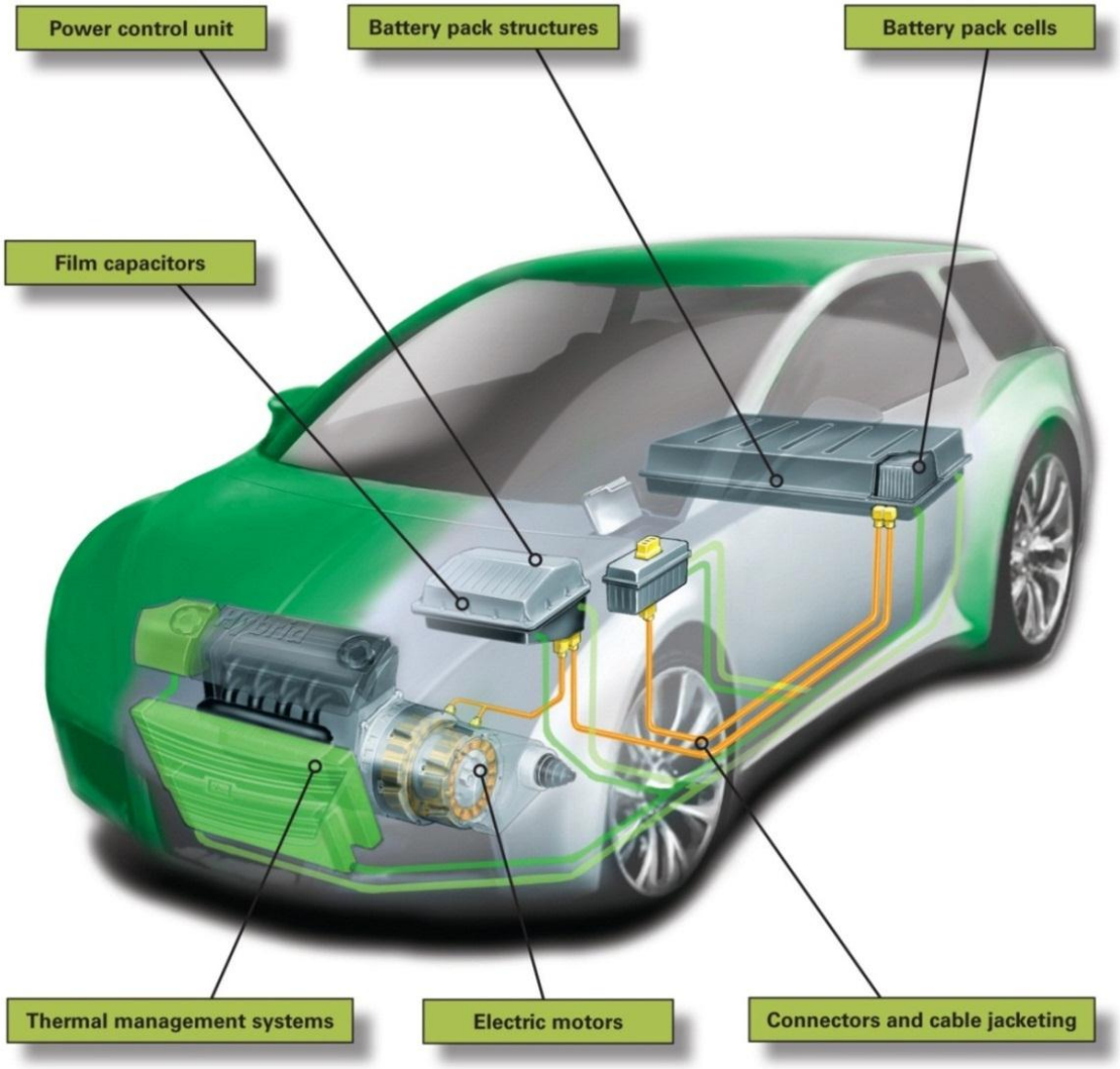

Figure 1.2: An application of Lithium ion batteries (LIBs) in the use of an EV [5].

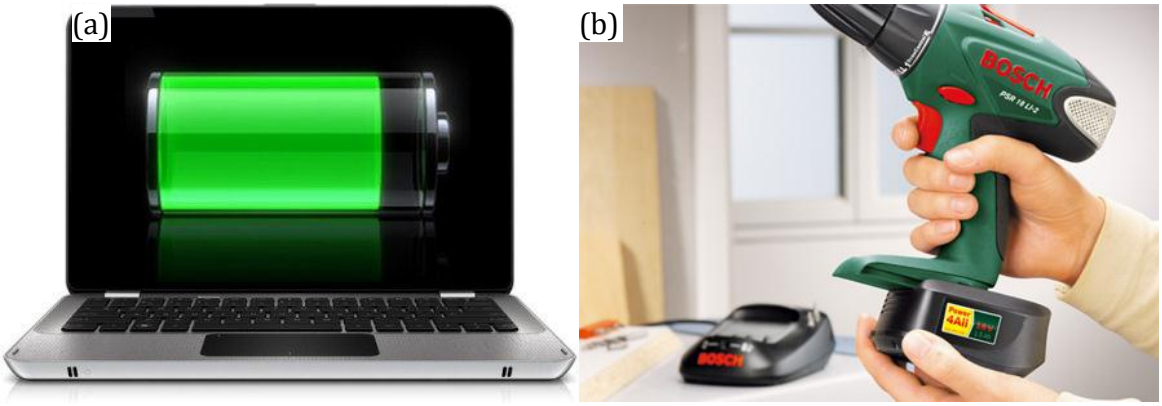

Figure 1.3: Other applications of LIBs [6, 7].

1.1.2 Opportunities for Energy Storage

Electrical energy storage represents an opportunity for basic and applied researchers to collectively overcome challenging scientific and technological barriers that directly address a critical societal and environmental necessity. In particular, development of high energy and power density batteries and ECs that are safe to operate could make a global electrified transportation industry a reality. Lithium battery and electrochemical capacitor technology is revolutionizing electrical energy storage; advances are recorded in periodic reviews [3, 8-12]. At present, however, state-of-the-art lithium-ion batteries, with a specific energy of ~ 150 $Wh.kg^{-1}$, do not yet have sufficient energy or life for use in electrified vehicles that would match the performance of internal combustion vehicles. Petrol, fuel for the internal combustion process, has a specific energy of ~ 13000 $Wh.kg^{-1}$ [13]. Thus the state of the art energy storage systems are still far from competing with the energy achieved by the internal combustion process. ECs do have the necessary specific power but energy density is also still a disabling factor. Another limiting factor for full commercialization of LIBs and ECs is their cost, but with increasing research and

development the cost can be lowered. The cost is also linked to production cost and acceptability within the market place.

1.2 Electrochemical Energy Storage Systems

Systems for electrochemical energy storage and conversion include, among others, batteries and ECs. Although the energy storage and conversion mechanisms are different, there are "electrochemical similarities" of these three systems as will be shown in **Chapter 2**. Common features are that the energy-providing processes take place at the phase boundary of the electrode/electrolyte interface and that electron and ion transport are separated.

Batteries and ECs have different strengths and weaknesses in terms of their power and energy densities, and thus can be categorized in terms of their power and energy density as in **Figure 1.4**.

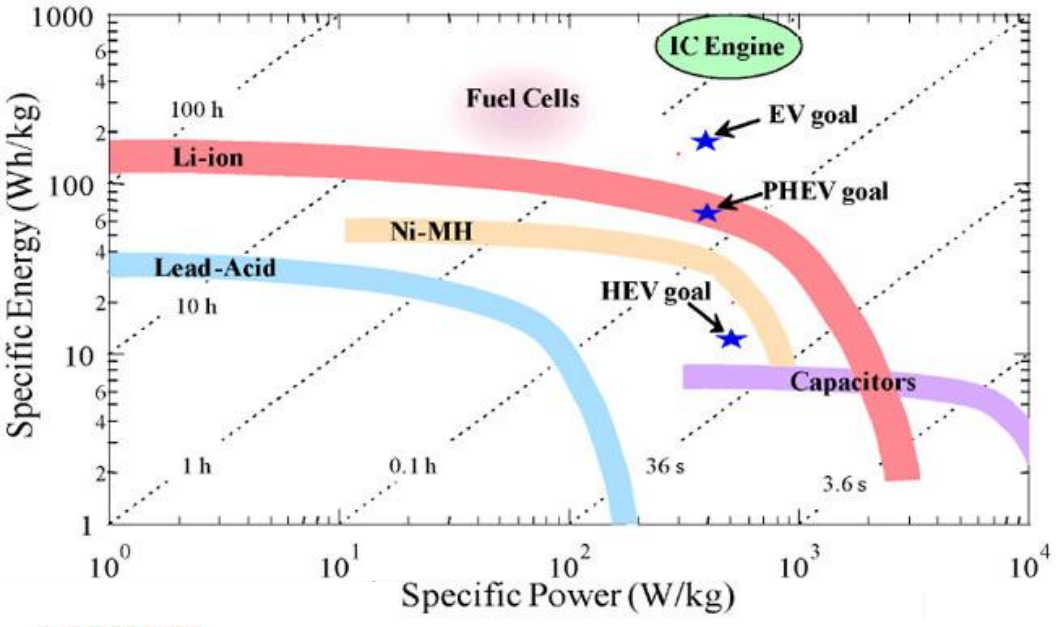

Figure 1.4: A simplified Ragonne plot of the energy storage domains for the various electrochemical energy storage and conversion systems [14].

According to the component of the battery systems' electrodes, rechargeable batteries can be classified as lead-acid, zinc-air, nickel-cadmium, nickel-hydrogen, sodium-sulfur, sodium-nickel-chloride, and Li ion batteries (LIBs) [15] and can further be categorized in terms of their discharge time capabilities (or energy density) and power ratings as seen in **Figure 1.5**.

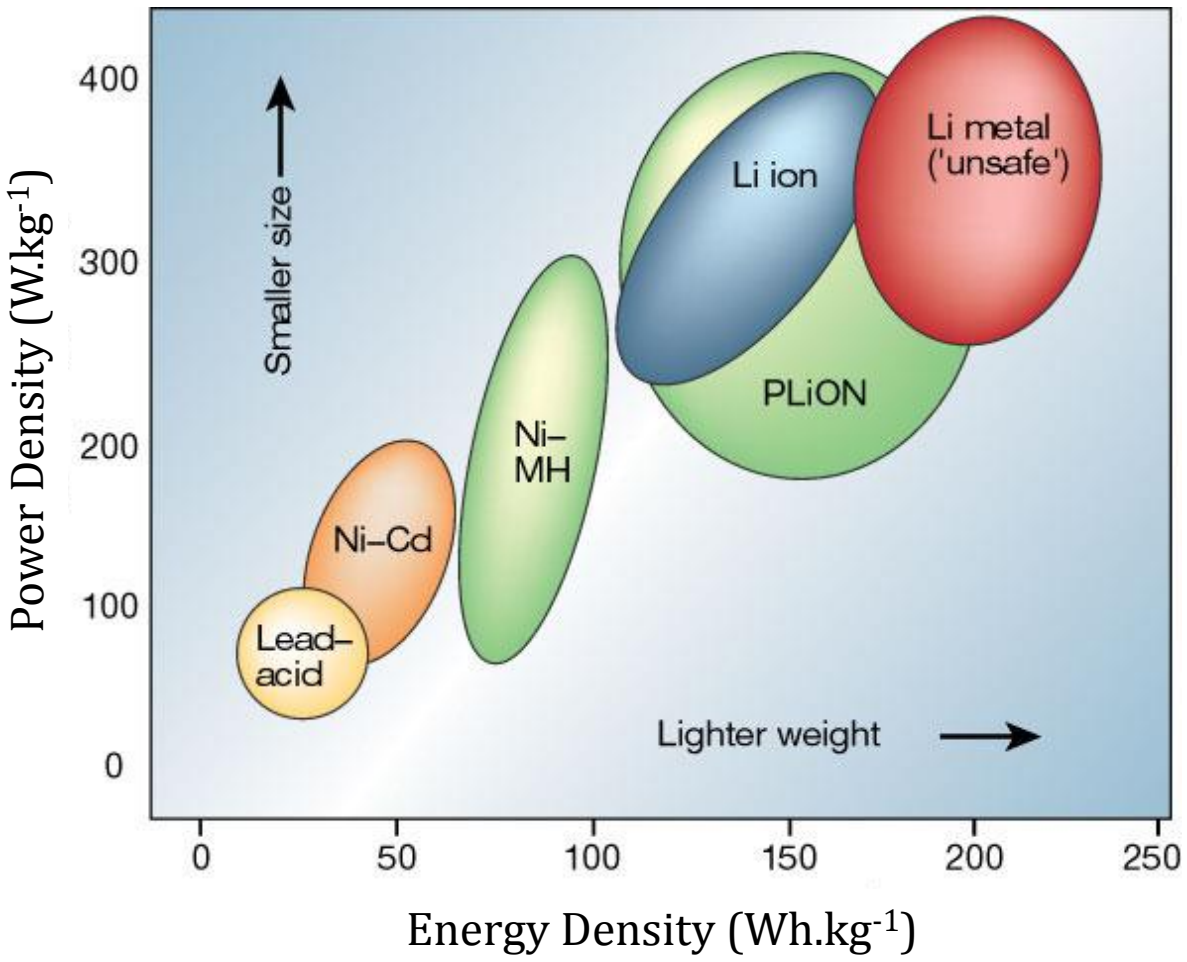

Figure 1.5: A Ragonne plot for the different battery technologies [8].

LIBs are the most important and widely used rechargeable battery with advantages of high voltage, low self-discharge, long cycling life, low toxicity, and high reliability. Other energy storage technologies, such as Li air batteries, have better specific energy and power densities, but are still plagued by safety issues, practicality and high cost.

Therefore, for the immediate future the focus, in terms of energy storage technology, lies with LIBs.

ECs have attracted increasing interest because of their high power storage capability, which is highly desirable for applications in EVs and hybrid electric vehicles (HEV). ECs can be used with LIBs for their high power attribute to compliment LIBs or they can be used independently as new research show that these energy storage systems have good energy density. Hence, research and development in the field of ECs are focused on increasing the energy density of these energy storage systems.

1.3 The Objectives / Scope of this Study

The development of high performance LIBs and ECs is at the forefront of electrochemical energy storage research globally. LIBs and ECs are characterised by their high energy and power densities, respectively and are used in most of today's portable electronics and EV. Regrettably, despite the commercial success of LIBs and ECs, it still fall short of these satisfying needs for applications such as power tools, EVs and efficient utilisation of renewable energies such as solar and wind power. The performance of LIBs and ECs is intimately dependent on the properties of their electrode materials; as such it is not surprising that greater attention has been devoted to research and development of electrode materials [8, 12]. There is a need to substantially improve their performance to meet the requirements, as stated including cycle stability, safety, and cost, of future systems. This can be done by developing innovative materials and advancing our understanding of the physics and chemistry underlying their performance. Breakthroughs in materials development hold the key to new generations of LIBs and ECs as against the *status quo*. Such materials will lead to the development of batteries and ECs that can meet the current needs. LIBs and ECs are used simultaneously as they complement each other, with batteries having higher energy density and lower power density compared to the ECs.

The LIB cathode (positive electrode) materials offer the greatest opportunity for research. The cathode accounts for about 25% of the cost of any LIB while the anode (negative electrode) contributes only 10% [16]. The most successful cathode materials thus far are the lithium transition metal oxides which include the layered lithium cobalt oxide ($LiCoO_2$) commercialised by Sony in 1991 [17], lithium manganese spinel ($LiMn_2O_4$) and olivine lithium iron phosphate ($LiFePO_4$). ECs offer research opportunities for both the

positive and negative electrodes. One of the main parameters playing a role in the development of ECs is the surface area of the electrodes, which makes nanosizing of electrode material an important part of this research.

The manganese oxide based (MnO) materials (e.g., $LiMn_2O_4$, high voltage $LiMn_{1.5}Ni_{0.5}O_4$ and high capacity $Li_{1.2}Mn_{0.54}Ni_{0.13}Co_{0.13}O_2$) are well recognised for their low cost, environmental friendliness and are safer compared to other materials such as $LiCoO_2$. The use of MnO in ECs is also very attractive for research due to the same reasons mentioned above [18].

It is well established that the capacity (LIBs) / capacitance (ECs) and lifetime of electrodes can be tailored by the (i) synthesis method, (ii) selection of the electrochemically redox-active centres, and (iii) structure of the insertion electrode. Thus, the main objectives of this thesis are as follows:

I. It has been reported that as the size of Li insertion materials become smaller, the surface area for charge transfer becomes higher and the diffusion length smaller. The improvement due to smaller particles are expected to be the kinetics of, and hence, the rate capabilities of the cathode materials [19]. On the other hand, the high surface area accompanied by the nanomaterials also means high surface reactivity and thus detrimental surface side reactions causing capacity fading. Another factor playing a role is the Mn^{3+} content available in the high voltage $LiMn_{1.5}Ni_{0.5}O_4$ cathode material. This is considered quite critical as it is intricately linked to the performance of this cathode material [20]. Due to the advantages of the nanoparticulate cathode an objective is to develop a new microwave-assisted synthesis method that will

yield nanoparticles and control the Mn^{3+}/Mn^{4+} ratio in the $LiMn_{1.5}Ni_{0.5}O_4$ cathode material.

The high capacity Li rich material, $Li_{1.2}Mn_{0.54}Ni_{0.13}Co_{0.13}O_2$, is plagued by a low conductivity that negatively affects the rate capability [21]. The different synthesis methods used cause mixing of cations that have a negative effect on the cycle stability of the cathode material [22]. The objective is to dope the Li rich, high capacity $Li_{1.2}Mn_{0.54}Ni_{0.13}Co_{0.13}O_2$ cathode material with Al^{3+} that can occupy the Mn^{4+} sites due to its similar ionic radii. The Al^{3+} ionic radius is slightly bigger compared to the Mn^{4+}, therefore by doping the cathode material with Al^{3+}, the *c*-lattice should increase and cation mixing decrease giving rise to faster diffusion of Li. As a result the diffusion coefficient will increase and the rate capability will improve. The Al will also have a positive effect on the structural stability of the cathode material.

II. Another objective is to control the Mn^{3+}/Mn^{4+} ratio by making use of the microwave-assisted synthesis method. The microwave assisted method will be used on both the undoped $Li_{1.2}Mn_{0.54}Ni_{0.13}Co_{0.13}O_2$ and its Al doped counterpart. The Al doping causes an increase in the Mn^{3+} concentration and in contrast the microwave irradiation changes the oxidation state of Mn from 3+ to 4+. The microwave assisted synthesis method combined with Al doping can thus be employed on this cathode material in order to control the Mn^{3+}/Mn^{4+} ratio

III. Mn is one of the most abundant elements (12^{th}) in the crust of the earth with South Africa as one of the world's leading suppliers of high grade Mn ore [23]. MnO_2 crystallizes into several crystallographic structures, namely, α, β, γ, δ and λ structures [24]. Electrolytic manganese dioxide (EMD) is not mono-phased

and takes on more than one of the possible crystallographic structures. According to literature the electrochemical performance of MnO_2 is dependent on the crystallographic structure, with α being the superior crystal structure [24]. The EMD that consists of micron sized particles and multiple phases can be chemically treated to give nanosized particles and an appropriate structural phase (α) in order to synthesize a Mn based electrode for electrochemical applications. A surfactant can also be used in the synthesis of this α phased MnO_2 in order to increase crystallinity of the material that would increase the electrochemical properties.

1.4 Outline of thesis

Chapter 1 discusses renewable energy and how it affects society today and in the future. In this chapter energy storage is put in perspective and the opportunities in this research field are discussed.

Chapter 2 gives a broad background on electrochemistry and the basic principles of LIBs. The different cathode materials are discussed and a more comprehensive background is given on spinel and layered structured cathode materials. The basic principles of ECs are also discussed in this chapter and the three different types of ECs are discussed in more detail. A brief overview is also given on the techniques that were used for characterisation in this thesis. A major part of this thesis is on the effects of microwave irradiation and thus this mechanism is also discussed. The different syntheses used for LIB cathode materials are also tabled.

In **Chapter 3** the experimental techniques and methods are presented and the materials and reagents are tabled. A modified Pechini synthesis method, for the spinel ($LiMn_{1.5}Ni_{0.5}O_4$) and layered ($Li_{1.2}Mn_{0.54}Ni_{0.13}Co_{0.13}O_2$ and $Li_{1.2}Mn_{0.52}Ni_{0.13}Co_{0.13}Al_{0.02}O_2$) cathode materials, with and without microwave irradiation are presented. A synthesis method to produce nano MnO_2 is also shown in this chapter. The fabrication of coin cells with these LIB cathode and nano MnO_2 electrode materials are also presented.

Chapter 4 reports on a diffusion formula that is wrongly used in literature and thus corrected. It also shows the modification of a diffusion equation in order to make use of both Cyclic Voltammetry and Electrochemical Impedance Spectroscopy parameters.

Chapter 5 reports on controlling of the Mn^{3+} concentration in $LiMn_{1.5}Ni_{0.5}O_4$ cathode material via a hybrid microwave synthesis method.

Chapters 6 and **7** reports on the effects of Al doping and microwave irradiation, respectively, on the layered cathode materials ($Li_{1.2}Mn_{0.54}Ni_{0.13}Co_{0.13}O_2$ and $Li_{1.2}Mn_{0.52}Ni_{0.13}Co_{0.13}Al_{0.02}O_2$). These two chapters show that controlling the Mn oxidation state via Al doping and microwave irradiation is possible.

Chapter 8 shows that the South African abundant Electrolytic Manganese Dioxide can be successfully converted to an excellent high energy electrochemical capacitor electrode material.

Chapter 9 gives concluding remarks showing the significance of this study and also paves the way forward with some recommendations and possible future work.

References

[1] UNEP. (2013), Green Economy and Trade – Trends, Challenges and Opportunities, Available at: http://www. unep. org/greeneconomy/GreenEconomyandTrade (Accessed on 22nd November 2013).

[2] IEA (2013), International Energy Outlook 2013: With Projections to 2040, Available at www. eia. gov/ieo/ (Accessed on 22nd November 2013).

[3] M.M. Thackeray, C. Wolverton, E.D. Isaacs, Energy & Environ. Sci. **5** (2012) 7854.

[4] D. Linden, T.B. Reddy, Handbook of batteries, 3rd ed., McGraw-Hill, New York, 2002.

[5]http://www2.dupont.com/Energy_Storage/en_US/assets/downloads/DuPont%20Automotive%20Hybrid%20Cars%20Brochure%20Web. pdf (Accessed on 11th February 2014).

[6] http://codesupport. info/increase-battery-life-laptop (Accessed on 11th February 2014).

[7] http://www. home-dzine. co. za/diy/2012tool-index. htm (Accessed on 11th February 2014).

[8] J. Tarascon, M. Armand, Nature **414** (2001) 359.

[9] M.S. Whittingham, Chem. Rev. **104** (2004) 4271.

[10] M. Armand, J. Tarascon, Nature **451** (2008) 652.

[11] V. Etacheri, R. Marom, R. Elazari, G. Salitra, D. Aurbach, Energy & Environ. Sci. **4** (2011) 3243.

[12] P. Simon, Y. Gogotsi, Nature Mater. **7** (2008) 845.

[13] P.P. Edwards, V.L. Kuznetsov, W.I.F. David, N.P. Brandon, Energy Policy **36** (2008) 4356.

[14] V. Srinivasan, AIP Conf. Proc. **1044** (2008) 283.

[15] B. Dunn, H. Kamath, J. Tarascon, Science **334** (2011) 928.

[16] G. Nazri, G. Pistoia, Lithium batteries: science and technology, Springer, New York, 2004.

[17] M.V. Reddy, G.V. Subba Rao, B.V.R. Chowdari, Chem. Rev. **113** (2013) 5364.

[18] F. Beguin, E. Frackowiak, Supercapacitors: Materials, Systems and Applications, John Wiley & Sons, Weinheim, 2013.

[19] Y. Talyosef, B. Markovsky, R. Lavi, G. Salitra, D. Aurbach, D. Kovacheva, M. Gorova, E. Zhecheva, R. Stoyanova, J. Electrochem. Soc. **154** (2007) A682.

[20] J. Xiao, X. Chen, P.V. Sushko, M.L. Sushko, L. Kovarik, J. Feng, Z. Deng, J. Zheng, G.L. Graff, Z. Nie, D. Choi, J. Liu, J. Zhang, M.S. Whittingham, Adv. Mater. **24** (2012) 2109.

[21] J. Liu, B. Reeja-Jayan, A. Manthiram, J. Phys. Chem. C **114** (2010) 9528.

[22] J. Kim, H. Chung, Electrochim. Acta **49** (2004) 3573.

[23] http://www. manganese. org/about_mn/reserves (Accessed on 25th November 2013).

[24] S. Devaraj, N. Munichandraiah, J. Phys. Chem. C **112** (2008) 4406.

Chapter 2

LITERATURE STUDIES / BACKGROUND

2.1. Electrochemistry Basic Principles

Electrochemistry is defined as the branch of chemistry that examines the phenomena resulting from combined chemical and electrical effects [1, 2]. The chemical effects involve the transfer of electrons to and from molecules or ions and are referred to as redox (reduction-oxidation) reactions. There are two types of processes; (i) Electrolytic processes, where reactions in which chemical changes occur on the passage of an electric current; and (ii) Galvanic or Voltaic processes, where chemical reactions result in the production of electrical energy. The latter process is found in LIBs and ECs which is the focus of this thesis.

2.2. Lithium Ion Battery Principles

An electrochemical cell is a chemical device for generating electrical energy from chemical energy (or converting chemical energy into electrical energy). This is done by means of an electrochemical redox reaction. This redox reaction involves the transfer of electrons from one material to another through an electric circuit. Due to the electrochemical process whereby the chemical energy is converted into electrical energy the cell is not

subject to the limitations of the Carnot cycle dictated by the second law of thermodynamics [3]. Therefore electrochemical cells are capable of having higher energy conversion efficiencies.

When two or more cells are joined together electrically, either in series or in a series-parallel array, it is termed a battery. Strictly speaking, a battery is a multi-cell array, although in common usage, single cells are called batteries. Thus onwards the term 'battery' will be used for the Lithium ion cells. An electrochemical cell consists of three major components:

I. The positive electrode (called the cathode) which is the oxidising electrode that accepts electrons from the external circuit and is reduced during the electrochemical reaction.

II. The negative electrode (called the anode) which is the reducing (fuel) electrode that provides electrons to the external circuit and is oxidised during the electrochemical reaction.

III. The electrolyte that is itself an electronic insulator but is an ionic conductor and thus the medium for transfer of charge as ions between the anode and the cathode. The choice of electrolyte solution is crucial in the operation of Li-ion Batteries (LIBs). It was found that alkyl carbonates are the best and most suitable solvents for LIBs. A binary or ternary solvent mixture with ethyl carbonate (EC) and either dimethyl carbonate (DMC), ethylene methyl carbonate (EMC), diethyl carbonate (DEC) or a binary mixture of these solvents with the Li salt, lithium hexafluorophosphate ($LiPF_6$) is successfully used as electrolyte in LIBs [4, 5]. $LiPF_6$ is very soluble in all alkyl carbonate solvents thereby forming high conducting

solutions and possesses good anodic stability (having high oxidation potentials) [6].

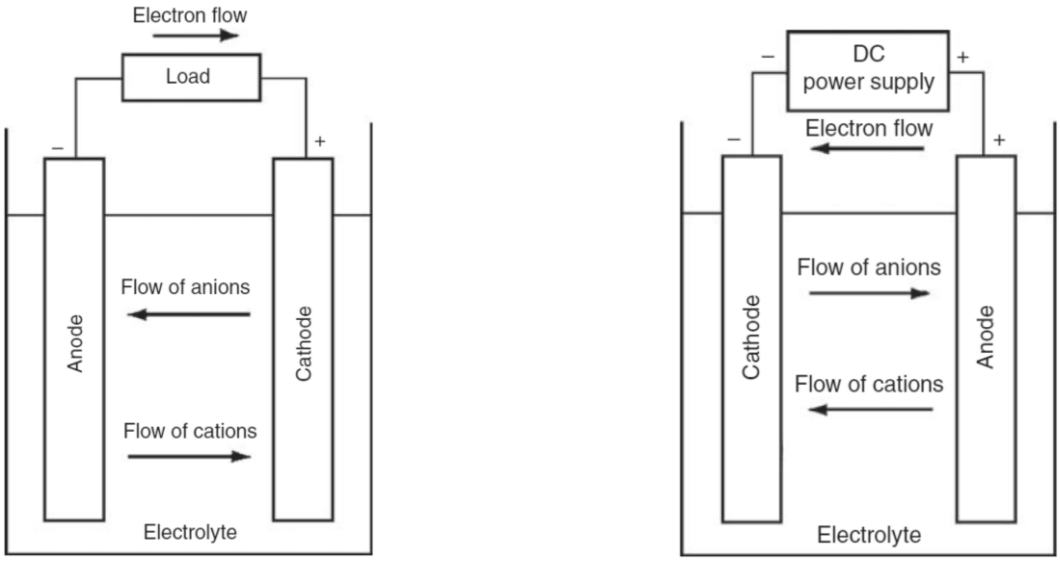

Figure 2.1: Schematic representation of the working of an electrochemical cell.

The redox reaction is divided into two half-cell reactions with the absorption of electrons by the cathode (I) and the release of electrons by the anode (II):

$$\text{Cathode:} \quad aA + n \cdot e^- \rightleftharpoons cC \tag{2.1}$$

$$\text{Anode:} \quad bB \rightleftharpoons dD + n \cdot e^- \tag{2.2}$$

Both the reactions together form the full cell reaction:

$$aA + bB \rightleftharpoons cC + dD \tag{2.3}$$

where A is the positive electrode (cathode), B the negative electrode (Anode) and n the number of electrons (see **Figure 2.1**). The cathode and the anode have standard

potentials (E^0), respectively. These standard potentials are a function of the Gibbs free energy ($-\Delta G^0$) and the number of electrons (n) involved in the stoichiometric reaction:

$$E^0 = \frac{-\Delta G^0}{nF} \tag{2.4}$$

where F is the Faraday constant (≈ 96487 C or 26.8 Ah). The driving force in a cell reaction is the change in the Gibbs free energy ($-\Delta G^0$) which enables a battery to deliver electrical energy to the external circuit. Since it is practically impossible to determine directly the standard potential of a single electrode, they are measured with reference to a standard electrode (Standard Hydrogen Electrode (SHE) at T = 25 °C and P = 1 bar). Therefore in a nonstandard environment (different electrode at different temperatures and pressures) the potential of a cell (E_{cell}) is given by the Nernst equation [7]:

$$E_{cell} = E^0_{cell} - \frac{RT}{nF}\ln Q \tag{2.5}$$

where E^0_{cell} is the standard cell potential, R the gas constant, T the absolute temperature and Q the reaction quotient.

The determination of the performance of LIBs is experimentally and theoretically determined through many parameters. Some of the important parameters are the cell potential or more specifically the nominal working potential of the cell, the rate capability, the charge capacity, the energy and power of the cell. Although all these parameters can be determined via experimental methods it is also possible to calculate the parameters theoretically from the thermodynamics of the cell reactions. The experimentally determined parameters are more practical than the theoretical values.

The cell potential can be derived from the maximum accessible energy, which is the Gibbs free energy ΔG^0. The energy density depends on the capacities and operating potentials of

the respective electrodes. Thus it is possible to select electrode materials that can give high energy. This is done by using electrodes that have the largest difference in electrochemical potential and thus calculated from the following equation:

$$U^0 = E_+^0 - E_-^0 = \Delta E^0 = \frac{-\Delta G^0}{nF} \quad 2.6$$

where U^0 is the cell potential in V, E_+^0 the positive electrode potential and E_-^0 the negative electrode potential.

In order to determine the rate capability of the cell, it has to be charged and discharged at different current densities (j). The current density is the electric current per unit mass or area. In this work the gravimetric units are used. This can be calculated from the equation [1]:

$$j(A.g^{-1}) = \frac{i(A)}{m(g)} \quad 2.7$$

where i is the current in A and m the mass used in g. The charge discharge rate or C rate is a term used in order to describe the time it will take to either have the cell fully charged or discharged. The C rate can be determined as follow [7, 8]:

$$C = \frac{i(A)}{theoretical\ capacity\ (Ah)} \quad 2.8$$

where for example C/10 indicates a 10 hour full charge or discharge and C/20 a 20 hour full charge or discharge. It is also important to note that the rate at which a cell is charged or discharged is a function of the total delivered capacity where a high C rate compromises the capacity.

The charge capacity (Q) is a very important parameter as this is the total amount of charge available from a cell. It can be determined by integrating the total current over the total charge or discharge time within specified potential limits with units in Ah [7].

$$Q = \int_{t2}^{t1} i(t)\, dt \qquad 2.9$$

The theoretical specific capacity of the cell can be calculated by using Faraday's 1st law of electrochemistry [9]:

$$C_s = n\frac{F}{M}(1/3.6) \qquad 2.10$$

where n is the number of electrons involved in the stoichiometric reaction, F the Faraday constant (≈ 96487 C.mol^{-1} or 26.8 Ah.mol^{-1}) and M is the molar mass of the electrode material in g.mol^{-1}. The value $(1/3.6)$ is a conversion constant to obtain units in mAh.g^{-1}.

The quantity of electrical energy per unit mass provided by a cell is termed the theoretical specific energy and can be calculated as follow [7]:

$$E_{th} = \frac{nF\Delta E^0}{\sum_i M} \qquad 2.11$$

where ΔE^0 is the difference in the electrode potentials (i.e. $E_+^0(cathode) - E_-^0(anode)$).

The energy density of a cell can also be determined experimentally which gives a more practical quantity in units of Wh.kg^{-1}. This is calculated from the product of the nominal working potential and the specific capacity [7]:

$$E = C_s \times \mathrm{V} \qquad 2.12$$

The comparison of the rate capability of cells or the amount of power delivered per unit mass is termed the power density. The cell has an internal resistance r with a load R than the current through the cell according to Ohm's law is:

$$I = \frac{V_{oc}}{(R+r)} \qquad 2.13$$

where V_{oc} is the open circuit voltage. The power output per unit mass can thus be calculated with the following equation [7]:

$$P = \frac{I^2 R}{m} = \frac{V_{oc}^2 \mathrm{R}}{m(R+r)^2} \qquad 2.14$$

It is observed from **equation 2.14** that the power is proportional to the open circuit potential. Also with higher current there will be more power distributed to the internal resistance and heat will be generated in the cell. The power output is mainly restricted by the internal resistance.

A LIB converts chemical energy into electrical energy through a controlled thermodynamically chemical reaction. When discharging a LIB the Li ions diffuse through the electrolyte from the anode to the cathode and from the cathode to the anode when charged. The Li ions which are the guest species can thus diffuse reversibly into / out from a host matrix, which is the electrode material also known as the insertion compound, during the charge / discharge process. The diffusion of Li ions through the electrolyte is accompanied by a redox reaction. Thus, by convention, the reduction reaction with the diffusion of Li ions into the host matrix and simultaneously the gain of electrons from the outer circuit takes place at the cathode. The oxidation reaction takes place at the anode with the Li ions diffusing out of the host matrix and a simultaneous loss of electrons to the

outer circuit. This flux of electrons from the electrodes causes a current that can power a load. The anode and the cathode are electrically separated by a porous polymeric membrane (see **Figure 2.2**).

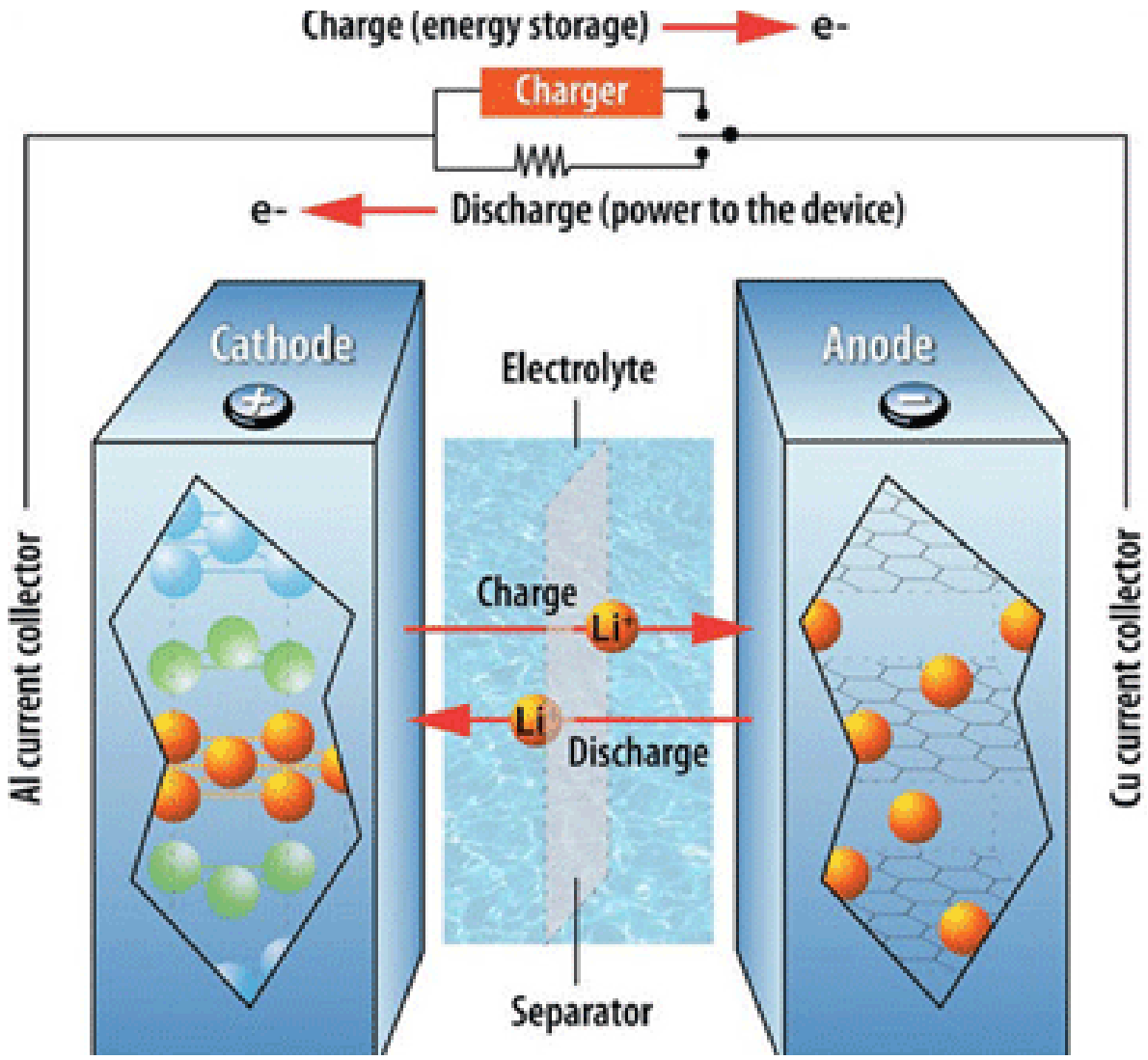

Figure 2.2: The working of a LIB [10].

2.3. Cathode Material Electrodes

The first feasible inorganic intercalation compound for non-aqueous rechargeable batteries with high specific power density was proposed by Whittingham [11] as TiS_2 during the 1970's. This material has been restricted for commercialization as Li_xTiS_2/Li cells due to the difficulties with practical non-aqueous batteries and reversible deposition over lithium cathodes. In the early 1980's Mizushima *et al*. [12] (Goodenough's group at the University of Oxford at the time) proposed the layered $LiCoO_2$ cathode material with a α-$NaFeO_2$ structure as cathode material for LIBs. This material was further developed and commercialized in the following 10 years by Sony Co., Japan [13]. The $LiCoO_2/C$ (cathode/Anode) was the first commercialized LIB in a non-aqueous electrolyte which is still popular in modern day mobile electronics applications [14]. Since then, research on and commercialization of other cathode materials has increased and today can be divided into three different families [14-17]:

I. The family of the spinel structured cathodes (**Figure 2.3 (a)**) with its archetype being the $LiMn_2O_4$ that are discussed in **section 2.2.1.**

II. The second family is the layered structured cathodes (**Figure 2.3 (b)**), to which the $LiCoO_2$ cathode belongs to, with its archetype being the $LiMn_{0.33}Ni_{0.33}Co_{0.33}O_2$ that are discussed in **section 2.2.2.**

III. The third family is the olivine structured cathodes (**Figure 2.3 (c)**) with its archetype being the $LiFePO_4$ [18, 19]. This material is plagued by its low intrinsic electronic conductivity [20].

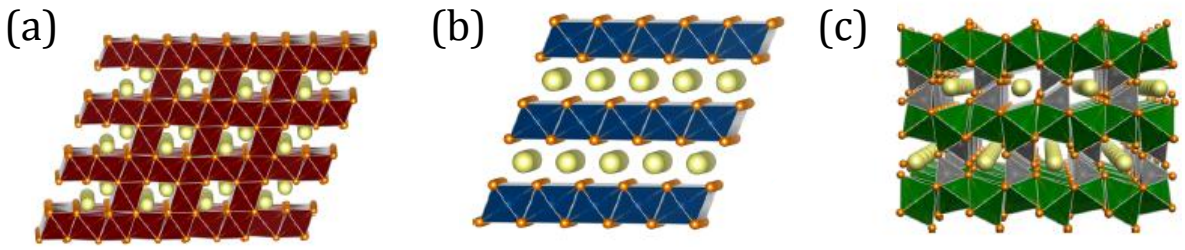

Figure 2.3: Visual illustration of the crystal structures of the different families of cathode materials: (a) Spinel structure, (b) Layered structure and (c) Olivine structure [21].

2.3.1. Spinel Structured Cathodes

A considerable amount of research has gone in to replacing the layered $LiCoO_2$ as cathode material due to the high cost and toxicity of the Co. The spinel $LiMn_2O_4$ has thus received considerable attention as a cathode material for LIBs as it is a low cost and eco-friendly cathode material that can replace the $LiCoO_2$ cathode material.

2.3.1.1. $LiMn_2O_4$

The use of spinel $LiMn_2O_4$ as cathode material for Li insertion was first proposed by Thackeray *et al.* [22] in 1983. The $LiMn_2O_4$ spinel cathode material has ever since been extensively researched and developed, particularly at Bellcore Laboratories [4, 5, 23-25] in order to improve on its properties as cathode material for LIBs [26].

The spinel $LiMn_2O_4$ has the general formula AB_2O_4 with space group symmetry $Fd\bar{3}m$ shown in **Figure 2.3 (a)**. The edge shared Mn_2O_4 octahedral framework of the spinel $LiMn_2O_4$ allows for good structural stability with Li ions being reversibly inserted and

extracted at regular tetrahedral sites. This structure forms a face centered cubic (*fcc*) close packing with the O atoms occupying the 32e sites. The A cations (Li) occupy tetrahedral 8a sites and the B cations (Mn) are located in the octahedral 16d sites while the octahedral 16c sites remain vacant [27]. Thus, when the Li diffuse, it does so from the tetrahedral 8a sites to the neighboring vacant octahedral 16c sites and to then to the next tetrahedral 8a site. These vacant octahedral and tetrahedral interstitial sites provide the three dimensional structure pathways for Li diffusion [22].

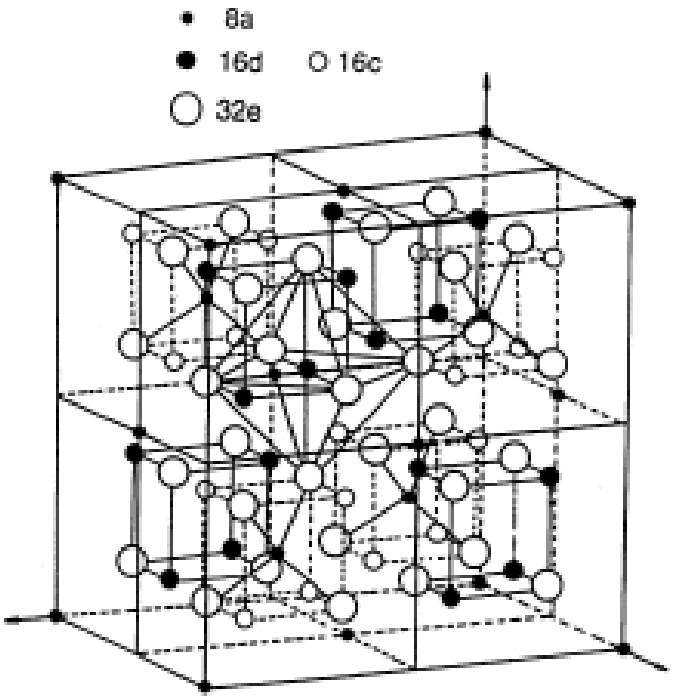

Figure 2.4: Schematic representation of the primitive cell of the $LiMn_2O_4$ spinel [28].

The Li ions are extracted from the tetrahedral sites of the spinel structure at ~ 4 V in a two stage process [29]. The high voltage associated with the two process reaction that takes place is due to the Li ions that are situated in the deep energy well 8a sites (see

Figure 2.5 (a)) and the high activation energy, ΔE, needed for the Li ions to diffuse from one 8a site to the next via an energetically unfavorable neighboring 16c octahedron site as shown in **Figure 2.5 (a)** [30].

Upon increased Li ion insertion ($1 < x < 2$) into the spinel $Li_{1+x}Mn_2O_4$ at a potential of ~ 3 V, the Li ions are inserted into the octahedral 16c sites of the structure. Due to the 16c octahedral sites that share faces with the 8a tetrahedral sites, electrostatic interactions between the Li ions cause an immediate displacement of the Li ions, in the 8a tetrahedral sites, into vacant 16c octahedral sites. Also, the average valence of the Mn ions significantly decreases with the further insertion of Li ions [31]. This leads to a Jahn-Teller distortion that is accompanied by the degradation of the capacity [32]. The reason for the capacity decrease is due to leaching of the increased lower valence Mn ions into the electrolyte. The Jahn-Teller distortion reduces the crystal symmetry from cubic (c/a = 1.0) to tetragonal symmetry (c/a = 1.16). This reaction results in the cubic spinel $LiMn_2O_4$ evolving to $Li_2Mn_2O_4$ with a stoichiometric rock salt composition on the surface of the electrode particle. The octahedral 16c sites have lower energy wells as shown in **Figure** 2.5 **(b)**. In the rock salt structure the activation energy for the diffusion of Li ions out of the octahedral sites is less than the activation energy needed for the removal of Li ions from the tetrahedral sites in the $LiMn_2O_4$ spinel structure. This indicates that the activation energy needed for diffusion of Li ions is lower in the rock salt phase compared to the spinel phase.

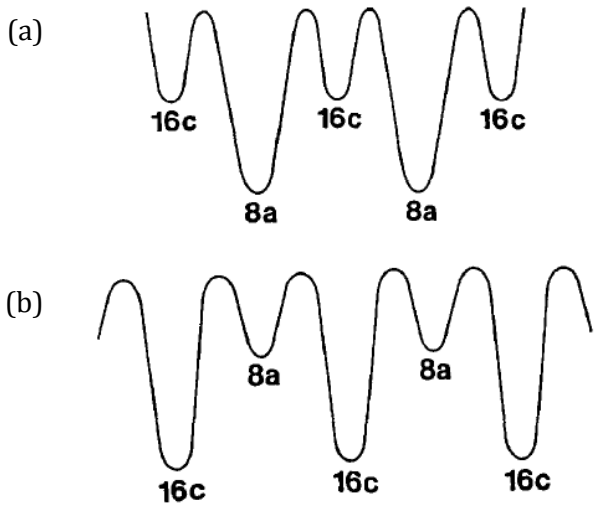

Figure 2.5: Schematic representation of the difference in energy sites for (a) spinel $LiMn_2O_4$ and (b) rock salt $Li_2Mn_2O_4$ [33].

In order to circumvent the capacity degradation, the potential window needs to be limited between 4.2 V to 3.5 V as the spinel $Li_xMn_2O_4$ demonstrates good structural stability for reversible Li ion insertion/extraction in the range $0 < x < 1$. Nevertheless, this limits the accessible capacity of $Li_xMn_2O_4$ to ~ 120 mAh/g and a practical operating voltage of ~ 4 V [34].

Attempts to mitigate the limitations of this material include research on slightly modifying the composition of the spinel cathode by substituting a small fraction of the Mn ions with Li, Mg or Zn [35]. This causes an increase in the average Mn ion valency to above 3.5 due to charge compensation. The substitution of the Mn ions with Li, Mg or Zn also induces shrinkage in the lattice due to the smaller ionic radii of these ions which in turn will increase cycle stability. Unfortunately this strategy causes a decrease in the total capacity with an increase in the substituted ion. Other dopants such as the transition metals Co, Cr, Fe, Cu and Ni, were also investigated as possible substitutions in the spinel $LiMn_{2-x}M_xO_4$ ($0 < x < .033$) [36, 37].

2.3.1.2. $LiMn_{1.5}Ni_{0.5}O_4$

Sigala et al. [37] substituted Mn with Cr in the spinel $LiMn_{2-x}M_xO_4$ up to x = 1, where they observed a higher discharge voltage plateau. It was observed that the plateau at ~ 4 V decreased and a plateau at ~ 4.8 V increased with increasing Cr content in the range 0.25 to 0.75. It was found that the total specific capacitance of the $LiCr_{0.25}Mn_{1.75}O_4$ and $LiCr_{0.5}Mn_{1.5}O_4$ cathodes was higher than the $LiMn_2O_4$ cathode. This meant that the $LiCr_{0.25}Mn_{1.75}O_4$ and $LiCr_{0.5}Mn_{1.5}O_4$ cathodes had higher specific energy density than the spinel $LiMn_2O_4$ cathode. Further investigation undertaken by Zhong et al. [38] on doping $LiMn_2O_4$ with a higher Ni content ($0 \leq Ni \leq 0.5$), revealed that $LiMn_{1.5}Ni_{0.5}O_4$ is the most promising and attractive due to its good cycling ability and its relatively high capacity with one dominant discharge plateau at ~ 4.8 V. This Ni doped spinel thus started receiving considerable attention due to its suitability for especially electric vehicles (EV). It was pointed out by Zhong et al. [38, 39] that the high voltage plateau originated from the oxidation of Ni^{2+} to Ni^{4+} ions which is a two electron process. There is a fundamental difference in the electrochemistry between the spinel $LiMn_2O_4$ and the spinel $LiMn_{1.5}Ni_{0.5}O_4$ in that the redox reaction takes place on Ni and the Mn remains in the 4+ valence state. This behaviour was explained by Gao et al. [39] with respect to **Figure 2.6**. The 3*d* electronic levels of Mn and Ni are split by the crystal field into e_g and t_{2g} levels. Among the four $3d^4$ electrons, with a majority of spin (↑), three electrons are on the t_{2g}(↑) level and one on the e_g(↑) level. The $3d^8$ electrons of Ni^{2+} have six electrons on the t_{2g}(↑↓) levels and two electrons on the e_g(↑) level. As an electron is removed from Mn^{3+}, it is removed from Mn e_g(↑), which has an electron binding energy at ~ 1.5 – 1.6 eV, and this is on the 4.1 V plateau (see **Figure 2.7** at label **II**). When there are no more electrons left on Mn e_g(↑), meaning that all Mn are oxidised to Mn^{4+}, electrons are removed from Ni e_g(↑↓) which has

an electron binding energy of ~ 2.1 eV, the voltage plateau moves up to 4.7 V (see **Figure 2.7** at label **I**) because of increased energy needed to remove the electrons.

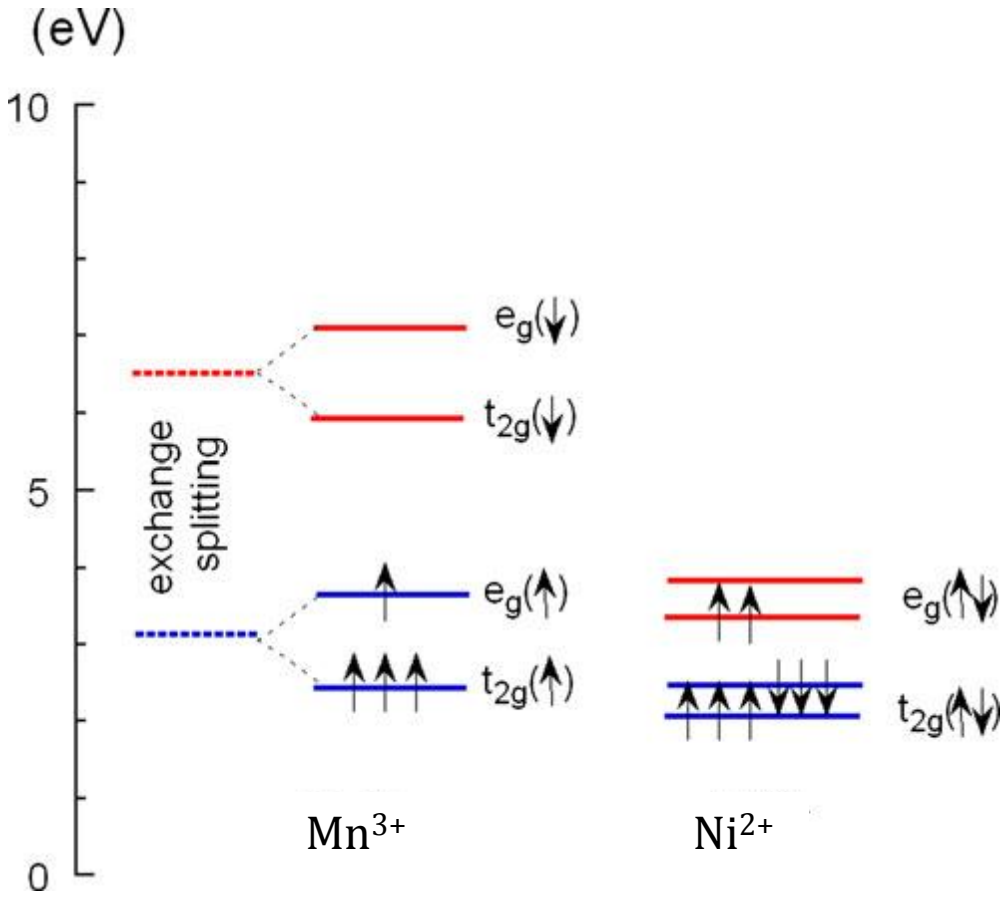

Figure 2.6: Schematic diagram showing the 3d electronic levels of Mn^{3+} and Ni in the $LiMn_{2-x}Ni_xO_4$ spinel. Note that Ni^{2+} favours the low spin configuration in $LiMn_{2-x}Ni_xO_4$ [40].

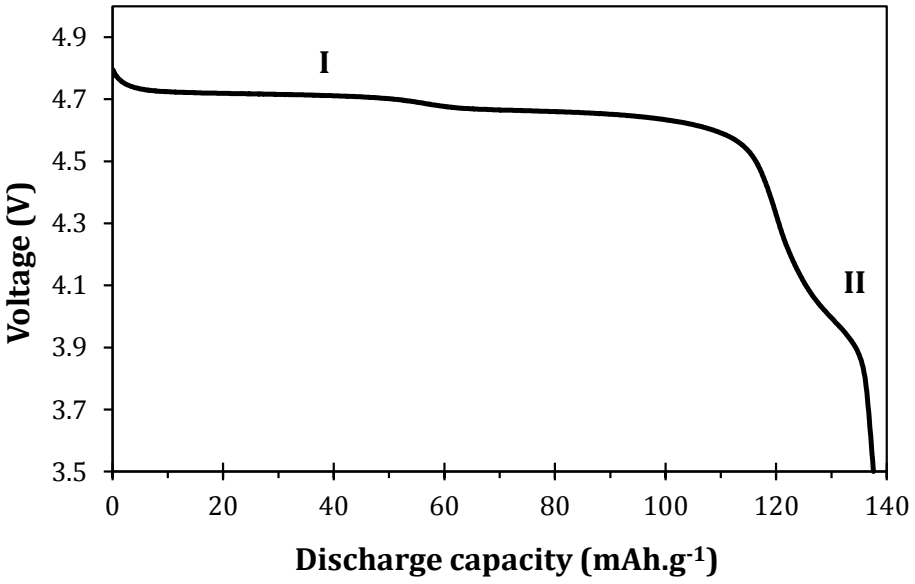

Figure 2.7: A typical discharge profile of $LiMn_{1.5}Ni_{0.5}O_4$.

$LiMn_{1.5}Ni_{0.5}O_4$ has two possible crystallographic structures, the cation ordered spinel with a space group symmetry $P4_332$ (face centered cubic) and the cation disordered spinel with space group symmetry $Fd\bar{3}m$ (simple cubic) as shown in **Figure 2.8**. The cation disordered spinel shows a higher Mn^{3+} content compared to the cation ordered spinel with a higher Mn^{4+} content. For $LiMn_{1.5}Ni_{0.5}O_4$ with the $Fd\bar{3}m$ space group (disordered), the Li ions are found in the 8a sites, the Mn and Ni ions are randomly distributed in the 16d sites. The O ions occupy the 32e sites and form a cubic closed packed structure. With the $LiMn_{1.5}Ni_{0.5}O_4$ containing the $P4_332$ space group (ordered) the Li ions are found in the 8c sites while the Mn and the Ni ions are located in the 12d and 4b sites, respectively [41]. In this case the Mn and Ni ions are ordered regularly and thus the ordered spinel.

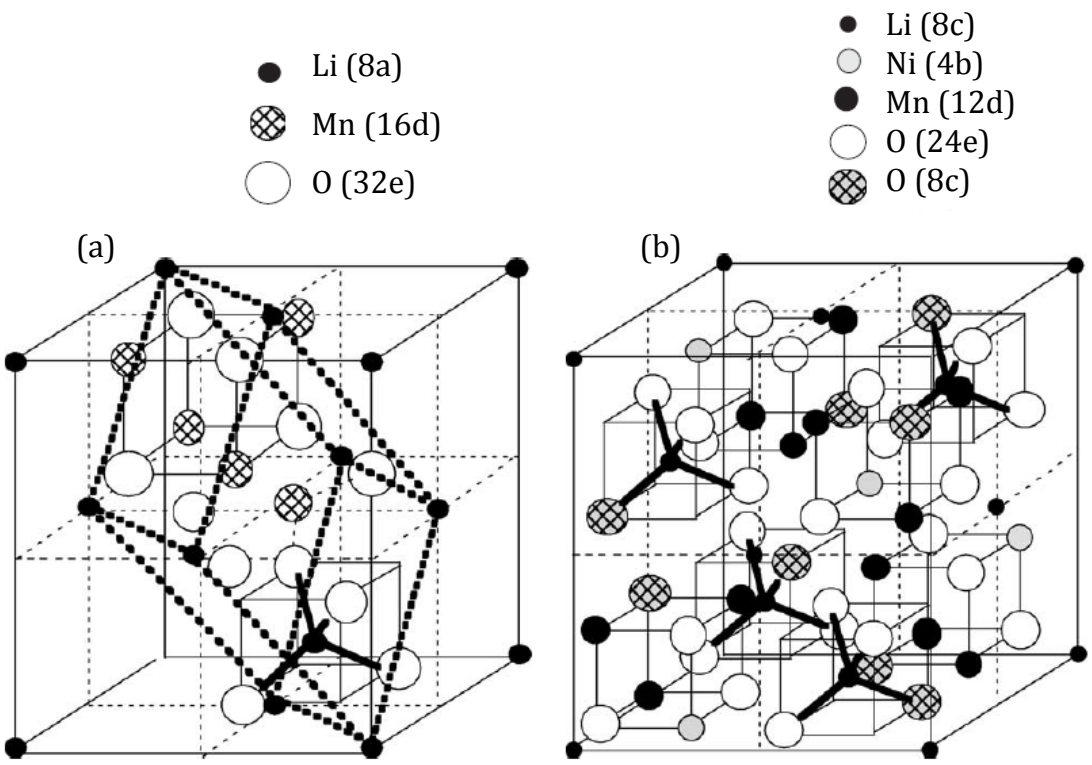

Figure 2.8: Schematic representation of (a) the **$Fd\bar{3}m$** disordered structure and (b) the ***P*4$_3$32** ordered structure [42].

The efforts to distinguish between the two structures, cation ordered and disordered, are inspired by a superior disordered phase with better electrochemical properties compared to its cation ordered counterpart. Different structures can be obtained by varying syntheses methods and parameters, for example by controlling the cooling rate [43]. The order-disorder transition was pointed out by Zhong et al. [38] and Myung et al. [44], although the transition was not named in the mentioned literature, by comparing the electrochemical performance and phases on both sides of the transition temperature. Kunduraci and Amatucci [45] experimentally determined the transition temperature to be between 700 °C and 730 °C.

The loss of oxygen in the lattice leads to Mn^{4+} being converted to Mn^{3+} in order to keep electric neutrality. This in turn leads to a larger cell volume (or an increased *a* lattice) due to the larger ionic radii of Mn^{3+} (58 pm) compared to Mn^{4+} (53 pm). Furthermore, with higher content of Mn^{3+} the dissolution of Mn is increased, increasing the polarization and decreasing the cyclebility [46]. This causes a drastic capacity fade that will decrease the lifetime of the cathode material. It was also shown that an increased Mn^{3+} increases the spinel's conductivity and would in fact also increase the power of the spinel cathode material [45]. Therefore, recent efforts have been towards controlling the Mn^{3+}/Mn^{4+} ratio. These include four methods used up to date; (i) control of the cooling rate after annealing [43] which is energy intensive due to the increased time needed for furnace operation; (ii) the partial substitution of Ni and / or Mn with elements such as Co, Al, Ti, Fe, Cr, Ru or Mg [46-51] which is not always cost effective and sometimes toxic; (iii) a combined post-synthesis annealing and partial substitution of Ni with Cr [46]; and (iv) long-hour acidic treatment [52]. It is evident that these aforementioned methods are not plausible for commercialization due to their intensive energy needs and toxicity. In conclusion on $LiMn_{1.5}Ni_{0.5}O_4$, the oxygen deficiency is a key factor in controlling the performance of the high voltage spinel and more research is needed in order to come up with a plausible method to control the Mn^{3+}/Mn^{4+} ratio. Therefore, in this work a novel microwave assisted synthesis method, that is not energy intensive and non-toxic, is employed to control the Mn^{3+}/Mn^{4+} ratio.

2.3.2. Layered Structured Cathodes

The higher capacity offered by layered cathode materials compared to the spinel cathode materials have drawn much attention. The most popular layered structured cathode

material is the $LiCoO_2$ that was first commercialized by Sony in 1992 [13]. Due to the practical limited energy density, toxicity and high cost of the Co of this layered cathode material, a huge amount of interest has been sparked in the development of alternative layered cathode materials, whereby the Co content is reduced or ultimately removed.

2.3.2.1. $LiMn_{0.33}Ni_{0.33}Co_{0.33}O_2$

Ever since the first report, by Liu et al. [53], on layered cathode materials with di- and tri-transition metal oxides these have become promising new positive electrode materials for LIBs. The layered $LiMn_{0.33}Ni_{0.33}Co_{0.33}O_2$ particularly has attracted much attention due to its high reversible capacity, cost effectiveness, eco-friendliness and enhanced safety compared to the famous $LiCoO_2$ [54-57]. The layered cathode materials have the general formula …ABCABC… with O ions arranged nearly cubic close packed, and with the Li and transition metal ions situated in alternative layers of the octahedral sites (see **Figure 2.9**).

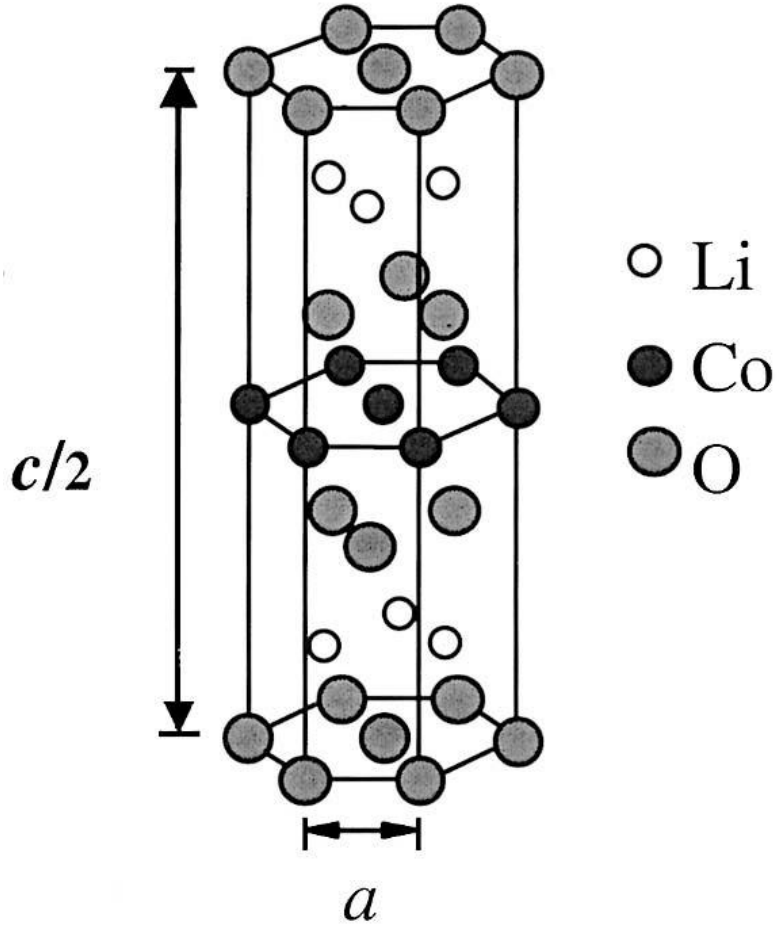

Figure 2.9: Schematic representation of the crystal structure of the layered $LiCoO_2$ [58].

This layered structure is ideal for Li diffusion, nonetheless when mixing occurs between the transition metal ions and Li ions the Li diffusion is hindered and Li mobility is decreased (see **Figure 2.10 (a & b)**) [54, 59]. In the layered $LiCoO_2$ only 0.5 Li per formula can be reversibly extracted (charged up to 3.9 V) without causing a dramatic structure transformation [60]. Further extraction of Li ions would cause evolution of oxygen gas from the Li deficient phase. This phenomenon is known as over charge. Attempts to mitigate this phase transformation lead to the replacement of Co with Ni to obtain a $LiNiO_2$.

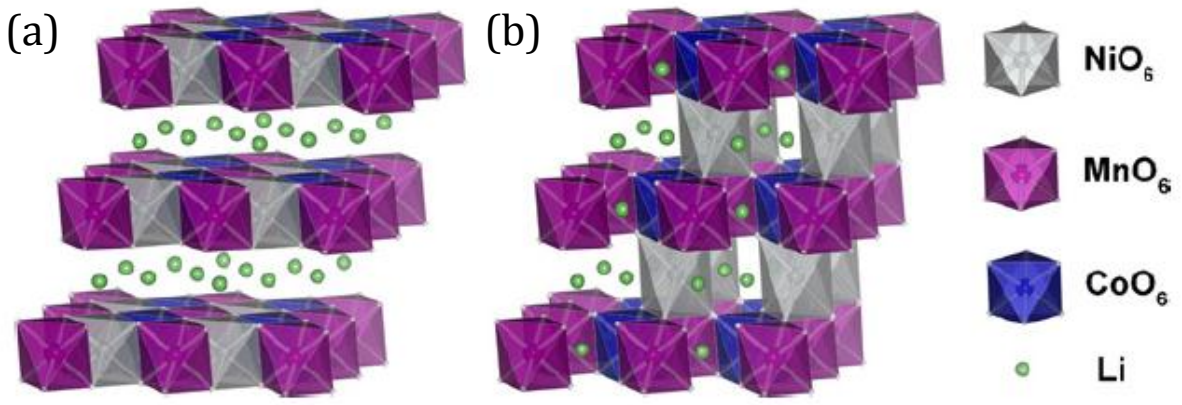

Figure 2.10: Schematic representation of (a) the ideal layered $\boldsymbol{\alpha - NaFeO_2}$ structure of $LiMn_{0.33}Ni_{0.33}Co_{0.33}O_2$ without Li-Ni intermixing and (b) layered $\boldsymbol{\alpha - NaFeO_2}$ structure of $LiMn_{0.33}Ni_{0.33}Co_{0.33}O_2$ with a high content of Li-Ni intermixing [59].

This layered $LiNiO_2$ has the same layered structure as $LiCoO_2$ and is more cost effective and less toxic [58]. However, the $LiNiO_2$ comes with its own problems; (i) the difficulty in synthesizing a pure $LiNiO_2$ without impurity phases causing Li ions and Ni^{3+} ions mixing in the Li plane [61, 62]; (ii) the Jahn-Teller distortion associated with the low spin Ni^{3+}:d^7 ($t_{2g}^6 e_g^1$) ions [63]; (iii) the irreversible phase transformation occurring during the charge discharge process [64]; and (iv) the exothermic release of O at elevated temperatures and safety concerns in the charged state [65, 66]. Therefore $LiNiO_2$ was not seen as a promising replacement. $LiMnO_2$ is also isostructural with $LiCoO_2$ and Mn is environmentally friendly which made it a possible alternative for $LiCoO_2$. The practical reversible capacity of $LiMnO_2$ is severely limited due to the structural transformation, to spinel $LiMn_2O_4$, during cycling since the transformation is irreversible [67]. In order to circumvent these phase transformations, Mn is partially substituted with Co and Ni with the best ratio being the M = 0.5 giving the layered cathode material $LiMn_{0.5}Ni_{0.5}O_2$.

Because $LiMn_{0.5}Ni_{0.5}O_2$ suffers from a strong propensity for Li-Ni mixing, this material is plagued by an inferior rate capability [68]. It was shown that by doping $LiMn_{0.5}Ni_{0.5}O_2$ with Co, the Li-Ni mixing is reduced which has a beneficial effect on the rate capability [67]. Thus the layered cathode material $LiMn_{0.33}Ni_{0.33}Co_{0.33}O_2$ has emerged as the material with the best Li : Ni : Co ratio (also known as 1:1:1). However, the layered $LiMn_{0.33}Ni_{0.33}Co_{0.33}O_2$ cathode material still suffers from oxygen loss when charged beyond 4.2 V which leads to an irreversible capacity loss. In the next section stabilization of this cathode material is discussed.

2.3.2.2. $x(Li_2MnO_3)\bullet(1-x)LiMO_2$ (M = $Mn_{0.13}Ni_{0.13}Co_{0.13}$)

In 2001 the compositions $x(Li_2MnO_3)\bullet(1-x)LiMn_{0.5}Ni_{0.5}O_2$ were first described by Lu et al. [69] as a solid solution as $Li[Ni_xLi_{(1/3-2x/3)}\text{-}Mn_{(2/3-x/3)}]O_2$ with $0 < x < 0.5$. With further work done at Argonne National Laboratory (ANL) by Thackery and co-workers [70-73] it was proposed that the composition be considered as a composite or "integrated" structure composed of nanodomains with two different local structures. These claims are based on the existence of Li_2MnO_3 nanodomains in the composite electrode of $x(Li_2MnO_3)\bullet(1-x)LiMn_{0.5}Ni_{0.5}O_2$ [67]. In general the charging, which is the oxidation of transition metals, of layered cathode material is limited by the amount of transition metals in the trivalent state. Therefore, Li_2MnO_3 (consisting of Mn^{4+}) was considered to be electrochemically inactive. It is thus considered that Li_2MnO_3 acts as a stabilizer and insulator in the electrode [74]. Conversely, Li-excess Mn layered oxides [70-73] and even pure Li_2MnO_3 [75] are shown to be electrochemically active. This means that there exists some trace amount of Mn in the Mn^{3+} valence state. When charging below 4.4 V Li ions are extracted from the electrochemically active $LiMO_2$ and Ni^{2+} is oxidised, after which Li_2O is

extracted from Li_2MnO_3 above 4.4 V. These types of positive electrodes still attract a huge amount of interest due to its high capacity of 200 $mAh.g^{-1}$ – 300 $mAh.g^{-1}$. To further improve on these layered cathode materials, in 2009 Dahn's group published works on Al substitution for Co [76, 77]. In the following years there were more works reported on Al and other metals (Ti and Fe) doping, reducing the Co content [78-81]. The Al doping showed better structural and thermal stability. Nevertheless, the Al doping caused a decrease in the discharge capacity, due to the Al that is redox inactive. Li et al. [81] also showed that a high Mn content is detrimental to both high rate and thermal stability.

In this work, the layered $Li_{1.2}Mn_{0.54}Ni_{0.13}C_{0.13}O_2$ cathode material is also doped with Al, but replacing the Mn. This is possible due to the similar but slightly bigger ionic radius of Al^{3+} compared to Mn^{4+}. This allowed the opportunity to reduce the Mn^{4+} content and also increase the *c* lattice allowing faster Li diffusion and hence increase the rate capability. With the use of the microwave assisted synthesis method it is also possible to change the oxidation state of the Mn. Therefore, part of the work in this thesis is also to combining the Al doping and the microwave assisted synthesis method.

2.4. Electrochemical Capacitors

Capacitors are charge storage devices and in general can be divided into three types:

I. Electrostatic capacitors,

II. Electrolytic capacitors, and

III. ECs, which is the topic of this section.

In brief, electrostatic capacitors consists of two metal plates parallel to each other and separated by a dielectric that is a non-conducting material (i.e. air or ceramic) as shown in **Figure 2.11** [82]. With the two plates carrying charge of equal magnitude but opposite sign, a potential difference (ΔV) will exist between them. The amount of charge that is measured in Coulombs (Q) stored on the plates is linearly proportional to the potential difference between the conducting plates ($Q\ \alpha\ \Delta V$). Therefore, the capacitance that is measured in Farads (F) can be defined as follow:

$$C = \frac{Q}{\Delta V} \qquad 2.15$$

As mentioned, *vide supra*, the charge is stored on the plates and thus the capacitance is also proportional to the surface area of (A) of the plates and inversely proportional to the distance between the plates (d). The formula for capacitance is described as:

$$C = \frac{\varepsilon_0 A}{d} \qquad 2.16$$

where ε_0 is dielectric constant [83]. Two other important parameters of capacitors are its energy and power density. The energy (E), in Joule, stored in a capacitor is related to the charge (Q) at each interface and the potential difference between the two plates is therefore directly proportional to the capacitance descried follow:

$$E = \frac{CV^2}{2} \qquad 2.17$$

where C is the capacitance and V the potential difference. This formula will be discussed more practically in **chapter 7**. Power, in general, is the rate at which energy is delivered per unit time. The power density will also be discussed in more detail in **chapter 7**.

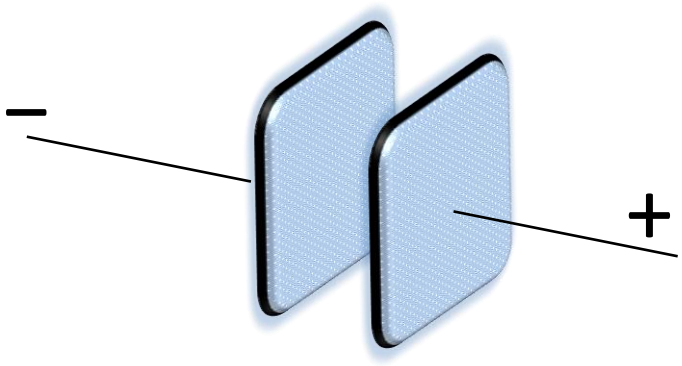

Figure 2.11: Schematic of a simplified parallel plate capacitor.

Electrolytic capacitors are structurally similar to electrostatic capacitors except for the addition of a conductive electrolyte that is in direct contact with the electrodes. A thin oxide layer formed on the plates serve as the dielectric, which is typically Al_2O_3 on Al plates that will result in a higher capacitance per unit volume compared to the electrostatic capacitors [84].

ECs, also called supercapacitors or ultracapacitors (commercial names), themselves are also divided in three different groups, (i) electrochemical double layer capacitors that store energy by means of ion adsorption (see **section 2.3.1**), (ii) pseudocapacitors with an energy storing mechanism of fast surface redox reactions (**section 2.3.2**), and (iii)

asymmetric ECs that make use of both the ion adsorption and fast surface redox reactions mechanisms to store energy.

2.4.1. Electrical Double Layer Capacitors (EDLC)

EDLC are ECs that store their charge electrostatically and were first defined by Helmholtz in 1879 [85]. Typically, the electrodes used for EDLC are Carbon [86]. The electrostatic charge storing allows reversible ion adsorption from the electrolyte onto active material that is electrochemically stable and has a high surface area. Charge separation occurs on polarization at the electrode-electrolyte interface producing the double layer capacitance:

$$C = \frac{\varepsilon_r \varepsilon_0 A}{d} \qquad 2.18$$

where ε_r is the electrolyte dielectric constant, d is the effective thickness of the double layer (charge separation distance) and A the surface area of the electrode. The double layer capacitance obtained is a function of the electrolyte used. Specific capacitance achieved with aqueous electrolytes (acidic or alkaline) is generally higher than in organic electrolytes [87]. The advantage of using an organic electrolyte is their ability to sustain a higher operating voltage. According to **equation 2.17**, that shows that the energy is proportional to the voltage square, EDLC in organic electrolytes will have a much higher energy at the same capacitance compared to EDLC in aqueous electrolytes. There are no redox reactions taking place at the EDLC electrodes due to the electrostatic charge storage and thus allow for very fast energy uptake and delivery that is interpreted as high power performance. In addition, this energy storage mechanism also allows for a very high amount of cycling due to the reversibility of the process. However, as a consequence of the electrostatic surface charging the mechanism the EDLC suffer from a limited energy density.

2.4.2. Pseudocapacitors

The main difference between EDLC and pseudocapacitors is the energy storage mechanism, where pseudocapacitors make use of fast redox reactions on the surface of the electrodes with the electrolytes. The accumulation of electrons on the surface of the electrode is due to the faradaic process where the electrons produced are transferred across the electrode-electrolyte interface. The redox active materials typically used for pseudocapacitors are metal oxides such as RuO_2 [88], Fe_3O_4 [89], MnO_2 [90] (see **chapter 7**) and even electronically conductive polymers [91]. Recently the use of metallophthalocyanine was also demonstrated as a good pseudocapacitor [92, 93]. The pseudocapacitance obtained from these electrodes exceeds that obtained by the carbon materials using the double layer charge storage. Due to the redox reactions taking place on the electrode surfaces, these pseudocapacitors suffer from a lack of stability during cycling, as is the case for LIBs.

2.4.3. Asymmetric Electrochemical Capacitors

Asymmetric ECs or sometimes called hybrid super capacitors due to their combined LIB and electrochemical properties (structure) are characterised by their high power and energy densities. These asymmetric ECs make use of a battery like electrode, i.e. , which is the energy source of the cell, and a capacitor like electrode, which is the power source of the cell. Double layer and pseudocapacitance are simultaneously generated in such devices giving rise to the asymmetric electrochemical capacitor. These capacitors have the advantages of both the EDLC, with high power, and the pseudocapacitors, with high energy. Thus asymmetric ECs have good energy and power density while keeping the

good cycling stability (from EDLC) [94]. One of the first designs for asymmetric capacitors was proposed and produced by MP Pulsar (now Elit Co, Kursk, Russia) in 1989 [95]. This original design made use of a $Ni(OH)_2$ based positive electrode and activated C as the negative electrode. This was the start of a huge research topic. The use of different positive electrodes were explore, such as $NiO/Ni(OH)_2$ [96, 97], RuO_2 [98, 99], V_2O_5 [100, 101], CoTPyxPz with graphene oxide [92], MnO_2 [102], Mn2O3/Mn3O4 with reduced graphene oxide [103] to name a few. Also many C materials have been explored as possible negative electrode for asymmetric capacitors, such as activated C, graphene oxide, reduced graphene oxide, C onions, C nanotubes, etc as described by a review article by Gu et al. [95]. In this work graphene oxide and C nanotubes are studied and compared. The positive electrodes are also coated with these C materials in order to increase the electrochemical performance of the asymmetric capacitors.

2.5. Electrochemistry, Microscopy and Spectroscopy Techniques

This section includes the basic principles of all the techniques used for the characterisation of all the materials synthesized.

2.5.1. Cyclic Voltammetry (CV)

One of the first electrochemical characterisations done on the assembled half cells is CV. This is to determine the redox potentials of the cathode material, as well as to determine the Li extraction / insertion behaviour from / into the host matrix.

CV is a potentiodynamic electrochemical measurement technique that obtains information on the electrochemical behaviour of a voltaic cell. It gives information on the thermodynamics of the redox reactions that take place. It can also give information on the electron-transfer reactions. In the CV experiments the potential of the working electrode (the cathode material in this case) versus the reference and counter electrode (Li metal foil in this case) is measured. This experiment consists of scanning the potential of the working electrode using a triangular waveform as depicted in **Figure 2.12.** The electrode potential is thus increased linearly with time at a specific scan rate. In **Figure 2.12** the time range $t_0 - t_2$ represents the first cycle t_1 indicating the start of the reverse sweep and $t_2 - t_4$ indicating the second cycle. During these potential sweeps the current, which results from the electrochemical reactions taking place at the electrode interface, is measured as a function of the potential. Therefore a cyclic voltammogram is a current response plot against the applied potential.

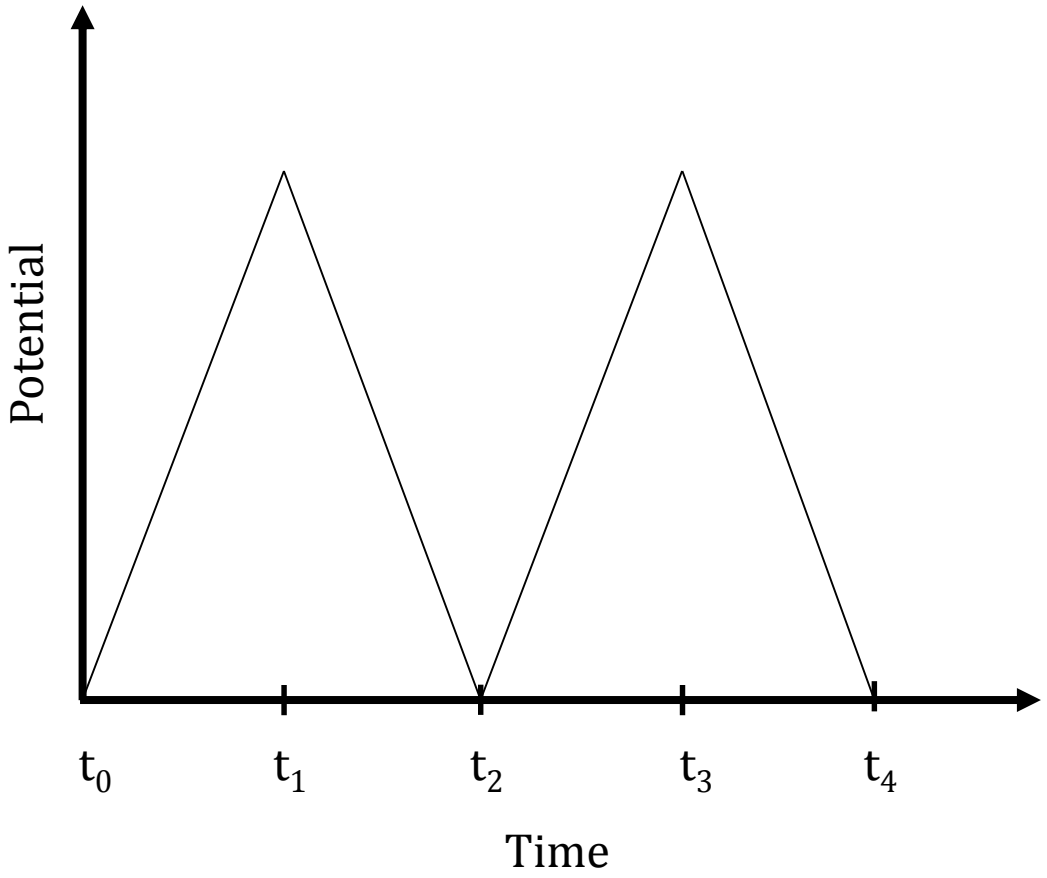

Figure 2.12: The potential profile for two cyclic voltammetry scans.

By taking $LiMn_2O_4$ as a general example with the $LiMn_2O_4$ acting as the cathode material and thus the working electrode and Li metal foil acting as both the counter and reference electrode. A typical cyclic voltammogram obtained from such a cell is shown in **Figure** 2.13 with two pairs of redox peaks. This indicates two stages of Li extraction and insertion from the 8a sites [104]:

$$LiMn_2O_4 \rightleftharpoons Li_{0.5}Mn_2O_4 + \frac{1}{2}Li^+ + \frac{1}{2}e^- \qquad 2.19$$

$$Li_{0.5}Mn_2O_4 \rightleftharpoons 2MnO_2 + \frac{1}{2}Li^+ + \frac{1}{2}e^- \qquad 2.20$$

where **equation 2.19** shows the removal of the first half of the Li ions (oxidation peak at lower potential) and **equation 2.20** the removal of the remaining Li ions (oxidation peak at the higher potential) in the 8a sites.

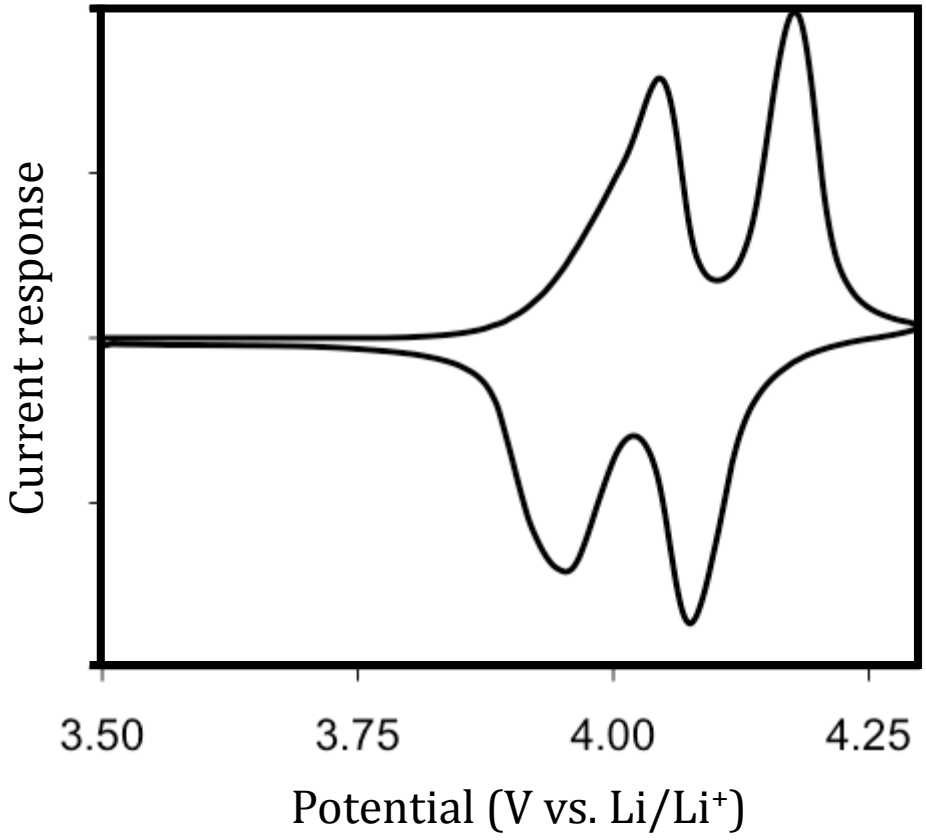

Figure 2.13: A typical cyclic voltammogram showing two redox peaks.

2.5.2. Electrochemical Impedance Spectroscopy (EIS)

A very important electrochemical characterisation technique is EIS. The promise of EIS is that a broad range of the physical and the chemical phenomena can be characterised by a single experimental run encompassing a sufficient range of frequencies. This

electrochemical technique was used in order to study and determine many parameters as can be seen in the chapters following.

Ohm's law dictates that resistance (R) is equal to the potential (V) over the current (I):

$$R = \frac{V}{I} \tag{2.21}$$

Unfortunately this well-known relation is limited to only one circuit element; the ideal resistor. The ideal resistor has several simplifying properties, such as (i) the ideal resistor follows Ohm's law at all currents and voltages, (ii) its resistance is independent of frequency and (iii) AC current and voltage signals through a resistor are in phase with each other. But this is not the case in the real world applications where much more complex circuit elements are involved. Therefore the more general circuit parameter which is the impedance, is used.

Impedance is the measure of the electrical current flow resistance without the above mentioned simplifications. EIS [105] is usually measured by applying an AC potential (sinusoidal) to the electrochemical cell and then measuring the current through the cell. This current response can be analysed as a sum of sinusoidal functions (a Fourier series) at the same frequency but at a different phase. The AC potential signal expressed as a function of time has the form:

$$V(t) = V_0 \sin(\omega t) \tag{2.22}$$

where $V(t)$ is the potential at time t, V_0 the amplitude of the signal and ω is the radial frequency expressed as:

$$\omega = 2\pi f \tag{2.23}$$

The current response signal can be expressed as:

$$I(t) = I_0 \sin(\omega t + \varphi) \tag{2.24}$$

where *I(t)* is the response signal at time *t*, I_0 the amplitude of the response signal and φ is the phase shift. An expression analogous to Ohm's law allows for the calculation of impedance as:

$$Z = \frac{V(t)}{I(t)} = \frac{V_0 \sin(\omega t)}{I_0 \sin(\omega t + \varphi)} = Z_0 \frac{\sin(\omega t)}{\sin(\omega t + \varphi)} \tag{2.25}$$

The impedance is thus expressed in terms of a magnitude, Z_0, and a phase shift, φ. By making use of Euler's relation:

$$exp(j\varphi) = \cos(\varphi) + j\sin(\varphi) \tag{2.26}$$

it is possible to express the impedance as a complex function:

$$Z(\omega) = Z_0 \frac{\sin(\omega t)}{\sin(\omega t + \varphi)} = Z_0 \exp(j\varphi) = Z_0[\cos(\varphi) + j\sin(\varphi)] \tag{2.27}$$

E**quation 2.27** consists of both a real and an imaginary part, where the real part is plotted on the x-axis and the imaginary part on the y-axis producing the "Nyquist plot" as shown in **Figure 2.14 (b)**. This Nyquist plot results from the electrical circuit in **Figure 2.14 (a).** Every point in this graph is the impedance at a specific frequency.

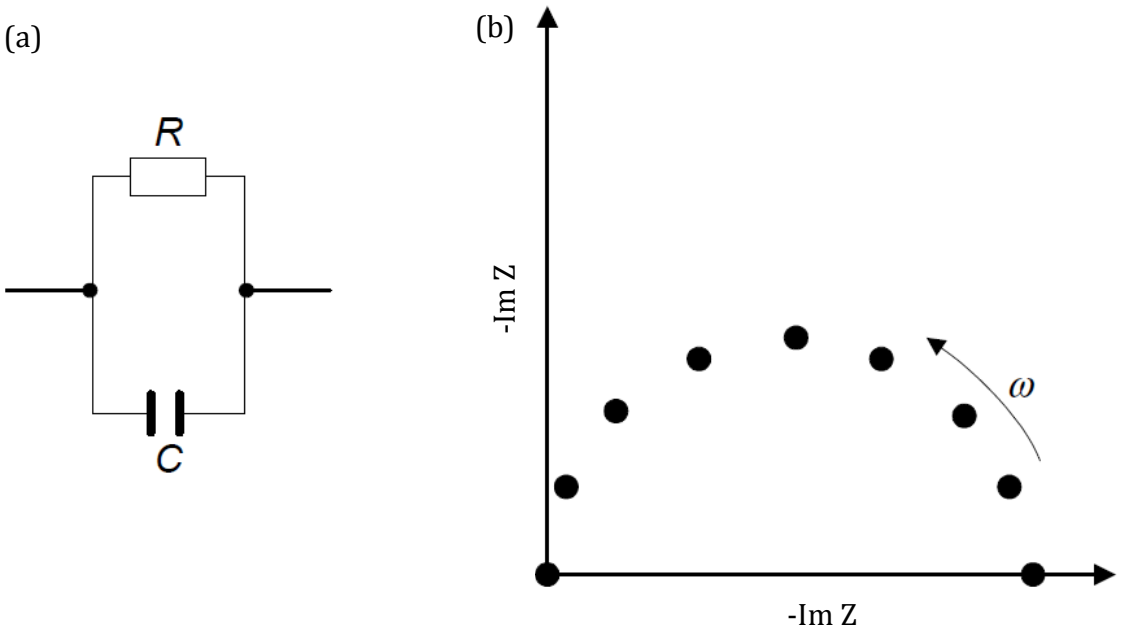

Figure 2.14: Illustration of (a) a simple equivalent electric circuit and (b) the Nyquist plot.

The high frequency data is on the left hand side and the low frequency data is on the right hand side of the Nyquist plot. A major shortcoming of the Nyquist plot is that it does not show the frequency of each point, but the Bode plot accounts for this. The Bode plot is a graph with the log of frequency plotted on the x-axis and the absolute values of the impedance and the phase shift on the y-axes.

A simplified overview of the mass transfer phenomena which occur in LIBs is seen in **Figure 2.15**.

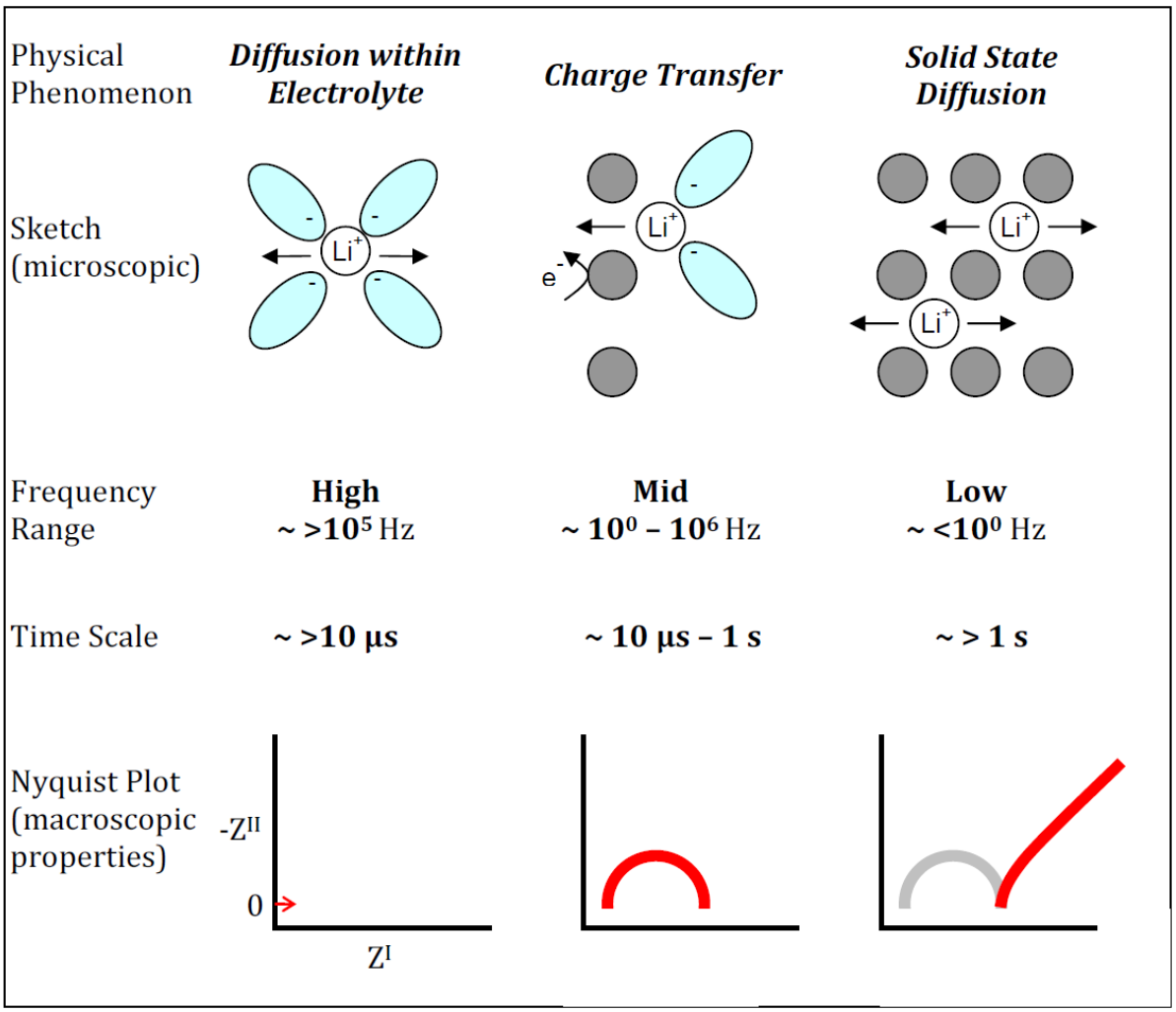

Figure 2.15: Schematic representation of Li ion mass transfer phenomena which occur in LIB electrodes and their respective Nyquist plots [106].

The diffusion of Li ions with interactions with the ligands of the organic solvent is represented in **Figure 2.15**. The impedance represented in the Nyquist plot is only a real component, indicating that this mass transfer phenomenon has no capacitive component and its impedance is purely resistive. For Li ion diffusion within the electrolyte, the Ohmic resistance can be calculated as the distance between the first point of the real component of the first semi-circle and the y-axis [107]. Charge transfer between the electrode

material and the surrounding electrolyte is represented by a semi-circle, as charge transfer at the electrode/electrolyte interface is both a capacitive and resistive process [107-110]. It can occur over a wide range of frequencies depending on properties of the active material, electrolyte, and composite electrode. The low frequency range can be seen to be less than 100 Hz, the Nyquist plot at this frequency is often at a 45° angle. The impedance represents the solid state diffusion which occurs in the material [107-110]. At lower frequencies, the impedance will become purely capacitive because the Li ions can no longer diffuse into the material and there is a capacitive build-up of the ions surrounding the material [107].

2.5.3. Galvanostatic Charge-Discharge

The galvanostatic charge-discharge technique is the most important characterisation tool for LIBs and ECs. From this characterisation technique most of the important parameters are extracted, such as the charge and discharge capacity of LIBs, the capacitance of ECs, the power and energy densities of both LIBs and ECs.

A constant current is applied while the working electrode potential relative to the reference electrode is monitored with time. Upper and lower potentials limits are set for the working electrode. Once one of these limits is reached the charge or the discharge is stopped and the current is reversed, the next step in the cycle begins as depicted in

Figure 2.16.

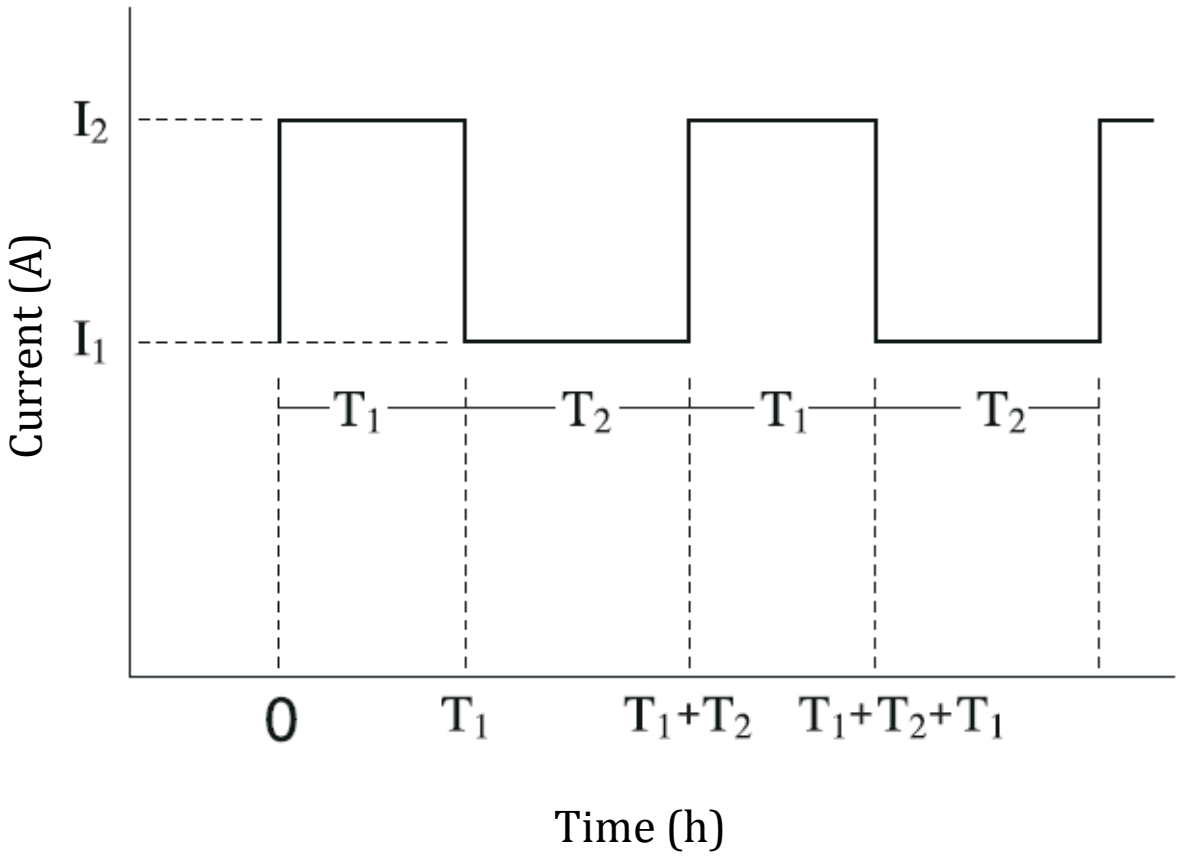

Figure 2.16: The current versus time profile during galvanostatic charge discharge.

2.5.4. Atomic Force Microscopy (AFM)

AFM is a very useful tool in order to study surface morphology, but AFM is not limited to only imaging surface morphology. It can also be used for other purposes such as determining the surface conductivity by means of current sensing AFM.

With AFM [111, 112], a tip interacts with the sample surface and measures forces acting between the fine tip and the sample. The tip is attached to the free end of a cantilever and is brought very close to a surface. Attractive or repulsive forces resulting from interactions between the tip and the surface will cause a positive or negative bending of

the cantilever. The bending is detected by means of a laser beam, which is reflected from the back side of the cantilever (see **Figure 2.17**). The resulting signal from the detector is the deflection, in volts which is manipulated by software into an image.

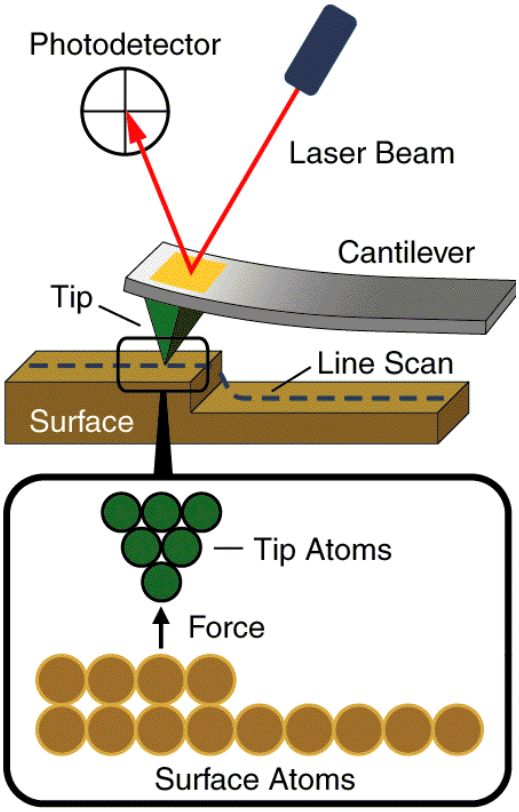

Figure 2.17: Illustration of the working principle of AFM.

The AFM has various modes of operation of which two were used in this study. A commonly used mode is the so called contact mode, where the tip makes soft "physical contact" with the surface of the sample. For contact mode AFM imaging, it is necessary to have a cantilever which is soft enough to be deflected by very small forces and has a high enough resonant frequency not be susceptible to vibrational instabilities.

One of the modes used in this study is the tapping mode or intermittent contact mode. The force measured by AFM can be classified into long-range forces and short-range forces. The first class dominates when scanned at large distances from the surface and they can be Van der Waals forces or capillary forces. When the scanning is in contact with the surface the short range forces are very important, in particular the quantum mechanical forces (Pauli Exclusion Principle forces). In tapping mode-AFM the cantilever is oscillating close to its resonance frequency. An electronic feedback loop ensures that the oscillation amplitude remains constant, such that a constant tip-sample interaction is maintained during scanning. Forces that act between the sample and the tip will not only cause a change in the oscillation amplitude, but also change in the resonant frequency and phase of the cantilever. The amplitude is used for the feedback and the vertical adjustments of the piezo scanner are recorded as a height image. Simultaneously, the phase changes are presented in the phase image (topography). For a good phase contrast, larger tip forces are of advantage, while minimization of this force reduces the contact area and facilitates high-resolution imaging. Silicon probes are used primarily for Tapping Mode applications.

The other mode used in this study is the Current Sensing AFM (CS-AFM) mode [112]. CS-AFM uses the commonly used AFM Contact Mode, including a special nose cone containing a pre-amp along with an ultra-sharp AFM cantilever coated with a conducting film, to probe the conductivity and topography of the sample. By applying a voltage bias between the conducting cantilever and sample, a current is generated which is used to construct a conductivity image.

2.5.5. Scanning Electron Microscopy (SEM)

SEM is used in order to image small particles of the electrode powders, where a resolution up to 10 nm is possible depending on the system. In a typical SEM [113], an electron beam is thermionically mitted from an electron gun fitted with a W filament cathode. W is normally used in thermionic electron guns because it has the highest melting point and lowest vapour pressure of all metals, thereby allowing it to be heated for electron emission, and because of its low cost. Other types of electron emitters include lanthanum hexaboride (LaB_6) cathodes. These types of electron guns produce electron beams with an average diameter of ~ 15 – 20 µm. In order to decrease the electron beam diameter (~ 0.5 – 5 nm) and thus the resolution of the image obtained, a Field Emission (FE) electron gun is used. This FE electron gun is a W wire, with the tip as a single crystal W shaped to a curvature radius of ~ 100 nm. Due to this sharp point effect the electric field at the tip is very strong. The beam produced, by electrons that are *pulled out* from the tip by the strong electric field, passes through pairs of scanning coils or pairs of deflector plates in the electron column. To avoid ion bombardment to the tip from the residual gas ultra-high vacuum (UHV, ~ 10^{-9} Torr) is needed. The final lens as shown in **Figure 2.18** is used to deflect the beam in the *x* and *y* axes so that it scans in a raster fashion over a rectangular area of the sample surface.

When the primary electron beam interacts with the sample, the electrons lose energy by repeated random scattering and absorption within a teardrop shaped volume of the specimen known as the interaction volume. The energy exchange between the electron beam and the sample results in the reflection of high-energy electrons by elastic scattering, emission of secondary electrons by inelastic scattering and the emission of electromagnetic radiation, each of which can be detected by specialized detectors. The

beam current absorbed by the specimen can also be detected and used to create images of the distribution of specimen current. Electronic amplifiers of various types are used to amplify the signals, which are displayed as variations in brightness.

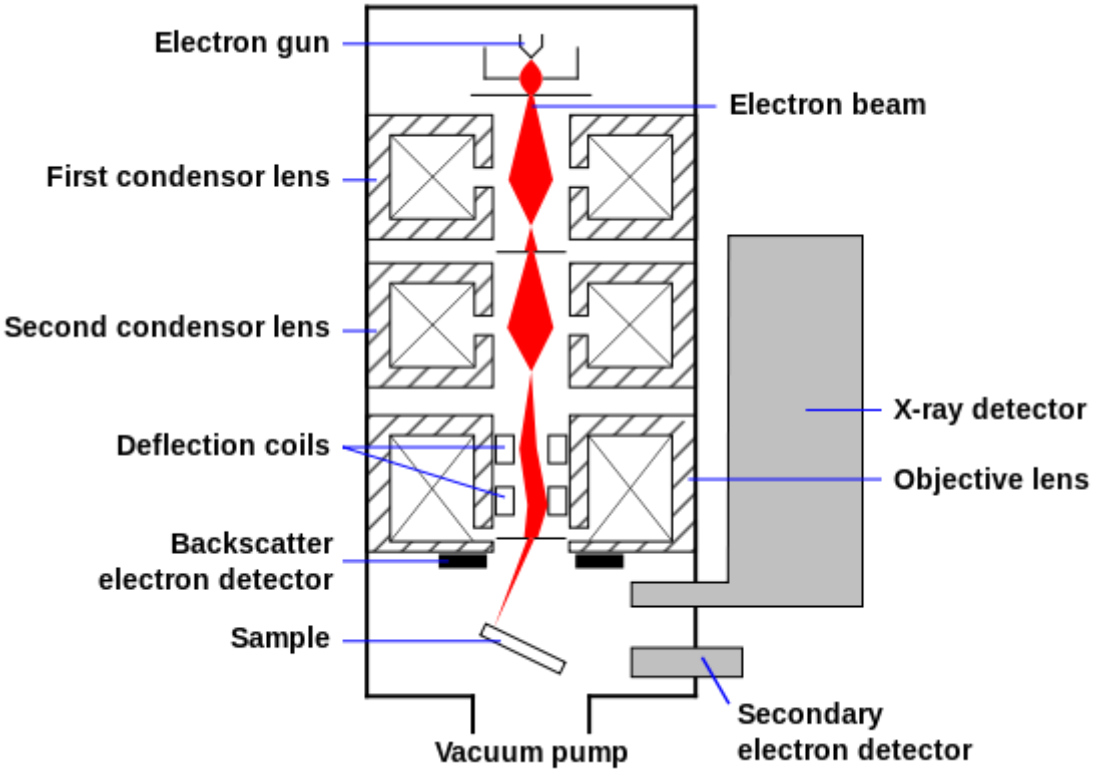

Figure 2.18: Schematic diagram of a typical Scanning Electron Microscope.

2.5.6. X-Ray Diffraction (XRD)

XRD is mainly used in this study to determine the phases of different cathode materials and to calculate the lattice parameters. The lattice parameters were calculated by hand making use of data extracted from the XRD patterns. Rietveld refinement can also be done on the accumulated XRD patterns, where information such as lattice parameters and phase distribution can be extracted.

X-rays are generated from electrons that are accelerated towards and bombarded against an anode material (for the purposes of this thesis; Co or Cu) producing characteristic x-rays (Cu – λ = 1.5406 Å and Co – λ = 1.7890 Å). When a sample is bombarded with the x-rays, constructive interference of X-ray radiation occurs in the material when Bragg's law is satisfied:

$$n\lambda = 2dsin\theta;\ n = 1, 2, 3, \ldots \qquad 2.28$$

where d is the distance between two atomic planes, θ is the angle between the incident beam and normal to the reflecting crystalline plane, n is an integer and λ is the wavelength. The scattered intensity can be measured as a function of scattering angle 2θ. Analysis of the resulting XRD pattern is an effective method for determining the different phases present in the sample. Since the wavelength of X-rays used is of the same order of magnitude as the interatomic distances and bond lengths in crystalline solids (~1 Å), the XRD method serves well to determine the structure of crystalline materials.

2.5.7. X-Ray Photoelectron Spectroscopy (XPS)

XPS is based on the photoelectric effect where electrons are emitted from solids (or other mediums) when they absorb energy from X-ray photons ($h\upsilon$). Thus electrons emitted in this manner are called photoelectrons [82, 114]. The X-ray radiation (1 – 15 keV) usually applied is capable to induce electrons not only from the outer shells but also from core levels of elements. The sample, in UHV, is irradiated with the X-ray radiation, photoionization occurs and the kinetic energy of the ejected photoelectrons is measured by an electron energy analyser. Determination of the kinetic energy of the photoejected

electrons permits identification of the elemental composition of the composite surface. The binding energy (E_b) of the core electron is given by the Einstein relation:

$$h\nu = E_b + E_k + \phi \qquad 2.29$$

or

$$E_b = h\nu - E_k - \phi \qquad 2.30$$

where $h\nu$ is the X-ray photon energy (for this study it is either monochromated Al K_α, = 1486.6 eV or Mg K_α, = 1253.6 eV), E_k the kinetic energy of the photoelectron and ϕ is the work function induced by the analyser.

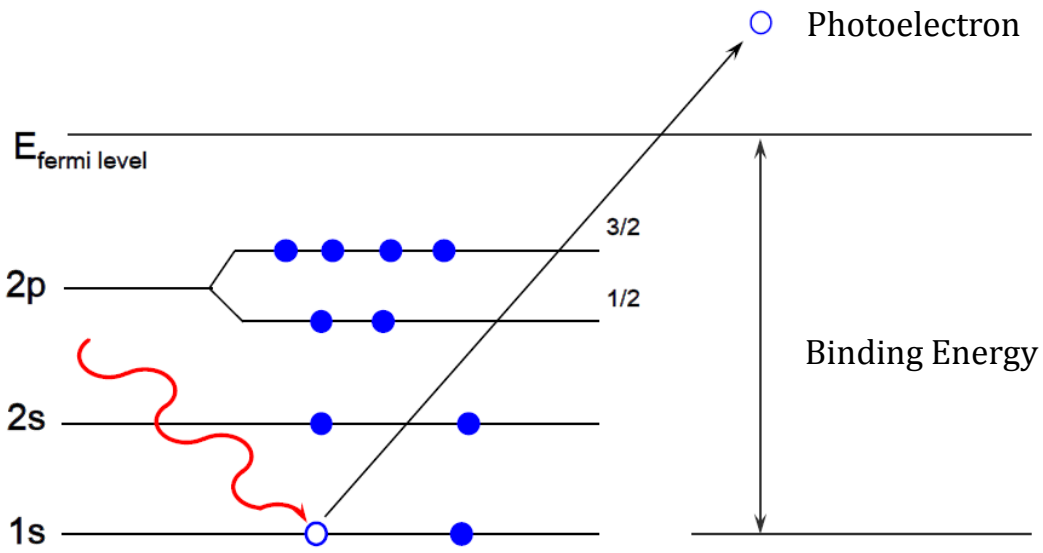

Figure 2.19: The photoionization process.

An important advantage of XPS is its ability to obtain information on chemical states from the variations in binding energies, or chemical shifts, of the photoelectron lines.

2.6. Microwave Irradiation

Microwave irradiation is a crucial part of this study, where samples are irradiated and the effects of this irradiation is studied. Microwaves are electromagnetic waves containing an electric and a magnetic component. Microwave irradiation transfers energy by two main mechanisms making as a result of the former component; (i) dipolar polarization and (ii) ionic conduction [115]. When a sample is irradiated at microwave frequencies (0.3 – 300 GHz), the dipoles or ions of the sample align in the applied electric field. As the applied field oscillates (see **Figure 2.20 (a)**), the dipole or ion field attempts to realign itself with the alternating electric field (see **Figure 2.20 (b)**) and, in the process, energy is lost in the form of heat through molecular friction and dielectric loss [116]. The ability of a specific material or solvent to convert microwave energy into heat at a given frequency and temperature is determined by the so-called loss tangent (tan δ) [117]. In contrast to conventional heating methods relying on conduction and convection principles, microwave irradiation produces efficient internal ‘‘in core’’ volumetric heating by direct coupling of microwave energy with the molecules that are present in the reaction mixture. Therefore, microwave irradiation raises the temperature from the inside, whereas in a conventionally heated vessel, the reaction mixture in contact with the hot vessel walls is heated first.

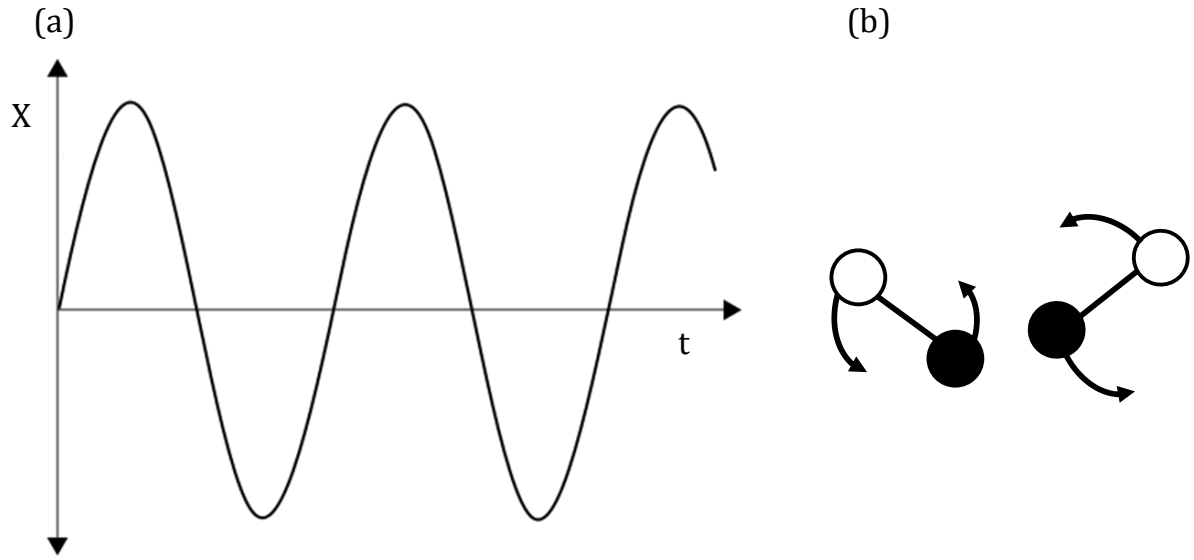

Figure 2.20: Schematic diagram showing (a) the electric field oscillation and (b) the dipole realignment.

2.7. Syntheses of Lithium Ion Battery Cathode Materials

To enhance the performance of LIBs, homogeneity and phase purity is a necessity. In order to synthesize such materials, the selection of an appropriate synthetic method is the key step to obtain such final products. While the hunt for high performance electrode materials for Li-ion batteries remains the main research objective, cost associated with producing these materials is now becoming another overriding factor [16, 60]. Notions of sustainability, renewability, and green chemistry must be taken into consideration when selecting electrode materials for the next generation of Li-ion cells, especially when designing materials for mass production and high volume applications. The Most favourable synthesis methods are high temperature solid- state reactions [40, 118] and sol-gel methods [119].

Table 2.1: Comparative table of different synthesis methods

Syntheses Methods	Cathode material	Advantages	Disadvantages	References
Sol-gel / Pechini	Spinel, Layered and Olivine	i. Nano crystallites ii. Phase pure materials iii. Energy efficient	i. Nano crystallites	[45, 120, 121]

Solid State	Spinel, Layered and Olivine	i. Simple technique for mass production ii. Use of little to no water	i. Time consuming ii. Energy intensive iii. Irregular morphology iv. Broad particle size distribution v. Impurity phase	[40, 118, 122]
Combustion	Spinel, Layered and Olivine	i. Particle size distribution small	i. Impurity phase	[123, 124]
Spray Pyrolysis	Spinel, Layered and Olivine	i. Can be used for mass production ii. Spherical formed particles	i. Micron sized particles	[125]
Hydrothermal	Spinel, Layered and Olivine	i. Different shaped materials ii. Low temperatures	i. Time consuming ii. Inconsistent iii. Difficult to obtain correct parameters	[126-128]

Co-precipitation	Spinel, Layered and Olivine	i. Simple synthesis process ii. Phase pure materials	i. Difficult controlling particle size and particle size distribution	[129, 130]
Microwave	Spinel, Layered and Olivine	i. Energy efficient ii. Time efficient iii. Heating from the core of the particles	i. Little understanding on the effect of microwave interaction with material for optimized microwave processing	[131] and references within

Literature where a combination of the synthesis methods mentioned above in **Table 2.1** is also common giving superior performance compared to a single synthesis method used [132]. The most common examples of these are co-precipitation and microwave [133], and solid state and microwave [134] synthesis.

The effort to further enhance the reaction acceleration should be made with the exploration of these mechanisms. The accomplishments like novel design or compatible material selection should be carried out. Generally, the compound formation and sintering primarily depends on the earlier stage of nuclei formation. Hence, a hybrid methodology

involving microwave reactors in primary stage and conventional furnaces in the later stage would be an optimal strategy for successful and economical application [131].

In this work the synthesis method used to prepare all the LIB cathode materials is a modified Pechini method. The basics of the Pechini method is thus described here. The Pechini method was proposed in 1967 by Pechini [135] as a technique of depositing dielectric films of titanates and niobates of lead and alkaline-earth elements in the production of capacitors. The Pechini process was later modified for the in-lab synthesis of multicomponent finely dispersed oxide materials.

The method is based on an intensive blending of positive ions in a solution, controlled transformation of the solution into a polymer gel, removal of the polymer matrix and growth of an oxide precursor with a high degree of homogeneity. During the synthetic process, metal salts or alkoxides are introduced into a citric acid (CA) solution with ethylene glycol (EG), in this case a 1 : 4 molar ratio (CA : EG). The formation of citric complexes balances the difference in individual behaviour of ions in solution, which results in a better distribution of ions and prevents the separation of components at a later stage of the process. The polycondensation of ethylene glycol and citric acid starts at ~ 100 °C, resulting in polymer citrate gel formation. The time consuming and more energy intensive step of removing the gel from the beaker (loss of material) and pasting it on a piece of pre heated stainless steel (~ 140 °C) is replaced. To replace this time consuming and energy intensive step the gel is left in the beaker at the temperature of ~ 100 °C. The gel starts to combust forming a powder. This replacement is the slight modification that is introduced. Additional heating of the powder in air at ~ 500 °C will result in the removal of organics and the formation of X-ray amorphous oxide and/or carbonate powder with a controlled cation stoichiometry, with little cation segregation. Further heating of this

amorphous powder will result in the formation of the required material (metal oxide) with a high degree of homogeneity and dispersion.

The method's advantages include its relative simplicity, almost complete independence of the process conditions from the chemistry of positive ions contained in the final material and a relatively low temperature of precursor treatment, due to which the process may occur almost completely without sintering, resulting in the production of nanocrystalline powders of refractory oxides. The modification introduced allows for the replacement of a time consuming and energy intensive step of pasting a gel on a piece of pre heated stainless steel.

Disadvantages of the Pechini method include the use of toxic ethylene glycol and significant volumes of organic reagents per unit of product mass. The exact processes and precursor materials used for the different materials will be discussed in the respective chapters.

References

[1] A.J. Bard, L.R. Faulkner, Electrochemical methods: fundamentals and applications, 2nd ed., Wiley, New York, 2000.

[2] D.A. Skoog, D.M. West, F.J. Holler, S.R. Crouch, Fundamentals of analytical chemistry, 8th ed., Grupo Editorial Norma, United States, 2004.

[3] M. Winter, R.J. Brodd, Chem. Rev. **104** (2004) 4245.

[4] D. Guyomard, J.M. Tarascon, J. Electrochem. Soc. **139** (1992) 937.

[5] J.M. Tarascon, W.R. McKinnon, F. Coowar, T.N. Bowmer, G. Amatucci, D. Guyomard, J. Electrochem. Soc. **141** (1994) 1421.

[6] V. Etacheri, R. Marom, R. Elazari, G. Salitra, D. Aurbach, Energy & Environ. Sci. **4** (2011) 3243.

[7] D. Linden, T.B. Reddy, Handbook of batteries, 3rd ed., McGraw-Hill, New York, 2002.

[8] J.O. Besenhard, Handbook of battery materials, Willey, Germany, 1999.

[9] P. Ramadass, B. Haran, R. White, B.N. Popov, J. Power Sources **123** (2003) 230.

[10] http://nuclear-news. net/2012/08/24/new-fast-lithium-ion-battery-for-electric-cars (Accessed on 17th January 2014).

[11] M.S. Whittingham, Prog. Solid State Chem. **12** (1978) 41.

[12] K. Mizushima, P. Jones, P. Wiseman, J. Goodenough, Mater. Res. Bull. **15** (1980) 783.

[13] M.V. Reddy, G.V. Subba Rao, B.V.R. Chowdari, Chem. Rev. **113** (2013) 5364.

[14] K. Zaghib, A. Mauger, H. Groult, J.B. Goodenough, C.M. Julien, Materials **6** (2013) 1028.

[15] M. Wakihara, Mater. Sci. Eng. R **33** (2001) 109.

[16] J.W. Fergus, J. Power Sources **195** (2010) 939.

[17] Y. Wang, G. Cao, Adv. Mater. **20** (2008) 2251.

[18] A.K. Padhi, K. Nanjundaswamy, J.B. Goodenough, J. Electrochem. Soc. **144** (1997) 1188.

[19] S. Chung, J.T. Bloking, Y. Chiang, Nature Mater. **1** (2002) 123.

[20] N. Ravet, Y. Chouinard, J. Magnan, S. Besner, M. Gauthier, M. Armand, J. Power Sources **97** (2001) 503.

[21] B.C. Melot, J. Tarascon, Acc. Chem. Res. **46** (2013) 1226.

[22] M.M. Thackeray, W.I.F. David, P.G. Bruce, J.B. Goodenough, Mater. Res. Bull. **18** (1983) 461.

[23] D. Guyomard, J.M. Tarascon, Solid State Ionics **69** (1994) 222.

[24] J.M. Tarascon, F. Coowar, G. Amatuci, F.K. Shokoohi, D.G. Guyomard, J. Power Sources **54** (1995) 103.

[25] J. Tarascon, E. Wang, F. Shokoohi, W. McKinnon, S. Colson, J. Electrochem. Soc. **138** (1991) 2859.

[26] S. Jayaraman, V. Aravindan, S. Kumar, W. Ling, S. Ramakrishna, S. Madhavi, Chem. Comm. **49** (2013) 6677.

[27] M. Yonemura, A. Yamada, H. Kobayashi, M. Tabuchi, T. Kamiyama, Y. Kawamoto, R. Kanno, J. Mater. Chem. **14** (2004) 1948.

[28] N. Amdouni, K. Zaghib, F. Gendron, A. Mauger, C. Julien, Ionics **12** (2006) 117.

[29] M.Y. Song, D.S. Ahn, H.R. Park, J. Power Sources **83** (1999) 57.

[30] T. Ohzuku, M. Kitagawa, T. Hirai, J. Electrochem. Soc. **137** (1990) 769.

[31] C.M. Hayner, X. Zhao, H.H. Kung, Annu. Rev. Chem. Biomol. Eng. **3** (2012) 445.

[32] X. Li, Y. Xu, C. Wang, J. Alloys Compounds **479** (2009) 310.

[33] M.M. Thackeray, Prog. Solid State Chem. **25** (1997) 1.

[34] A. Smith, J. Burns, J. Dahn, Electrochem. Solid-State Lett. **14** (2011) A39.

[35] R. Gummow, A. De Kock, M. Thackeray, Solid State Ionics **69** (1994) 59.

[36] L. Guohua, H. Ikuta, T. Uchida, M. Wakihara, J. Electrochem. Soc. **143** (1996) 178.

[37] C. Sigala, D. Guyomard, A. Verbaere, Y. Piffard, M. Tournoux, Solid State Ionics **81** (1995) 167.

[38] Q. Zhong, A. Bonakdarpour, M. Zhang, Y. Gao, J. Dahn, J. Electrochem. Soc. **144** (1997) 205.

[39] Y. Gao, K. Myrtle, M. Zhang, J. Reimers, J. Dahn, Phys. Rev. B **54** (1996) 16670.

[40] C. Julien, A. Mauger, Ionics **19** (2013) 951.

[41] J.H. Kim, S.-. Myung, C.S. Yoon, S.G. Kang, Y.-. Sun, Chem. Mater. **16** (2004) 906.

[42] N. Amdouni, K. Zaghib, F. Gendron, A. Mauger, C. Julien, J. Magn. Magn. Mater. **309** (2007) 100.

[43] J. Zheng, J. Xiao, X. Yu, L. Kovarik, M. Gu, F. Omenya, X. Chen, X. Yang, J. Liu, G.L. Graff, M.S. Whittingham, J. Zhang, Phys. Chem. Chem. Phys. **14** (2012) 13515.

[44] S. Myung, S. Komaba, N. Kumagai, H. Yashiro, H. Chung, T. Cho, Electrochim. Acta **47** (2002) 2543.

[45] M. Kunduraci, G. Amatucci, J. Electrochem. Soc. **153** (2006) A1345.

[46] J. Xiao, X. Chen, P.V. Sushko, M.L. Sushko, L. Kovarik, J. Feng, Z. Deng, J. Zheng, G.L. Graff, Z. Nie, D. Choi, J. Liu, J. Zhang, M.S. Whittingham, Adv. Mater. **24** (2012) 2109.

[47] J. Liu, A. Manthiram, J. Phys. Chem. C **113** (2009) 15073.

[48] A. Ito, D. Li, Y. Lee, K. Kobayakawa, Y. Sato, J. Power Sources **185** (2008) 1429.

[49] C. Locati, U. Lafont, L. Simonin, F. Ooms, E.M. Kelder, J. Power Sources **174** (2007) 847.

[50] G. Zhao, Y. Yang, Y. Lin, B. Zeng, T. Zhou, Y. Lin, Z. Huang, Power and Energy Engineering Conference (APPEEC) proceedings, Asia Pacific (2012) 1.

[51] M.V. Reddy, S.S. Manoharan, J. John, B. Singh, G.V. Subba Rao, B.V.R. Chowdari, J. Electrochem. Soc. **156** (2009) A652.

[52] J.S. Park, K.C. Roh, J. Lee, K. Song, Y. Kim, Y. Kang, J. Power Sources **230** (2013) 138.

[53] Z. Liu, A. Yu, J.Y. Lee, J. Power Sources **81** (1999) 416.

[54] B. Hwang, Y. Tsai, D. Carlier, G. Ceder, Chem. Mater. **15** (2003) 3676.

[55] Z. Wang, Y. Sun, L. Chen, X. Huang, J. Electrochem. Soc. **151** (2004) A914.

[56] X. Liu, W. Gao, B. Ji, J. Sol Gel Sci. Technol. **61** (2012) 56.

[57] A. Titov, Z. Eremenko, E. Goryacheva, N. Sokolova, N. Opolchenova, N. Stepareva, G. Korobko, Inorg. Mat. **49** (2013) 202.

[58] G. Nazri, G. Pistoia, Lithium batteries: science and technology, Springer, New York, 2004.

[59] H. Xia, H. Wang, W. Xiao, L. Lu, M.O. Lai, J. Alloys Compounds **480** (2009) 696.

[60] M.S. Whittingham, Chem. Rev. **104** (2004) 4271.

[61] T. Ohzuku, A. Ueda, M. Nagayama, J. Electrochem. Soc. **140** (1993) 1862.

[62] G. Dutta, A. Manthiram, J. Goodenough, J. Grenier, J. Solid State Chem. **96** (1992) 123.

[63] I. Nakai, K. Takahashi, Y. Shiraishi, T. Nakagome, F. Nishikawa, J. Solid State Chem. **140** (1998) 145.

[64] T. Ohzuku, A. Ueda, M. Nagayama, Y. Iwakoshi, H. Komori, Electrochim. Acta **38** (1993) 1159.

[65] J. Dahn, E. Fuller, M. Obrovac, U. Von Sacken, Solid State Ionics **69** (1994) 265.

[66] Z. Zhang, D. Fouchard, J. Rea, J. Power Sources **70** (1998) 16.

[67] B.L. Ellis, K.T. Lee, L.F. Nazar, Chem. Mater. **22** (2010) 691.

[68] Y. Makimura, T. Ohzuku, J. Power Sources **119–121** (2003) 156.

[69] Z. Lu, D. MacNeil, J. Dahn, Electrochem. Solid-State Lett. **4** (2001) A200.

[70] C.S. Johnson, J. Kim, C. Lefief, N. Li, J.T. Vaughey, M.M. Thackeray, Electrochem. Commun. **6** (2004) 1085.

[71] M.M. Thackeray, C.S. Johnson, J.T. Vaughey, N. Li, S.A. Hackney, J. Mater. Chem. **15** (2005) 2257.

[72] M.M. Thackeray, S.-. Kang, C.S. Johnson, J.T. Vaughey, S.A. Hackney, Electrochem. Commun. **8** (2006) 1531.

[73] C.S. Johnson, N. Li, C. Lefief, J.T. Vaughey, M.M. Thackeray, Chem. Mater. **20** (2008) 6095.

[74] M.M. Thackeray, S. Kang, C.S. Johnson, J.T. Vaughey, R. Benedek, S. Hackney, J. Mater. Chem. **17** (2007) 3112.

[75] P. Kalyani, S. Chitra, T. Mohan, S. Gopukumar, J. Power Sources **80** (1999) 103.

[76] F. Zhou, X. Zhao, J. Dahn, J. Electrochem. Soc. **156** (2009) A343.

[77] F. Zhou, X. Zhao, C. Goodbrake, J. Jiang, J. Dahn, J. Electrochem. Soc. **156** (2009) A796.

[78] J.D. Wilcox, E.E. Rodriguez, M.M. Doeff, J. Electrochem. Soc. **156** (2009) A1011.

[79] J. Wilcox, S. Patoux, M. Doeff, J. Electrochem. Soc. **156** (2009) A192.

[80] L. Croguennec, J. Bains, J. Bréger, C. Tessier, P. Biensan, S. Levasseur, C. Delmas, J. Electrochem. Soc. **158** (2011) A664.

[81] Z. Li, N.A. Chernova, J. Feng, S. Upreti, F. Omenya, M.S. Whittingham, J. Electrochem. Soc. **159** (2011) A116.

[82] R.A. Serway, Physics for scientists and engineers, 8th ed., Cengage Learning, 2012.

[83] P. Simon, Y. Gogotsi, Nature Mater. **7** (2008) 845.

[84] P. Sharma, T.S. Bhatti, Energ. Convers. Manage. **51** (2010) 2901.

[85] F. Beguin, E. Frackowiak, Supercapacitors: Materials, Systems and Applications, John Wiley & Sons, Weinheim, 2013.

[86] L.L. Zhang, X. Zhao, Chem. Soc. Rev. **38** (2009) 2520.

[87] A.G. Pandolfo, A.F. Hollenkamp, J. Power Sources **157** (2006) 11.

[88] W. Deng, X. Ji, Q. Chen, C.E. Banks, RSC Adv. **1** (2011) 1171.

[89] L. Wang, H. Ji, S. Wang, L. Kong, X. Jiang, G. Yang, Nanoscale **5** (2013) 3793.

[90] C.J. Jafta, F. Nkosi, L. le Roux, M.K. Mathe, M. Kebede, K. Makgopa, Y. Song, D. Tong, M. Oyama, N. Manyala, Electrochim. Acta (2013) in Press.

[91] A. Burke, J. Power Sources **91** (2000) 37.

[92] J.N. Lekitima, K.I. Ozoemena, C.J. Jafta, N. Kobayashi, Y. Song, D. Tong, S. Chen, M. Oyama, J. Mater. Chem. A **1** (2013) 2821.

[93] A.T. Chidembo, K.I. Ozoemena, B.O. Agboola, V. Gupta, G.G. Wildgoose, R.G. Compton, Energy & Environ. Sci. **3** (2010) 228.

[94] M. Zhi, C. Xiang, J. Li, M. Li, N. Wu, Nanoscale **5** (2013) 72.

[95] W. Gu, G. Yushin, WIREs Energy Environ. (2013) doi: 10.1002/wene.102.

[96] D. Wang, F. Li, H. Cheng, J. Power Sources **185** (2008) 1563.

[97] J. Lang, L. Kong, M. Liu, Y. Luo, L. Kang, J. Solid State Electrochem. **14** (2010) 1533.

[98] V. Subramanian, C. Luo, A. Stephan, K. Nahm, S. Thomas, B. Wei, J. Phys. Chem. C **111** (2007) 7527.

[99] Z. Algharaibeh, X. Liu, P.G. Pickup, J. Power Sources **187** (2009) 640.

[100] Z. Chen, V. Augustyn, J. Wen, Y. Zhang, M. Shen, B. Dunn, Y. Lu, Adv. Mater. **23** (2011) 791.

[101] Q. Qu, Y. Shi, L. Li, W. Guo, Y. Wu, H. Zhang, S. Guan, R. Holze, Electrochem. Commun. **11** (2009) 1325.

[102] V. Khomenko, E. Raymundo-Pinero, F. Béguin, J. Power Sources **153** (2006) 183.

[103] A.T. Chidembo, S.H. Aboutalebi, K. Konstantinov, C.J. Jafta, H.K. Liu, K.I. Ozoemena, RSC Adv. **4** (2014) 886.

[104] M. Winter, J.O. Besenhard, M.E. Spahr, P. Novak, Adv. Mater. **10** (1998) 725.

[105] M.E. Orazem, B. Tribollet, Electrochemical impedance spectroscopy, John Wiley & Sons, New Jersey, 2011.

[106] T.J. Patey, Ph. D. Thesis, ETH Zurich (2009).

[107] M. Gaberscek, J. Moskon, B. Erjavec, R. Dominko, J. Jamnik, Electrochem. Solid-State Lett. **11** (2008) A170.

[108] M. Takahashi, S. Tobishima, K. Takei, Y. Sakurai, Solid State Ionics **148** (2002) 283.

[109] N.N. Bramnik, K. Nikolowski, C. Baehtz, K.G. Bramnik, H. Ehrenberg, Chem. Mater. **19** (2007) 908.

[110] A. Hjelm, G. Lindbergh, Electrochim. Acta **47** (2002) 1747.

[111] G. Binnig, C.F. Quate, C. Gerber, Phys. Rev. Lett. **56** (1986) 930.

[112] M. Lee, Nano Scale Electrochemistry: Application to Solid Electrolytes, ProQuest, 2007.

[113] J.J. Bozzola, L.D. Russell, Electron microscopy: principles and techniques for biologists, Jones & Bartlett Learning, 1999.

[114] A. Einstein, Ann. Physik **322** (1905) 132.

[115] C.O. Kappe, Chem. Soc. Rev. **42** (2013) 4977.

[116] P. Lidström, J. Tierney, B. Wathey, J. Westman, Tetrahedron **57** (2001) 9225.

[117] E. Grant, B.J. Halstead, Chem. Soc. Rev. **27** (1998) 213.

[118] T. Ohzuku, K. Ariyoshi, S. Yamamoto, Y. Makimura, Chem. Lett. **30** (2001) 1270.

[119] D. Jugović, D. Uskoković, J. Power Sources **190** (2009) 538.

[120] M. Kunduraci, J.F. Al-Sharab, G.G. Amatucci, Chem. Mater. **18** (2006) 3585.

[121] H. Duncan, Y. Abu-Lebdeh, I.J. Davidson, J. Electrochem. Soc. **157** (2010) A528.

[122] J.S. Park, K.C. Roh, J. Lee, K. Song, Y. Kim, Y. Kang, J. Power Sources (2012).

[123] K. Yang, J. Su, L. Zhang, Y. Long, X. Lv, Y. Wen, Particuology **10** (2012) 765.

[124] P. Kalyani, N. Kalaiselvi, Sci. Tech. Adv. Tech. **6** (2005) 689.

[125] K. Myoujin, T. Ogihara, I. Mukoyama, T. Kodera, M. Kojima, Key Eng. Mat. **388** (2009) 85.

[126] C.H. Jiang, S.X. Dou, H.K. Liu, M. Ichihara, H.S. Zhou, J. Power Sources **172** (2007) 410.

[127] S. Tajimi, Y. Ikeda, K. Uematsu, K. Toda, M. Sato, Solid State Ionics **175** (2004) 287.

[128] J. Tarascon, N. Recham, M. Armand, J. Chotard, P. Barpanda, W. Walker, L. Dupont, Chem. Mater. **22** (2009) 724.

[129] J. Feng, Z. Huang, C. Guo, N.A. Chernova, S. Upreti, M.S. Whittingham, ACS Appl. Mater. & Inter. **5** (2013) 10227.

[130] J. Zheng, X. Li, Z. Wang, H. Guo, S. Zhou, J. Power Sources **184** (2008) 574.

[131] S. Balaji, D. Mutharasu, N. Sankara Subramanian, K. Ramanathan, Ionics **15** (2009) 765.

[132] Y. Liu, C. Cao, Electrochim. Acta **55** (2010) 4694.

[133] K. Park, J. Son, H. Chung, S. Kim, C. Lee, H. Kim, Electrochem. Commun. **5** (2003) 839.

[134] L. Wang, Y. Huang, R. Jiang, D. Jia, Electrochim. Acta **52** (2007) 6778.

[135] M.P. Pechini, U.S. Pat. No. 3 330697 (1967).

Chapter 3

Experimental Techniques and Methods

3.1 Materials and Reagents

All the materials and chemical reagents used for synthesizing the LIB cathode materials and EC electrodes are listed in **Table 3.1**.

Table 3.1: List of materials and reagents used for this study

Reagents and materials	Purity and specifications	Supplier
Citric Acid ($C_6H_8O_7$)	≥ 99 %	Merck
Ethelyne Glycol	≥ 99 %	Sigma Aldrich
$LiNO_3$	≥ 99 %	Sigma Aldrich
$Mn(NO_3)_2{\cdot}4H_2O$	≥ 97 %	Sigma Aldrich
$Ni(NO_3)_2{\cdot}6H_2O$	≥ 98.5 %	Sigma Aldrich
$Co(NO_3)_2{\cdot}6H_2O$	≥ 98 %	Associated Chemical Enterprises (ACE)

$AlN_3O_9{\cdot}9H_2O$	≥ 98 %	Fluka Analytical
Electrolytic Manganese Dioxide (EMD)	-	Delta EMD (Pty) Ltd
Sodium Dodecyl Sulphate (SDS)	99 %	Sigma Aldrich
H_2SO_4	98 %	Sigma Aldrich
H_2O_2	30 %	Sigma Aldrich
NH_4OH	28 %	Sigma Aldrich
HCl	37 %	Sigma Aldrich
Li_2SO_4	≥ 99 %	Sigma Aldrich
Carbon Black	Control number: 030520	PRINTEX XE-2-B
Polyvinylidene Fluoride (PVDF)	≥ 99.5 %	MTI Corp
N-methyl-2-pyyolidone (NMP)	99.5 %	Sigma Aldrich
Lithium hexafluorophosphate ($LiPF_6$)	99.99 %	Sigma Aldrich
Ethylene Carbonate (EC)	99 %	Sigma Aldrich

Dimethyl Carbonate (DMC)	≥ 99 %	Sigma Aldrich
$NaNO_3$	≥ 99 %	Sigma Aldrich
$KMnO_4$	≥ 99 %	Sigma Aldrich
Multi-Walled Carbon Nano Tubes (MWCNT)	Bundles ≥ 94 % Diameter 10 – 20 nm Length 5 – 20 µm	NanoLab
Nickel Foam	-	-

3.2 Pechini Synthesis With and Without Microwave Irradiation

The parent cathode materials for the LIBs were prepared by a modified, one-step powder-forming Pechini method. Citric acid (CA) was dissolved in deionized water and ethylene glycol (EG) was added to the dissolvent to form a 1:4 molar ratio solution. The solution was heated at 90°C for 30 min while being stirred. This CA and EG solution is the reducing agent. The necessary stoichiometric amounts of nitrate salts were dissolved in the minimum amount of deionized water at room temperature. 40 mL of the reducing agent (CA:EG with a 1:4 molar ratio) was left stirring on a hot plate at 90°C. The dissolved salts were introduced, drop wise, to the 40 mL of the reducing agent. Depending on the cathode material being prepared the solution changed colour. The solution starts to dehydrate, the viscosity increases and a gel is formed. The gel is then kept at 90°C, for approximately 30 – 60 min, until it spontaneously starts to combust. The desired powders are thus formed.

The powder is preheated at 500°C for 6 h in order to burn of all carbonaceous impurities left from the previous step in the synthesis process. At this step of the process the powder is divided into two batches.

The one batch will be annealed at a specified temperature for a specified time (see individual sections below) to form the desired crystalline cathode material.

The other batch is subjected to microwave irradiation, where the power was increased at 60 W per min up to 600 W. The powder is irradiated at 600 W for a specified amount of time. The temperature was measured by means of an infrared sensor (IR). The maximum temperature reached was 60°C. The microwaved sample was then annealed at a specified temperature for a specified time (see individual sections below) to form the desired crystalline microwaved cathode material.

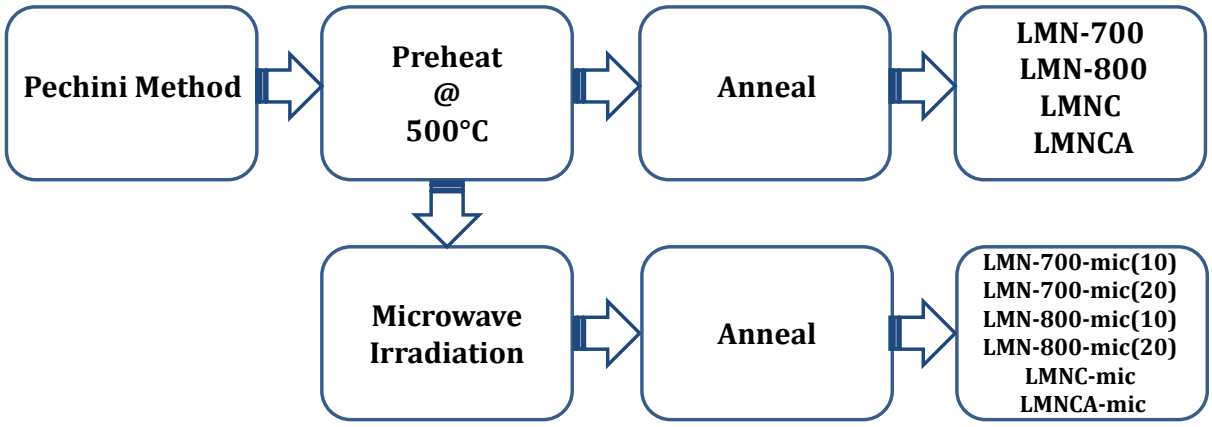

Figure 3.1: A flow chart of the synthesis process.

3.2.1 Synthesis of $LiMn_{1.5}Ni_{0.5}O_4$

Stoichiometric amounts of $LiNO_3$, $Ni(NO_3)_2{\cdot}6H_2O$, and $Mn(NO_3)_2{\cdot}4H_2O$ were dissolved in deionised water and then introduced, drop-wise, to the reducing solution. The powders

were preheated at 500°C for 6 h and annealed at 700°C or 800°C for 8 h in air to produce the crystalline $LiMn_{1.5}Ni_{0.5}O_4$ cathode materials. These samples will be referred to herein as LMN-700 and LMN-800, respectively.

The samples that were subjected to microwave irradiation after preheating at 500°C were transferred to the quartz vessels for microwave irradiation. The samples were irradiated at 600 W for 10 min or 20 min after which it were annealed at 700°C or 800°C for 8 h. These samples herein will be referred to as LMN-700-mic(10), LMN-700-mic(20), LMN-800-mic(10) and LMN-800-mic(20), respectively.

3.2.2 Synthesis of $Li_{1.2}Mn_{0.54}Ni_{0.13}Co_{0.13}O_2$ and $Li_{1.2}Mn_{0.52}Ni_{0.13}Co_{0.13}Al_{0.02}O_2$

The parent ($Li_{1.2}Mn_{0.54}Ni_{0.13}Co_{0.13}O_2$) and Al doped material ($Li_{1.2}Mn_{0.52}Ni_{0.13}Co_{0.13}Al_{0.02}O_2$) were prepared by dissolving stoichiometric amounts of $LiNO_3$, $Mn(NO_3)_2{\cdot}4H_2O$, $Ni(NO_3)_2{\cdot}6H_2O$, $Co(NO_3)_2{\cdot}6H_2O$, and $AlN_3O_9{\cdot}9H_2O$ (for the $Li_{1.2}Mn_{0.52}Ni_{0.13}Co_{0.13}Al_{0.02}O_2$) in deionised water and then introduced, drop-wise, to the reducing solution. The powders were preheated at 500°C for 6 h and annealed at 700°C for 8 h in air to produce the crystalline $Li_{1.2}Mn_{0.54}Ni_{0.13}Co_{0.13}O_2$ and $Li_{1.2}Mn_{0.52}Ni_{0.13}Co_{0.13}Al_{0.02}O_2$ cathode materials. These samples will be referred to herein as LMNC and LMNCA, respectively.

The samples that were subjected to microwave irradiation after preheating at 500°C were transferred to the quartz vessels for microwave irradiation. The samples were irradiated at 600 W for 15 min after which they were annealed at 700°C 8 h. These samples herein will be referred to as LMNC-mic for the $Li_{1.2}Mn_{0.54}Ni_{0.13}Co_{0.13}O_2$ microwaved cathode material and LMNCA-mic for the $Li_{1.2}Mn_{0.52}Ni_{0.13}Co_{0.13}Al_{0.02}O_2$ microwaved cathode material.

3.3 Fabrication of Coin Cells with Lithium Ion Battery Cathode Materials

The LIB coin cells were fabricated using the above cathode materials as the active material, polyvinylidene fluoride (PVDF) as a binder and Carbon Black as a conductive additive in the weight ratio of 80:10:10. *N*-Methyl-2-pyrrolidone (NMP) was used as a solvent. The Carbon Black, PVDF and the cathode material were ground in a mortar and pestle till the mixture was a very fine powder. NMP was added to the fine powder till a slurry was formed of appropriate viscosity. The slurry was used to coat an Al foil substrate that acted as the current collector. The doctor blade technique [1] was used to coat the electrode uniformly with a slurry thickness of ~20 µm. The coated Al foil was placed in an oven at 90°C under medium vacuum (~10^{-1} Torr) for 24 h. It was then put through a roller press to press the cathode material and the foil substrate together to increase contact between them. This was then punched into discs (electrodes) with a 1.6 cm diameter (2.0 cm^2 geometric area) using an electrode cutter. The electrodes were weighed and the active mass was calculated. The active mass of the cathode materials was between 1 mg – 4 mg.

The coin cells (LIR2032) were assembled in an Ar filled glovebox with partial pressures, O_2 < 0.5 ppm and H_2O < 0.5 ppm. Li metal was used as the anode and 1 M Lithium hexafluorophosphate ($LiPF_6$) in a mixtureof 1:1 EC and DMC (v:v) was used as the electrolyte. A polypropylene film (Cellgard 2300) was used as the separator. The coin cells were assembled as follow (see **Figure 3.2**):

Figure 3.2: Schematic diagram of the assembling of a coin cell.

The negative case, spring, spacer, electrolyte, Li metal, separator, electrolyte, Al foil with active material and positive cap was assembled in this order as depicted in **Figure 3.2**. The Li metal was scraped on the surface to ensure there was no oxide layer. The coin cell

was pressed using a coin cell press. The coin cells were left overnight before any measurements to ensure proper wetting of the electrodes.

3.4 Synthesis of Nano MnO_2

A mixture containing 1 g of Electrolytic Manganese Dioxide (EMD), 1 g of SDS and 50 mL of 5% NH_4OH was stirred overnight and ultrasonicated for 30 min. The ultrasonicated mixture was transferred to a Teflon lined stainless steel beaker in an autoclave and heated at 130°C for 24 h, to produce a nanostructured material, and then cooled to room temperature. The material was washed several times with a copious amount of distilled water via centrifugation. The final product was dried overnight at 50°C in a vacuum oven ($\sim 10^{-1}$ Torr). These dried powders were then annealed at 620°C for 2 h to produce multi-phased Mn_2O_3. The multi-phased Mn_2O_3 powder was subjected to an acid treatment in order to get the material mono-phased. The acid treatment was carried out by reacting 10 mL of 8 M H_2SO_4 with 30 mg of the nanostructured Mn_2O_3 sample at ~100°C for 6 h under continuous stirring, and then at room temperature for 16 h. These samples were washed to a neutral pH with deionized water and then dehydrated at 300°C to obtain the desired product, α-MnO_2 synthesized with SDS. This sample herein will be referred to as α-$MnO_{2(SDS)}$. For comparison reasons with the α-$MnO_{2(SDS)}$, another product was obtained using the above method but without the use of SDS (abbreviated herein as α-MnO_2) during the synthesis.

Graphene oxide (GO) was prepared using the modified Hummer's method from graphite powders [2]. A mixture of 0.5 g of graphite powders and 0.5 g of $NaNO_3$ were prepared with 23 mL of concentrated H_2SO_4 under constant stirring for 10 min in a flask at 0°C. 3 g of $KMnO_4$ was then added slowly to the above solution over a 3 min period to prevent a sudden temperature increase. Then the dark greenish solution was transferred to a 35 ± 5°C water bath and stirred for about 1 h. Next, 50 mL of deionised water was added slowly, and the solution was stirred for another 30 min while the temperature was raised

to 90 ± 5°C. After adding 150 mL of water, 3 mL of H_2O_2 was added drop wise, resulting in the formation of a brownish solution. Finally, the warm solution was filtered and washed with 50 mL of 0.1 M HCl solution and 500 mL of water, respectively. The filter cake was then dispersed in water by sonicated. The products were then separated via centrifugation for 5 min to remove all visible particles. The last sediment was re-dispersed in water under mild sonication, which resulted in a homogeneous brown solution of exfoliated.

3.5 Fabrication of Coin Cells with Nano MnO_2 as electrodes for Electrochemical Capacitors

The EC coin cells were fabricated using the above Mn oxides as the active material. The α-$MnO_{2(SDS)}$, α-MnO_2 and EMD was mixed with GO to give α-$MnO_{2(SDS)}$/GO, α-MnO_2/GO and EMD/GO composites, respectively. The α-$MnO_{2(SDS)}$ and EMD were also mixed with MWCNT to give α-$MnO_{2(SDS)}$/MWCNT and EMD/MWCNT, respectively. The mixtures were obtained by grounding them in a mortar and pestle to a fine powder. The Mn oxides were mixed with the GO or MWCNT to a mass ratio of 85:15. The α-$MnO_{2(SDS)}$/GO, α-MnO_2/GO, EMD/GO, α-$MnO_{2(SDS)}$/MWCNT and EMD/MWCNT acted as the active material of the EC. The positive electrodes were prepared by mixing the active materials with Carbon Black and PVDF at a mass ratio of 70:20:10. The Carbon Black, PVDF and the cathode material were ground in a mortar and pestle till the mixture was a very fine powder. NMP was added to the fine powder till a slurry was formed of appropriate viscosity. Nickel foam was used as the current collector and thus the slurry was pasted onto it. The Nickel foam was cleaned, before pasting, in a 1 M HCl solution, washed with a copious amount of deionized water, and dried under vacuum (~10^{-1} Torr). The slurry was then coat onto the Nickel foam substrate that acted as the current collector. The doctor blade technique [1] was used to coat the electrode uniformly. The coated Nickel foam was placed in an oven at 90°C under medium vacuum (~10^{-1} Torr) for 8 h. It was then put through a roller press to press the electrode material and the Nickel foam substrate together to increase contact between them. This was then punched into discs (electrodes) with a 1.6 cm diameter (2.0 cm^2 geometric area) using an electrode cutter. The electrodes were weighed and the active mass was calculated. The active mass loading was between 1 mg – 6 mg. The

negative electrodes were prepared using the same procedure but with Carbon Black, GO or MWCNT and PVDF at a mass ratio of 80:10:10.

The coin cells (LIR2032) were assembled with a positive and negative electrode. A 1 M Li_2SO_4 solution served as the electrolyte while a glass microfiber served as the separator. The coin cells were assembled in a similar manner as to **Figure 3.2.** The coin cells were left overnight before any measurements to ensure proper wetting of the electrodes.

3.6 Equipment and procedures

3.6.1 X-ray Diffraction (XRD)

The XRD systems used in this study are (i) a Bruker AXS D8 ADVANCE X-ray Diffractometer with Ni filtered Cu K_α radiation (λ = 1.5406 Å) and (ii) a PANalytical X'Pert Pro Powder Diffractometer with Fe filtered Co K_α radiation (λ = 1.7890 Å). For all samples, the scanning speed was set at 0.02° per step with a dwell time of 5 s.

3.6.2 Galvanostatic Charge-Discharge

Galvanostatic charge discharge measurements were performed in two electrode coin cells (LIR2032) assembled with the cathode materials as the positive electrode and lithium metal foil as the negative electrode, for the Lithium Ion Batteries, using a MACCOR series 4000 tester.

For the Electrochemical Capacitors galvanostatic charge discharge measurements were also performed in two electrode coin cells (LIR2032) assembled with a positive and negative electrode using an Autolab PGSTAT 302N controlled by the general purpose Electrochemical Systems data processing software, GPES version 4.9.

3.6.3 Cyclic Voltammetry (CV)

For this study the potentiostat used for CV is an Autolab PGSTAT 302N controlled by the general purpose Electrochemical Systems data processing software, GPES version 4.9. All the parameters for the different cells are reported in the specific chapters.

3.6.4 Electrochemical Impedance Spectroscopy (EIS)

For this study the EIS measurements was done on the same system where CV measurements were done (Autolab PGSTAT 302N) where the potentiostat is controlled by the general purpose Electrochemical Systems data processing software, FRA version 4.9. All the parameters for the different cells are reported in the specific chapters.

3.6.5 Atomic Force Microscopy (AFM)

AFM was used in one of the experiments (see **chapter 5**) where the layered cathode material was doped with Al. Specifically; the current sensing AFM was used in order to determine if there is an increase in the surface conductivity of the electrode with the Al dopant compared to the undoped cathode material. The SPM system used in this study is a commercial Agilent 5500 SPM. The AFM measurements were carried out in air under ambient conditions with a commercial Agilent 5500 AFM (Agilent Technologies, USA) in the Acoustic AC mode (tapping mode) for the morphological images at a scanning frequency of 1 Hz. Silicon cantilevers with a nominal resonant frequency of 190 kHz and a nominal force constant of 48 N/m was used. The current sensing images were obtained in the contact mode (CSAFM) with their corresponding topography images at a scanning rate of 0.5 Hz. For these images, a platinum coated (to allow conductivity) silicon probe with a force constant of 0.35 N/m was used. The bias voltage between the samples and the tip, which creates the current which is used to construct a conductivity map, was set at 1 V. All the images were analysed by the imaging processing software by Agilent, Pico Image version 6.2.

3.6.6 X-ray Photoelectron Spectroscopy (XPS)

The XPS systems used in this study are (i) a PHI 5400 ESCA and (ii) a PHI 5000 Versaprobe–Scanning ESCA Microprobe. The vacuum chambers during measurement had base pressures ≤ 1×10^{-8} Torr. All XPS data analysis was performed with the XPS Peak 4.1 program and a Shirley function was used to subtract the background. The parameters used for measurement are reported in the specific chapters.

References

[1] H. Yang, P. Jiang, Langmuir **26** (2010) 13173.

[2] W.S. Hummers Jr, R.E. Offeman, J. Am. Chem. Soc. **80** (1958) 1339.

Chapter 4

Diffusion Formulae

4.1 Diffusion Coefficient

The well-known diffusion formula derived by Bard and Faulkner [1] presented as **4.1** is used extensively for the calculation of Li^+ ion diffusion coefficients in the field of LIB research.

$$\sigma = \frac{RT}{\sqrt{2}n^2F^2A}\left(\frac{1}{\sqrt{D_{ox}}C_{ox}} + \frac{1}{\sqrt{D_{red}}C_{red}}\right) \quad 4.1$$

The popularity of this formula is due to its simplicity in terms of the variables needed to extract a value for the diffusion of ions in materials.

In literature [2-8] there seem to be no attempts to derive this formula to a point where extracted variables can be plugged into the formula and a diffusion coefficient value can be calculated. Rather, the wrongfully used formula is copied [9-13] from an untraceable source and **4.2** keeps on being used:

$$D_{Li} = \frac{1}{2}\left(\frac{RT}{\sigma n^2F^2C_{Li}A}\right)^2 \quad 4.2$$

instead of the correct formula as **4.3**:

$$D_{Li} = 2\left(\frac{RT}{\sigma n^2F^2C_{Li}A}\right)^2 \quad 4.3$$

The correct formula was used by Ikpo et al. [14], where the error was also pointed out. Thus the purpose of this report is not only to point out the error, but to show the correct derivation of this formula.

In an attempt to correct formula **4.2** used, **4.3** is derived as follows, starting from equation **4.1**. Assuming the diffusion coefficients of the oxidised (D_{ox}) and reduced (D_{red}) Li species to be equal ($D_{ox} = D_{red} = D_{Li}$) and the concentration to be equal ($C_{ox} = C_{red} = C_{Li}$) [1], equation **4.1** can be simplified to obtain:

$$\sigma = \frac{RT}{\sqrt{2}n^2F^2A}\left(\frac{1}{\sqrt{D_{Li}}C_{Li}} + \frac{1}{\sqrt{D_{Li}}C_{Li}}\right) \tag{4.4}$$

$$\sigma = \frac{RT}{\sqrt{2}n^2F^2A}\left(\frac{2}{\sqrt{D_{Li}}C_{Li}}\right) \tag{4.5}$$

$$\sigma = \frac{2RT}{\sqrt{2}\sqrt{D_{Li}}C_{Li}n^2F^2A} \tag{4.6}$$

Making D_{Li} the subject of the formula it becomes:

$$\sqrt{D_{Li}} = \frac{2RT}{\sqrt{2}C_{Li}n^2F^2A\sigma} \tag{4.7}$$

$$D_{Li} = \left(\frac{2RT}{\sqrt{2}C_{Li}n^2F^2A\sigma}\right)^2 \tag{4.8}$$

$$D_{Li} = \frac{2R^2T^2}{C_{Li}^2n^4F^4A^2\sigma^2} \tag{4.9}$$

where D_{Li} is the diffusion coefficient, R the gas constant, T the absolute temperature, A the geometric surface area of the cathode, F the Faraday constant, n the number of electrons transferred per molecule during oxidation or reduction, C_{Li} the lithium concentration in the cathode material and σ is the Warburg factor obtained from the slope of the real

impedance (Z') vs. the reciprocal square root of the frequency in the low frequency region ($\omega^{-1/2}$) according to:

$$Z_w = \sigma(1-j)\omega^{-1/2} \qquad 4.10$$

The error made in the literature cited above is a factor 4. This may seem to be insignificant, but this could lead to confusion and reporting of wrong results (even if it is only by a factor of 4).

For example, Yi et al. [13] calculated the diffusion coefficient at room temperature (25 °C) to be 4.99×10^{-16} $cm^2.s^{-1}$. When calculated with the correctly derived formula (**4.9**) the actual value is 2×10^{-15} $cm^2.s^{-1}$, which is an order higher. In fact, Yi et al. [13] make use of the calculated diffusion coefficients, at different temperatures, in order to determine the apparent diffusion activation energy from an Arrhenius equation:

$$D_{Li} = D_A e^{-E_a/RT} \qquad 4.11$$

where D_A.is the pre-exponential factor, R the gas constant, T the temperature and E_a the apparent diffusion activation energy. From these calculations, Yi et al.[13] obtained a value of 87.9 $kJ.mol^{-1}$ (0.9 eV). This value is higher compared to values calculated with first principle calculations based on density functional theory (DFT) by Ma et al. [15]. These values are between 0.31 eV and 0.54 eV. Okubo et al. [16] also calculated an average activation energy for $Li_{1-x}CoO_2$ as 0.32 eV by means of experimental and ab initio calculations. Due to the fact that $D_{Li} \propto \frac{1}{E_a}$ (see **4.11**) it is expected that lower diffusion coefficients would result in higher activation energies as is seen from this example.

With the realization that calculating diffusion coefficients is not trivial and that many factors play a role that affects the calculated outcome of the diffusion coefficient. It is still very important to minimize the error as much as possible.

The above derived formula **4.9** will be used in the subsequent chapters to calculate correct diffusion coefficients.

4.2 A Diffusion Coefficient Formula Making Use of Electrochemical Impedance Spectroscopy and Cyclic Voltammetry

The diffusion coefficient of intercalation material can be determined by extracting variables from among others, EIS spectra or CV. In order to calculate the diffusion coefficient from the formula reported in the literature [17] and here as equation **4.12** the variable C_{int} is needed:

$$D_{Li} = \left(\frac{QM_w l}{\sqrt{2}nF\sigma C_{int}}\right)^2 \qquad 4.12$$

where Q is the specific capacity in Coulombs per mass unit, and M_{w} is the molecular weight, l is the diffusion pathway (i.e., thin film thickness) while C_{int} is the 'apparent' intercalation capacitance. This variable (C_{int}) is not always easy to extract from impedance spectra. It is the intercalation capacitance which describes the accumulation of Li at the very low frequency range, and can be obtained from the equivalent electric circuit (EEC) of the Nyquist plot. In order to make use of equation **4.12,** the EEC needs to have this specific intercalation capacitance (C_{int}) component, which is not always possible. Unfortunately, it is usually a problem to fit some Nyquist plots with an EEC that containsd the C_{int}.

As an alternative, the C_{int} variable can be estimated from the cyclic voltammograms obtained at slow scan rate (equation **4.13**) using a well-known equation as also applied by Goonetilleke *et al.* in their recent work [18]:

$$C_{int} \approx {}^{i}/_{v} \qquad 4.13$$

where i is the peak current from the CV and v the slow scan rate used for the CV experiment.

The Formula **4.12** thus becomes:

$$D_{Li} = \frac{1}{2}\left(\frac{QM_w lv}{nF\sigma i}\right)^2 \qquad 4.14$$

where C_{int} is replaced by the scan rate over the redox peak current, both obtainable from CV.

C_{int} is cautioned to be strictly regarded as an 'apparent' intercalation capacitance because it is estimated from an approximation, equation **4.13**.

In conclusion, it is shown here that the difficult obtainable C_{int} from EIS and its EEC can be replaced by the scan rate of a cyclic voltammogram and the current response of the redox peak.

References

[1] A.J. Bard, L.R. Faulkner, Electrochemical methods: fundamentals and applications, 2nd ed., Wiley, New York, 2000.

[2] X. Zhang, A. Mauger, Q. Lu, H. Groult, L. Perrigaud, F. Gendron, C.M. Julien, Electrochim. Acta **55** (2010) 6440.

[3] Y. Zhou, J. Wang, Y. Hu, R. O'Hayre, Z. Shao, Chem. Commun. **46** (2010) 7151.

[4] H. Liu, C. Li, H. Zhang, L. Fu, Y. Wu, H. Wu, J. Power Sources **159** (2006) 717.

[5] X. Fang, J. Li, K. Huang, S. Liu, C. Huang, S. Zhuang, J. Zhang, Journal of Solid State Electrochemistry **16** (2012) 767.

[6] X. Qin, X. Wang, J. Xie, L. Wen, J. Mater. Chem. **21** (2011) 12444.

[7] Y. Yang, G. Zheng, S. Misra, J. Nelson, M.F. Toney, Y. Cui, J. Am. Chem. Soc. **134** (2012) 15387.

[8] H. Liu, Q. Cao, L.J. Fu, C. Li, Y. Wu, H. Wu, Electrochem. Commun. **8** (2006) 1553.

[9] P. Gao, Y. Li, H. Liu, J. Pinto, X. Jiang, G. Yang, J. Electrochem. Soc. **159** (2012) A506.

[10] L. Wang, J. Zhao, X. He, J. Gao, J. Li, C. Wan, C. Jiang, Int. J. Electrochem. Sci. **7** (2012) 345.

[11] S. Sarkar, H. Banda, S. Mitra, Electrochim. Acta **99** (2013) 242.

[12] J. Zhao, L. Wang, X. He, C. Wan, C. Jiang, Int. J. Electrochem. Sci. **5** (2010) 478.

[13] T. Yi, S. Yang, H. Ma, X. Li, Y. Ma, H. Qiao, R. Zhu, Ionics **DOI 10.1007/s11581-013-0975-1** (2013) In press.

[14] C.O. Ikpo, C.J. Jafta, K.I. Ozoemena, N. West, N. Njomo, N. Jahed, P.G. Baker, E.I. Iwuoha, Int. J. Electrochem. Sci **8** (2013) 753.

[15] X. Ma, B. Kang, G. Ceder, J. Electrochem. Soc. **157** (2010) A925.

[16] M. Okubo, Y. Tanaka, H. Zhou, T. Kudo, I. Honma, J. Phys. Chem. B **113** (2009) 2840.

[17] M. Mohamedi, M. Makino, K. Dokko, T. Itoh, I. Uchida, Electrochim. Acta **48** (2002) 79.

[18] P. Goonetilleke, J. Zheng, D. Roy, J. Electrochem. Soc. **156** (2009) A709.

Chapter 5*

Controlling the Mn^{3+} Concentration in $LiMn_{1.5}Ni_{0.5}O_4$ Cathode Material via a Microwave Assisted Synthesis Method

5.1 Introduction to the Importance of Mn^{3+} in $LiMn_{1.5}Ni_{0.5}O_4$ Cathode Material

The material $LiMn_2O_4$ has received considerable attention as a cathode material for LIBs as it is a low cost and eco-friendly cathode material that can replace $LiCoO_2$ which is expensive and toxic [1, 2]. Considering that $LiMn_2O_4$ has a relatively low operating voltage and suffers from capacity loss during cycling, the Mn sites in $LiMn_2O_4$ have been substituted by various cations such as Co, Cr, Al, etc. [3-5]. The spinel cathode material, $LiMn_{1.5}Ni_{0.5}O_4$, is considered an advanced LIB material and has been receiving major research attention because of its high operating voltage (~4.8 V) and high intrinsic rate capability [6]. Due to this high operating voltage the $LiMn_{1.5}Ni_{0.5}O_4$ full cells are shown to have an average (operating) voltage of ~3.4 V with an appropriate anode [1]. Despite its many advantages, $LiMn_{1.5}Ni_{0.5}O_4$ still encounters many obstacles for high-rate applications. It is very difficult to synthesize a pure and stoichiometric $Li_{1-x}[Ni_{0.5}Mn_{1.5}]O_4$

*The following publication resulted from part of the research work presented in this chapter and is not referenced further:
C. J. Jafta, M. K. Mathe, N. Manyala, W. D. Roos and K. I. Ozoemena, "Microwave-Assisted Synthesis of High-Voltage Nanostructured $LiMn_{1.5}Ni_{0.5}O_4$ Spinel: Tuning the Mn^{3+} Content and Electrochemical Performance", *ACS Appl. Mater. Interfaces* **5** (2013) 7592 – 7598

spinel as $Li_yNi_{1-y}O$ (impurity) appears as a second phase, negatively impacting on the electrochemical behaviour [6, 7].

$LiMn_{1.5}Ni_{0.5}O_4$ has two different crystal structures; (i) the stoichiometric ordered with space group symmetry $P4_332$, composed predominantly of Mn^{4+}, and (ii) the non-stoichiometric disordered, face-centered cubic structure with space group symmetry $Fd\bar{3}m$ composed of Mn^{3+} and Mn^{4+}. The ordered phase ($LiNi_{0.5}Mn_{1.5}O_4$) is a primitive simple cubic structure ($P4_332$) in which Ni, Mn and Li atoms respectively occupy the 4b, 12d and 8c sites, whereas the O atoms reside in the 8c and 24e sites. The non-stoichiometric ($LiNi_{0.5}Mn_{1.5}O_{4-\delta}$) is a face-centred cubic structure ($Fd\bar{3}m$) where Ni and Mn atoms are randomly distributed in the 16d sites while Li and O occupy 8a tetrahedral sites and 32e sites, respectively [8] (see **Chapter 2**). It has been well-established that the preparation of either of the phases is determined by the annealing temperatures; ordered spinel at T = 700 °C while disordered spinel at T > 700 °C [9, 10]. See the following equation for the reaction taking place at T > 700 °C [11-13]:

$$LiMn_{1.5}Ni_{0.5}O_4 \rightleftharpoons \alpha Li_xNi_{1-x}O + \beta LiMn_{1.5+y}Ni_{0.5-y}O_{4-x} + \gamma O_4 \text{ (T} > 700\ ^\circ\text{C)} \qquad 4.1$$

The electrochemical performance of this spinel as a cathode material for lithium ion battery is intricately linked to (i) the presence of Mn^{3+} ions and/or the degree of disorder, (ii) doping/substitution with cations, and (iii) presence of $Li_yNi_{1-y}O$ impurity phase. These factors explain why it still remains a huge challenge to correlate synthesis, structure and performance of this spinel material. The electrochemical performance of the disordered spinel is better than the ordered one due mainly to the enhanced Li^+ diffusion and increased electronic conductivity because of the increased Mn^{3+} in the former [9]. The formation of the disordered spinel is usually accompanied with a $Li_xNi_{1-y}O$ phase that

lowers the obtainable capacity [14]. To maintain charge neutrality in the disordered spinel, which is a result of the loss of oxygen, part of the inactive Mn^{4+} ions are reduced to Mn^{3+} ions. The ionic radius of the Mn^{3+} (58.0 pm) ions are larger compared to the Mn^{4+} (53.0 pm) ions which will result in an increase in the lattice [10, 15]. As a result, the diffusion of Li^{+} ions will be enhanced. The redox-active Mn^{3+} also improves the spinel electronic conductivity, and gives a signature plateau around 4 V in the discharge profile. Higher Mn^{3+} ion content will have a positive effect on the diffusion of Li^{+} as well as on the discharge capacity at higher charge / discharge rates due to the improved electronic conductivity. However, a high concentration of Mn^{3+} would lead to disproportionation reactions that produce soluble Mn^{2+} in the electrolyte, which may cause severe capacity fading [14, 16]. In a nutshell, if every Mn ion in the spinel is maintained at the 4+ oxidation state the cathode material will be a stoichiometrically ordered $LiNi_{0.5}Mn_{1.5}O_4$, which is an undesirable situation that may conspire against the fast Li^{+} transportation. It is understandable therefore why the amount of Mn^{3+} ions is considered quite critical in determining the electrochemical performances of the spinel. In a recent report, Xiao *et al.* [14] elegantly showed that the concentration of Mn^{3+} ions in the spinel lattice is controlled by combining post-synthesis annealing and partially substituting Ni^{2+} with Cr^{2+}. In summarizing their findings, the authors concluded that the "co*mparison of the electrochemical performances of spinels with different* Mn^{3+} *contents demonstrates that careful control of the amount of* Mn^{3+} *ions and, thus, the disordered phase, is the key for synthesis of high performance spinel and provides valuable clues for understanding the structure–property relationships in energy materials*". Up to date, there are four reported methods for controlling the Mn^{3+} content in $LiNi_{0.5}Mn_{1.5}O_4$; (i) careful control of the cooling rate after high temperature calcination [16], (ii) partial substitution of Ni and/or Mn with elements such as Co, Al, Ti, Fe, Cr, Ru, or Mg [6, 14, 17-20], (iii) combined post-

synthesis annealing and partial substitution of Ni with Cr [14] and (iv) long-hour acidic treatment [21].

It is thus the focus of this chapter where it is shown that a microwave-assisted synthesis can be used as an elegant strategy to control the Mn^{3+} concentration (degree of disorder) and enhance the electrochemical performance of the $LiMn_{1.5}Ni_{0.5}O_4$ spinel material. This proposed strategy is novel, simple, fast, efficient and, importantly, promises to avoid many of the disadvantages associated with the state-of-the-art procedures such as (i) the use of energy-intensive and time-consuming careful controlling of the cooling rates after high temperature calcination or the post-synthesis annealing, (ii) partial substitution of Ni or Mn with expensive metals (e.g., Ru) which may be toxic and environmentally unfriendly (e.g., Cr), and (iii) long-hour acid treatment.

The use of microwave irradiation to improve the performance of metallic materials has long been known [22, 23], and it has was recently showed how microwave irradiation can be used to induce top-down nanostructuring for enhanced performance of core-shell palladium-based catalyst [24]. The microwave-enhanced chemical reaction is dependent upon the efficient interaction of molecules with the electromagnetic waves. Unlike the traditional heating process, the temperature of the surroundings in the microwave heating process is colder than that of the target sample (i.e., 'in-core' heating, generated from within the sample).

5.2 Results and Discussion

Figure 5.1 shows typical FE-SEM images of (a) LMN-700, (b) LMN-700-mic, (c) LMN-800 and (d) LMN-800-mic.

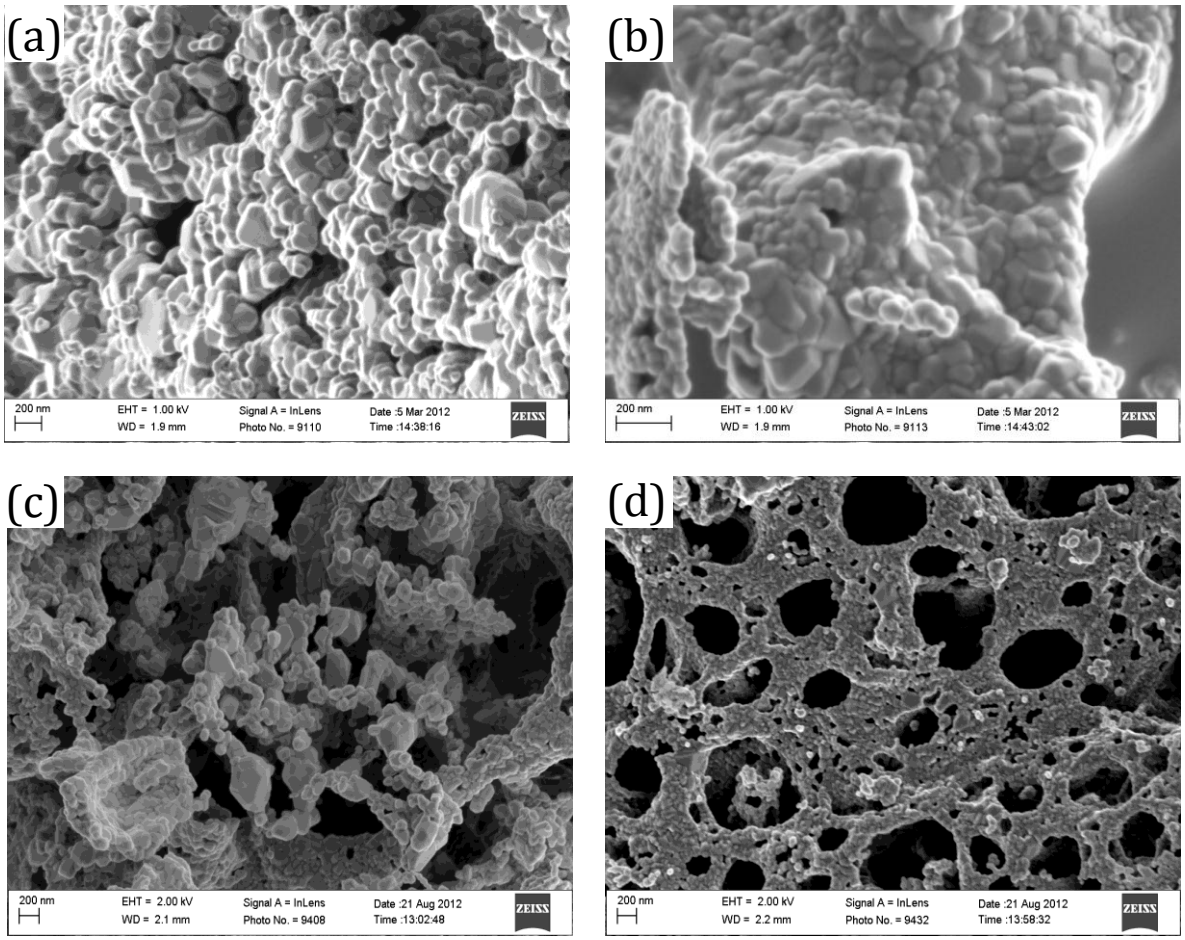

Figure 5.1: FE-SEM images of (a) LMN-700, (b) LMN-700-mic, (c) LMN-800 and (d) LMN-800-mic.

The particle sizes of LMN-700 range between ~ 100 and 200 nm while those of the LMN-700-mic range between ~ 50 and 100 nm. The LMN-800 particle sizes range between ~ 50 and 200 nm and that of LMN-800-mic between ~ 50 and 100 nm. It is evident that the particle sizes of the microwaved samples (LMN-700-mic and LMN-800-mic) are smaller (≤

100 nm) compared to the un-microwaved samples (≥ 100, but ≤ 200 nm). The LMN-800-mic in particular, depicts a spider web-like layered morphology made up of interconnected primary crystallites with hierarchical pores. The difference in the morphology of the different samples is due to the microwave irradiation that changes the growth kinetics. It is theorized that due to the sample that is heated from the core by the microwave irradiation, the particles crystallizes during the microwave stage and reach a growth maxima. Thus when the samples are subjected to annealing at the higher temperatures (700°C or 800°C) the particles tend to grow at a slower rate compared to the particles in the sample that was not subjected to the microwave irradiation. This results in the microwaved samples having smaller particle sizes.

The powder XRD patterns (see **Figure 5.2 (a-d)**) are characteristic of the cubic spinel structures with the microwave treated samples (**Figure 5.2 (b,d)**) showing sharper diffraction peaks compared to the un-microwaved samples (**Figure 5.2 (a,c)**).

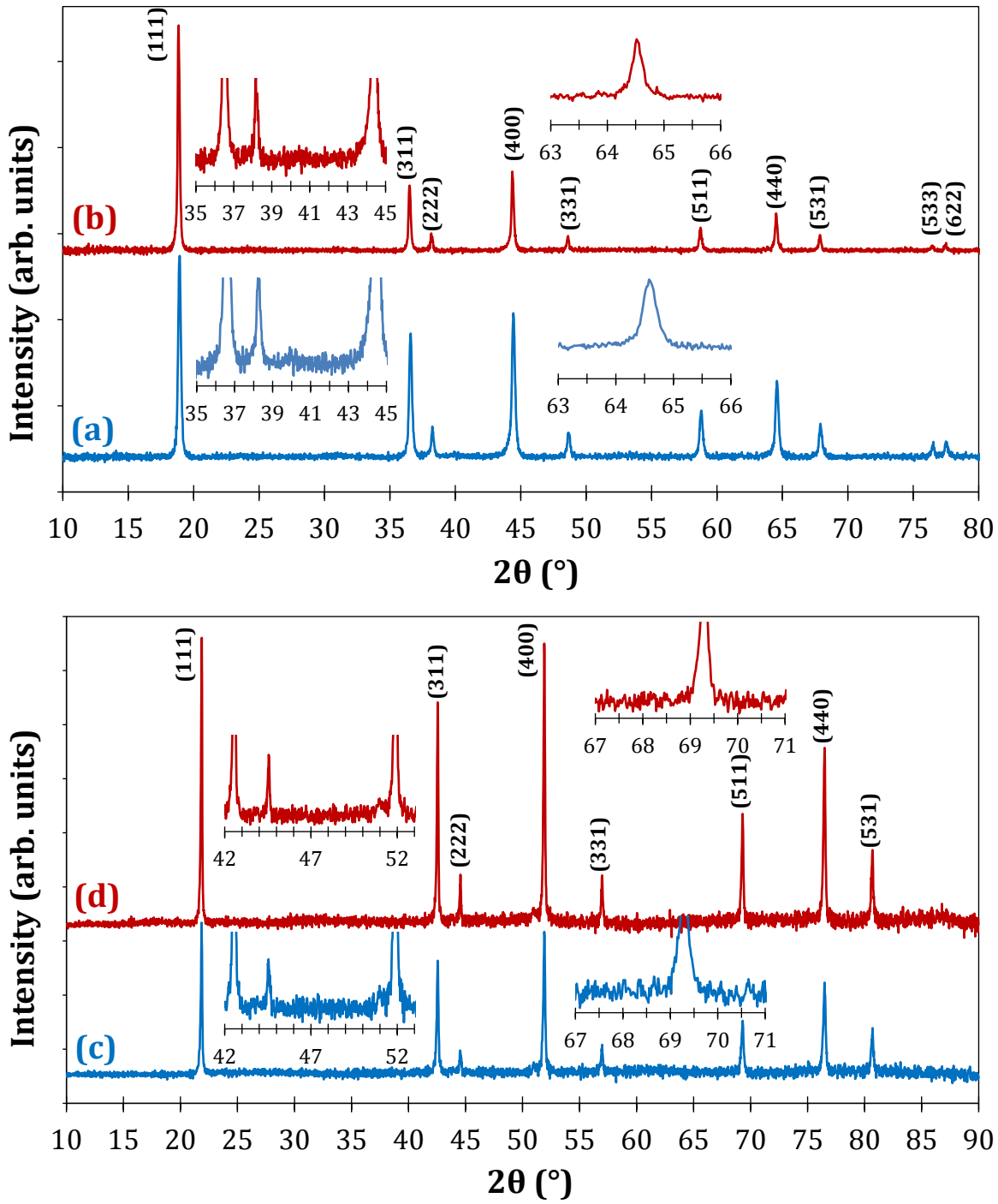

Figure 5.2: Typical powder X-ray diffraction patterns of (a) LMN-700, (b) LMN-700-mic, (c) LMN-800 and (d) LMN-800-mic.

This indicates an enhanced crystallinity of the microwave treated spinel materials. The calculated lattice parameters, making use of the Miller indices and the interplanar spacings, for these materials are comparable to values in literature [25]. The microwave irradiation changes the crystal growth kinetics. A common impurity phase, $Li_yNi_{1-y}O$, in the spinel $LiMn_{1.5}Ni_{0.5}O_4$ are observed as weak peaks at 2θ angles of ~37.6°, 43.7° and 63.7° (Cu K_α radiation, λ = 1.5406 Å) [26, 27]. The insets in **Figure 5.2** show that this impurity phase is virtually non-existent in the materials. The calculated lattice parameters are shown in **Table 5.1.**

Table 5.1: Structure parameters of the $LiMn_{1.5}Ni_{0.5}O_4$ samples

Sample	Lattice parameter, *a* (Å)	Unit cell volume (Å^3)
LMN-700	8.153	541.907
LMN-700-mic	8.160	543.170
LMN-800	8.180	547.417
LMN-800-mic	8.179	547.109

The slight increase in the lattice parameters for the LMN-800 sample compared to its LMN-700 (and LMN-700-mic) counterpart further proves that the LMN-800 (and LMN-800-mic) samples are Mn^{3+} enriched (disordered phase). The increase in the lattice parameter for the LMN-700-mic indicates the creation of oxygen vacancies in the spinel structure following the microwave irradiation process which causes Mn^{4+} ions to be converted to Mn^{3+} due to charge compensation [14, 28]. On the other hand, the lattice parameters for the LMN-800 and LMN-800-mic suggest a slight decrease in the oxygen vacancies for the microwave-irradiated disordered material. This is interesting as it suggests that the experimental conditions employed in this work, microwave irradiation simply adjusts the Mn^{3+} content to a lower value. As will be demonstrated later, these adjustments of the Mn^{3+}/Mn^{4+} ratios (or oxygen vacancy concentration) have profound

effects on the electrochemical properties of the spinel as a cathode material for lithium ion battery.

In order to determine the actual contribution amounts of the Mn^{3+} and Mn^{4+} in the spinel, XPS experiments were performed for the powdered spinel samples. **Figure 5.3** shows the deconvoluted, detailed XPS of the Mn $2p_{3/2}$ peaks of the LMN-700 / LMN-700-mic and LMN-800 / LMN-800-mic samples.

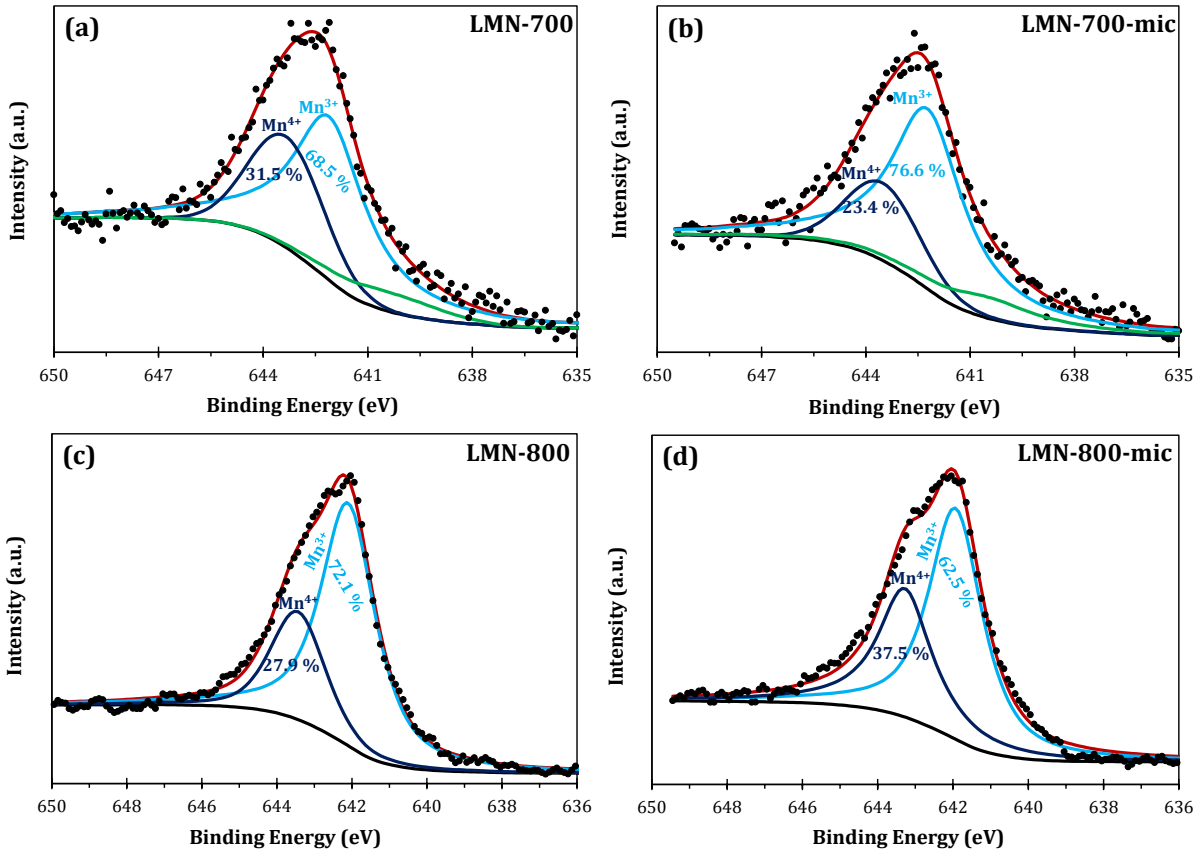

Figure 5.3: Detailed fitted X-ray Photoelectron Spectroscopy spectra of the Mn $2p_{3/2}$ peak of (a) LMN-700, (b) LMN-700-mic, (c) LMN-800 and (d) LMN-800-mic.

There is a broadening in the peak widths (known from the spectrometer resolution), an indication that the Mn exist in more than one oxidation state. In order to confirm the

oxidation states and to approximate their contribution to the total peak, the Mn $2p_{3/2}$ of the LMN-700, LMN-700-mic, LMN-800 and LMN-800-mic peaks were deconvoluted into two and three peaks (see **Figure 5.3**) as this gives the best statistical fit. Two peaks (as marked), in all four spectra respectively, are attributed to Mn^{3+} and Mn^{4+} and another (in the LMN-700 / LMN-700-mic spectra) to a Ni Auger peak. The binding energy peak positions corresponding to Mn^{4+} and Mn^{3+} are comparable with other binding energy values reported in literature [29, 30].

As shown in **Table 5.2**, the ratio of Mn^{3+} to Mn^{4+} (i.e., Mn^{3+}/Mn^{4+}) is 2.2 and 3.3 for the LMN-700 and LMN-700-mic, respectively. This increase in the Mn^{3+} content in in good agreement with the XRD data of increased *a*-lattice parameter, further confirming that microwave irradiation causes oxygen deficiency causing the Mn^{4+} to be converted to Mn^{3+} in the ordered spinel. For the LMN-800 and LMN-800-mic, the Mn^{3+}/Mn^{4+} is 2.6 and 1.7, respectively. Again, this is in good agreement with the XRD data that predicted a slight downward adjustment of the Mn^{3+} content of the disordered sample.

Table 5.2: Mn $2p_{3/2}$ peak positions and cation distribution

Sample	Binding energy position (eV)		Cation distribution		
	Mn^{4+}	Mn^{3+}	Mn^{4+}	Mn^{3+}	Mn^{3+}/Mn^{4+}
LMN-700	643.2	642.1	31.5 %	68.5 %	2.17
LMN-700-mic	643.4	642.2	23.4 %	76.6 %	3.27
LMN-800	643.4	642.1	27.9 %	72.1 %	2.58
LMN-800-mic	643.3	641.9	37.5 %	62.5 %	1.67

Figure 5.4 displays the cyclic voltammetric evolutions of LMN-700 / LMN-700-mic and LMN-800 / LMN-800-mic cathode materials, depicting the Li extraction / insertion behaviour of the samples.

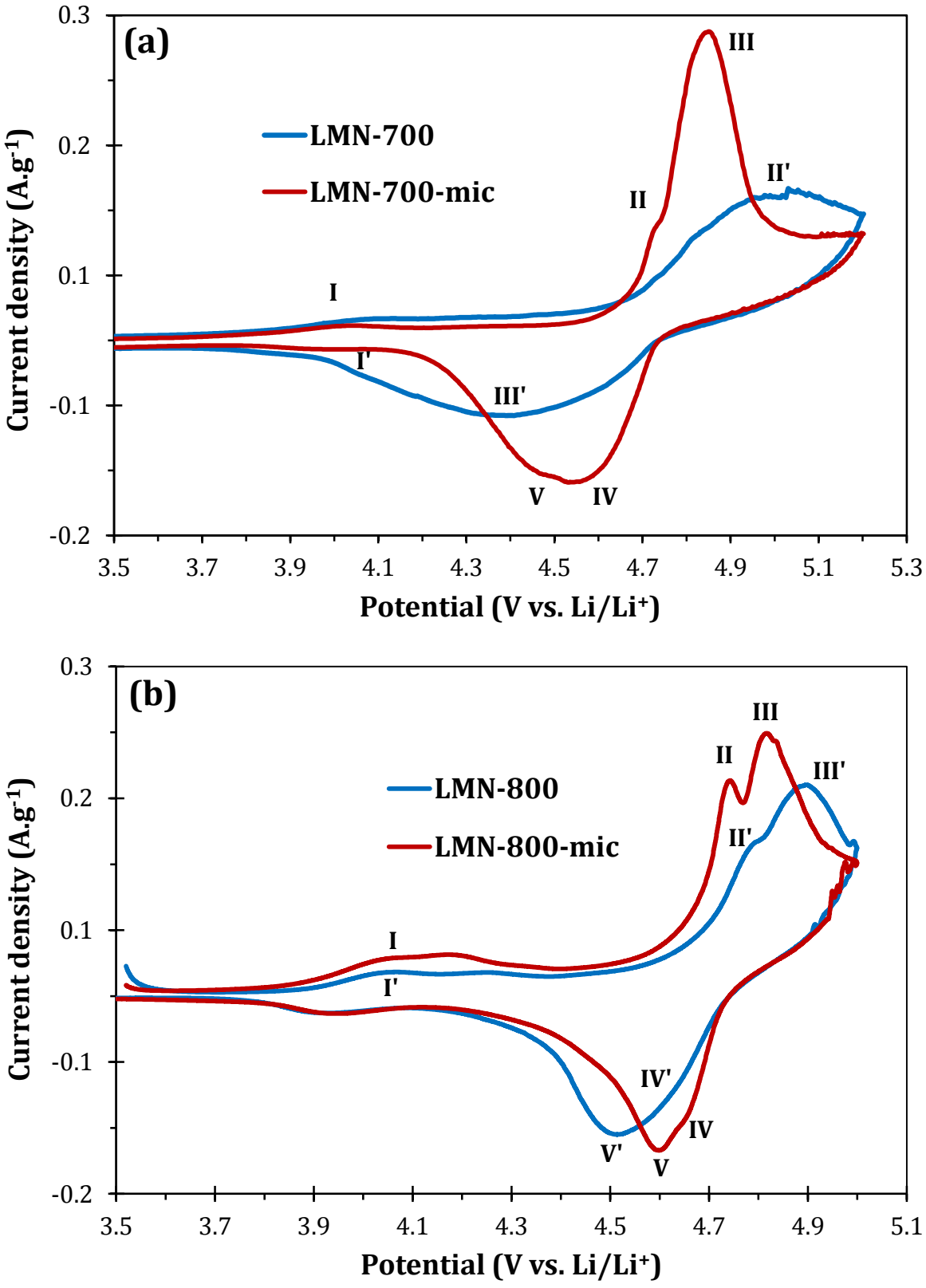

Figure 5.4: Representative cyclic voltammograms of (a) LMN-700 / LMN-700-mic and (b) LMN-800 / LMN-800-mic obtained at a scan rate of 100 $\mu V.s^{-1}$.

The cyclic voltammograms of the un-microwaved (LMN-700 and LMN-800) and the microwaved (LMN-700-mic and LMN-800-mic) samples are significantly different, with the latter showing better resolved and sharper peaks than the former. For the LMN-700 and the LMN-700-mic the difference in the peak-to-peak potential (ΔE_p), for the Ni^{2+}/Ni^{3+} redox couple, is smaller for the LMN-700-mic (II/V) with ΔE_p = 0.288 V vs Li/Li^+, than the LMN-700 (II'/III') with ΔE_p = 0.637 V vs Li/Li^+. This is a clear indication that the microwave treated sample (LMN-700-mic) is more reversible with faster electrochemical kinetics than the un-microwaved sample (LMN-700). In addition, the Mn^{3+}/Mn^{4+} redox wave at ~ 4 V (I/I') for the microwaved samples (LMN-700-mic and LMN-800-mic) is more defined than that of the un-microwaved samples (LMN-700 and LMN-800). For the LMN-800 and the LMN-800-mic the peaks for the disordered spinel, or the Mn^{3+} enriched sample, are more resolved with narrower ΔE_p than those of the ordered spinels, or Mn^{3+} deprived sample. The ΔE_p for the nickel peaks of the LMN-800 and LMN-800-mic samples, Ni^{2+}/Ni^{3+} (II/V or II'/V') and Ni^{3+}/Ni^{4+} (III/IV or III'/IV') are smaller with ΔE_p = 0.219 V and 0.165 V for the LMN-800-mic compared to the LMN-800 with ΔE_p = 0.371 V and 0.287 V. Again, this is an indication that the LMN-800-mic (microwaved sample) gives faster lithium extraction/insertion kinetics.

Figure 5.5 compares the 1st and 25th charge-discharge profiles of LMN-700 / LMN-700-mic and LMN-800 / LMN-800-mic discharged at 0.1 C (14 $mA.g^{-1}$).

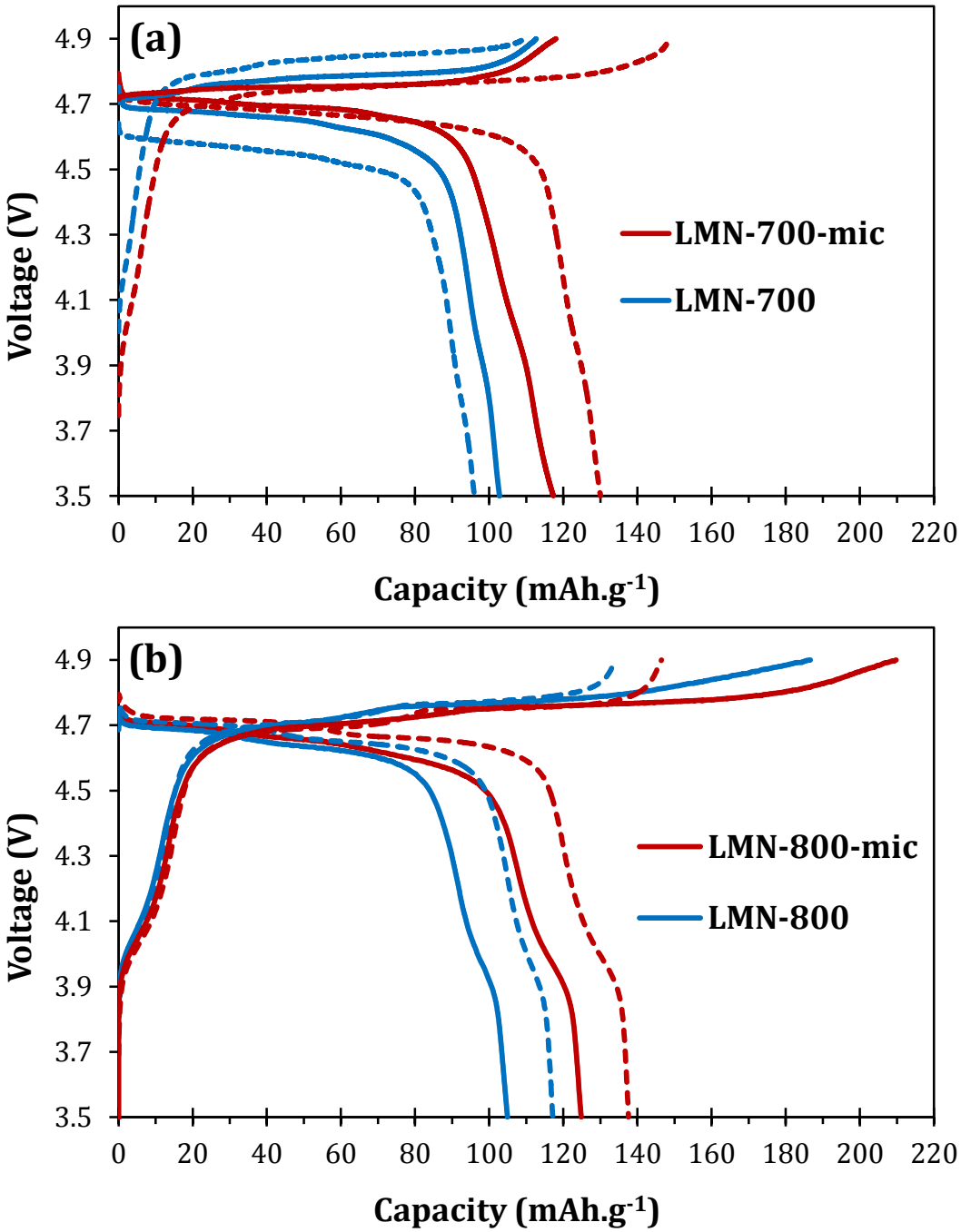

Figure 5.5: The 1st (solid line) and 25th (broken line) charge and discharge curves of (a) the LMN-700 / LMN-700-mic and (b) the LMN-800 / LMN-800-mic at 0.1 C or 14 mAh.g^{-1}.

Unlike the materials obtained at 700°C, the samples from 800°C showed well-defined plateaus at ~ 4 V due to the Mn^{3+}/Mn^{4+} redox couple, signature of 'disordered' spinel. In

addition, the Ni^{2+}/Ni^{3+} and Ni^{3+}/Ni^{4+} redox couples of the disordered spinel are activated upon cycling, suggesting some structural changes induced by electrochemical cycling. The Mn^{3+}/Mn^{4+} peaks are well-defined from the samples prepared at 800°C compared to the samples prepared at 700°C. The discharge capacity of the LMN-700 decreased from the 1st cycle with a capacity of 103 $mAh.g^{-1}$ to the 25th cycle with discharge capacity of 96 $mAh.g^{-1}$, which is typical of ordered spinel [27]. However, upon microwave treatment, the initial discharge capacity of the LMN-700-mic of 117 $mAh.g^{-1}$ increased to 130 $mAh.g^{-1}$ at the 25th cycle. For the samples prepared at 800 ^{o}C, the initial cycles of the un-microwaved (LMN-800) and the microwave treated (LMN-800-mic) samples having discharge capacities of 105 $mAh.g^{-1}$ and 125 $mAh.g^{-1}$, respectively increased upon cycling to 117$mAh.g^{-1}$ and 138 $mAh.g^{-1}$ at the 25th cycle, respectively. This increase in discharge capacity upon cycling could be atributed to the wetting process of the electrodes with the electrolytes prior to stabilisation of the electrochemical reactions [31]. The higher performance of the LMN-800-mic over the LMN-800 sample suggests the intrinsic ability of microwave irradiation to adjust the Mn^{3+} concentration in the spinel for enhanced electrochemistry. It is also observed that for all the samples, the initial Coulombic efficiency is poor but improves with cycling. It should also be noted that the main discharge voltage platauefor the samples prepared at 800°C is higher compared to that of the samples prepared at 700°C. As with the discharge capacity of the LMN-800 and LMN800-mic samples the voltage plataue increases with cycle number. In contrast to the LMN-800 and LMN-800-mic, the LMN-700 and LMN-700-mic shows a decrease in the voltage plataue with cycling. Also very interesting is the voltage plateau of all the samples that underwent microwave irradiation are superior to that of the corrosponding un-microwaved samples.

Next, the cycle stability is explored of the spinel samples at 50 repetitive cycles. This number of cycle was chosen as it provided enough information for the comparative studies, and also considering that other workers have used the same number [32] or even less [33] for the same LMN spinel. **Figure 5.6** compares the cycle stability of the un-microwaved and microwave treated samples, which clearly proves that microwave irradiation improves the cyclability of the spinels (for both the ordered and disordered structures, with the latter benefitting the most).

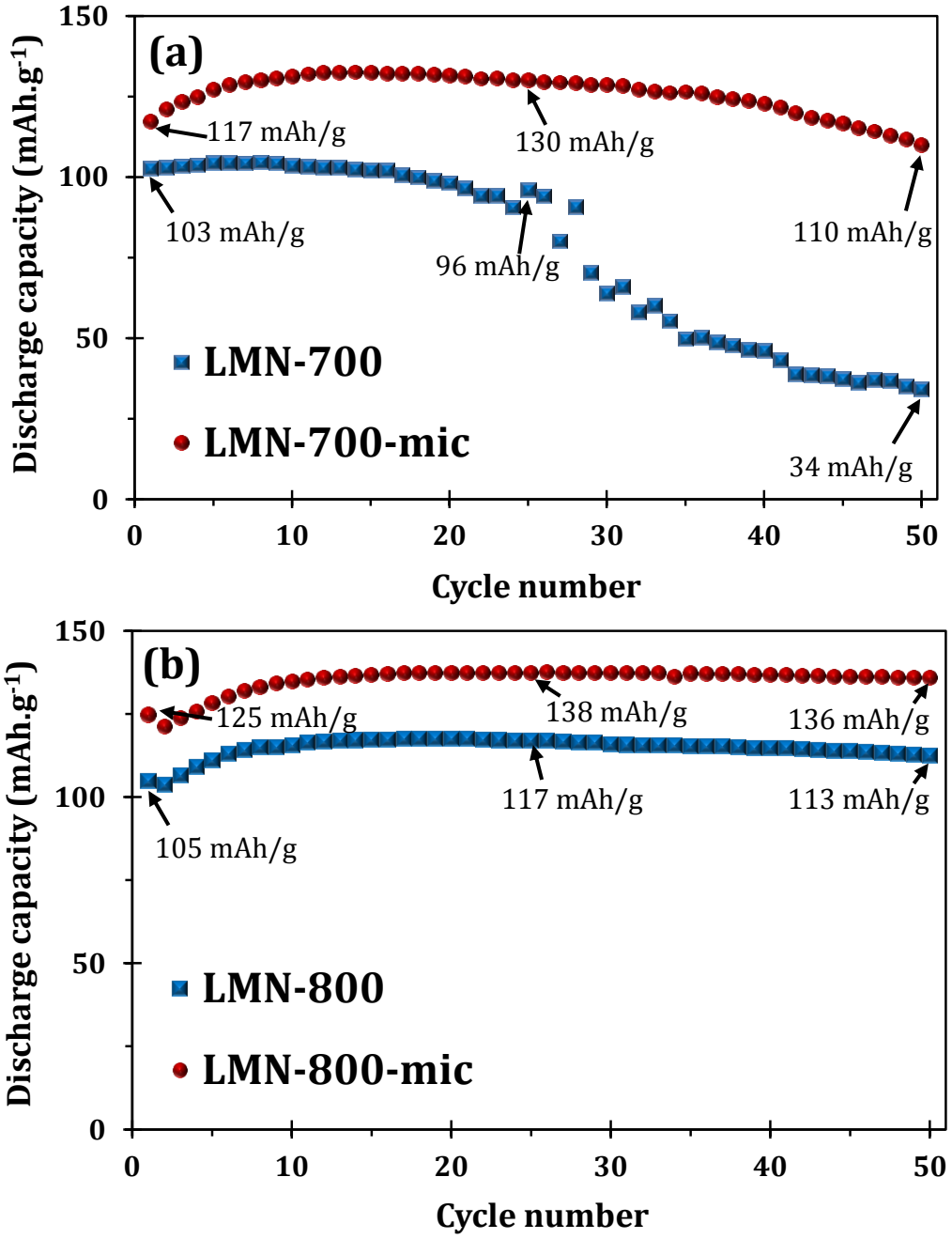

Figure 5.6: Cycle stability of (a) LMN-700 / LMN-700-mic and (b) LMN-800 / LMN-800-mic at 0.1C or 14 mAh.g^{-1}.

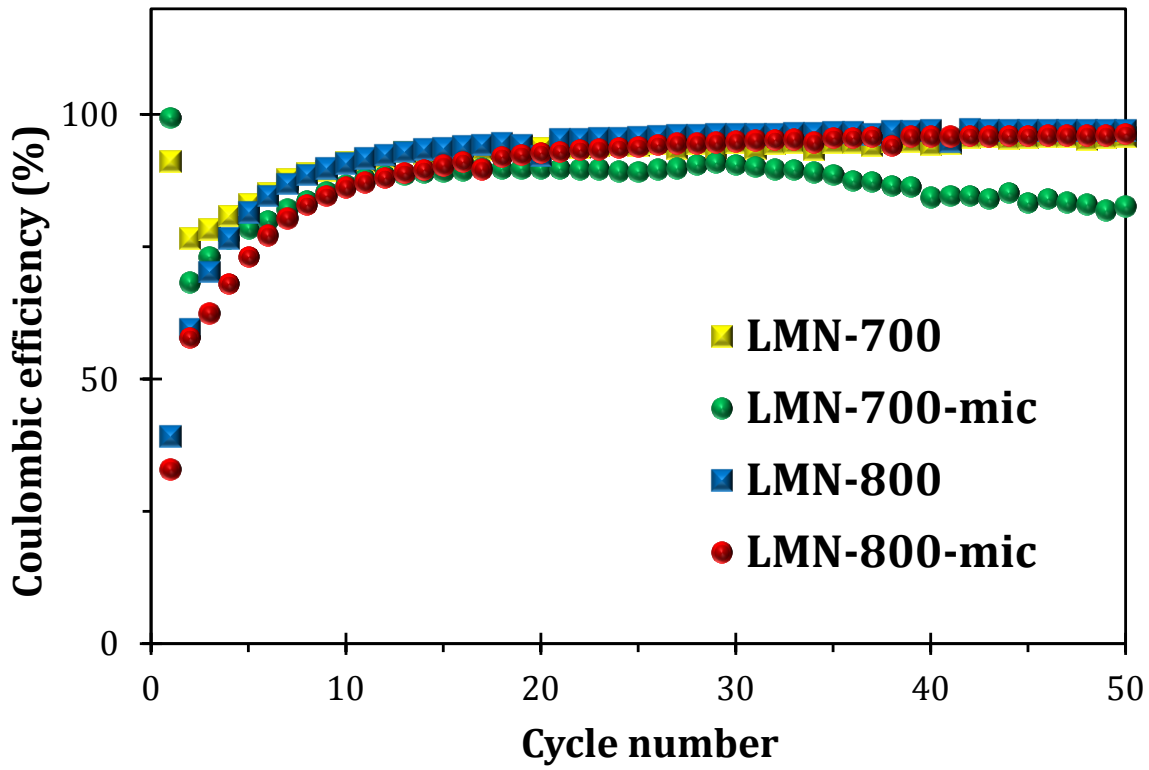

Figure 5.7: The Coulombic efficiency of LMN-700, LMN-700-mic, LMN-800 and LMN-800-mic of the charge discharge cycles in **Figure 5.6 (a)** and **(b)**.

The extreme capacity fading for the LMN-700 sample after the 25th cycle is related to different factors. These factors are, (i) particle size, where nanosized particles are associated with a higher surface area at the electrolyte/cathode interface which leads to capacity degradation and cycle instability [21] and (ii) the high amount of the non-conductive Mn^{4+} ions in the spinel. Also, this is consistent with LMN obtained at 700°C irrespective of the synthetic method or particle size [13, 32]. It is thus interestingly, however, to observe that microwave irradiation may serve as a viable strategy to improve the capacity retention for such spinels prepared at lower temperatures (700°C). The best performance is always obtained by the LMN-800-mic sample, with a capacity retention of ~ 100 % between the 10th and 50th cycle, compared to the capacity retentions of ~ 97 %

and 84 % for LMN-800 and LMN-700-mic, respectively. The excellent capacity retention of the LMN-800-mic may be partly due to the higher connectivity of the nanoparticles as seen in the FESEM images, and partly to the 'appropriate' amount of Mn^{3+} induced by the microwave irradiation. In general, it is common knowledge that LMN sample obtained at higher temperature (800 ^{o}C, disordered) shows better electrochemical performance than the 700 ^{o}C (ordered). Some of the reasons may be due to the better crystallinity and increased conductivity due to the Mn^{3+} compared to the Mn^{4+}. From **Figure 5.7** it is also observed that LMN-800 and LMN-800-mic has superior Coulombic efficiencies.

For high power applications, good rate capability is of utmost importance for any cathode materials for lithium ion batteries. In this study, all the samples were charged at 14 $mA.g^{-1}$ (0.1 C) and discharged at 140 $mA.g^{-1}$ (1C) as shown in **Figure 5.8**. These results show that the samples synthesized at 800°C performed better than the samples synthesized at 700°C in terms of discharge capacity at higher rates. The latter samples have low discharge capacities that did not justify increasing the discharge current density. Therefore only the samples that were synthesized at 800°C were discharged at higher current densities as shown in **Figure 5.9**. The LMN-800 and LMN-800-mic samples were charged at 14 $mA.g^{-1}$ (0.1C) and discharged between 70 $mA.g^{-1}$ (0.5 C) and 1400 $mA.g^{-1}$ (10 C). **Figure 5.9** clearly proves that microwave treatment greatly enhances the rate capability of the spinel material.

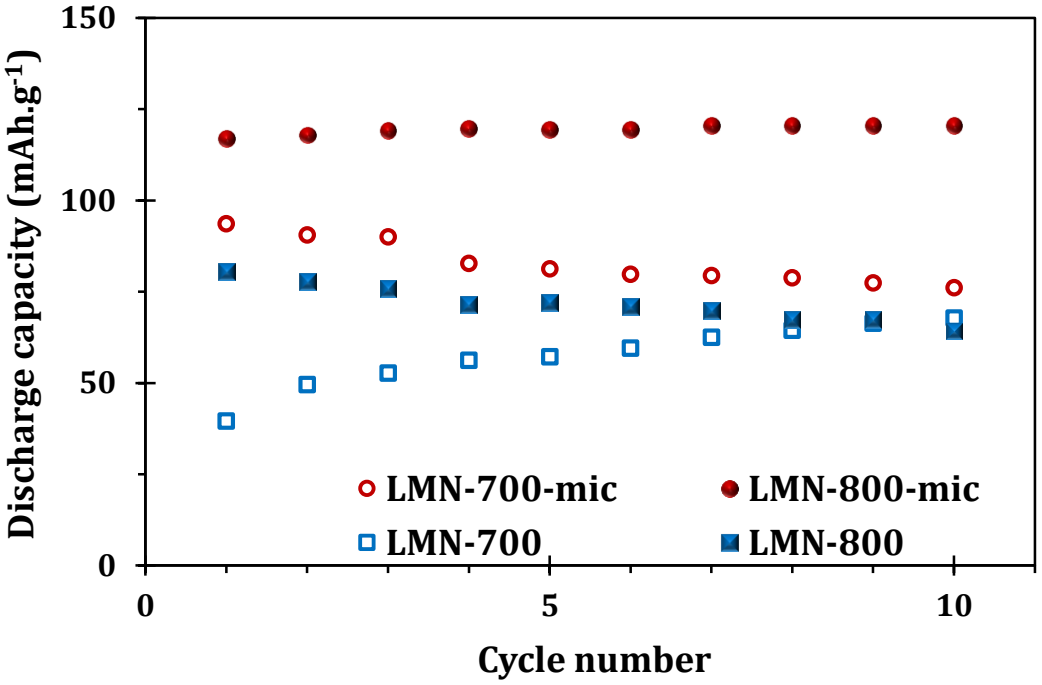

Figure 5.8: Discharge capacities versus the cycle number at a charge rate of 0.1C (14 mA.g^{-1}) and discharge rate of 1C (140 mA.g^{-1}) of all the samples.

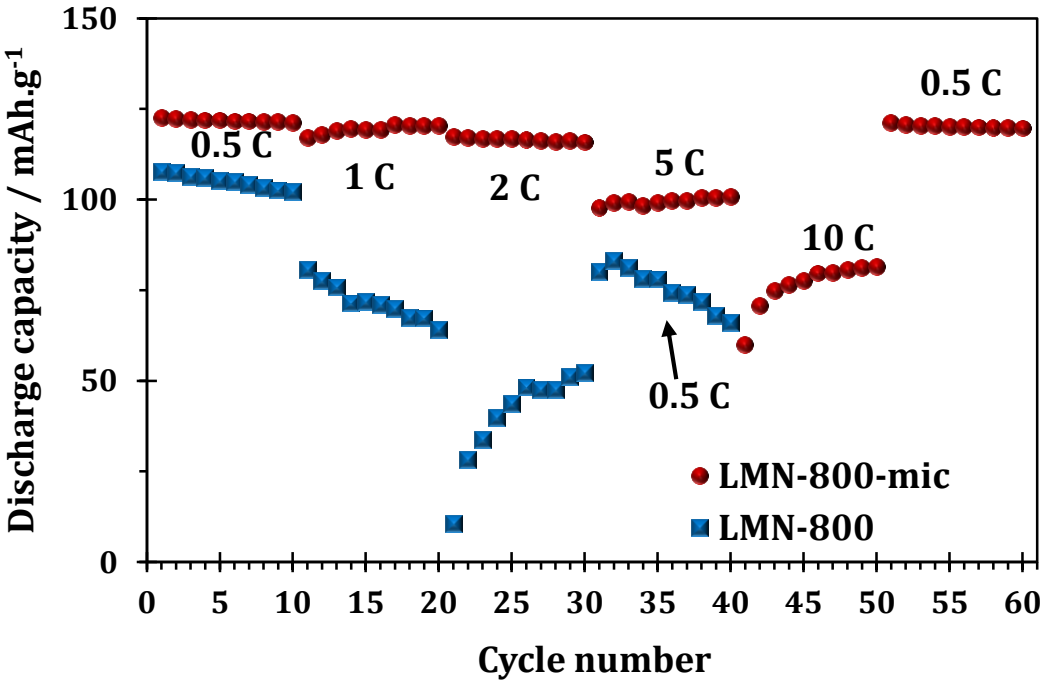

Figure 5.9: Typical rate capability plots for the LMN-800 and LMN-800-mic, charged at 0.1 C but discharged at different rates, 0.5 – 10 C.

The high rate capability of the LMN-800-mic compared to the LMN-800 suggests that lithium-ion diffusion path length is shorter in the former than the latter. Our results are comparable and even superior to many $LiMn_{1.5}Ni_{0.5}O_4$ samples obtained by Pechini method [9, 13] and other methods [32, 34]. For example, at a high current density (e.g., 5 C) our LMN-800-mic recorded above 100 $mAh.g^{-1}$, which compares with the values for the micron-sized carbon-coated $LiMn_{1.5}Ni_{0.5}O_4$ obtained by carbonisation of sucrose at 850 °C, and even much better than the uncoated $LiMn_{1.5}Ni_{0.5}O_4$ sample that gave only about 70 $mAh.g^{-1}$ [34].

In order to gain a better understanding on the impact that the microwave irradiation has on the $LiMn_{1.5}Ni_{0.5}O_4$ cathodes, electrochemical impedance spectroscopy (EIS) was done. Each plot consists of a depressed semicircle in the high frequency range and a Warburg region at the lower frequencies. The impedance spectra can be explained on the basis of the simulated electronic equivalent circuit (EEC) shown in **Figure 5.10 (c)** and **(d)**. Here R_s is the series or Ohmic resistance incorporating the electrolyte resistance (which is non-existent for the LMN-800 and LMN-800-mic), R_{SEI} is the surface electrolyte interface resistance, C / CPE_{SEI} and C_{dl} are the capacitance and / or constanst phase element due to the surface layer and the surface charge build up, respectively. R_{ct} is the charge transfer resistance and W the Warburg impedance. The EEC for the LMN-800 and LMN-800-mic includes a C_{int} parameter which is the intercalation capacitance describing the accumulation of Li at the very low frequency range.

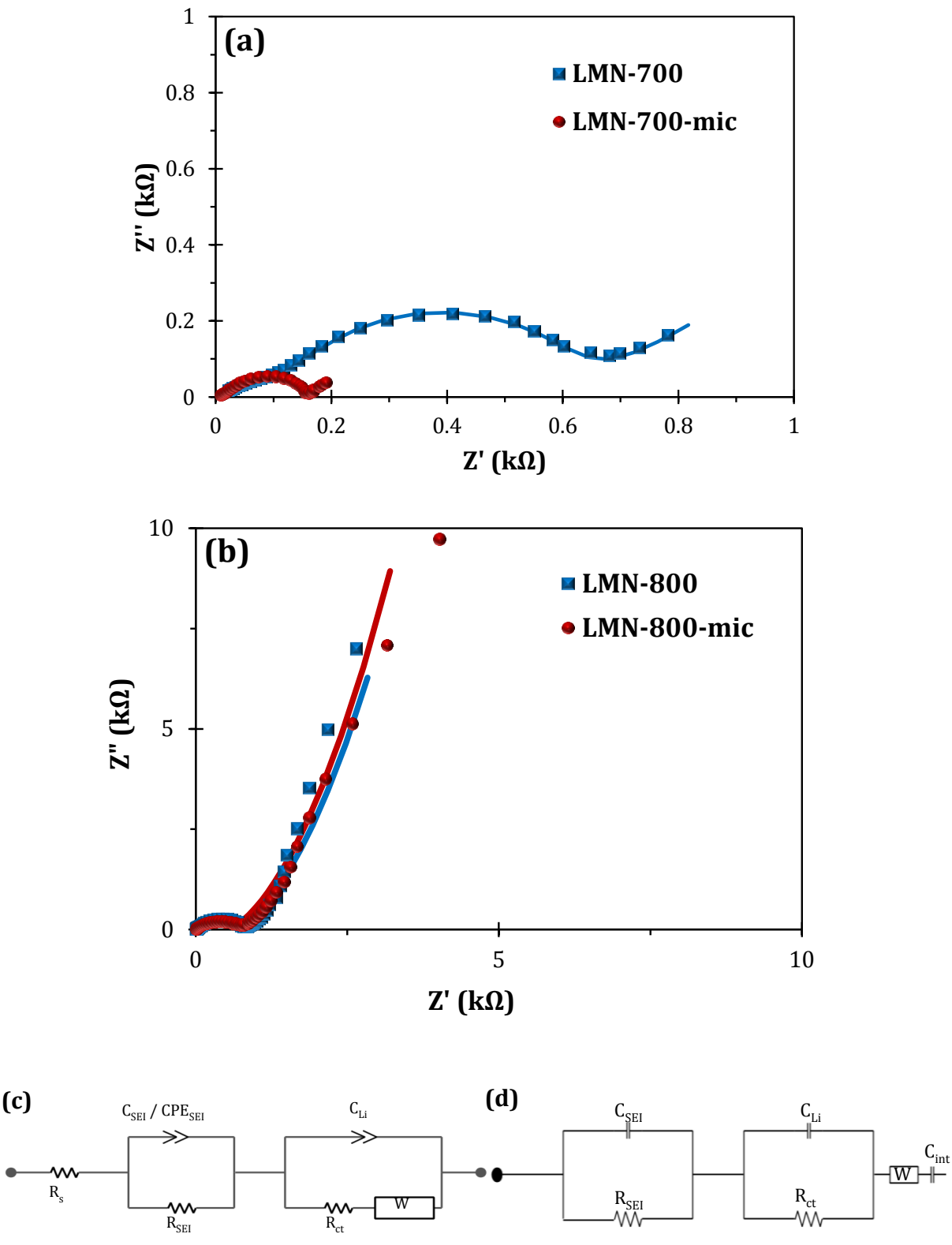

Figure 5.10: Nyquist plots of (a) LMN-700 / LMN-700-mic and (b) LMN-800 / LMN-800-mic where the solid lines are fittings to the data points. The equivalent electrical circuits (EECs) for (c) LMN-700 / LMN-700-mic and (d) LMN-800 / LMN-800-mic.

The simulated values are reported in **Table 5.3**. It is evident from the data in the table that the charge transfer resistance, for the LMN-700 and LMN-700-mic, decreases when the sample is microwaved. The opposite is observed for the LMN-800 and LMN-800-mic. The R_{ct} values for LMN-700 (334.0 Ω) is thus higher compared to its microwaved counterpart, LMN-700-mic (70.3 Ω). This can be explained by the surface films that develop with surface electrolyte interphase (SEI) resistances (R_{SEI}) of the LMN-700 (324.0 Ω) that is higher than that for the LMN-700-mic (83.1 Ω), suggesting that the surface film formed is thinner. The LMN-800 with a R_{ct} value of 42.9 Ω compared to its microwaved counterpart LMN-800-mic with a slightly higher R_{ct} value of 59.7 Ω is observed. The LMN-800 and LMN-800-mic has thicker SEIs formed than the LMN-700 and LMN-700-mic. This could be the reason for the better stability of the LMN-800 and LMN-800-mic (as is shown in **Figure 5.6**).

Table 5.3: Simulated equivalent electrical circuit data

Sample	R_s (Ω)	R_{SEI} (Ω)	C_{SEI} / CPE_{SEI} (μF)	n	C_{dl} (μF)	R_{ct} (Ω)	W (×10^{-4})	C_{int} (mF)
LMN-700	5.0 ± 1.9	324.0 ± 33.1	107.8 ±20.9	0.4	6.8 ± 0.4	334.0 ± 17.4	27.2 ± 2.0	
LMN-700-mic	3.9 ± 0.4	83.1 ± 3.3	173.8 ± 0.9	0.5	4.6 ± 0.2	70.3 ± 4.8	171.1 ± 11	
LMN-800	-	655.0 ± 40.8	1.5 ± 0.2	-	0.3 ± 0.04	42.9 ± 6.0	41.7 ± 7.1	38.4 ± 9.6
LMN-800-mic	-	525.0 ± 35.7	1.6 ± 0.2	-	0.2 ± 0.02	59.7 ± 7.2	34.0 ± 5.4	25.2 ± 5.0

Further studies on the lithium diffusive properties were explored using the electrochemical impedance spectroscopy and employing the correctly derived equation in **Chapter 4**:

$$D_{Li} = \frac{2R^2T^2}{C_{Li}^2 n^4 F^4 A^2 \sigma^2} \quad 5.1$$

where D_{Li} is the diffusion coefficient of lithium ions, R the gas constant, T the absolute temperature, A the geometric surface area of the cathode, F the Faraday constant, n the number of electrons transferred per molecule during oxidation and C_{Li} the lithium

concentration in the cathode material. The Warburg factor, σ, is obtained from the slope of the real impedance (Z') vs. the reciprocal square root of the frequency in the low frequency region ($\omega^{-1/2}$) (**Figure 5.11**).

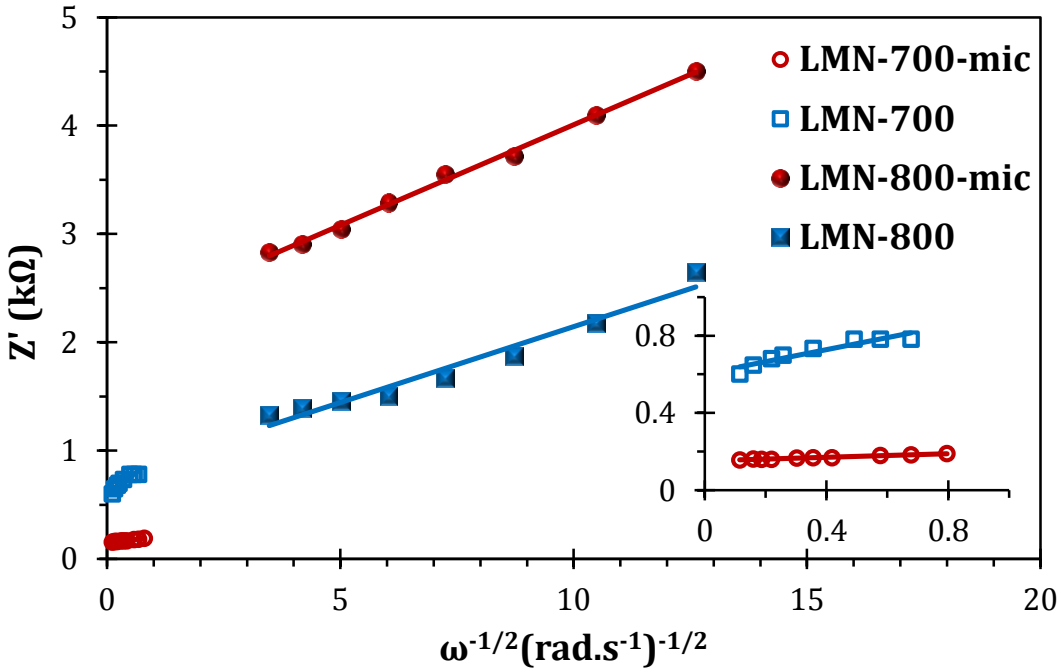

Figure 5.11: Plots of *Z'* vs. $\omega^{-1/2}$ of LMN-700, LMN-700-mic, LMN-800 and LMN-800-mic.

Table 5.4: The calculated diffusion coefficients

Sample	Diffusion Coefficient (cm^2s^{-1})
LMN-700	2.25×10^{-13}
LMN-700-mic	6.00×10^{-12}
LMN-800	2.69×10^{-13}
LMN800-mic	1.26×10^{-12}

The estimated diffusion coefficients (see **Table 5.4**) showed that the microwave treated samples are about an order of a magnitude (*ca.* $\sim10^{-12}$ cm^2s^{-1}) higher compared to its un-microwaved counterparts (*ca.* $\sim10^{-13}$ cm^2s^{-1}). Also, when comparing these values with

those calculated with the wrongly used formula it is higher as discussed, in an example, in Chapter 4.

5.3 The Proposed Mechanism

During the microwave treatment that follows the pre-heating process, the microwave energy exerted onto the sample penetrates the sample and oxygen vacancies are created. Then the sample is annealed at a temperature lower than the onset temperature to create oxygen vacancies (T = 700 °C) [9], which will cause no further increase in the oxygen vacancies in the lattice. Therefore, it is seen that with the microwave treatment, oxygen vacancies are created and with the annealing process at T = 700 °C it remains in the lattice. When the LMN-800 is treated with microwave radiation, oxygen vacancies are created in the lattice. When annealed at 800 °C the oxygen-deficient cathode material will allow oxygen back into the lattice to achieve an equilibrium concentration. Also, the so-called *specific* or *non-thermal* microwave effects can still play a role, though this is still a subject of some controversy [35, 36].

5.4 Conclusion on the Impact of the Mn^{3+} Concentration of $LiMn_{1.5}Ni_{0.5}O_4$

The SEM images show that microwave irradiation changes the growth kinetics of the particles. The calculated lattice parameters from the XRD patterns show that the Mn^{3+} increase with microwave irradiation for the samples prepared at 700°C. The calculated lattice parameters showed a decrease with microwave irradiation for the samples prepared at 800°C. This finding is confirmed with XPS analyses. CV analyses show that the

microwave irradiated samples have faster lithium extraction/insertion kinetics. The microwave irradiated samples showed superior discharge capacities and cycle stability after 50 cycles. EIS spectra, for the samples prepared at 700 °C, show that the charge transfer resistance decreases when samples are irradiated with microwaves. The charge transfer for the samples prepared at 800 °C is consistent. The diffusion coefficients calculated also showed that the microwave irradiated samples are superior to their un-microwaved counterparts. This work has shown, for the first time, that microwave irradiation is capable of tuning the Mn^{3+} concentration for enhanced electrochemical performance (high capacity, high capacity retention, excellent rate capability, and fast Li^{+} insertion/extraction kinetics) of the high-voltage $LiMn_{1.5}Ni_{0.5}O_4$ spinel cathode material for lithium ion battery. Also, a mechanism is proposed for the interaction of microwaves with the material.

References

[1] M.V. Reddy, G.V. Subba Rao, B.V.R. Chowdari, Chem. Rev. **113** (2013) 5364.

[2] M.V. Reddy, M.J.S. Raju, N. Sharma, P.Y. Quan, S.H. Nowshad, H.E. Emmanuel, V.K. Peterson, B.V.R. Chowdari, J. Electrochem. Soc. **158** (2011) A1231.

[3] A. Sakunthala, M.V. Reddy, S. Selvasekarapandian, B.V.R. Chowdari, P.C. Selvin, Electrochim. Acta **55** (2010) 4441.

[4] M.V. Reddy, A. Sakunthala, S.S. Pandian, B.V.R. Chowdari, J. Phys. Chem. C **117** (2013) 9056.

[5] C. Sigala, D. Guyomard, A. Verbaere, Y. Piffard, M. Tournoux, Solid State Ionics **81** (1995) 167.

[6] J. Liu, A. Manthiram, J. Phys. Chem. C **113** (2009) 15073.

[7] D. Liu, J. Han, J.B. Goodenough, J. Power Sources **195** (2010) 2918.

[8] J.H. Kim, S.-. Myung, C.S. Yoon, S.G. Kang, Y.-. Sun, Chem. Mater. **16** (2004) 906.

[9] M. Kunduraci, J.F. Al-Sharab, G.G. Amatucci, Chem. Mater. **18** (2006) 3585.

[10] J. Yang, X. Han, X. Zhang, F. Cheng, J. Chen, Nano Research **6** (2013) 679.

[11] S.H. Oh, K.Y. Chung, S.H. Jeon, C.S. Kim, W.I. Cho, B.W. Cho, J. Alloys Compounds **469** (2009) 244.

[12] L. Wang, H. Li, X. Huang, E. Baudrin, Solid State Ionics **193** (2011) 32.

[13] M. Kunduraci, G. Amatucci, J. Electrochem. Soc. **153** (2006) A1345.

[14] J. Xiao, X. Chen, P.V. Sushko, M.L. Sushko, L. Kovarik, J. Feng, Z. Deng, J. Zheng, G.L. Graff, Z. Nie, D. Choi, J. Liu, J. Zhang, M.S. Whittingham, Adv. Mater. **24** (2012) 2109.

[15] H. Kishi, N. Kohzu, Y. Iguchi, J. Sugino, M. Kato, H. Ohsato, T. Okuda, J. Eur. Cera. Soc. **21** (2001) 1643.

[16] J. Zheng, J. Xiao, X. Yu, L. Kovarik, M. Gu, F. Omenya, X. Chen, X. Yang, J. Liu, G.L. Graff, M.S. Whittingham, J. Zhang, Phys. Chem. Chem. Phys. **14** (2012) 13515.

[17] A. Ito, D. Li, Y. Lee, K. Kobayakawa, Y. Sato, J. Power Sources **185** (2008) 1429.

[18] C. Locati, U. Lafont, L. Simonin, F. Ooms, E.M. Kelder, J. Power Sources **174** (2007) 847.

[19] G. Zhao, Y. Yang, Y. Lin, B. Zeng, T. Zhou, Y. Lin, Z. Huang, (2012) 1.

[20] M.V. Reddy, S.S. Manoharan, J. John, B. Singh, G.V. Subba Rao, B.V.R. Chowdari, J. Electrochem. Soc. **156** (2009) A652.

[21] J.S. Park, K.C. Roh, J. Lee, K. Song, Y. Kim, Y. Kang, J. Power Sources **230** (2013) 138.

[22] R. Roy, R. Peelamedu, L. Hurtt, J. Cheng, D. Agrawal, Mater. Res. Innov. **6** (2002) 128.

[23] C. Nithya, R. Thirunakaran, A. Sivashanmugam, S. Gopukumar, ACS Appl. Mater. & Inter. **4** (2012) 4040.

[24] O.O. Fashedemi, B. Julies, K.I. Ozoemena, Chem. Comm. **49** (2013) 2034.

[25] M.V. Reddy, H.Y. Cheng, J.H. Tham, C.Y. Yuan, H.L. Goh, B.V.R. Chowdari, Electrochim. Acta **62** (2012) 269.

[26] J. Song, D.W. Shin, Y. Lu, C.D. Amos, A. Manthiram, J.B. Goodenough, Chem. Mater. **24** (2012) 3101.

[27] K.M. Shaju, P.G. Bruce, Dalton Trans. (2008) 5471.

[28] Y. Idemoto, H. Narai, N. Koura, J. Power Sources **119–121** (2003) 125.

[29] Y. Wei, L. Yan, C. Wang, X. Xu, F. Wu, G. Chen, J. Phys. Chem. B **108** (2004) 18547.

[30] K.M. Shaju, G.V. Subba Rao, B.V.R. Chowdari, Electrochim. Acta **48** (2003) 1505.

[31] J. Saint, A. Best, A. Hollenkamp, J. Kerr, J. Shin, M. Doeff, J. Electrochem. Soc. **155** (2008) A172.

[32] Y. Dong, Z. Wang, H. Qin, X. Sui, RSC Adv. **2** (2012) 11988.

[33] B. Hai, A.K. Shukla, H. Duncan, G. Chen, J. Mater. Chem. A **1** (2013) 759.

[34] T. Yang, N. Zhang, Y. Lang, K. Sun, Electrochim. Acta **56** (2011) 4058.

[35] M. Nüchter, B. Ondruschka, W. Bonrath, A. Gum, Green Chem. **6** (2004) 128.

[36] A. de la Hoz, Á. Díaz-Ortiz, A. Moreno, Chem. Soc. Rev. **34** (2005) 164.

Chapter 6*

The Effect of Al Doping on the $Li_{1.2}Mn_{0.54}Ni_{0.13}Co_{0.13}O_2$ Cathode Material

6.1 Introduction to the Importance of Al Doping in $Li_{1.2}Mn_{0.54}Ni_{0.13}Co_{0.13}O_2$ Cathode Material

Research interests in the $xLi_2MnO_3{\cdot}(1-x)LiNi_{1/3}Co_{1/3}Mn_{1/3}O_2$ series of compounds for application in lithium ion batteries have continued to grow due to the high capacities of these compounds [1-4]. They are also considered as viable alternatives to the famous Sony-commercialised product ($LiCoO_2$) of relative low discharge capacity (~ 160 $mA.h.g^{-1}$) but has been characterised by toxicity concerns and high cost. The $Li[Li_{0.2}Mn_{0.54}Ni_{0.13}Co_{0.13}]O_2$ (abbreviated herein as the LMNC) is a member of the series (x = 0.5). Thackeray and co-workers have continually reported that the integration of two structurally compatible, layered rock-salt components, Li_2MnO_3 (redox-inactive) and $LiMO_2$ (redox-active), permits the possibility of using a redox-silent Li_2MnO_3 structural component to be dispersed within and to stabilize an electro-active $LiMO_2$ component matrix, in which M = Mn, Ni, or Co (or combinations thereof) [2]. These manganese-rich,

*The following publication resulted from part of the research work presented in this chapter and is not referenced further:
C. J. Jafta, K. I. Ozoemena, M. K. Mathe and W. D. Roos, "Synthesis, characterisation and electrochemical intercalation kinetics of nanostructured aluminium-doped $Li[Li_{0.2}Mn_{0.54}Ni_{0.13}Co_{0.13}]O_2$ cathode material for lithium ion battery", *Electrochim. Acta* **85** (2012) 411 – 422

two-component materials offer cost, stability and safety advantages, and can deliver capacities approximately twice that of the famous $LiCoO_2$ cathode material commercialised in 1992 by Sony.

Low rate capability makes lithium-rich cathode materials less attractive for electric vehicle applications. Current preparation methods (notably the mixed hydroxides or carbonates co-precipitation [3]) lead to micron-sized to large spherical aggregates resulting in poor rate capability. The poor rate performance of $Li[Li_{0.2}Mn_{0.54}Ni_{0.13}Co_{0.13}]O_2$ may be related to the poor electron transport (i.e., low electronic conductivity due to the insulating Li_2MnO_3 component) while the large spherical agglomerates would hinder mass transport (i.e., lithium diffusion especially during the activation of Li_2MnO_3 component at high current rates).

The work in this chapter is thus motivated mainly by these reasons:

I. The fact that the electrochemical performance of electrode materials that is strongly dependent on the preparation method. Thus the modified Pechini method is used to prepare nanosized LMNC and its aluminium-doped counterpart, $Li[Li_{0.2}Mn_{0.52}Ni_{0.13}Co_{0.13}Al_{0.02}]O_2$ (LMNCA) of mixed sizes (nano- and sub-micron).

II. A need to study the intercalation kinetics, and determine the interplay of aluminium-doping on the kinetics, rate capability and cyclability of LMNC and LMNCA. A proposition made by Thackeray *et al.* [4] that the addition of metal ions (such as Co^{3+}) to the transition metal layers in the compounds at the expense of Mn^{4+} and Ni^{2+} reduced the amount and size of the Li_2MnO_3-like regions. Thus, we explore the impact of introducing Al^{3+} at the expense of Mn^{4+} on the structural and

electrochemical properties of the cathode material. It is worth noting that this is the first study where this LMNC is doped with Al^{3+}.

III. Doping of Li/Mn rich cathode material [5] (as reported in this work) or any other LMNC compounds [6-10] with very low amount of aluminium improves the rate capability and cycling stability. However, there is no report on the intercalation kinetics of Al-doped Li/Mn rich compounds. This work presents the first report on the impact of Al-doping on the structural and electrochemical properties of Li/Mn rich cathode materials for lithium ion battery.

It is demonstrated in this chapter that Al doping reduces cation mixing and improves cyclability, rate capability, and reaction kinetics (Li ion diffusivity and rate constant) of the $Li[Li_{0.2}Mn_{0.54}Ni_{0.13}Co_{0.13}]O_2$. The work in this chapter is also seen as provisional to that reported in **chapter 7**, where the impact of Al doping on the Mn^{3+}/Mn^{4+} ratio is studied.

6.2 Results and Discussion

Figure 6.1 compares the SEM images of LMNC and LMNCA, showing that the synthesised materials comprised of nanosized particles with sizes in the 50 – 100 nm range for the LMNC, and 50 – 200 nm range for the LMNCA.

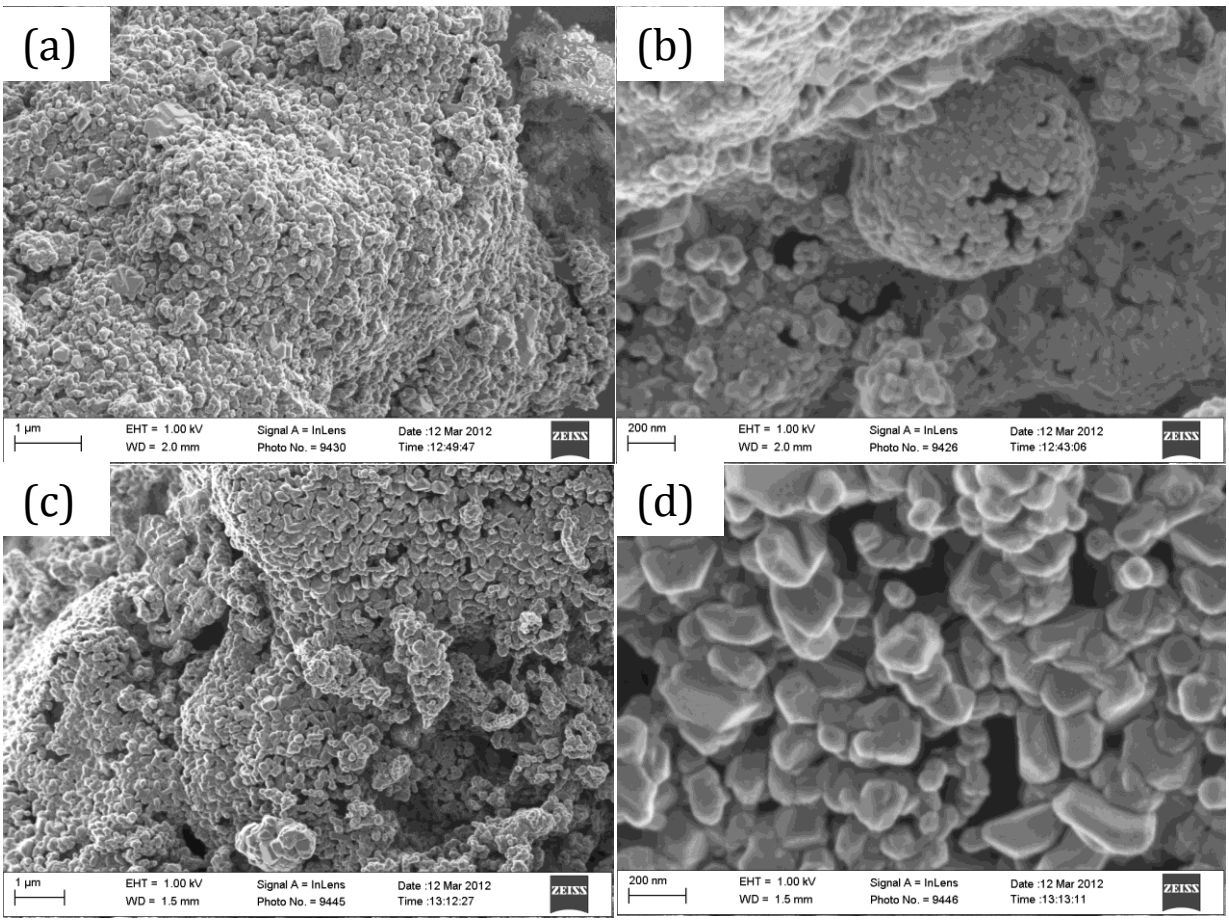

Figure 6.1: FESEM images of (a) LMNC at low magnification, (b) LMNC at high magnification, (c) LMNCA at low magnification and (d) LMNCA at high magnification.

Figure 6.2 shows the XRD spectra of the LMNC and LMNCA recorded from 2θ = 10° – 90°. All the peaks are attributed to the typical peaks of a hexagonal phase with space group $R\bar{3}m$, except for the super lattice peaks found between 2θ = 22° – 30° [11] characteristic of the presence of a Li_2MnO_3-type integrated phase, which by contrast adopts the C2/m space group [11-13]. The intensity ratio of the 101/(006 + 102) peaks are greater than 2 which is an indication that the cation mixing between Li and transition metal layers is small [14]. The lattice parameters were calculated by hand and are summarized in **Table** 6.1.

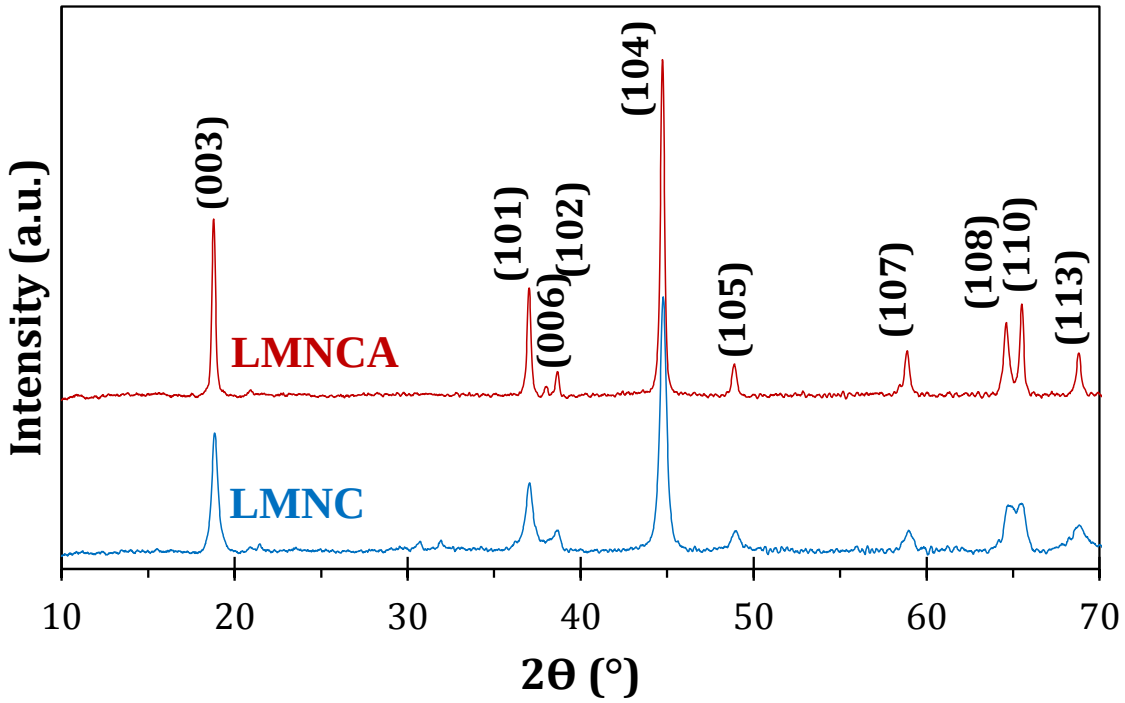

Figure 6.2: XRD patterns of LMNC ($Li[Li_{0.2}Mn_{0.54}Ni_{0.13}Co_{0.13}]O_2$) and LMNCA ($Li[Li_{0.2}Mn_{0.52}Ni_{0.13}Co_{0.13}Al_{0.02}]O_2$)

Table 6.1: Structure parameters of the LMNC and LMNCA samples

Sample	*a* (Å)	*c* (Å)	*c*/*a*
LMNC	2.852	14.173	4.970
LMNCA	2.853	14.238	4.990

The lattice parameters *a* and *c* represent the interlayer metal-metal distance and the inter-slab distance, respectively. The LMNCA has a higher *c*/*a* ratio compared to the LMNC, indicating a higher cation ordering of the LMNCA. There is a clear splitting of the (006) and the (102) peaks in the LMNCA pattern (not so clear in the LMNC pattern) suggesting that LMNCA exhibits better crystallinity compared to the LMNC. The data show that when doping with a minute amount of Al (x = 0.02) that there is almost no change in

the *a* lattice parameter but a slight increase in the *c* lattice parameter. This is attributed to the increased ionic radius of Al^{3+} ($r(Al^{3+})$ = 53.5 pm) [15] compared to the smaller ionic radius of Mn^{4+} ($r(Mn^{4+})$ = 53.0 pm) [16]. Also, the increase in the *c* lattice parameter, in layered materials, is associated with faster Li diffusion due to the decrease in the activation energy of Li hopping [17]. The c/a ratio is an indication of the hexagonal setting, with a larger ratio indicating higher cation ordering. Partial cation mixing is said to occur if the c/a ratio falls below 4.96 [18-22]. The high c/a ratio, well above that required for distortion of the oxygen lattice, clearly confirm the formation of the layered structure. Note that Lu *et al.* [21] showed that the c/a ratio increases as the Ni occupancy decreases. Thus, with the introduction of Al^{3+} ions the cation mixing is reduced. These ratios are in good agreement with other reported values [19-22]. The ratio $c/3a$ is a measure of how layered the materials are, with a ratio of 1.657 for LMNC which is in good agreement with a mean value (1.657) calculated for $LiNi_{0.33}Mn_{0.33}Co_{0.33}O_2$ by Whittingham [20], the LMNCA, with a ratio of 1.663, proves to be a more layered material and thus has a higher cation ordering than the parent LMNC.

Also, Xiao et al. [23] showed that for a layered structure ($LiNi_{0.9-y}Mn_yCo_{0.1}O_2$, when $y \geq 0.5$) the material loses its layered structure and an impurity spinel structure is introduced. In this work we show that even though the Mn content is high and the Ni and Co content low ($Li_{1.2}Mn_{0.54}Ni_{0.13}Co_{0.13}O_2$) the material still holds its layered structure without any impurities present.

Figure 6.3 shows the detailed XPS spectra of the Mn $2p_{3/2}$ peaks of the LMNC (**Figure 6.3 (a)**) and LMCA (**Figure 6.3 (b)**).

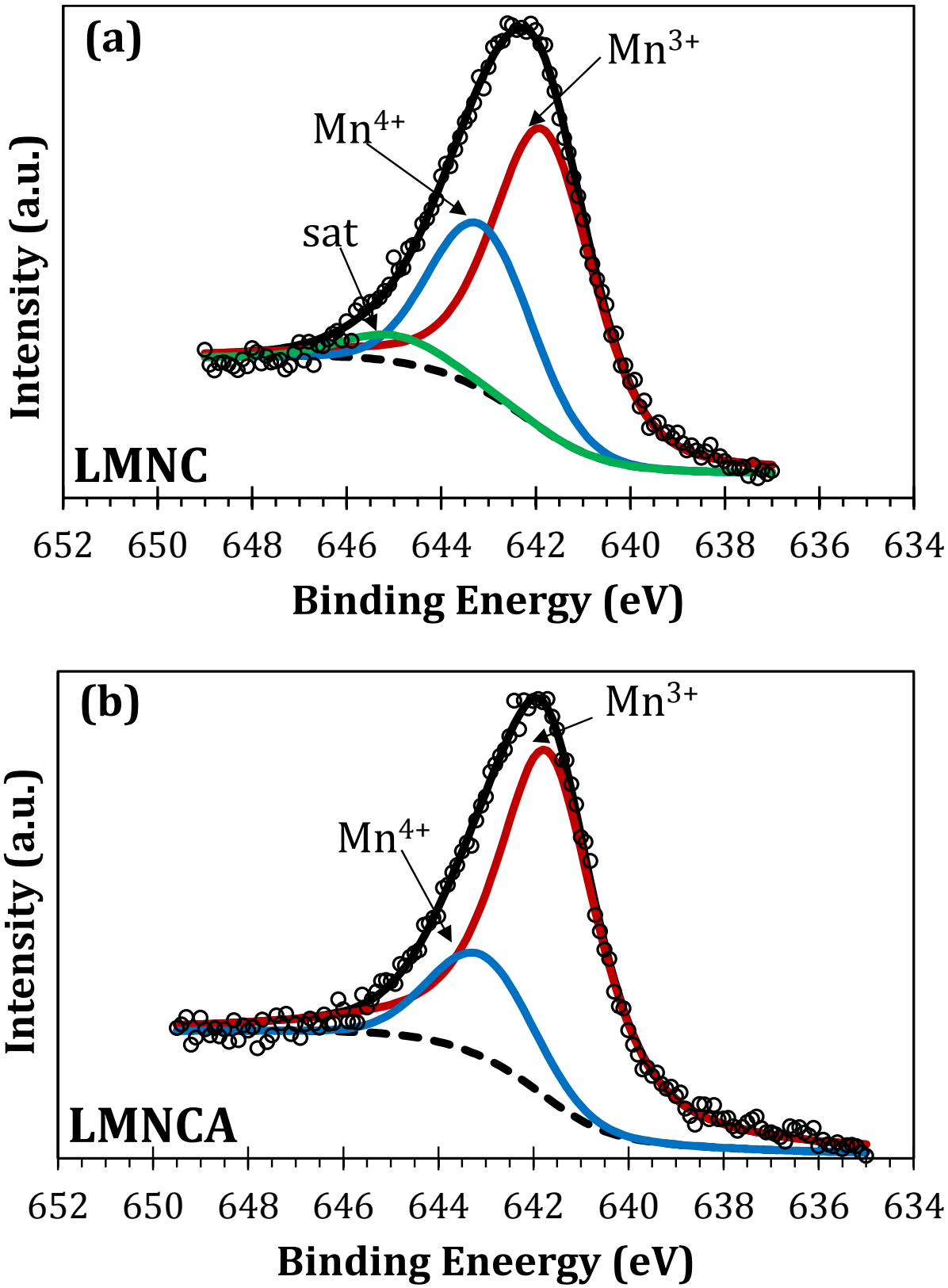

Figure 6.3: The X-ray Photoelectron Spectroscopy spectra of (a) LMNC and (b) LMNCA, showing the Mn $2p_{3/2}$ peak.

There is a broadening in both the peak widths, an indication that the Mn exist in more than one oxidation state. In order to confirm the oxidation states and to approximate their contribution to the total peak, the Mn $2p_{3/2}$ of the LMNC and the LMNCA peaks were deconvoluted into two and three peaks, respectively, as this gives the best statistical fit. The obtained binding energy positions and cation distribution are summarised in **Table** 6.2. The binding energy peak positions corresponding to Mn^{4+} and $Mn^{3+/2+}$ are comparable with other binding energy values reported in the literature [22, 24]. The XPS results indicate a 13% decrease in the Mn^{4+} for the Al doped material (LMNCA), suggestive of a possible substitution of the Mn^{4+} by the Al^{3+}. It may be noted that the ionic radius of Al^{3+} (*53.5 pm*) is almost the same as that of the Mn^{4+} (*53.0 pm*) suggesting that Al^{3+} would preferably sit in the Mn^{4+} ion sites. It can be thus concluded that when LMNC is doped with Al the Al^{3+} ions would preferably occupy the Mn^{4+} sites. The satellite peak at approximately 645 eV in **Figure 6.3 (a)** for the Mn $2p_{3/2}$ peak of LMNC is due to an electron hole, with a relatively longer lifetime, created in the core levels [25]. Of course such a replacement of the Mn^{4+} by the Al^{3+} should lead to other charge compensation from either the Ni or the Co by oxidation to the next higher oxidation state.

Table 6.2: Mn $2p_{3/2}$ peak positions and cation distribution

Sample	Binding energy position(eV)		Cation distribution	
	Mn^{4+}	$Mn^{3+/2+}$	Mn^{4+}	$Mn^{3+/2+}$
LMNC	643.2	641.8	31.6 %	68.4 %
LMNCA	643.1	641.7	18.2 %	81.8 %

Figure 6.4 presents the detailed XPS of the Co 2p peaks and the Ni 2p peaks, respectively.

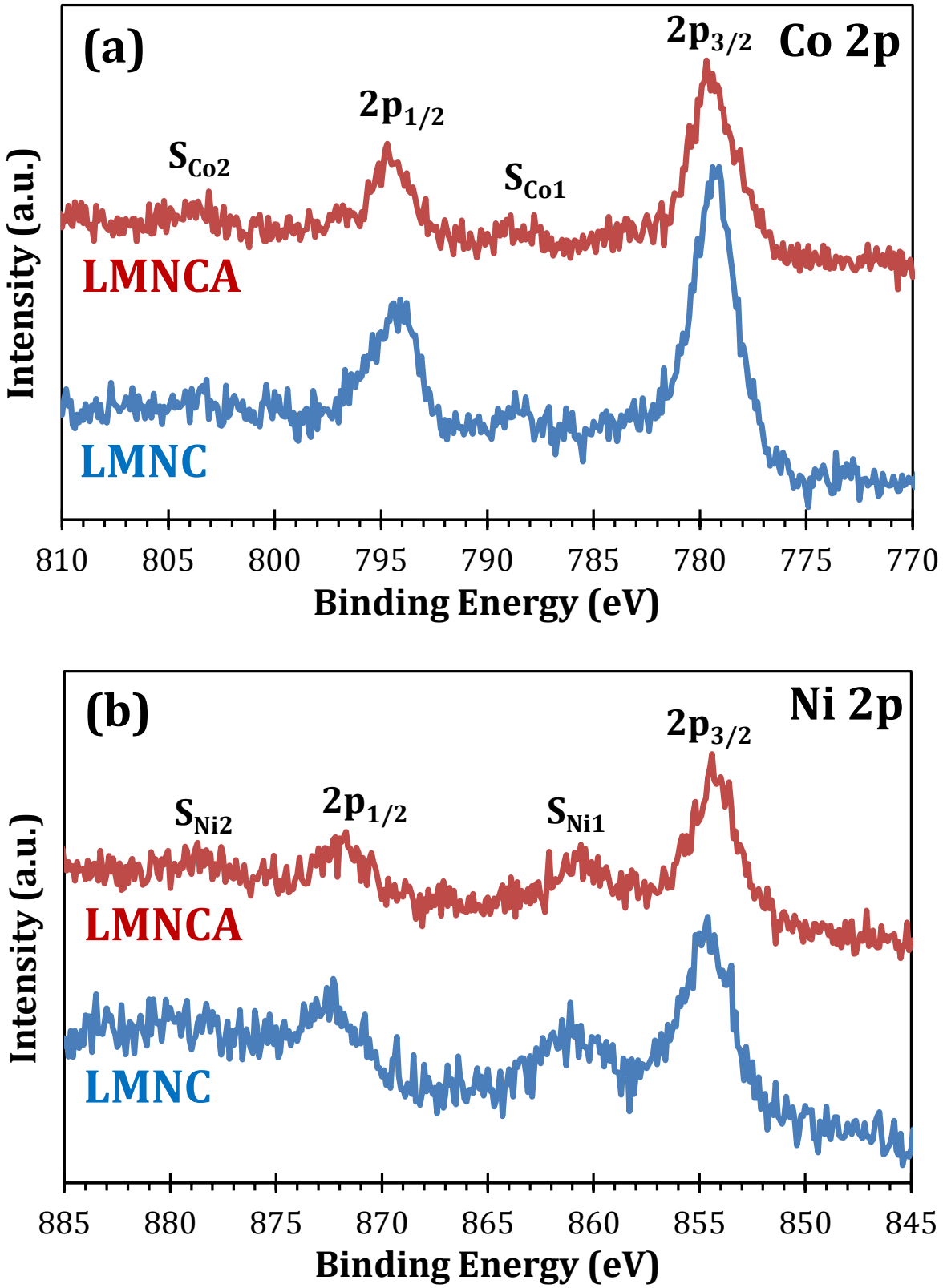

Figure 6.4: The X-ray Photoelectron Spectroscopy spectra of LMNC and LMNCA showing the (a) Co 2p and (b) Ni 2p peaks.

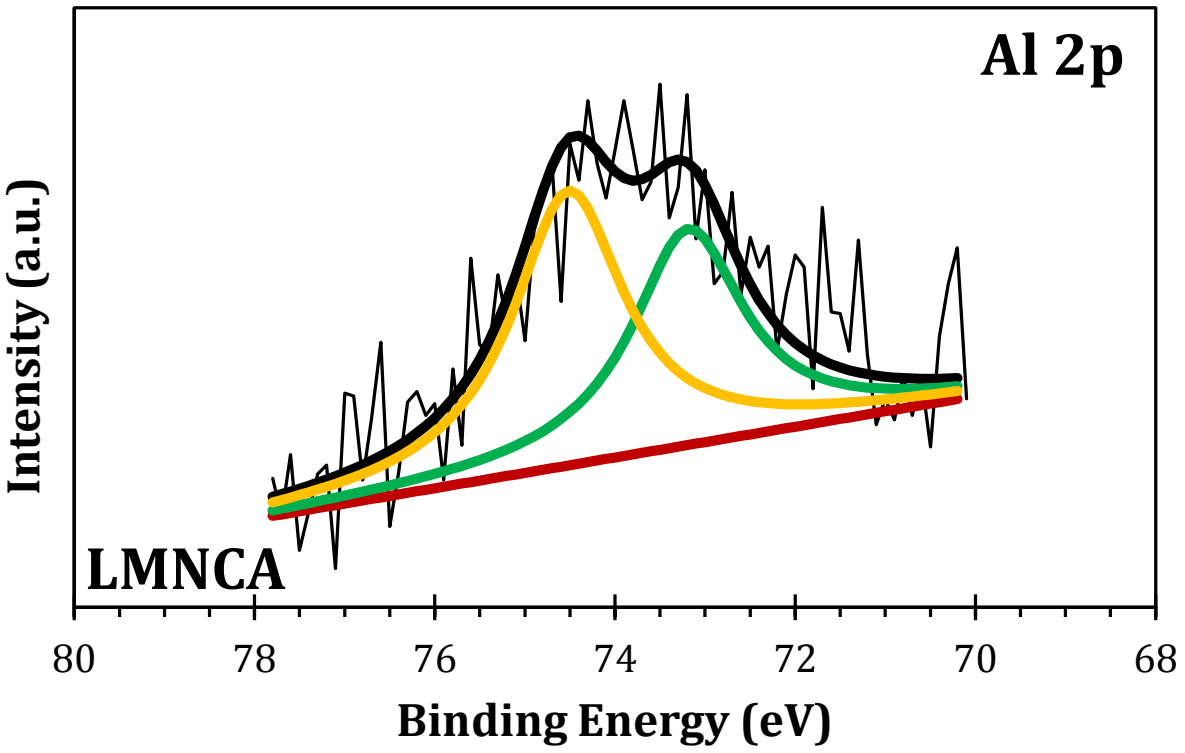

Figure 6.5: The X-ray Photoelectron Spectroscopy spectra of Al 2p peak of the LMNCA.

The Co 2p spectra consist of the Co $2p_{3/2}$, and the Co $2p_{1/2}$ peaks due to the spin-orbit coupling and weak satellite peaks (S_{Co1} and S_{Co2}). The presence of a peak (Co $2p_{3/2}$ or Co $2p_{1/2}$), together with a satellite peak (S_{Co1} or S_{Co2}), results from a ligand–to–metal charge transfer (LMCT) during the photo-emission process as seen from the spectra in **Figure 6.4 (a)** [26]. The Co $2p_{3/2}$ peak also shows a weak shoulder at approximately 781 eV. Co^{2+} in oxygen environment are characterised by a broadening of the Co $2p_{3/2}$ and Co $2p_{1/2}$ peaks and very intense satellite peaks [27], which is not observed in the Co 2p spectra. Thus, this fine structure of the Co 2p peaks cannot be explained by a small amount of Co^{2+} ions in oxygen environment, but may be related to the Co^{3+} ions in the LMNC and LMNCA similar to the Co^{3+} in $LiCoO_2$ [28-30]. In fact, a broadening in the peaks

of both LMNC and LMNCA are observed and specifically a shoulder at ~ 778 eV for the LMNCA. This gives rise to the possibility that both Co^{2+} and Co^{3+} exist in the materials due to the broadening of the peak widths as seen in **Figure 6.4 (a)**, which is the most likely case. Also, there is a change in the oxidation state of the Co in the LMNCA compared to the LMNC.

The Ni 2p spectra in **Figure 6.4 (b)** are also characterised by two main peaks (Ni $2p_{3/2}$ and Ni $2p_{1/2}$) and two satellite peaks (S_{Ni1} and S_{Ni2}), which are characteristic of, predominantly, Ni^{2+} ions in NiO [30]. The Ni spectra (LMNC and LMNCA) consist of a well visible shoulder at approximately 854 eV which is the binding energy corresponding to NiO. Dou *et. al.* [31] observed a Ni peak at 854.6 eV which was labelled as NiO and thus the most intense peaks of the Ni $2p_{3/2}$ in **Figure 6.4 (b)** which is also found at 854.6 eV could be assigned to Ni^{2+} in NiO. From these XPS results it is shown that the Ni in the LMNC and LMNCA materials are predominantly in the Ni^{2+} form.

Unfortunately, the XPS spectra of the Ni and Co could not be resolved in order to quantify the oxidation states, due to their low concentrations in the cathode material.

The Al 2p peak from the LMNCA is shown in **Figure 6.5** also shows a broadened peak which is fitted with two peaks, one at 74.4 eV and the other at 73.0 eV. The peak at 73.0 eV is attributed to Al in the bulk material (Al_b, up to ~10 nm in the bulk from the surface) while the peak at 74.4 eV is mainly due to oxidised aluminium on the surface (Al_s). The Al concentration is less than the concentration of the Co and Ni in the LMNCA. The Al (0.185) also has a much lower Atomic Sensitivity Factor (ASF) compared to both the Co (3.8) and Ni (4.5) [32]. Therefore, Al was not suspected to be picked up by the XPS instrument

seeing that the Co and Ni were barely observable. This therefore suggests that the doped Al segregated during the annealing process enriching the cathode surface.

Figure 6.6 represents the AFM images of the LMNC and LMNCA with average size distribution and roughness of ~90 nm and 32 nm for LMNC and ~ 140 nm and 33 nm for the LMNCA, respectively. The AFM confirms the SEM images that showed the LMNC has a smaller average particle size compared to the LMNCA.

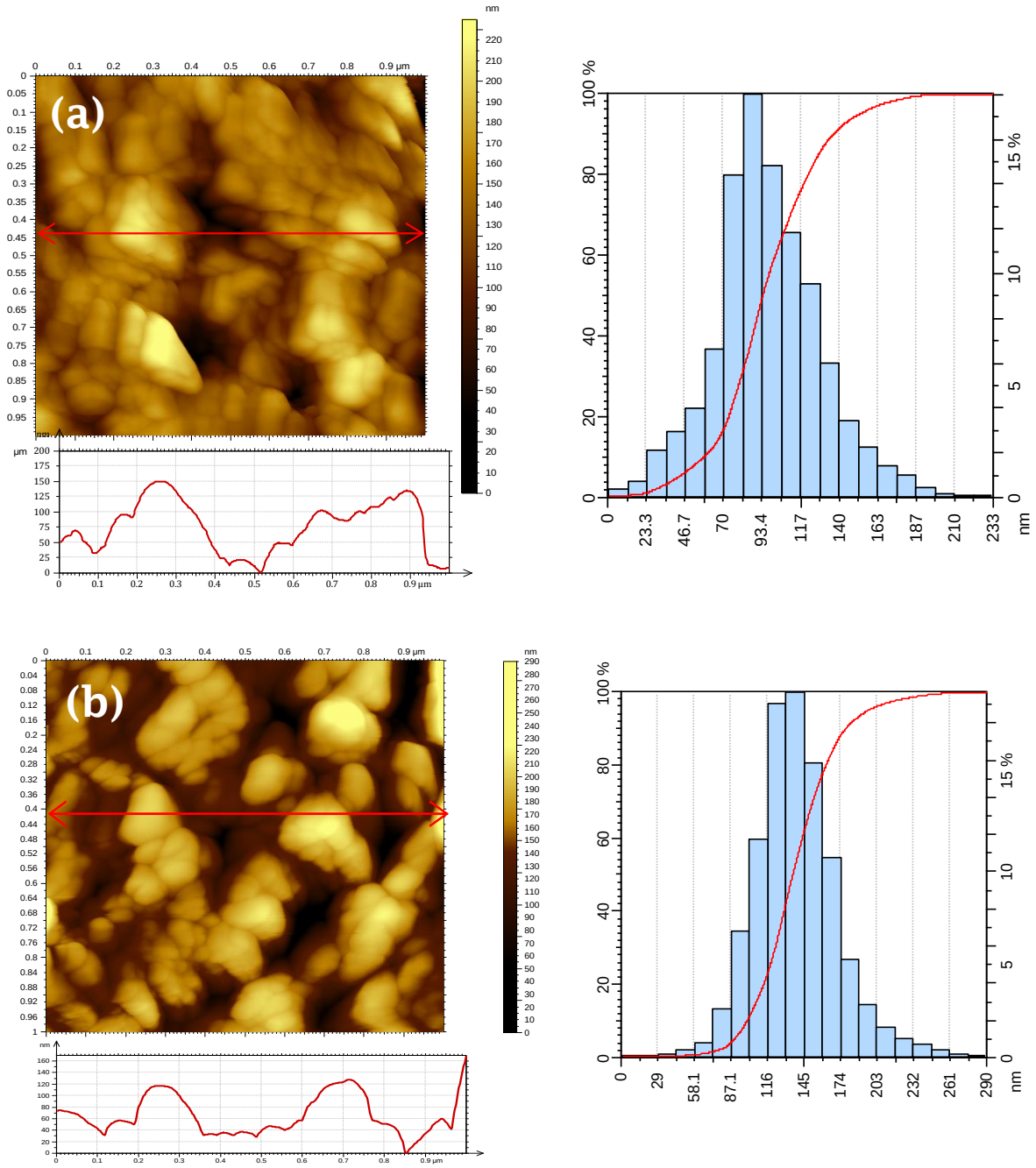

Figure 6.6: Typical AFM images of (a) LMNC and (b) LMNCA, and their corresponding histograms depicting particle size distributions.

CSAFM is a unique and emerging technique for providing insights into the surface conductivity of materials. **Figure 6.7** and **Figure 6.8** compare the CSAFM obtained for LMNC and LMNCA, respectively.

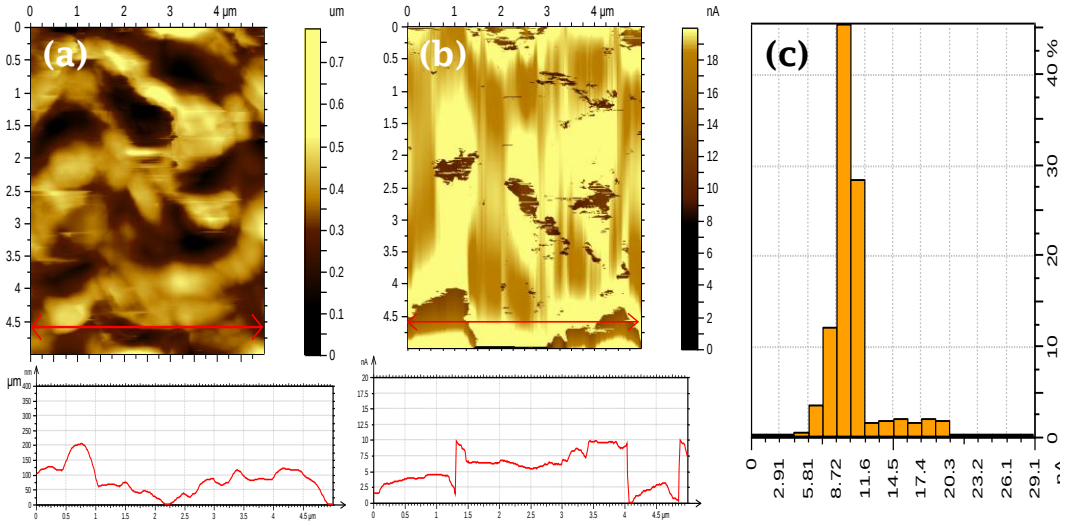

Figure 6.7: The (a) morphology image, (b) conductivity map, and (c) histogram of the distribution of the current in the conductivity maps of LMNC.

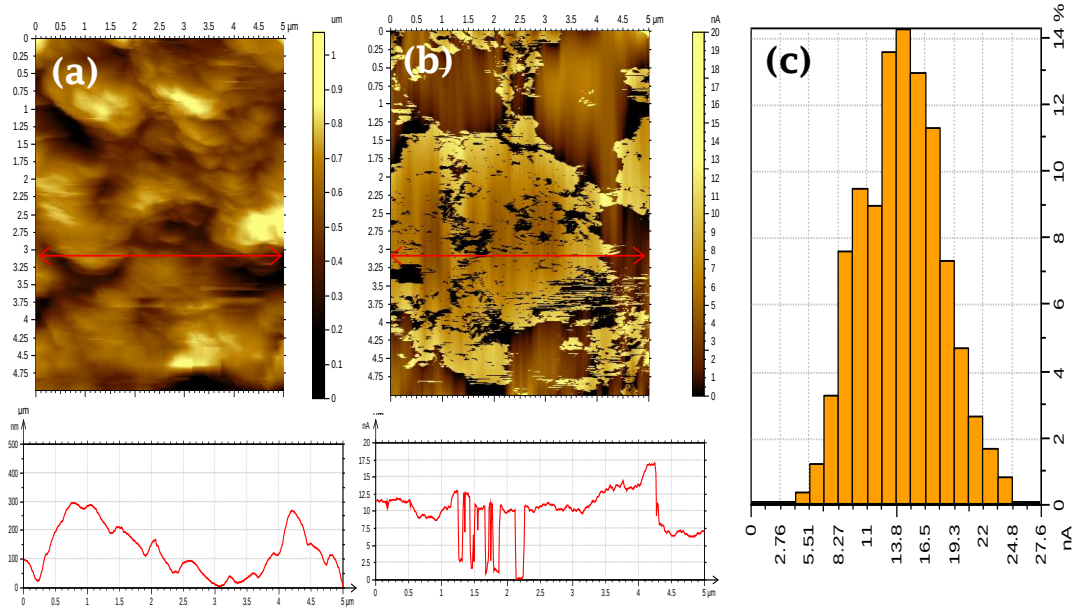

Figure 6.8: The (a) morphology image, (b) conductivity map, and (c) histogram of the distribution of the current in the conductivity maps of LMNCA.

The brighter areas in these conductance images represent areas of good conductivity in comparison to the darker areas that represent low or no conductivity. The surface conductance images show a non-uniform surface conductivity. The data depict (on average) lower currents for the LMNC (**Figure 6.7**) compared to the LMNCA (**Figure 6.8**) thin film prior to their study as battery fabrication. The high current values signify high conductive surface area; meaning that the Al doped LMNCA is more conductive than the undoped pristine LMNC. This finding is interesting, but perhaps should not be surprising considering that Al has an increased conductivity. The result is a further proof of the successful doping of the LMNC with small amount of aluminium.

Figure 6.9 shows the voltage as a function of charge-discharge capacities for LMNC (Fig 7a) and LMNCA (Fig 7b) between 2.0 V and 4.8 V at a rate of C/10 (i.e., ~ 22.5 $mA.g^{-1}$, note that 1C corresponds to 225 $mA.g^{-1}$ current density in this work).

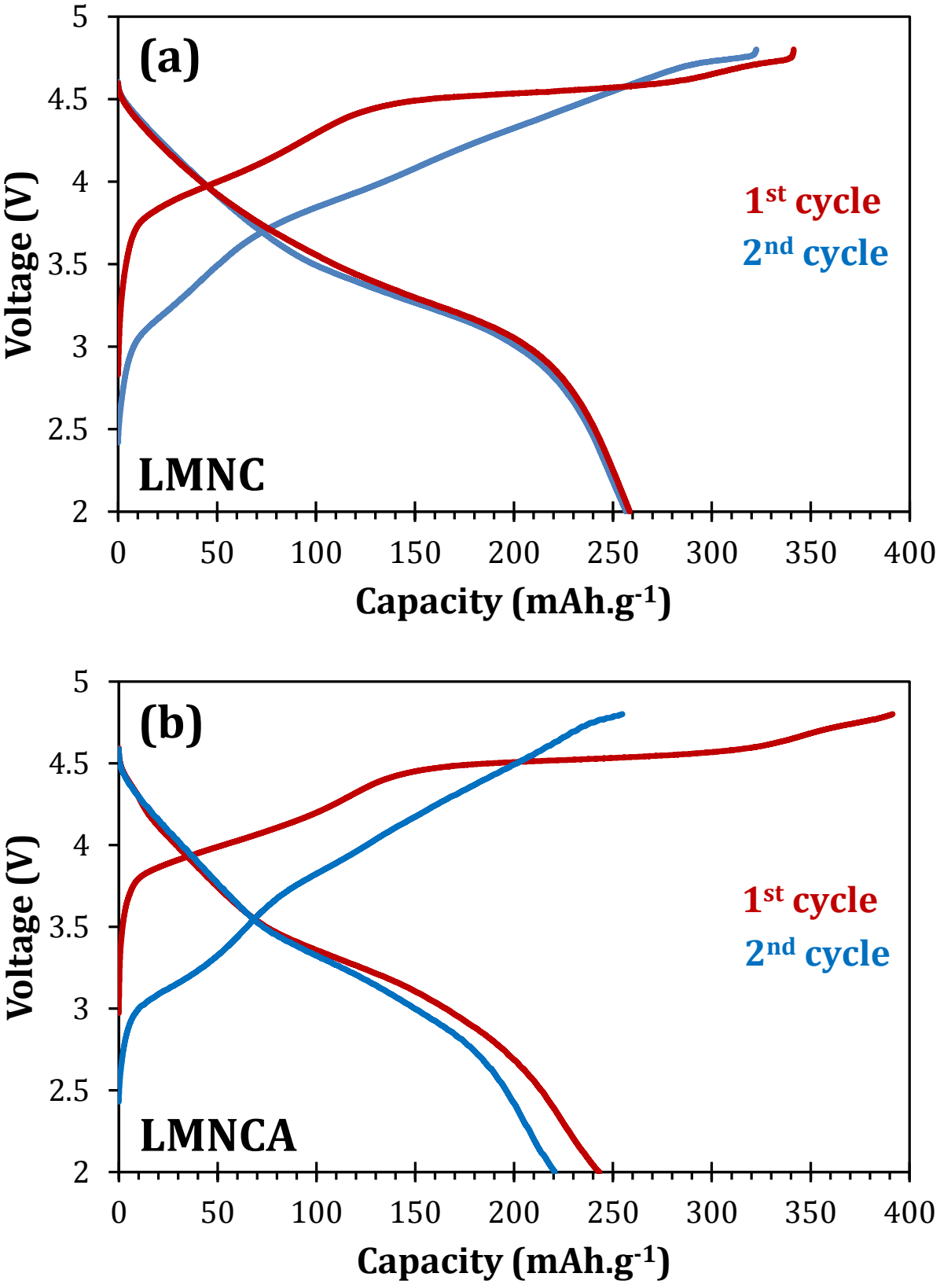

Figure 6.9: The first and second charge and discharge profiles of (a) LMNC and (b) LMNCA.

The two layered active materials show distinctive features that should be emphasised. First, the initial charge of LMNC over 4.4 V yields a specific capacity of 340 mA.h.g^{-1}, while the initial discharge capacity was 258 mAh.g^{-1}, which is 76% of the first charge capacity. On the other hand, the initial charge capacity of LMNCA yields a specific capacity of 380 mAh.g^{-1}, while the initial discharge capacity was 243 mAh.g^{-1}, which is ~ 64% of the first charge capacity. The voltage profiles of both materials clearly show the lithium extraction occurring first between 2.5 V and 4.4 V, followed by lithium extraction and oxygen loss (net loss Li_2O) between 4.4 V and 4.8 V. During the first charge to 4.6 V, a plateau was observed at an inflection point of ~ 4.4 V. This voltage plateau is consistent with the extraction of lithium and/or oxygen from the active material above 4.4 V [1-4]. The second charge capacity of the LMNC (320 mAh.g^{-1}) is higher than the second charge of the LMNCA (250 mAh.g^{-1}). The ability of the LMNC to sustain higher discharge capacity on second cycle may be related to the higher content of the Mn^{4+} based Li_2MnO_3, corroborating our XPS data (**Table 6.2**). Recently, Abouimrane *et. al.* [33] observed higher charge capacity (340mA.h.g^{-1}) for first charge cycle for $Li_{1.12}Mn_{0.55}Ni_{0.145}Co_{0.1}O_2$ (obtained after reductive treatment at low temperature, 250 °C) compared to the pristine $Li_{1.12}Mn_{0.55}Ni_{0.145}Co_{0.1}O_2$ (343 mA.h.g^{-1}) and attributed the lower charge capacity of the reductively treated $Li_{1.12}Mn_{0.55}Ni_{0.145}Co_{0.1}O_2$ to the less presence of the Mn^{4+} based material Li_2MnO_3. The smaller discharge capacity recorded for the LMNCA compared to its parent LMNC should be expected considering that Al is a redox silent element and so does not participate in the redox process. Al does not have available d-states near the Fermi energy level and, so cannot participate in the electron transfer process during electrochemical cycling [34].

Second, the large irreversible capacity loss during the first cycle has been reported for other lithium and manganese enriched materials, and has been attributed to the structural complexity of these layered oxide materials [4]. As already indicated in the introduction section, these materials are synergistically integrated between two layered components: Li_2MnO_3-type (C2/m structure) and $LiMO_2$-type ($R\bar{3}m$ structure) (where M is Mn, Ni, and/or Co). The activation of the Li_2MnO_3-type component at *ca.* 4.4 V has been shown to be highly irreversible due to the permanent loss of lithia and/or oxygen during activation [1-4].

Third, the first and second discharge capacities of the LMNC are the similar (~ 260 $mAh.g^{-1}$), consistent with lithium and manganese rich layered material as recently observed by Koenig Jr. *et. al.* [13] for another LMNC material, ($Li_{1.2}[Mn_{0.5}Ni_{0.4}Co_{0.1}]O_{2+y}$).

Figure 6.10 and **Figure 6.11** compare the cycle stability, at two different charge discharge rates, of LMNC with LMNCA when charged between 2.0 V and 4.8 V.

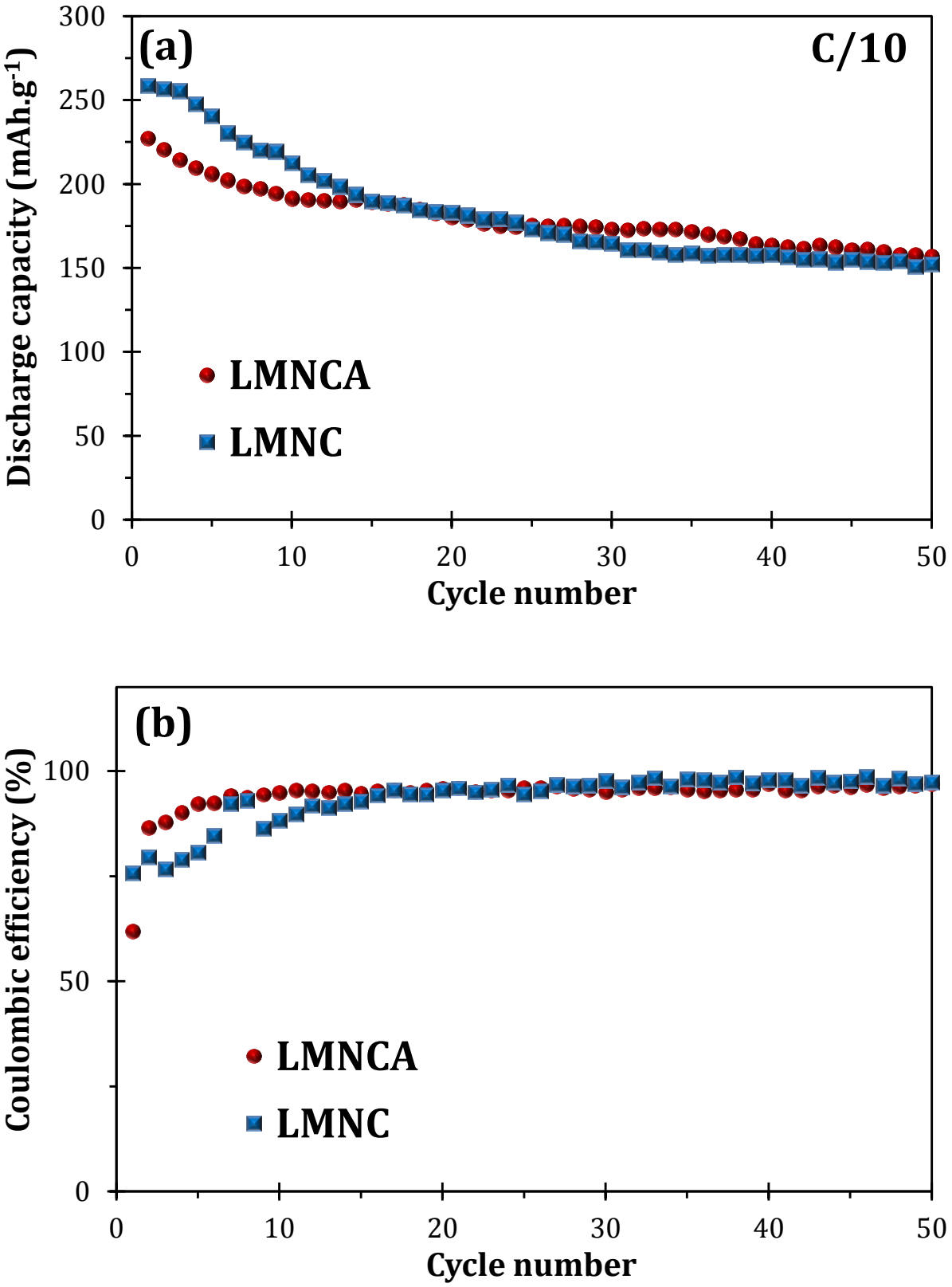

Figure 6.10: (a) The cycle stability at C/10 and (b) the Coulombic efficiency of LMNC and LMNCA for 50 charge discharge cycles.

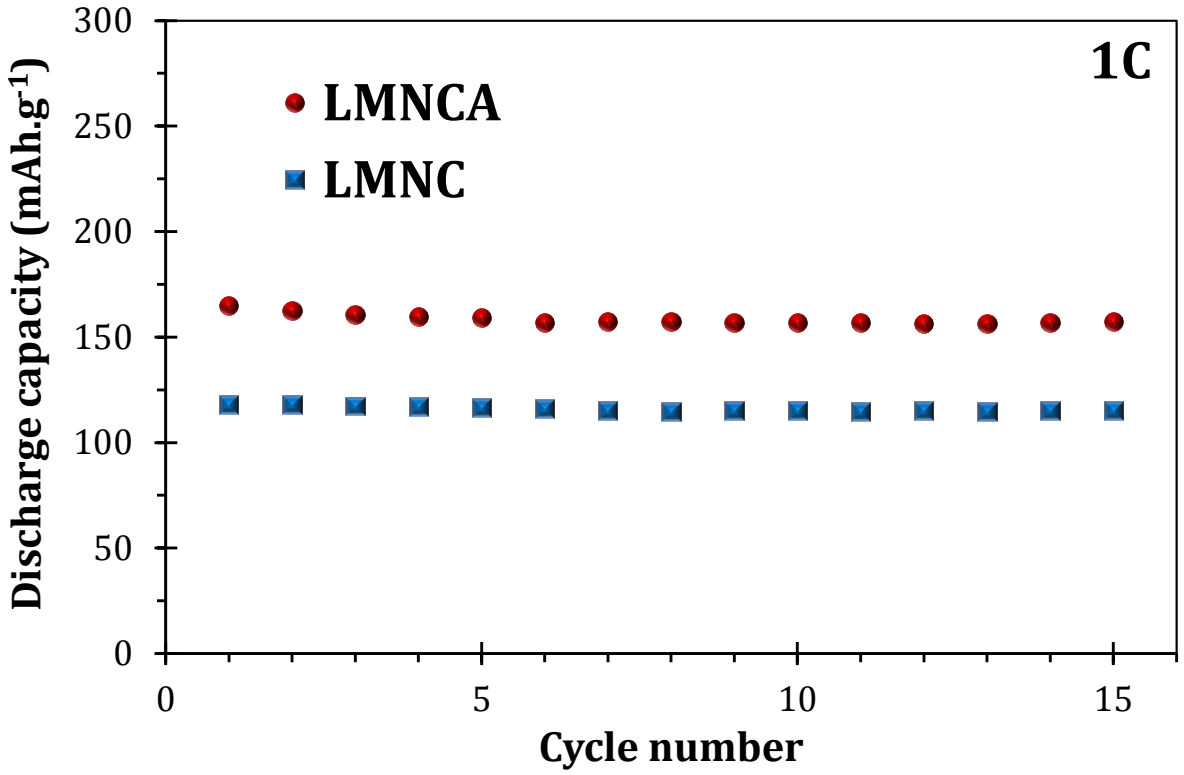

Figure 6.11: The cycle stability of LMNC and LMNCA at 1C for 15 charge discharge cycles.

The results clearly show that even though the LMNC has slightly lower discharge capacities, at the lower current density, for the first few cycles compared to LMNCA it has a better stability. **Figure 6.10 (a)** and **Figure 6.11**, also compares the rate capability of LMNC and LMNCA when charged and discharged at rates of C/10 (**Figure 6.10 (a)**) and 1C (**Figure 6.11**). At both rates, the LMNCA exhibit better stability than its LMNC counterpart. The discharge capacities at 1C for the LMNC and LMNCA are 118 mAh.g^{-1} and 165 mAh.g^{-1}, respectively. The enhanced performance of the LMNCA result may be ascribed to the increased *c*-lattice that increases Li diffusivity and the increase in the Mn^{3+} cations that increases the electron conduction. **Figure 6.10 (b)** also shows that LMNCA has a better Coulombic efficiency than the LMNC.

Figure 6.12 displays the cyclic voltammetric evolutions (initial and second cycles) of the parent LMNC (**Figure 6.12 (a)**) and LMNCA (**Figure 6.12 (b)**) at a scan rate of 0.1 mV.s^{-1}.

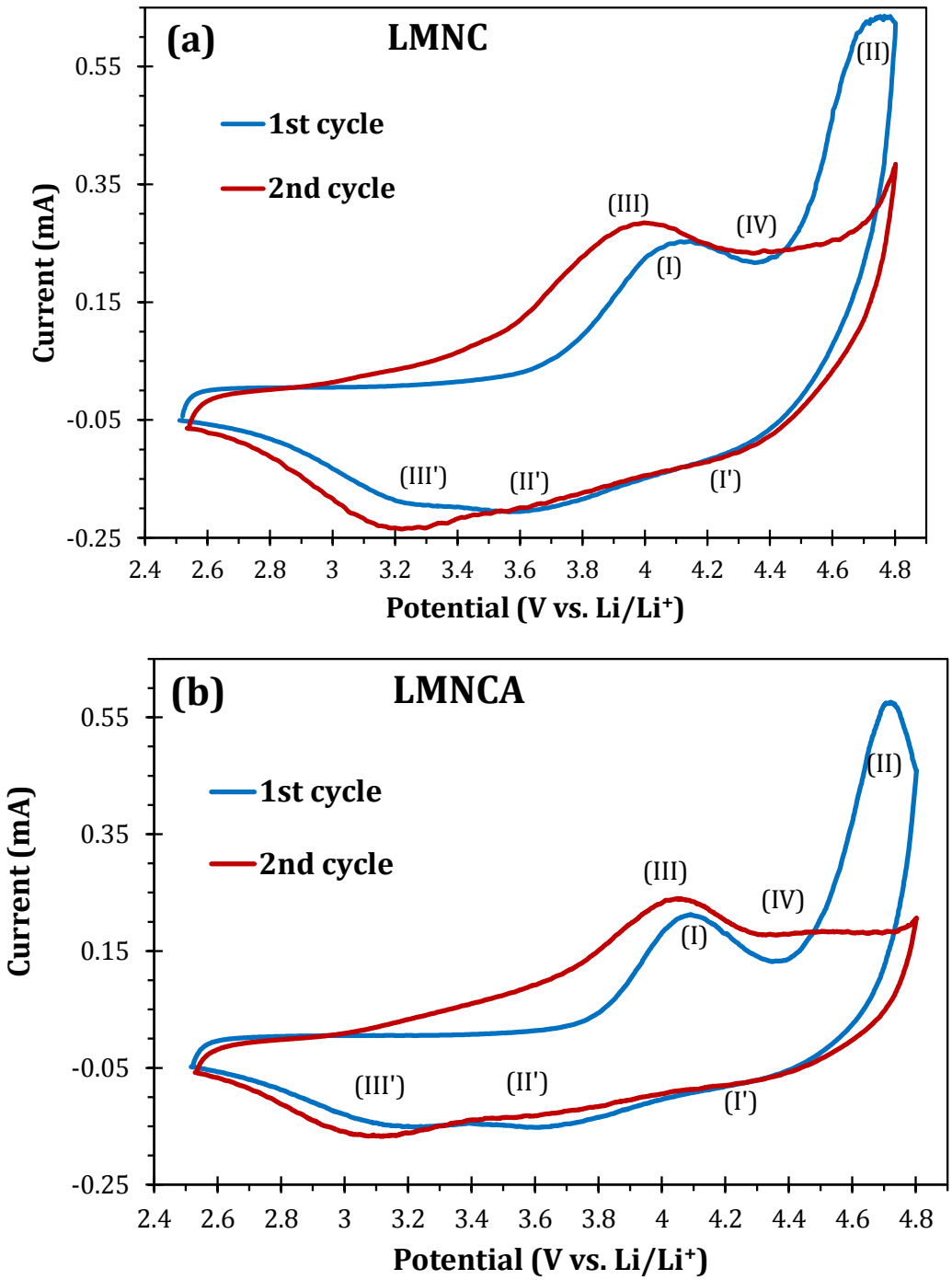

Figure 6.12: The cyclic voltammograms of (a) LMNC and (b) LMNCA obtained at a scan rate of 0.1 mV.s^{-1} (first and second cycle).

Thus motivated by the results of the charge-discharge experiments, the initial and second cycles of the LMNC and LMNCA was interrogated using low scan rate cyclic voltammetry. During the first cycle, the first anodic peak at ~4.1 V (I), corresponds to lithium extraction and simultaneous oxidation of the transition metals, predominantly the oxidation of Ni^{2+} to Ni^{4+} [13] and Co since both occurs at the same potential. The next peak at ~ 4.7 V (II) is the result from the irreversible removal of Li_2O from the Li_2MnO_3 component and the formation of an electrochemically active MnO_2 component, ignoring side products from electrode/electrolyte reactions. The peak (II) at ~ 4.7 V disappeared during the second cycle, confirming its irreversibility. During the second cycle, the main anodic peak shifted from ~ 4.1 V (first anodic curve, I) to ~ 3.9 V (III), indicating that the bulk material structure and/or the electrode/electrolyte interface may have been modified after the first cycle. During the second cycle, a broad anodic peak corresponding to the extraction of lithium ions occurred at ~ 3.9 V (III) and ~ 4.4 V (IV) that is more pronounced in LMNCA than in LMNC. During the initial discharge, we observed two weak cathodic peaks at ~ 4.2 V (I') and ~ 3.6 V (II'), which correspond with lithium insertion and reduction of nickel and cobalt in the material. These two peaks have previously been reported to be associated with lithium occupation of tetrahedral and octahedral sites [35-37]. A weak cathodic peak (III') also appeared for the LMNC (at 3.30 V in the first cycle and at 3.25 V in the second cycle) and for the LMNCA (at 3.13 V for first cycle and at 3.07 V at second cycle). This weak cathodic peak has been observed at 3.25 V for $0.5Li_2MnO_3{\cdot}0.5LiNi_{0.44}Co_{0.25}Mn_{0.31}O_2$ electrode reported by Kang *et. al.* [38] and, recently, at 3.2 V for $Li_{1.2}(Mn_{0.5}Ni_{0.4}Co_{0.1})O_{2+y}$ by Koenig Jr. *et. al.* [13] and was suggested to be related to the reduction of a small concentration of Mn^{4+}. Kang *et. al.* [38] first hypothesised that this peak is due to the reduction of small Mn^{4+} that resides either in the $LiNi_{0.44}Co_{0.25}Mn_{0.31}O_2$ component or at interconnecting and atomically disordered regions

between the $LiNi_{0.44}Co_{0.25}Mn_{0.31}O_2$ and Li_2MnO_3 components. The hypothesis was that these ions become electrochemically activated during the initial charge to 4.3 V. In a nutshell, the results of our cyclic voltammetric experiments provide further evidence of possible interfacial modifications of the LMNC and LMNCA as well as irreversible losses due to the electrochemical activation of the Li_2MnO_3-type component.

Next, we examine the cyclic voltammetric profiles of LMNC and LMNCA that have undergone 50 repetitive charge-discharge cycles at a 0.1 C rate. As presented in **Figure 6.13**, the CVs obtained after 50 repetitive charge-discharge cycles showed marked differences from those obtained from freshly prepared LMNC and LMNCA (shown in **Figure 6.12**).

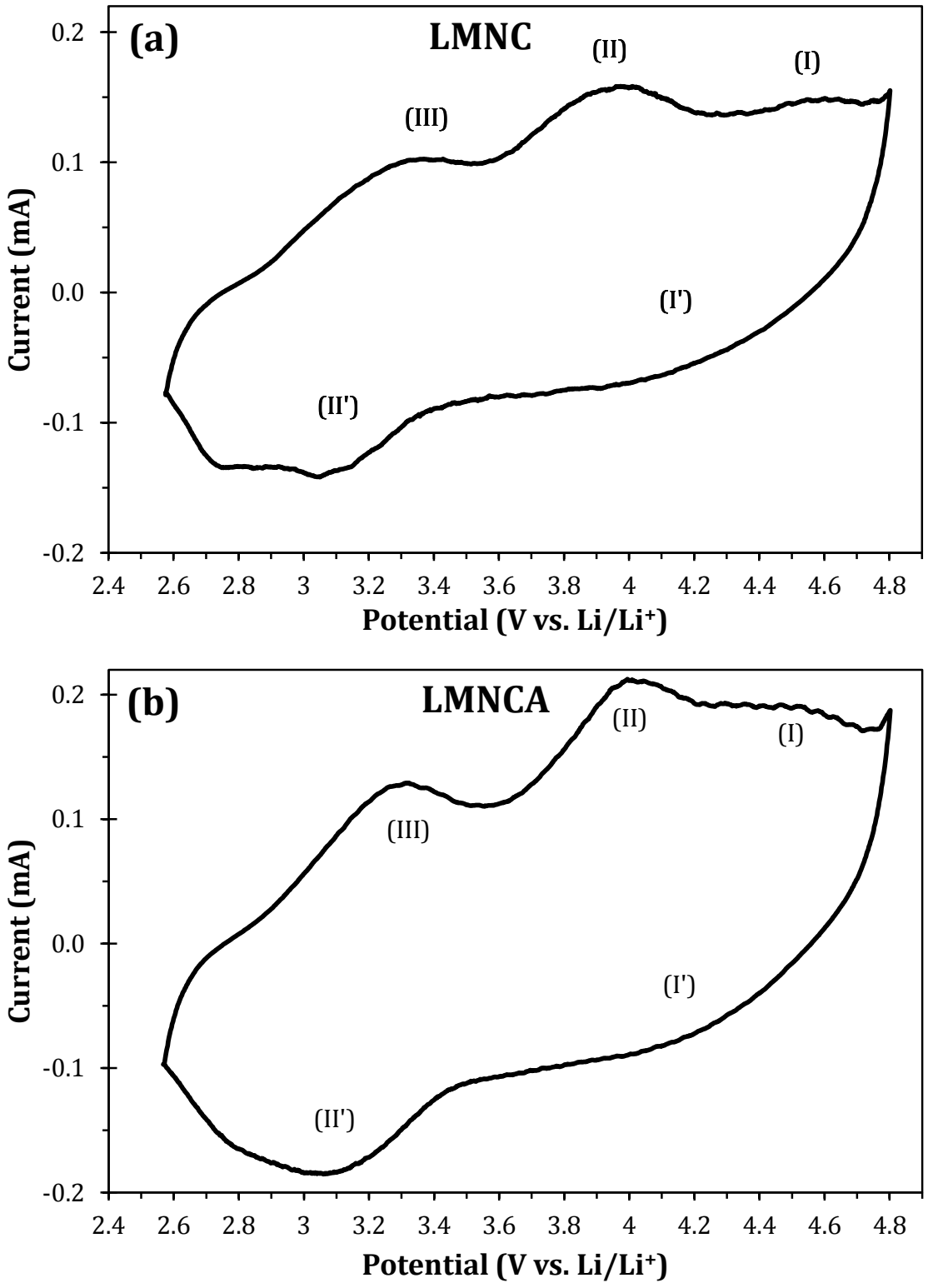

Figure 6.13: The cyclic voltammograms of (a) LMNC and (b) LMNCA after 50 repetitive charge discharge cycles obtained at a scan rate of 0.1 $mV.s^{-1}$.

First, we see three anodic peaks at ~ 4.5 V (I), ~ 3.9 V (II) and ~ 3.3 V (III) relating to the oxidation of Ni, Co and Mn ions respectively. The broad cathodic peak at ~ 4.2 V (I'), which may be related to the combined peaks I' and II" seen for the pristine active materials shown in **Figure 6.12**, is due to the reduction of both Ni and Co ions. The combination of I' and II' to form one broad peak means that the electrochemical time constants of the two peaks becomes very close on repetitive cycling of the electrodes. The cathodic peak at ~ 3.0 V (II') relates to the reduction of Mn ions. The reversible redox couple (III and II') with equilibrium potential ($E_{1/2}$ or E^0) of ~ 3.10 V is associated with the reversible lithium insertion/extraction (lithiation/delithiation) reaction with MnO_2 derived from the Li_2MnO_3 component [38]. When compared with the pristine electrodes, it is evident that the Li_2MnO_3 component contributes significantly to the redox processes in the electrode over the voltage range 2.0 V – 4.3 V upon cycling than the pristine. The broad oxidation peak (II) at ~ 3.90 V for LMNC and at a slightly higher potential for LMNCA is associated only with the oxidation of the cobalt and nickel ions. It also suggests that Al doping raises the potential for the oxidation of Ni and Co ions, in agreement with the report of Croguennec [6]. Overall, the results show that the weak redox peaks seen in pristine active materials are activated upon cycling.

Electrochemical impedance spectroscopy (EIS) represents an important technique for evaluating interfacial electrochemistry [34, 39-41], and the reaction kinetics and diffusion coefficient of lithium ion in lithium ion battery materials [42-44]. The impedance spectra for the LMNC and LMNCA were measured at different potentials. The spectra were recorded before the 1st cycle and after the 50 cycles. Prior to every measurement, the cell was relaxed for 1 h. **Figure 6.14** and **Figure 6.15** presents typical Nyquist plots (Z' vs –Z") obtained for the LMNC and LMNCA cells, respectively.

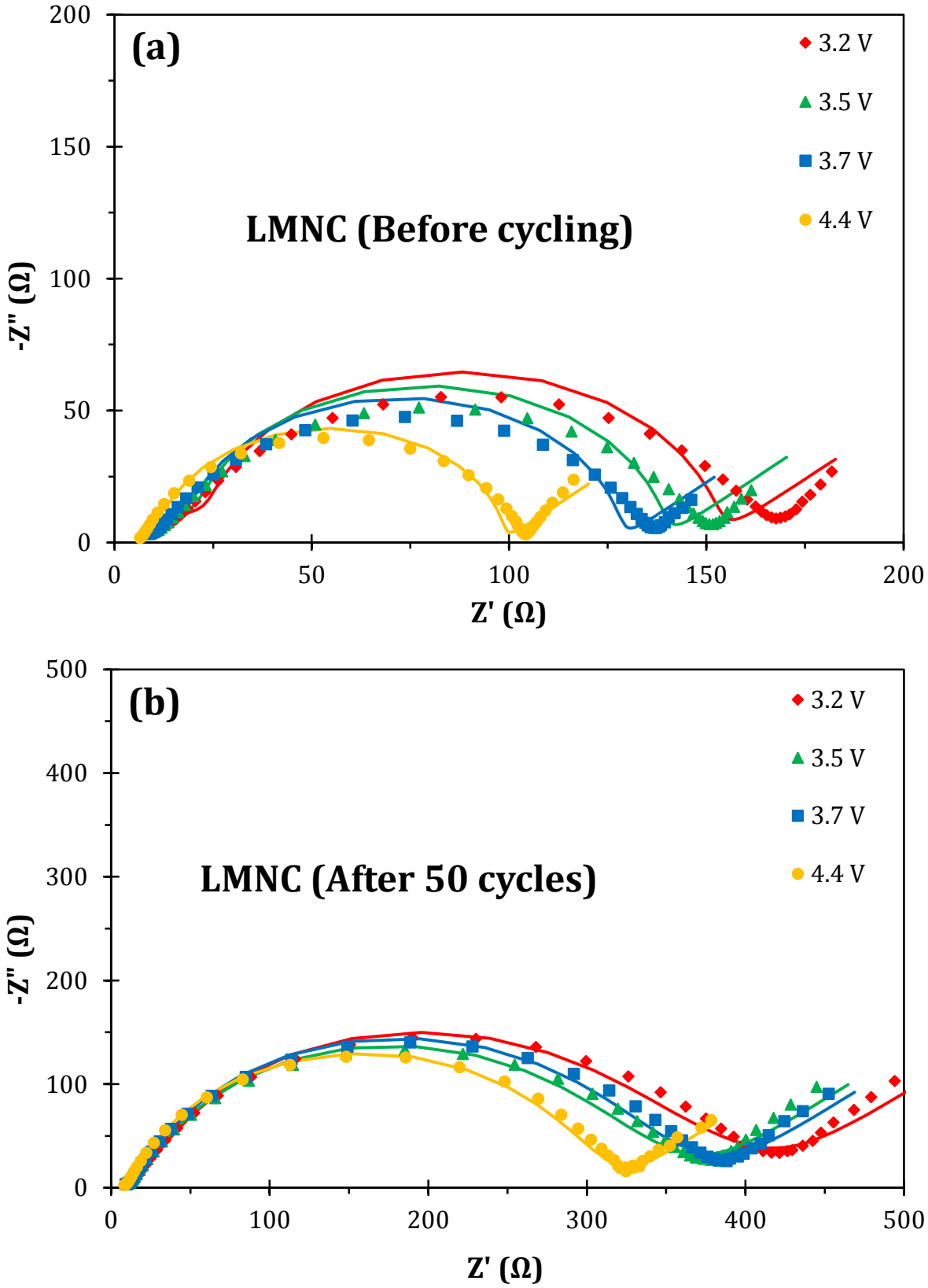

Figure 6.14: Nyquist plots of LMNC (a) before the 1st cycle and (b) after 50 cycles. Data points are experimental while solid lines are fitted data.

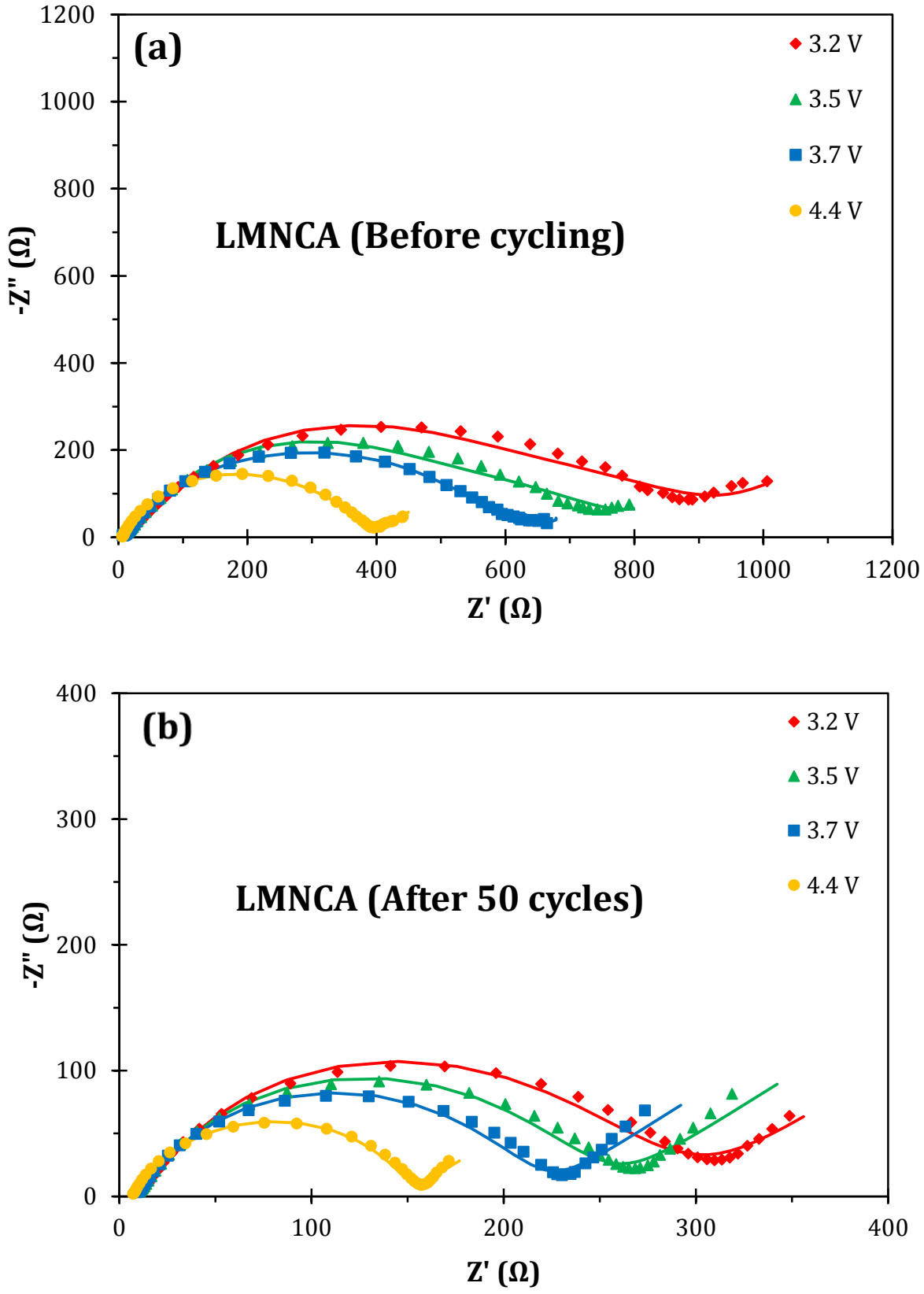

Figure 6.15: Nyquist plots of LMNCA (a) before the 1st cycle and (b) after 50 cycles. Data points are experimental while solid lines are fitted data.

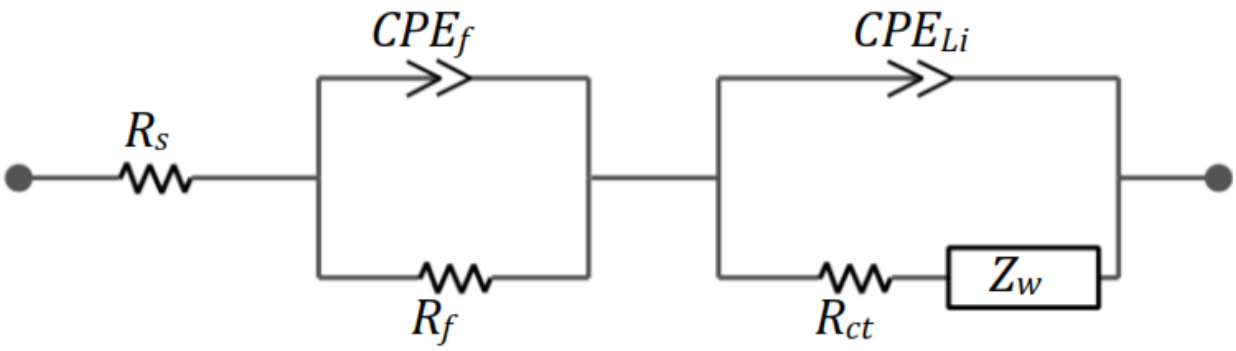

Figure 6.16: The Electrical Equivalent Circuit (EEC) used to fit the experimental EIS data.

A high frequency semi-circle and an intermediate frequency semi-circle composed into one semi-circle, and low frequency tails are observed. Generally, the high frequency semi-circle is related to the passivating surface film, the SEI. The intermediate frequency semi-circle is ascribed to the charge transfer process resistance in the electrode/electrolyte interface. The low frequency tail is associated with the Li^+ ion diffusion process in the positive electrode.

The EIS spectra were satisfactorily fitted with an equivalent electrical circuit (EEC) shown in **Figure 6.16**. The fitting parameters involve the solution Ohmic resistance of the electrode system (R_s), solid electrolyte interface (SEI) film resistance (R_f), charge transfer resistance (R_{ct}) due to lithium intercalation/de-intercalation process, the constant phase element of the surface film (CPE_f) and the interfacial capacitance (CPE_{Li}), and the Warburg element (Z_w) describing the solid state diffusion of lithium ion inside the active particles, signified by the straight sloping line ($\sim 45^\circ$) at the low frequency region.

The following observations are evident from the impedance plots. The spectra show overlapped semicircles at the high to medium frequencies and a straight slopping line at

the low frequency. The small semicircle in the high frequency region describes the resistance to the migration of Li^+ ions through the surface films (R_f) and the film capacitance (CPE_f). The middle frequency capacitive loop reflects the charge transfer resistance (R_{ct}) and interfacial capacitance (CPE_{Li}). The charge transfer resistance is considered as the rate determining step of the diffusion process of Li^+ during the charge discharge of the battery. The low frequency straight line is the diffusion process.

An attempt to include the intercalation capacitance (C_{int}) on the right side of the EEC, as seen in some reports [45, 46] and as discussed in **chapter 4**, was not successful. However, as in this case, other workers [47, 48] have used the fitting EEC, seen in **Figure 6.16**, without the inclusion of the C_{int}. EIS based measurement of C_{int} is dependent on the frequency range of the ac perturbation, and as long as the $Z'' >> (\omega C_{int})^{-1}$ the C_{int} cannot be detected by the EIS measurement. If this inequality is reversed (i.e., C_{int} ($\omega \rightarrow 0$) = $(\omega Z'')^{-1}$) then the C_{int} can be observed at such very low frequencies. Clearly, the C_{int} is beyond the detection limit of EIS reported in this work.

The EIS parameters obtained for the LMNC and LMNCA are summarised in **Table 6.3** and **Table 6.4**, respectively. The R_s values (reflecting the conductivity of the electrolyte, separator and electrodes) are essentially constant, with slight deviations with the fixed voltage. Of course, the constant R_s values should be expected considering that the electrolyte concentration remains unchanged during cycling, and any change in the lithium concentration of the electrode will not influence electrolyte conductivity.

Table 6.3: Summary of EIS parameters for the LMNC coin cells; all values were obtained from the fitted impedance spectra after several iterations using the proposed equivalent electrical circuit shown in **Figure 6.16**

Applied Potential	EIS parameters for LMNC						
	R_s (Ω)	R_f (Ω)	C/CPE_f (μF)	n	C_{Li} (μF)	R_{ct} (Ω)	Z_w ($\times 10^{-4}$)
Before cycling							
3.2 V	10.3 ± 0.5	13.3 ± 1.2	0.9 ± 0.1	-	3.3 ± 0.2	127.7 ± 3.1	173.2 ± 15.7
3.5 V	9.6 ± 0.4	11.2 ± 1.1	1.2 ± 0.1	-	3.5 ± 0.2	117.3 ± 2.7	234.5 ± 23.5
3.7 V	9.0 ± 0.4	10.0 ± 1.0	1.6 ± 0.2	-	3.6 ± 0.2	108.4 ± 2.4	305.9 ± 38.4
4.4 V	6.7 ± 0.2	5.9 ± 0.7	3.3 ± 0.3	-	3.6 ± 0.1	85.3 ± 1.2	403.3± 28.5
After 50th cycle							
3.2 V	8.8 ± 0.4	190.7 ± 14.8	251.2 ± 66.9	0.54 ± 0.03	6.8 ± 0.5	216.7 ± 12.6	138.5 ± 13.1
3.5 V	8.0 ± 0.4	158.8 ± 15.5	252.1 ± 69.0	0.55 ± 0.03	6.6 ± 0.4	202.6 ± 11.2	150.1 ± 13.1
3.7 V	7.8 ± 0.3	152.2 ± 12.9	275.4 ± 73.9	0.55 ± 0.03	6.2 ± 0.4	220.8 ± 10.6	162.4 ± 14.7
4.4 V	7.4 ± 0.2	104.9 ± 9.2	256.7 ± 64.1	0.58 ± 0.02	5.7 ± 0.2	208.3 ± 7.7	207.1± 16.9

Table 6.4: Summary of EIS parameters for the LMNCA coin cells; all values were obtained from the fitted impedance spectra after several iterations using the proposed equivalent electrical circuit shown in **Figure 6.16**

Applied Potential	EIS parameters for LMNCA						
	R_s (Ω)	R_f (Ω)	CPE_f (μF)	n	C_{Li} (μF)	R_{ct} (Ω)	Z_w ($\times 10^{-4}$)
Before cycling							
3.2 V	2.6 ± 0.4	666.0 ± 28.0	155.3 ± 19.4	0.51 ± 0.01	10.1 ± 0.8	264.9 ± 19.4	131.3 ± 25.9
3.5 V	3.9 ± 0.4	536.0 ± 24.6	174.5 ± 29.0	0.53 ± 0.02	8.3 ± 0.7	245.6 ± 19.3	224.6 ± 70.5
3.7 V	4.3 ± 0.4	413.0 ± 19.0	189.0 ± 32.9	0.53 ± 0.02	7.2 ± 0.5	242.6 ± 16.0	509.6 ± 263.5
4.4 V	5.5 ± 0.1	230.6 ± 14.9	66.3 ± 14.7	0.70 ± 0.02	7.7 ± 0.8	157.7 ± 15.2	258.9 ± 24.7
After 50th cycle							
3.2 V	8.4 ± 0.4	146.9 ± 12.8	170.0 ± 58.7	0.57 ± 0.03	5.2 ± 0.5	144.7 ± 11.7	91.7 ± 6.4
3.5 V	8.2 ± 0.4	123.2 ± 12.2	124.2 ± 44.9	0.60 ± 0.03	5.4 ± 0.6	123.6 ± 11.4	101.4 ± 5.4
3.7 V	7.8 ± 0.3	105.4 ± 11.3	113.0 ± 43.0	0.62 ± 0.03	5.3 ± 0.6	107.9 ± 10.5	124.6 ± 7.8
4.4 V	6.62 ± 0.2	67.5 ± 10.3	46.4 ± 16.1	0.73 ± 0.03	6.3 ± 0.9	75.3 ± 9.6	166.1 ± 7.7

From **Table 6.3** and **Table 6.4**, the R_f values decrease with increasing cell voltage from 3.2 V to 4.4 V. This trend may be explained using the SEI film model principle, relating between the R_f and SEI film conductivity ρ as follows [49]:

$$R_f = \frac{\rho l}{A} \quad 6.1$$

where ρ and l are the conductivity and thickness of the SEI film, respectively, while A is the surface area of the electrode. Since the A may not change significantly during the cycling process, it is likely that the film thickness is decreased and/or become more conductive with cycling. The R_{ct} values, for the LMNCA, follow the same trend as the R_f, suggesting that the SEI film covering the electrode surface is destroyed or replaced by redox-active active material, resulting in the decrease of the whole impedance of the battery cell. It is very interesting to observe that, although the LMNCA showed the highest impedance (both R_f and R_{ct}) before cycling, the impedance values dramatically decreased much lower than the corresponding values for the LMNC. For example, at the open circuit potential, the LMNC gave ~ 10 Ω (R_f) and ~ 108 Ω (R_{ct}) for the fresh cell and ~ 152 Ω (R_f) and ~ 220 Ω (R_{ct}) after 50 cycles, while the LMNCA gave ~ 413 Ω (R_f) and ~ 243 Ω (R_{ct}) for the fresh cell and ~ 105 Ω (R_f) and ~ 108 Ω (R_{ct}) after the 50th cycle. The data clearly show that charge transport is greatly enhanced upon cycling by simply doping the LMNC with a very small amount of Al. Since Al does not have available *d*-states near the Fermi level, it is impossible for it to participate in the electron transfer process; the enhanced conductivity of the LMNCA is related to the higher amount of the Mn^{3+} cation in the lattice, aided by the increased *c*-lattice that enhances the diffusivity of Li during the electrochemical cycling. Al and its oxides are known to enhance the stability or cyclability of battery cathode materials. The EIS

results seen in this work have provided some insights on how Al possibly accomplishes such tasks, destroying the SEI film or replacing it with redox-active active material(s).

The impedance of CPE is defined as **Equation** 6.2 [39]:

$$Z_{CPE} = \frac{1}{Q(j\omega)^n} \quad 6.2$$

where Q is the frequency independent constant relating to the interface, $j = \sqrt{-1}$, ω is the radial frequency, the exponent n reflects the degree of distortion of the impedance spectra and it is obtained from the slope of the plot of log Z vs log f (and has values $-1 \leq n \leq 1$). When n = 0, the CPE is identical to a pure resistor; n = 1, CPE is a pure capacitor, n = –1 CPE is an inductor; and when n = 0.5 CPE becomes identical to a Warburg impedance (Z_w). In general, the CPE is a consequence of several factors [39] including (i) the nature of the electrode (e.g., roughness and polycrystallinity), (ii) distribution of the relaxation times due to heterogeneities existing at the electrode/electrolyte interface, (iii) porosity and (iv) dynamic disorder associated with diffusion. Thus, although the proposed EEC modelled true double layer capacitance in some instances, the capacitance should generally be the CPE. From **Table 6.3** and **Table 6.4**, n values are close to 0.5 especially at the OCV, suggesting diffusion process of the lithium.

The Randles-Sevčik equation is used to determine the diffusion coefficients before and after charge discharge cycles making use of cyclic voltamograms:

$$D_{Li} = \frac{I_p}{2.69\times10^5 n^{3/2} A C_{Li} \upsilon^{1/2}} \quad 6.3$$

where D_{Li} is the diffusion coefficient of Li^+, I_p is the peak current, n is the number of electrons per reaction species (equals 1 for Li^+), A is the geometric area of the electrode (cm^2), υ is the scan rate, C_{Li} is the concentration of lithium ions (calculated as the stoichiometric amount of lithium per active mass of the LMNC or LMNCA divided by the volume of the cell). As seen in **Table 6.5**, the values of the diffusion coefficients are in the same magnitude (10^{-10} cm^2s^{-1}). However, after 50 repetitive cycling, the D_{Li} of LMNC lost about 70 % of its original value compared to the LMNCA that remained almost the same. This result shows that the LMNCA is very stable, essentially keeping its rate of Li diffusion even upon several continuous cycling more than the pristine LMNC would. The values are in the same range as observed by others using CV for other type of LMNC [50].

The diffusion coefficient (D_{app}) of Lithium ions can be obtained according to **Equation 6.4** as derived in **Chapter 4**:

$$D_{Li} = \frac{2R^2T^2}{C_{Li}^2 n^4 F^4 A^2 \sigma^2} \qquad 6.4$$

Assuming diffusion coefficients of the oxidised and reduced Li species to be equal ($D_{ox} = D_{red} = D_{Li}$) and equal concentrations ($C_{ox} = C_{red} = C_{Li}$). D_{Li} is the diffusion coefficient of the lithium ions, R the gas constant, T the absolute temperature, A the geometric surface area of the cathode, F the Faraday constant, n the number of electrons transferred per molecule during oxidation, C_{Li} the lithium concentration in the cathode material and σ is the Warburg factor obtained from the slope of the real impedance (Z') vs. the reciprocal square root of the frequency in the low frequency region ($\omega^{-1/2}$) according to **Equation 6.5**, and as exemplified in **Figure 6.17** for EIS obtained at the open circuit potential of the cells.

$$Z_w = \sigma(1 - j)\omega^{-1/2} \quad 6.5$$

Figure 6.17 shows clear differences in the behaviour of the two materials; LMNC showing higher impedance after cycling, while the LMNCA giving the opposite effect, corroborating the data in **Table 6.3** and **Table 6.4**. The values of the diffusion coefficient are summarised in **Table 6.5**.

The D_{Li} of the related LMNC ($LiNi_{1/3}Co_{1/3}Mn_{1/3}O_2$) is reported [51, 52], regrettably however, these reported values by other workers [51, 52] were obtained using the wrong derivation of the **Equation** 6.4, as is discussed in **Chapter 4,** which makes it unhelpful for us to compare our results with their values. Nevertheless, the values obtained by [51, 52] are as expected, lower compared to the values obtained. The LMNC lost its capacity to permit the diffusion of lithium ion within its crystal network more than the LMNCA, corroborating the CV data.

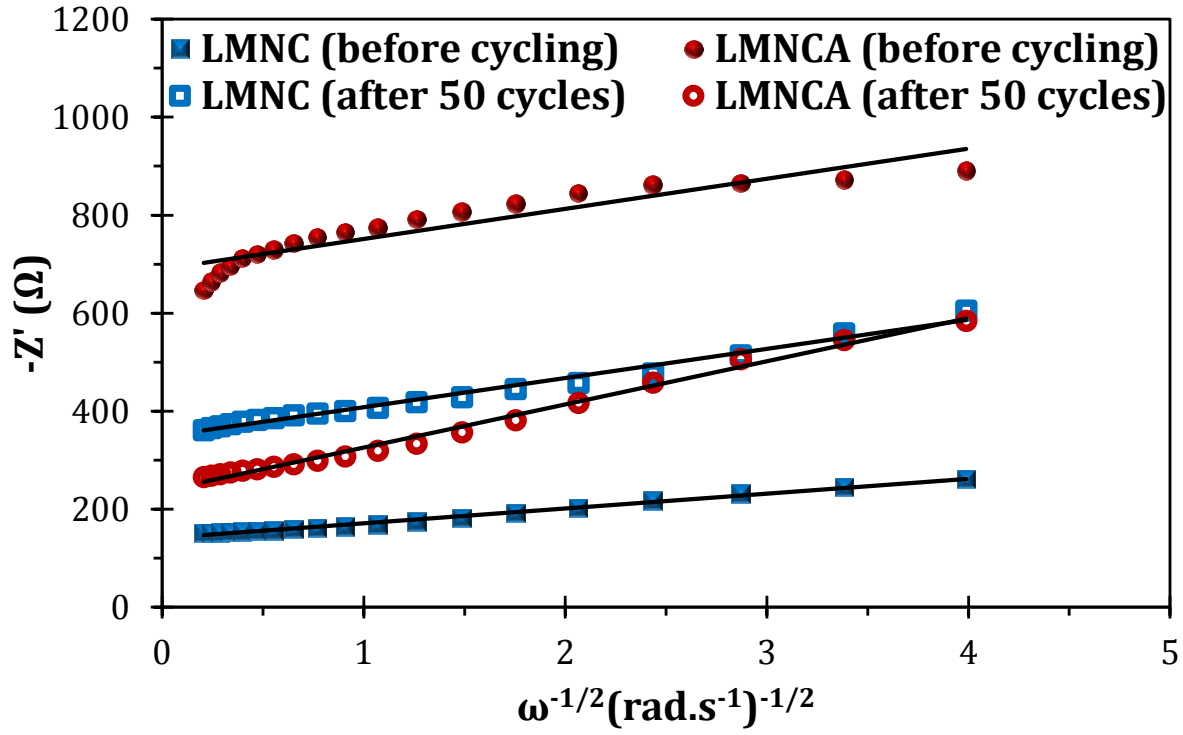

Figure 6.17: Plots of Z' vs $\omega^{-1/2}$ of the LMNC and LMNCA before and after 50 cycles.

Alternatively, the D_{Li} can be estimated from **Equation** 6.6 as was derived in **Chapter 4**:

$$D_{Li} = \left(\frac{QM_w l}{\sqrt{2}nF\sigma C_{int}}\right)^2 = \frac{1}{2}\left(\frac{QM_w l\upsilon}{nF\sigma i}\right)^2 \quad 6.6$$

where Q is the specific capacity of LMNC or LMNCA, and M_w is the molecular weight of LMNC and LMNCA, l is the diffusion pathway (i.e., thin film thickness) while C_{int} is the 'apparent' intercalation capacitance which can be estimated from the slow scan rate ($C_{int} \approx i/\upsilon$) as described in **Chapter 4**.

The CV value of the D_{Li} is about four orders of magnitude higher than those obtained from the EIS. This discrepancy may be related to several factors. First, the C_{int} used in **Equation** 6.6 has been cautioned to be strictly regarded as an 'apparent' intercalation capacitance because it is estimated from an approximate equation ($C_{int} \approx i/\upsilon$), using CV. Second, the use of 'apparent' geometric area rather than the true area characterised by high level of porosity/roughness and/or expansion/contraction of the host lattice during intercalation/deintercalation processes, could introduce some uncertainties. Therefore, it is more appropriate to treat the calculated diffusion coefficient as an apparent chemical diffusion coefficient.

Table 6.5: Comparison of the apparent diffusion coefficient of Lithium ion, D_{app} (cm^2 s^{-1}) in LMNC and LMNCA obtained at the equilibrium potential (3.5 V vs Li/Li^+)

Apparent diffusion coefficient of lithium ion, D_{app} (cm^2 s^{-1})			
Method		**LMNC**	**LMNCA**
CV (**eqn.** 6.3)	Before cycling	$(3.36\pm0.17)\times10^{-10}$ (anodic) $(2.26\pm0.11)\times10^{-10}$ (cathodic)	$(1.33\pm0.07)\times10^{-10}$ (anodic) $(7.33\pm0.37)\times10^{-11}$ (cathodic)
	After 50th cycle	$(9.39\pm0.47)\times10^{-11}$ (anodic) $(3.66\pm0.18)\times10^{-11}$ (cathodic)	$(1.45\pm0.07)\times10^{-10}$ (anodic) $(9.24\pm0.46)\times10^{-11}$ (cathodic)
EIS (**eqn.** 6.4)	Before cycling	$(1.02\pm0.02)\times10^{-12}$	$(2.48\pm0.22)\times10^{-13}$
	After 50th cycle	$(2.63\pm0.08)\times10^{-13}$	$(1.21\pm0.02)\times10^{-13}$
EIS (**eqn.** 6.6)	Before cycling	$(1.65\pm0.03)\times10^{-15}$	$(1.34\pm0.12)\times10^{-15}$
	After 50th cycle	$(1.02\pm0.03)\times10^{-16}$	$(3.82\pm0.08)\times10^{-16}$

The exchange current density (j_o) and the apparent electron transfer rate constant (k_{app}) can be calculated by means of the charge transfer resistance (R_{ct}) [53]:

$$j_0 = \frac{i_0}{A} = \frac{RT}{nFR_{ct}A} \quad 6.7$$

where n is the number of electron transferred, A is the geopmetric area of the electrode, R is the ideal gas constant, T is the absolute temperature and F is the Faraday constant.

$$i_0 = nFAk_{app}C_{ox}^{\infty}C_{red}^{\infty} \quad 6.8$$

Combining **Equations** 6.7 and 6.8, taking the activity coefficients (∞) equal to unity, and assuming the bulk concentrations of the oxidised and reduced Li species to be equal ($C_{ox}^{\infty} = C_{red}^{\infty} = C_{Li}$) such that the equilibrium potential ($E_{1/2}$) equals the formal redox potential ($E_{O/R}^{\emptyset}$), then the k_{app} becomes **Equation** 6.9:

$$k_{app} = \frac{RT}{n^2F^2AR_{ct}C_{Li}} \quad 6.9$$

From the plot of J_0 and k_{app} vs. applied potential (**Figure 6.18** and **Figure 6.19**), J_o varies between 17 and 90 μA cm^{-2}, while k_{app} varies between 0.7×10^{-7} cm.s^{-1} and 3×10^{-7} cm.s^{-1}, reaching maxima at 4.4 V after cycling, except for LMNC. The results clearly reveal that the lithium ion intercalation/de-intercalation process is different at different potentials, with higher intercalation/de-intercalation or electrochemical activity occurring at highest investigated potential (4.4 V).

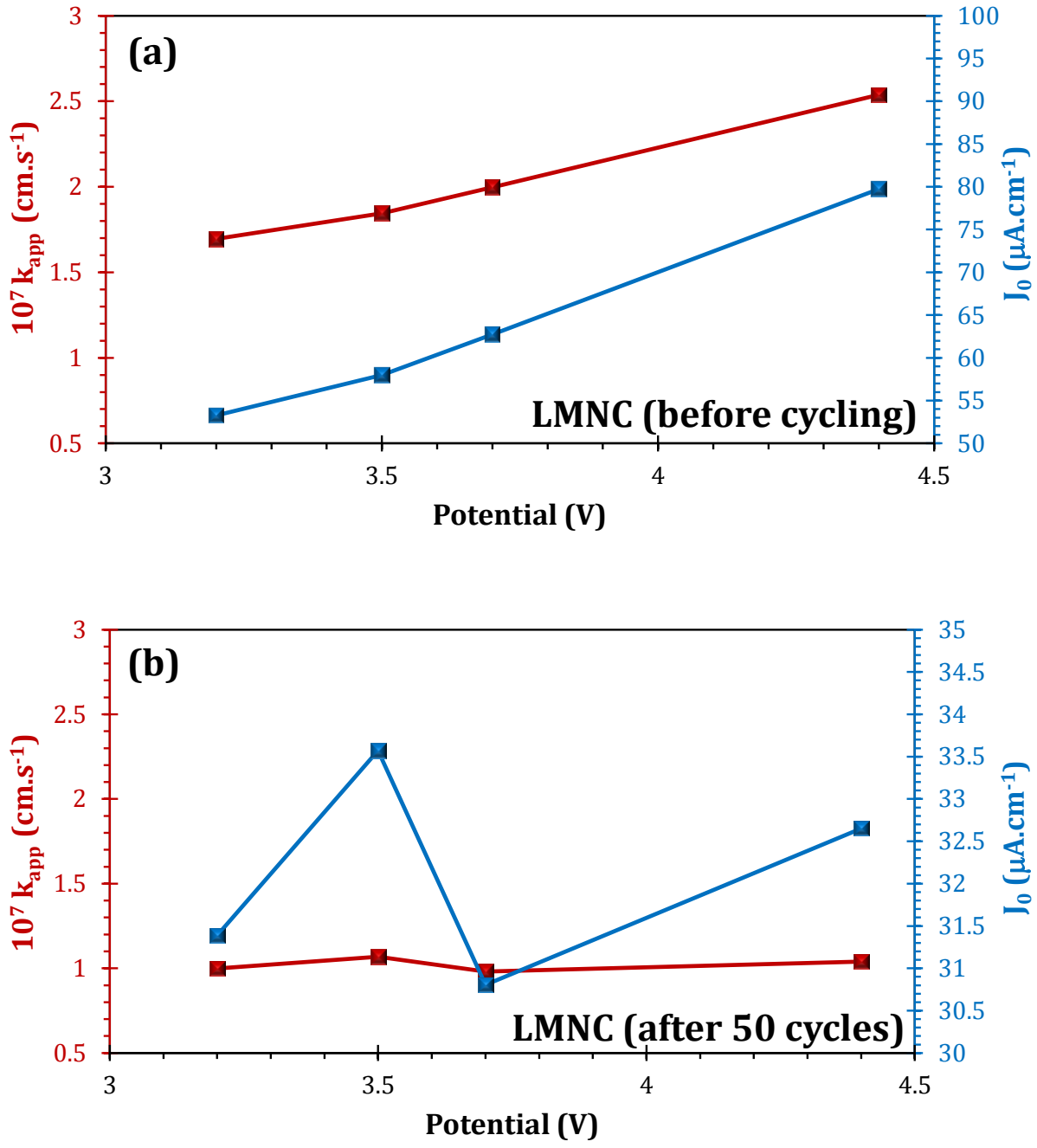

Figure 6.18: Plots of k_{app} and j_o vs applied potential of the LMNC (a) before the 1st cycle and (b) after 50 cycles.

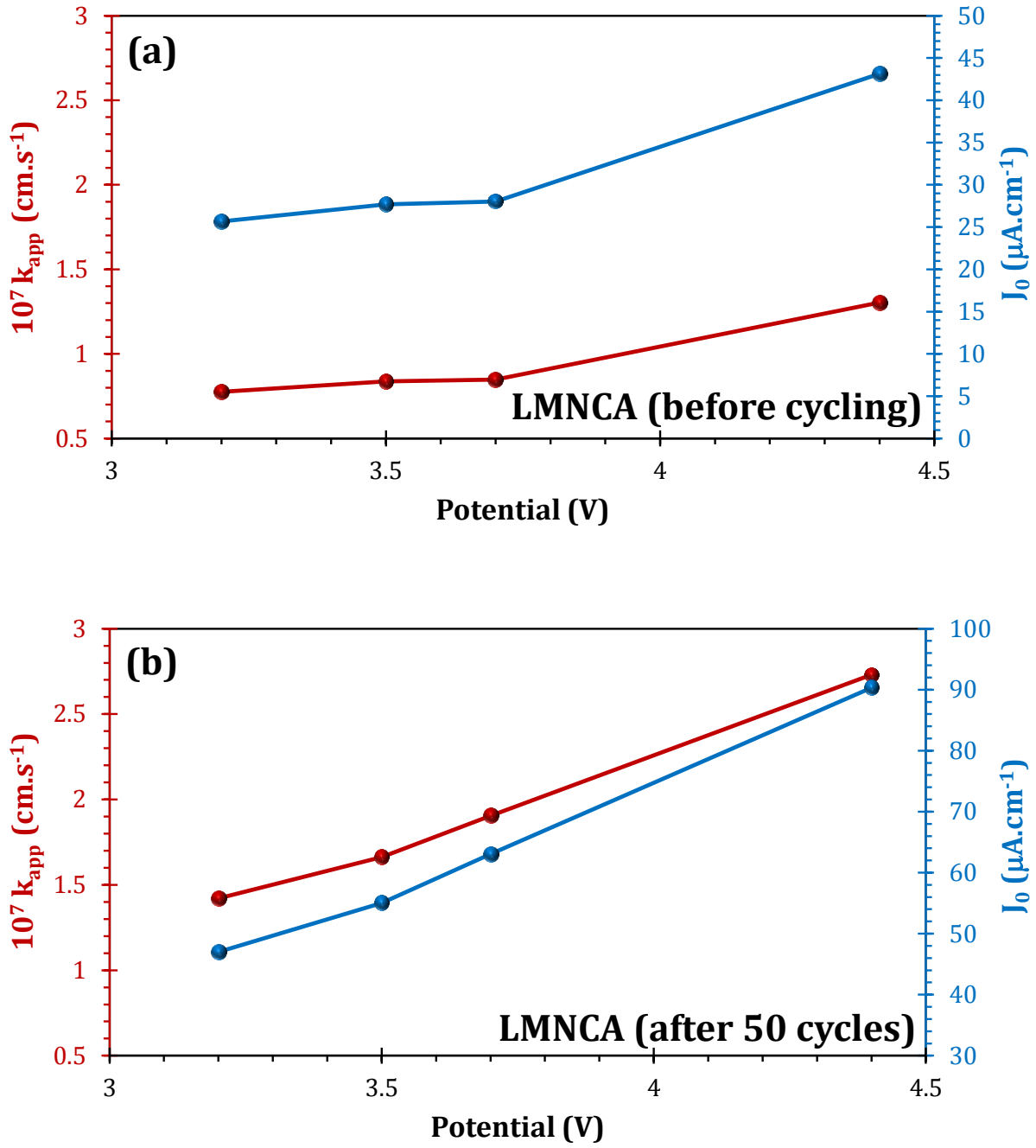

Figure 6.19: Plots of k_{app} and j_o vs applied potential of the LMNCA (a) before the 1st cycle and (b) after 50 cycles.

6.3 Conclusion on the Impact of Al Doping of $Li_{1.2}Mn_{0.54}Ni_{0.13}Co_{0.13}O_2$ Cathode Material

A modified, one-step powder-forming Pechini method was employed to synthesise $Li[Li_{0.2}Mn_{0.54}Ni_{0.13}Co_{0.13}]O_2$ and its Al doped counterpart, $Li[Li_{0.2}Mn_{0.52}Ni_{0.13}Co_{0.13}Al_{0.02}]O_2$ at a relatively low annealing temperature of 700°C. FESEM and AFM images showed the materials to be nanomaterials (in the 50 nm – 100 nm size range). CSAFM proved that LMNCA is more conductive than the LMNC. XRD results showed that Al doping increased the *c* lattice parameter that decreases the diffusional activation energy of Li and thereby increasing the diffusion flux of Li in the layered cathode. The *c* / *a* ratio of LMNC and LMNCA showed that LMNCA has a higher cation ordering than the pristine LMNC. The initial discharge capacity of LMNCA is lower than that of the LMNC, but LMNCA shows a better stability with cycling and a better discharge capacity. The EIS results show that the SEI layer of the LMNCA forms slower compared to that of the LMNC thus improving the cyclability of LMNCA. Variation of surface film resistance (R_f) and resistance to lithium intercalation/de-intercalation (R_{ct}) as a function of applied voltage before and after 50 cycles were interpreted in terms of the SEI. LMNCA showed the highest impedance (both R_f and R_{ct}) before cycling, however, the impedance values dramatically decreased much lower than the corresponding values for the pristine LMNC. The enhanced conductivity of the LMNCA is related to the higher amount of the Mn^{3+} cations in the lattice, aided by the increased *c* lattice that enhances the diffusivity of Li during the electrochemical cycling. Cyclic voltammetry indicates that Al doping raises the potential at which Li is extracted and re-inserted. LMNCA showed enhanced diffusion coefficient and electron transfer rate constant compared to the LMNC. This study has provided

further opportunities for possible improvement of the electrochemistry of the LMNC by modification of the synthesis conditions such as varying the Al content and annealing temperature. In the chapter following it is shown that electrochemistry can be further improved by controlling the Mn^{4+} concentration in the layered material via a hybrid microwave synthesis method.

References

[1] C.S. Johnson, N. Li, C. Lefief, M.M. Thackeray, Electrochem. Commun. **9** (2007) 787.

[2] M.M. Thackeray, C.S. Johnson, J.T. Vaughey, N. Li, S.A. Hackney, J. Mater. Chem. **15** (2005) 2257.

[3] S. Kang, P. Kempgens, S. Greenbaum, A. Kropf, K. Amine, M. Thackeray, J. Mater. Chem. **17** (2007) 2069.

[4] M.M. Thackeray, S.-. Kang, C.S. Johnson, J.T. Vaughey, S.A. Hackney, Electrochem. Commun. **8** (2006) 1531.

[5] Z. Li, N.A. Chernova, J. Feng, S. Upreti, F. Omenya, M.S. Whittingham, J. Electrochem. Soc. **159** (2011) A116.

[6] L. Croguennec, J. Bains, J. Bréger, C. Tessier, P. Biensan, S. Levasseur, C. Delmas, J. Electrochem. Soc. **158** (2011) A664.

[7] J. Wilcox, S. Patoux, M. Doeff, J. Electrochem. Soc. **156** (2009) A192.

[8] J.D. Wilcox, E.E. Rodriguez, M.M. Doeff, J. Electrochem. Soc. **156** (2009) A1011.

[9] F. Zhou, X. Zhao, J. Dahn, J. Electrochem. Soc. **156** (2009) A343.

[10] F. Zhou, X. Zhao, C. Goodbrake, J. Jiang, J. Dahn, J. Electrochem. Soc. **156** (2009) A796.

[11] M.M. Thackeray, S. Kang, C.S. Johnson, J.T. Vaughey, R. Benedek, S. Hackney, J. Mater. Chem. **17** (2007) 3112.

[12] H. Deng, I. Belharouak, Y. Sun, K. Amine, J. Mater. Chem. **19** (2009) 4510.

[13] G.M. Koenig Jr., I. Belharouak, H.M. Wu, K. Amine, Electrochim. Acta **56** (2011) 1426.

[14] J.N. Reimers, W. Li, J. Dahn, Phys. Rev. B **47** (1993) 8486.

[15] E. Malicka, J. Krok-Kowalski, J. Warczewski, T. Gron, H. Duda, T. Mydlarz, M. Pawelczyk, A. Pacyna, P. Rduch, G. Wladarz, Acta Phys. Pol. A **116** (2009) 967.

[16] D. Varshney, M. Shaikh, N. Dodiya, I. Mansuri, **1349** (2011) 155.

[17] K. Kang, Y.S. Meng, J. Breger, C.P. Grey, G. Ceder, Science **311** (2006) 977.

[18] Y. Choi, S. Pyun, S. Moon, Solid State Ionics **89** (1996) 43.

[19] S. Gopukumar, Y. Jeong, K.B. Kim, Solid State Ionics **159** (2003) 223.

[20] M.S. Whittingham, Chem. Rev. **104** (2004) 4271.

[21] Z. Lu, D. MacNeil, J. Dahn, Electrochem. Solid-State Lett. **4** (2001) A200.

[22] K.M. Shaju, G.V. Subba Rao, B.V.R. Chowdari, Electrochim. Acta **48** (2002) 145.

[23] J. Xiao, N.A. Chernova, M.S. Whittingham, Chem. Mater. **22** (2009) 1180.

[24] T. Yi, X. Hu, J. Power Sources **167** (2007) 185.

[25] M. Oku, K. Wagatsuma, T. Konishi, J. Electron Spectrosc. Relat. Phenom. **98–99** (1999) 277.

[26] S. Hufner, Adv. Phys. **43** (1994) 183.

[27] K. Kim, Phys. Rev. B **11** (1975) 2177.

[28] N.V. Kosova, V.V. Kaichev, V.I. Bukhtiyarov, D.G. Kellerman, E.T. Devyatkina, T.V. Larina, J. Power Sources **119–121** (2003) 669.

[29] L. Dahéron, R. Dedryvere, H. Martinez, M. Ménétrier, C. Denage, C. Delmas, D. Gonbeau, Chem. Mater. **20** (2007) 583.

[30] N.V. Kosova, E.T. Devyatkina, V.V. Kaichev, J. Power Sources **174** (2007) 735.

[31] S. Dou, W. Wang, J. Solid State Electrochem. **15** (2011) 399.

[32] C. Wagner, L. Davis, M. Zeller, J. Taylor, R. Raymond, L. Gale, Surf. Interface Anal. **3** (1981) 211.

[33] A. Abouimrane, O.C. Compton, H. Deng, I. Belharouak, D.A. Dikin, S.T. Nguyen, K. Amine, Electrochem. Solid-State Lett. **14** (2011) A126.

[34] S.A. Mamuru, K.I. Ozoemena, T. Fukuda, N. Kobayashi, J. Mater. Chem. **20** (2010) 10705.

[35] C.S. Johnson, N. Li, C. Lefief, J.T. Vaughey, M.M. Thackeray, Chem. Mater. **20** (2008) 6095.

[36] J. Bréger, Y.S. Meng, Y. Hinuma, S. Kumar, K. Kang, Y. Shao-Horn, G. Ceder, C.P. Grey, Chem. Mater. **18** (2006) 4768.

[37] H.H. Li, N. Yabuuchi, Y.S. Meng, S. Kumar, J. Breger, C.P. Grey, Y. Shao-Horn, Chem. Mater. **19** (2007) 2551.

[38] S. Kang, C. Johnson, J. Vaughey, K. Amine, M. Thackeray, J. Electrochem. Soc. **153** (2006) A1186.

[39] M.E. Orazem, B. Tribollet, Electrochemical impedance spectroscopy, John Wiley & Sons, New Jersey, 2011.

[40] K.I. Ozoemena, N.S. Mathebula, J. Pillay, G. Toschi, J.A. Verschoor, Phys. Chem. Chem. Phys. **12** (2010) 345.

[41] J. Pillay, K.I. Ozoemena, R.T. Tshikhudo, R.M. Moutloali, Langmuir **26** (2010) 9061.

[42] H. Xia, L. Lu, Phys. Scripta **2007** (2007) 43.

[43] K. Shaju, G.S. Rao, B. Chowdari, J. Electrochem. Soc. **151** (2004) A1324.

[44] K. Dokko, M. Mohamedi, M. Umeda, I. Uchida, J. Electrochem. Soc. **150** (2003) A425.

[45] M. Mohamedi, M. Makino, K. Dokko, T. Itoh, I. Uchida, Electrochim. Acta **48** (2002) 79.

[46] M. Umeda, K. Dokko, Y. Fujita, M. Mohamedi, I. Uchida, J.R. Selman, Electrochim. Acta **47** (2001) 885.

[47] P. Goonetilleke, J. Zheng, D. Roy, J. Electrochem. Soc. **156** (2009) A709.

[48] J.P. Zheng, D.J. Crain, D. Roy, Solid State Ionics **196** (2011) 48.

[49] T. Yi, C. Li, Y. Zhu, R. Zhu, J. Shu, Russian J. Electrochem. **46** (2010) 227.

[50] P. Gao, G. Yang, H. Liu, L. Wang, H. Zhou, Solid State Ionics **207** (2012) 50.

[51] L. Wang, J. Zhao, X. He, J. Gao, J. Li, C. Wan, C. Jiang, Int. J. Electrochem. Sci. **7** (2012) 345.

[52] P. Gao, Y. Li, H. Liu, J. Pinto, X. Jiang, G. Yang, J. Electrochem. Soc. **159** (2012) A506.

[53] A.J. Bard, L.R. Faulkner, Electrochemical methods: fundamentals and applications, 2nd ed., Wiley, New York, 2000.

Chapter 7*

Controlling the Mn^{4+} Concentration in $Li_{1.2}Mn_{0.54}Ni_{0.13}Co_{0.13}O_2$ Cathode Material via a Microwave Assisted Synthesis Method

7.1 Introduction to the Importance of Mn^{4+} Concentration in $Li_{1.2}Mn_{0.54}Ni_{0.13}Co_{0.13}O_2$ Cathode Material

This work is a continuation of the work presented in **Chapter 6** where the importance and interests of this material are also discussed. The work done in this chapter will be compared with the results reported in **Chapter 6**.

In **Chapter 5** it is shown that with the use of microwave irradiation, the Mn^{3+} concentration in the layered $LiMn_{1.5}Ni_{0.5}O_4$ cathode material can be controlled. The same methodology is used to investigate the effects of microwave irradiation on the layered $Li[Li_{0.2}Mn_{0.54}Ni_{0.13}Co_{0.13}]O_2$ and $Li[Li_{0.2}Mn_{0.52}Ni_{0.13}Co_{0.13}Al_{0.02}]O_2$ cathode materials.

*The following submitted manuscript resulted from part of the research work presented in this chapter and is not referenced further:
C. J. Jafta, M. K. Mathe, N. Manyala, W. D. Roos and K. I. Ozoemena, "Microwave Irradiation Controls the Manganese Oxidation States of Nanostructured ($Li[Li_{0.2}Mn_{0.52}Ni_{0.13}Co_{0.13}Al_{0.02}]O_2$) Layered Cathode Materials for high-Performance Lithium Ion Batteries", *Submitted* (2013)

In order to interpret observed microwave effects, two hypotheses were proposed. The first assumes the existence of a purely thermal effect (i.e. hot spots and temperature gradient) by dipolar polarization and ionic conduction [1]. The second theory assumes that, besides thermal effects there are also non-thermal effects like molecular interaction with the electromagnetic field as shown by Roy *et al*. [2]. It is generally accepted that there are a number of characteristics specific to microwaves as agents for promoting chemical reactions:

I. The quantum energy of microwaves (10^{-5} eV) which is much lower than that of chemical bonds making it improbable for microwaves to break or weaken bonds within molecules.

II. The intensity of electric and magnetic fields that cannot cause the shift of any chemical reaction equilibrium. However, many experiments with microwave heating reveal results different from those obtained with conventional heating [3].

The approach in this chapter is to develop an optimal strategy for producing a successful and economical synthesis procedure for cathode material. The strategy is to make use of microwave radiation in the primary stage procedure and of conventional annealing in the later stage of synthesis. This approach was suggested by Balaji et al. [4].

7.2 Results and Discussion

Figure 7.1 compares the SEM images of LMNC-mic and LMNCA-mic, showing that the synthesised materials comprised of nano-sized particles with sizes in the 250 – 300 nm range for the LMNC-mic, and 100 – 200 nm range for the LMNCA. These particle sizes

are comparable to the un-microwaved samples (LMNC and LMNCA) reported in **Chapter 6**.

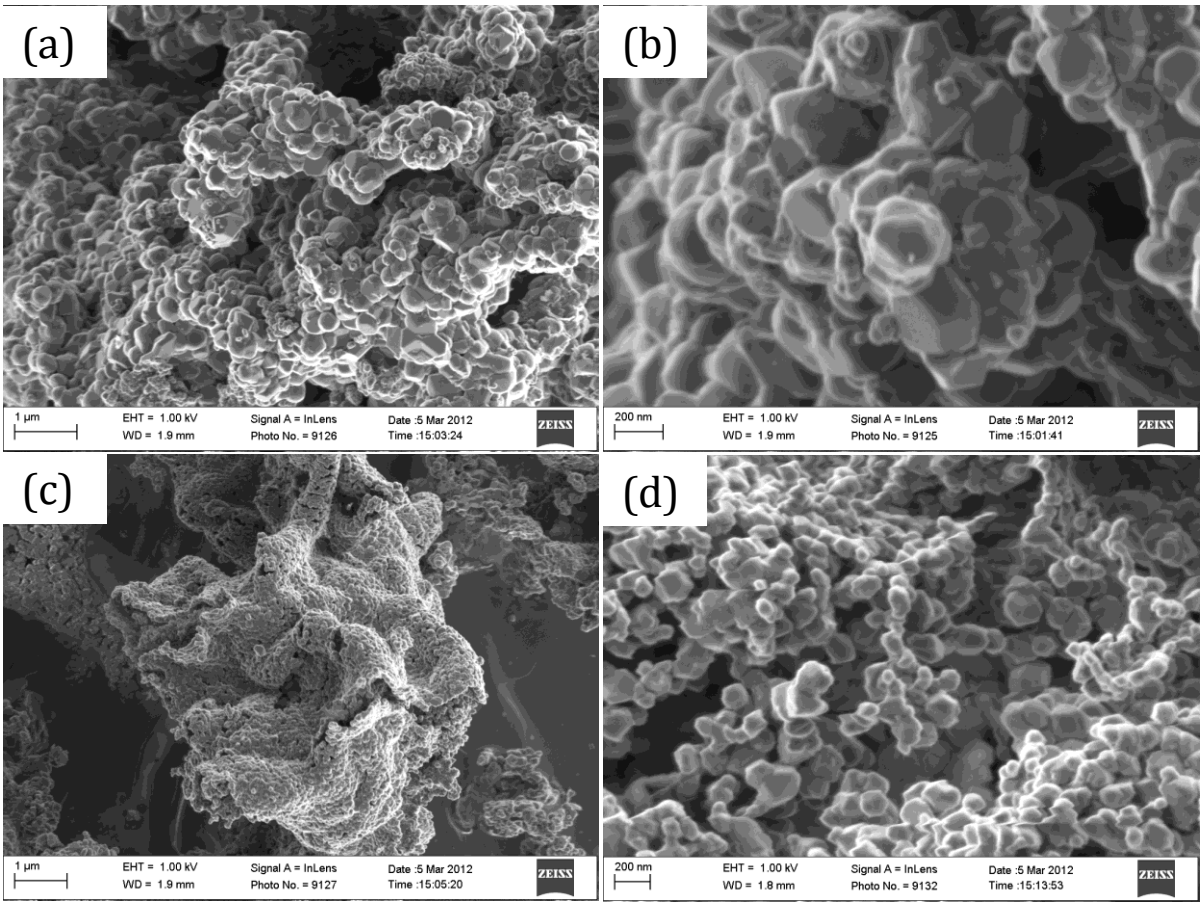

Figure 7.1: FESEM images of (a) LMNC-mic at low magnification, (b) LMNC-mic at high magnification, (c) LMNCA-mic at low magnification and (d) LMNCA-mic at high magnification.

Figure 7.2 shows the XRD spectra of the LMNC-mic and LMNCA-mic recorded from 2θ = 10° – 90°. All the peaks are attributed to the typical peaks of a hexagonal phase with space group $R\bar{3}m$, except for the super lattice peaks found between 2θ = 22° – 30° [5] characteristic of the presence of a Li_2MnO_3-type integrated phase, which by contrast adopts the C2/m space group [5-7]. The intensity ratio of the 101/(006 + 102) peaks are greater than 2 which is an indication that the cation mixing between Li and

transition metal layers is small [8]. The lattice parameters, *a* and *c*, were calculated and are summarized in **Table 7.1**.

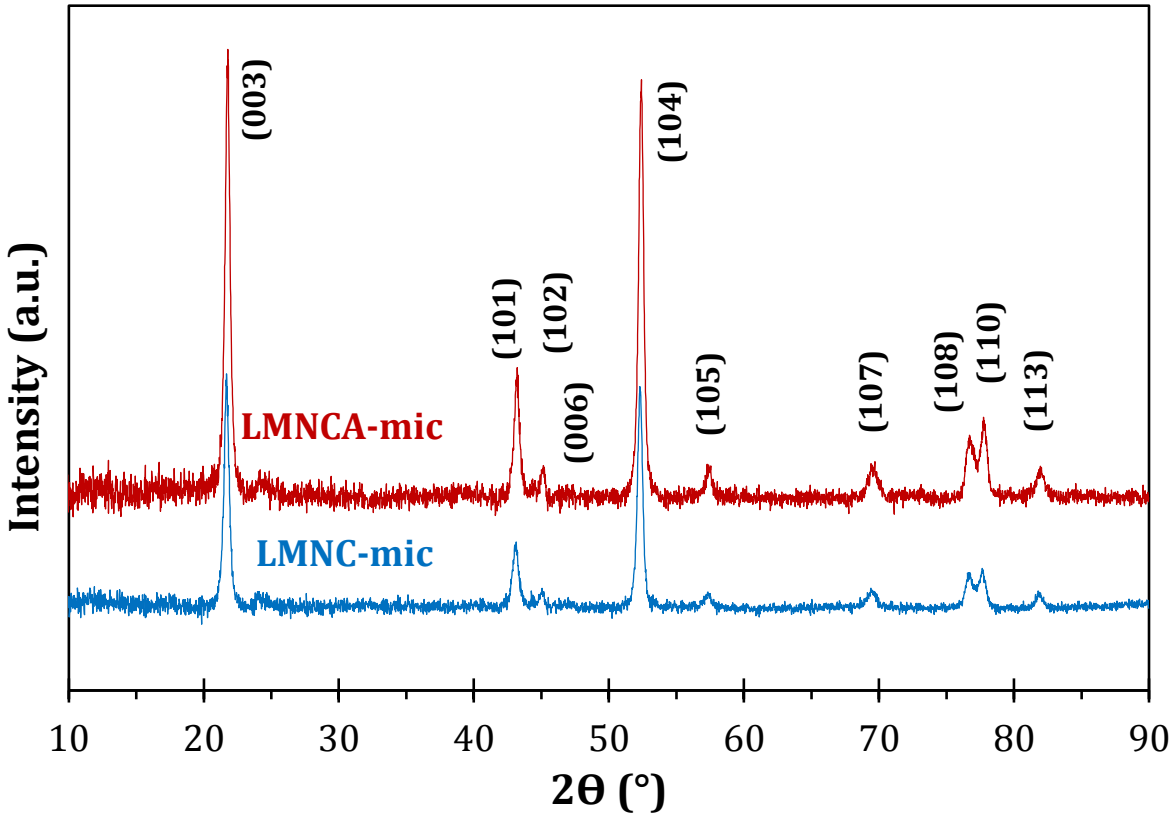

Figure 7.2: XRD patterns of LMNC-mic ($Li[Li_{0.2}Mn_{0.54}Ni_{0.13}Co_{0.13}]O_2$) and LMNCA-mic ($Li[Li_{0.2}Mn_{0.52}Ni_{0.13}Co_{0.13}Al_{0.02}]O_2$).

Table 7.1: Structure parameters of the LMNC and LMNCA samples

Sample	*a* (Å)	*c* (Å)	*c*/*a*
LMNC-mic	2.852	14.216	4.985
LMNCA-mic	2.846	14.233	5.001

The lattice parameters *a* and *c* represent the interlayer metal-metal distance and the inter-slab distance, respectively. The LMNCA-mic has a higher *c*/*a* ratio compared to the LMNC-mic, indicating a higher cation ordering of the LMNCA-mic. The LMNCA also showed a better cation ordering compared to the LMNC (**Chapter 6**), but the LMNCA-mic has a superior cation ordering. In **Chapter 6** it was showed that when doping with a

minute amount of Al (x = 0.02) that there is almost no change in the *a* lattice parameter but a slight increase in the *c* lattice parameter. This is attributed to the increased ionic radius of Al^{3+} ($r(Al^{3+})$ = 53.5 pm) [9] compared to the smaller ionic radius of Mn^{4+} ($r(Mn^{4+})$ = 53.0 pm) [10]. Also, the increase in the *c* lattice parameter, in layered materials, is associated with faster Li diffusion due to the decrease in the activation energy of Li hopping [11]. Again, the LMNCA-mic shows a greater *c* lattice and thus faster Li diffusion is expected that would result in better rate capability compared to the cathode materials LMNC, LMNCA and LMNC-mic. The *c*/*a* ratio is an indication of the hexagonal setting, with a larger ratio indicating higher cation ordering. Partial cation mixing is said to occur if the *c*/*a* ratio falls below 4.96 [12-16]. The high *c*/*a* ratio, well above that required for distortion of the oxygen lattice, clearly confirm the formation of the layered structure. These ratios are in good agreement with other reported values [13-16]. It is shown here that the samples that have been treated with microwaves (LMNC-mic and LMNCA-mic) show the highest *c*/*a* ratios (4.985 and 5.001 for LMNC-mic and LMNCA-mic, respectively), compared to the un-microwaved samples (LMNC and LMNCA) reported in **Chapter 6**, and thus has the least cation mixing.

Figure 7.3 shows the detailed XPS spectra of the Mn $2p_{3/2}$ peaks of the LMNC-mic (**Figure 7.3 (a)**) and LMCA-mic (**Figure 7.3 (b)**).

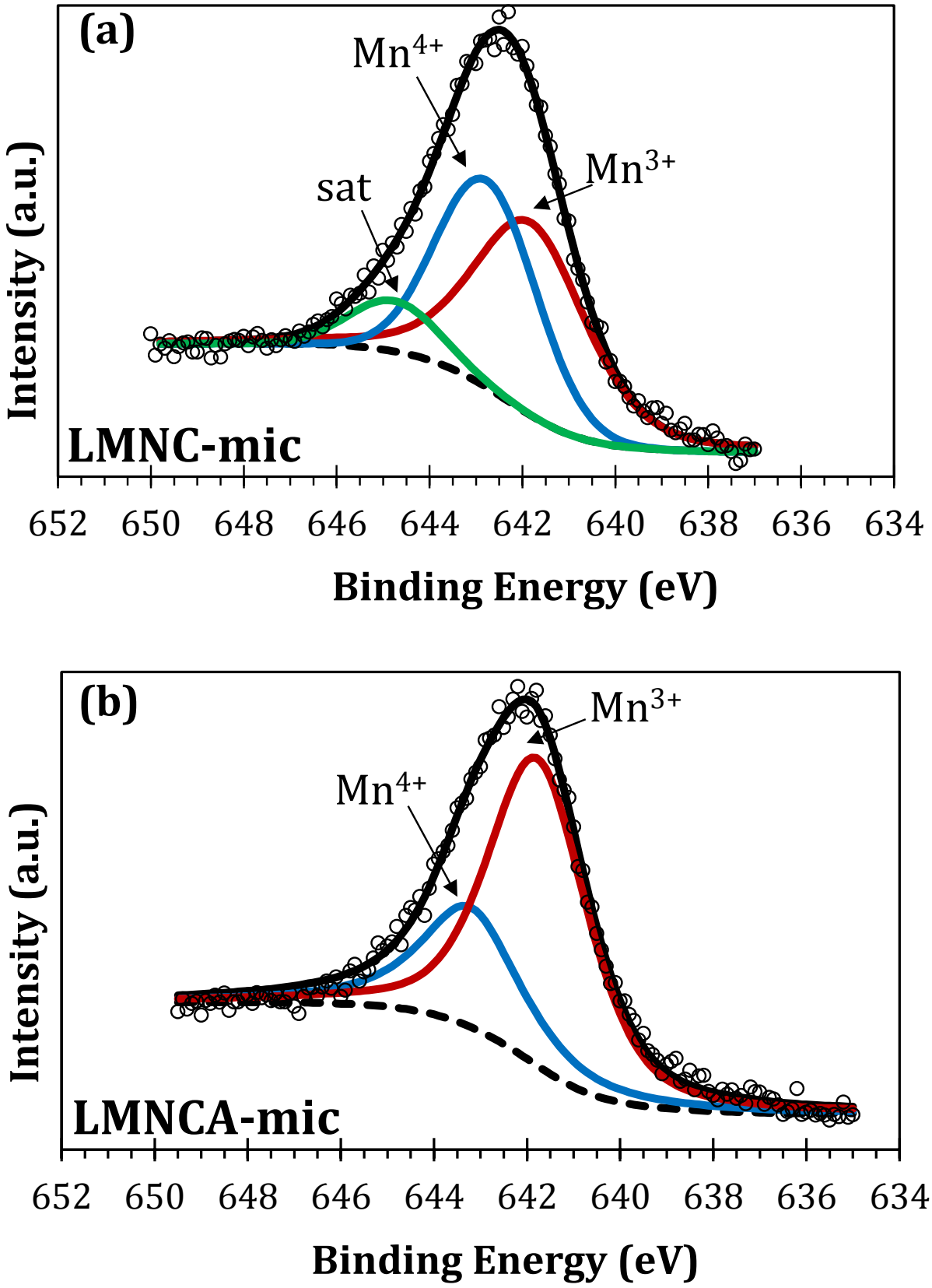

Figure 7.3: The X-ray Photoelectron Spectroscopy spectra of (a) LMNC-mic and (b) LMNCA-mic, showing the Mn $2p_{3/2}$ peak.

There is a broadening in both the peak widths, an indication that the Mn exist in more than one oxidation state. In order to confirm the oxidation states and to approximate their contribution to the total peak, the Mn $2p_{3/2}$ of the LMNC and the LMNCA peaks were deconvoluted into two and three peaks, respectively, as this gives the best statistical fit. The third peak observed from the LMNC-mic is a satellite peak that is explained in detail in **Chapter 6**. The obtained binding energy positions and cation distribution are summarised in **Table 7.2**.

Table 7.2: Mn $2p_{3/2}$ peak positions and cation distribution

Sample	Binding energy position(eV)		Cation distribution	
	Mn^{4+}	Mn^{3+}	Mn^{4+}	Mn^{3+}
LMNC	642.8	641.8	44.9 %	55.1 %
LMNCA	643.2	641.8	30.8 %	69.2 %

The binding energy peak positions corresponding to Mn^{4+} and Mn^{3+} are comparable with other binding energy values reported in the literature [16, 17]. The microwaved cathode materials show a slightly higher oxidation state for Mn than the un-microwaved cathode materials. The higher oxidation state of manganese with microwave radiation is also observed by Malinger *et. al.* [18]. This increased oxidation state of manganese of the microwaved samples could be the reason for the increased capacity and the better stability. It has recently been shown that the rapid transformation of layered $LiMnO_2$ to spinel is due to the ease at which Mn^{3+} disproportionate to Mn^{2+} and Mn^{4+} [19]. This then allows the Mn to rapidly move through tetrahedral sites as Mn^{2+}. Mn^{4+} however, has a very high activation energy barrier for diffusion through tetrahedral sites. Therefore layered materials with a higher oxidation state for their manganese are

expected to be more stable as seen in this study. Also the specific capacity of Li-rich layered cathode materials can be controlled by controlling the initial ratio of transition metal cations, particularly lithium and manganese ions [20].

This method of synthesizing $Li[Li_{0.2}Mn_{0.54}Ni_{0.13}Co_{0.13}]O_2$ and the Al doped $Li[Li_{0.2}Mn_{0.52}Ni_{0.13}Co_{0.13}Al_{0.02}]O_2$ thus provides an opportunity to control the Mn oxidation state and thus engineer a cathode material with better properties.

Figure 7.4 compares the first charge-discharge profiles of LMNC-mic and LMNCA-mic at a rate of C/10 (i.e., ~ 22.5 $mA.g^{-1}$, note that 1C corresponds to 225 $mA.g^{-1}$ current density in this work).

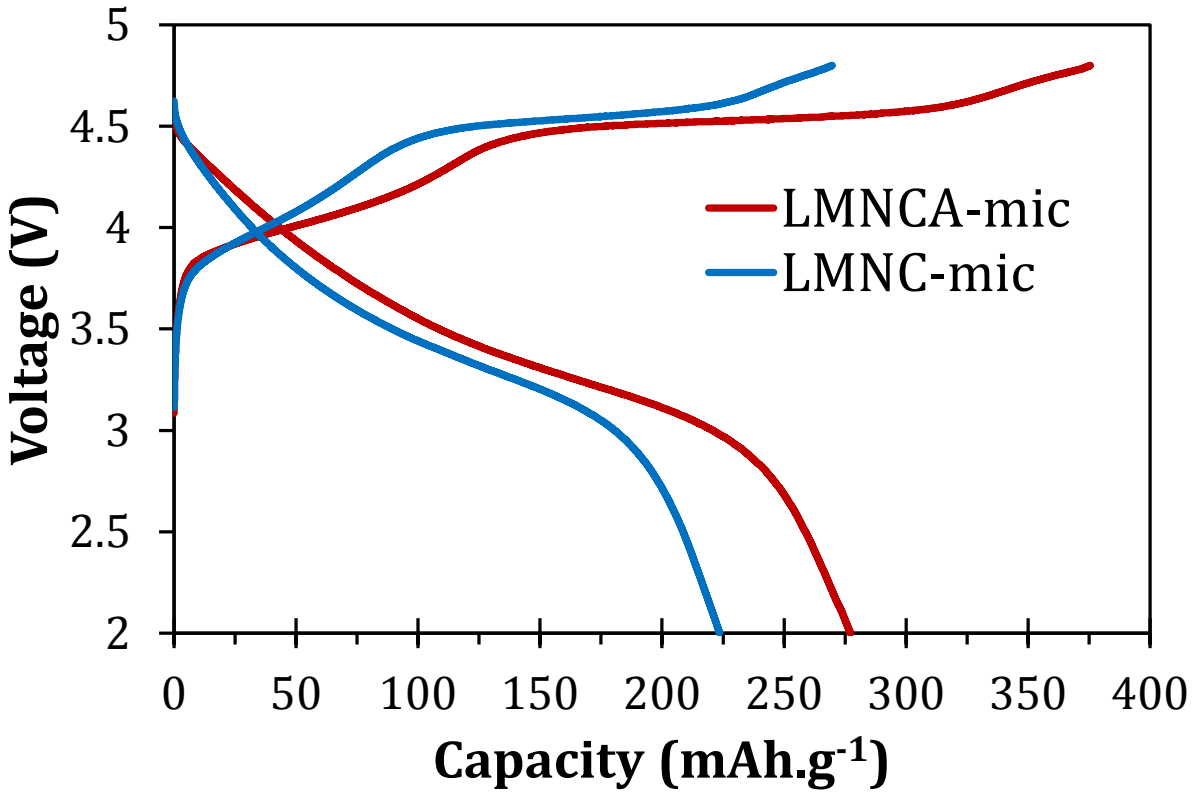

Figure 7.4: The first charge-discharge profiles of LMNC-mic and LMNCA-mic.

Both electrodes show similar charge profiles with a prolonged voltage plateau at ~ 4.5 V. The charge curve shapes are explained in detail in **Chapter 6**. The LMNCA-mic showed a higher charge capacity of ~ 375 mAh.g^{-1} compared to the LMNC-mic with a charge capacity of ~ 270 mAh.g^{-1}. This was also observed for the un-microwaved samples where the LMNCA had a higher charge capacity than the LMNC (**Chapter 6**). The LMNCA-mic also has a higher first discharge capacity of ~ 278 mAh.g^{-1} compared to the LMNC-mic with a discharge capacity of ~ 224 mAh.g^{-1}.

Figure 7.5 compares the cycle stability at a rate of C/10 of LMNC-mic and LMNCA-mic when charged between 2.0 V and 4.8 V.

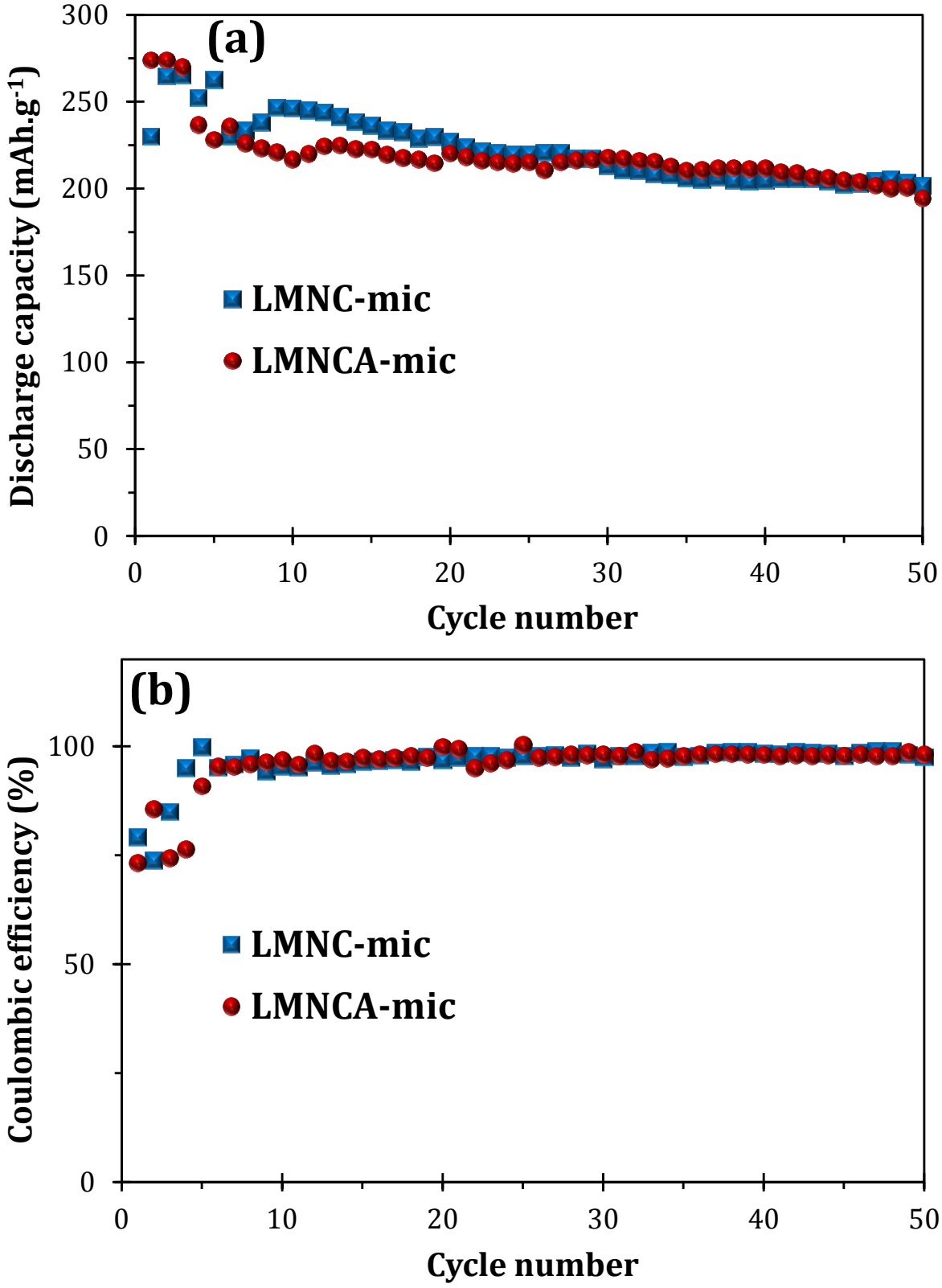

Figure 7.5: (a) The cycle stability at C/10 and (b) the Coulombic efficiency of LMNC-mic and LMNCA-mic for 50 charge discharge cycles.

During the first 6 cycles these microwave treated samples showed unstable discharge capacities. From the 7th cycle the discharge capacities starts to stabilize. The first 6 discharge capacities for LMNCA-mic and LMNC-mic, varies between ~ 270 mA.h.g^{-1} – ~ 220 mA.h.g-1 and ~ 265 mA.h.g-1 – ~ 230 mA.h.g-1, respectively. It is worth noting that even though the LMNC-mic material has a better capacity at first, the LMNCA-mic shows a higher capacity from the 28th cycle due to its better stability. The Coulombic efficiencies of LMNC-mic and LMNCA-mic are similar.

Because Al is electrochemically inactive [21] it is expected that the capacity of the Al doped cathode material (LMNCA-mic) to show a lower discharge capacity. This reduced discharge capacity with Al doping is also observed in the in the paper from Wilcox et al. [22]. When the Al doped material (LMNCA-mic) is synthesized by this hybrid microwave syntheses, the LMNCA-mic shows superior discharge capacity compared to the LMNC-mic. It is also worth noting that LMNC-mic and LMNCA-mic have better stability and discharged capacities compared to the un-microwaved materials reported in **Chapter 6.**

Figure 7.6 compares the rate capabilities, at charge and discharge rates of 0.5C, 1C, 2C and 5C, of the LMNC-mic and LMNCA-mic.

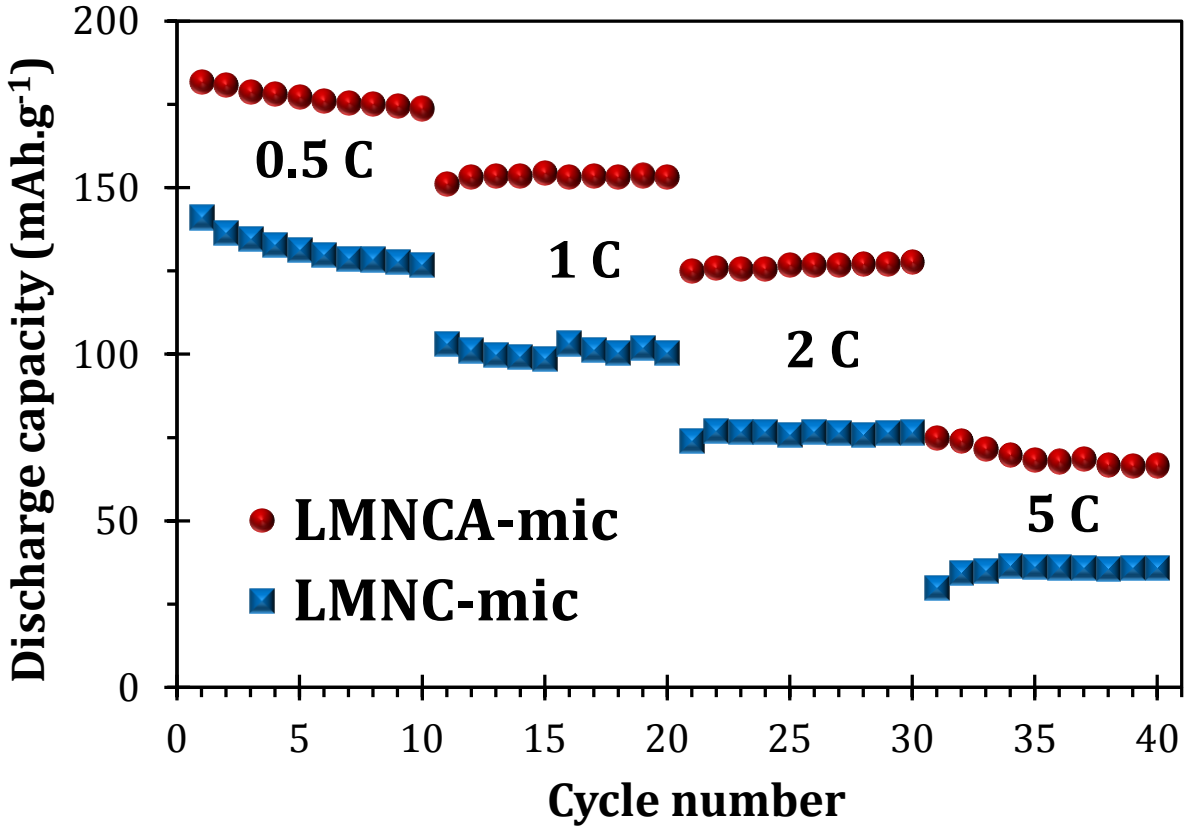

Figure 7.6: Typical rate capability of the LMNC-mic and LMNCA-mic, charged and discharged at 0.5C, 1C, 2C and 5C.

With the XRD data showing that LMNCA-mic has a bigger *c* lattice parameter compared to LMNC-mic it is thus expected that LMNCA-mic would have a better rate capability. As seen from **Figure 7.6** this is indeed the case. The *c* lattice is not the only factor responsible for high rate capability. The Mn cation state also plays a role, a high concentration Mn^{3+} will increase the electron conductivity and better the rate capability. The material with the highest Mn^{3+} concentration is also not the best in terms of rate capability, again as this is not the only factor contributing to better rate capability. Thus it is deduced that a good combination of the two (*c* lattice and Mn^{3+} concentration) is needed for high rate capability.

Figure 7.7 shows the cyclic voltammetric evolutions of LMNC-mic and LMNCA-mic.

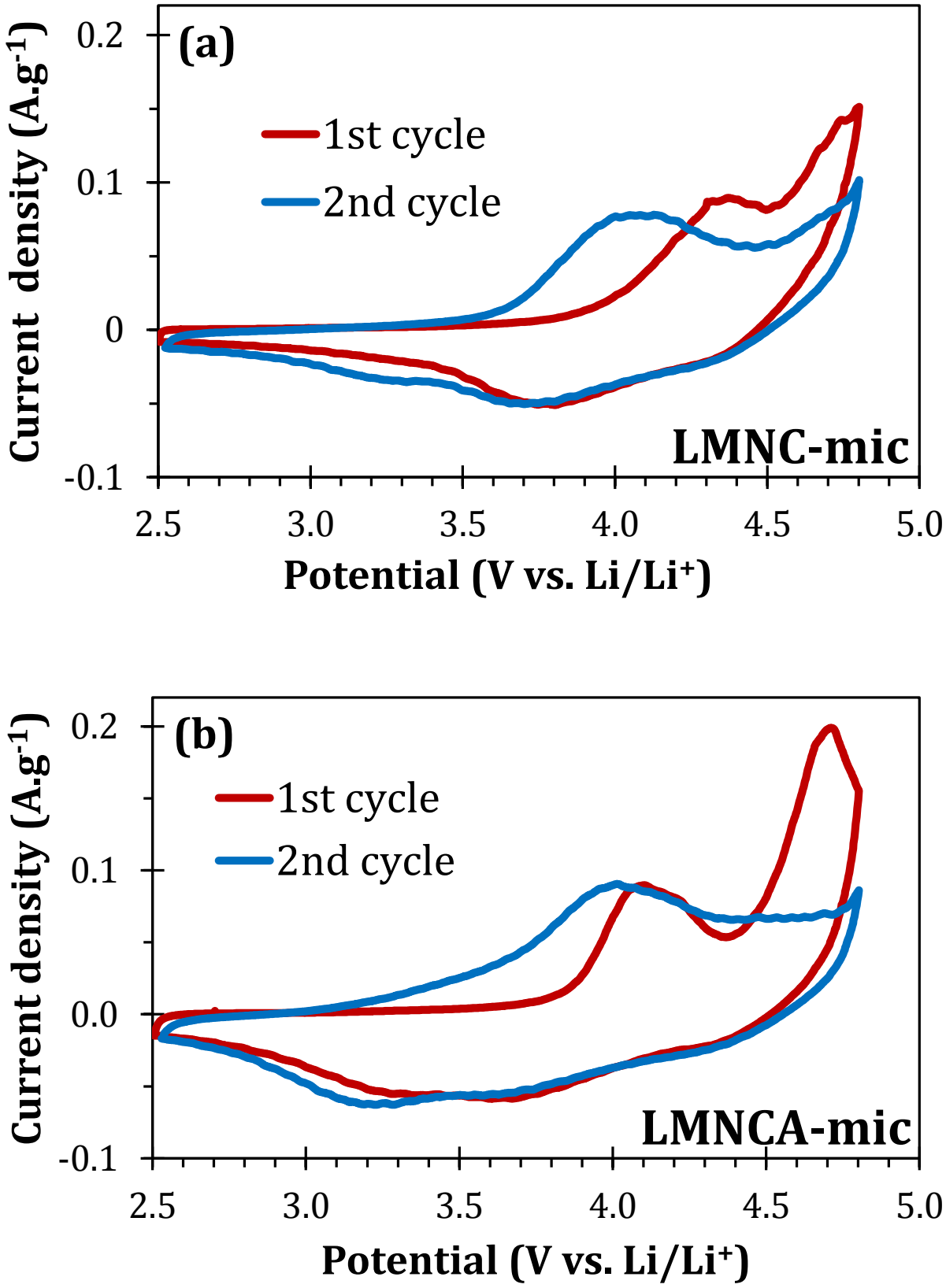

Figure 7.7: The cyclic voltammograms of (a) LMNC-mic and (b) LMNCA-mic obtained at a scan rate of 0.1 $mV.s^{-1}$ (first and second cycles).

The initial and second cycle of the LMNC-mic and LMNCA-mic is interrogated using low scan rate cyclic voltammetry (0.1 $mV.s^{-1}$). Again, the cyclic voltammograms of the LMNC and LMNCA, that are similar to LMNC-mic and LMNCA-mic, are discussed in detail in **Chapter 6**. The peaks at ~ 4.7 V, for both LMNC-mic and LMNCA-mic, of their initial cycles disappear with the 2nd cycle showing the irreversible removal of Li_2O. With the higher peak current at ~ 4.7 V for the LMNCA-mic, the higher first charge of the LMNCA-mic compared to the LMNC-mic can be explained (see **Figure 7.4**). Thus it can be assumed that the microwave irradiation in the LMNCA-mic causes more oxygen vacancies and therefore result in a higher concentration of Li_2O being removed.

Electrochemical impedance spectroscopy (EIS) represents an important technique for evaluating interfacial electrochemistry [23-26] and diffusion coefficient of lithium ion in lithium ion battery materials [27-29]. The impedance spectra for the LMNC-mic and LMNCA-mic were measured at a potential of 3.5 V. The spectra were recorded before the 1st cycle and after the 50th cycle. Prior to every measurement, the cell was relaxed for 1 h. **Figure 7.8** presents typical Nyquist plots (Z' vs –Z") obtained for the LMNC-mic and LMNCA-mic cells.

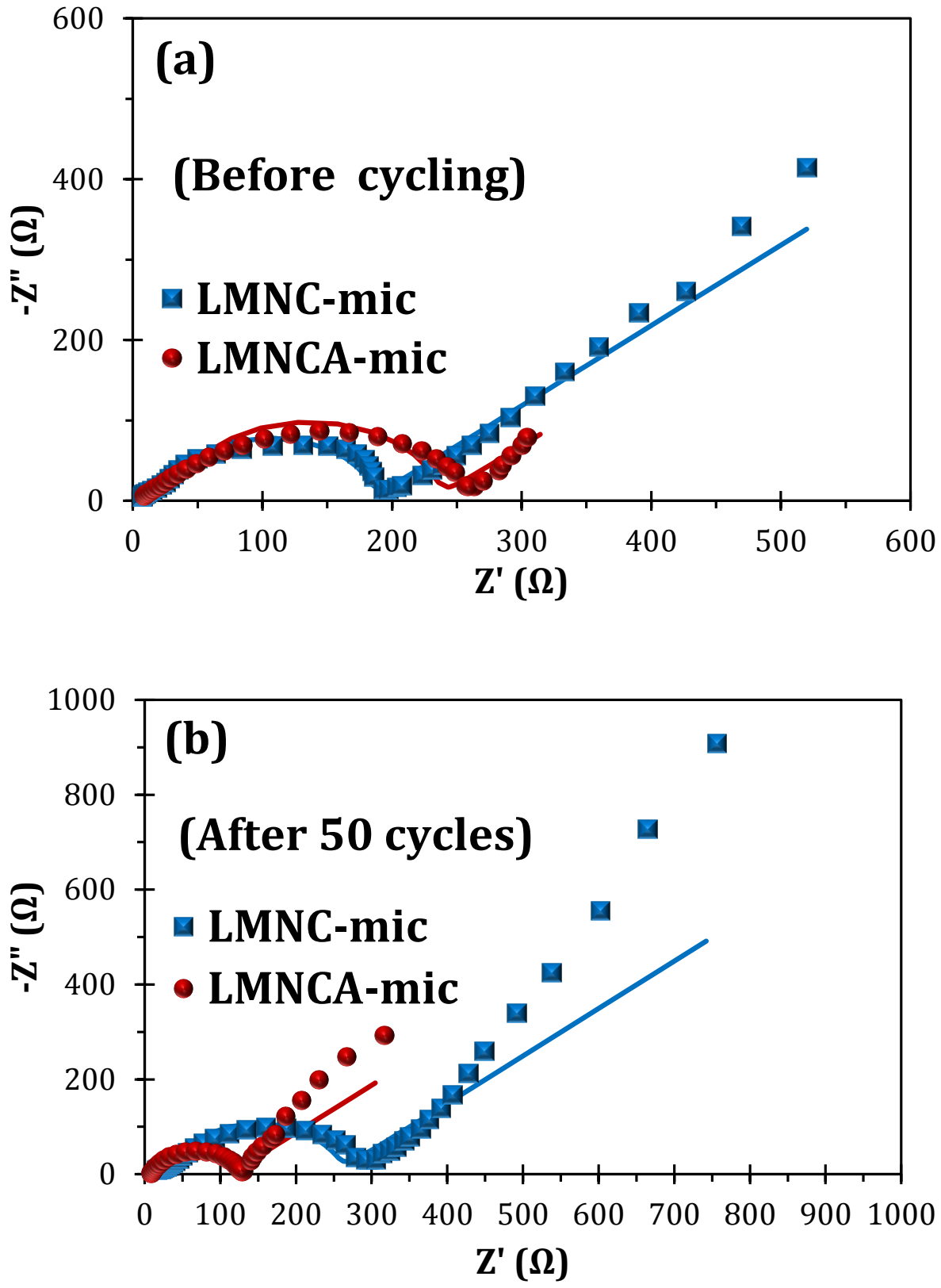

Figure 7.8: Comparative Nyquist plots of LMNC-mic and LMNCA-mic (a) before the 1st cycle and (b) after 50 cycles. Data points are experimental while solid lines are fitted data.

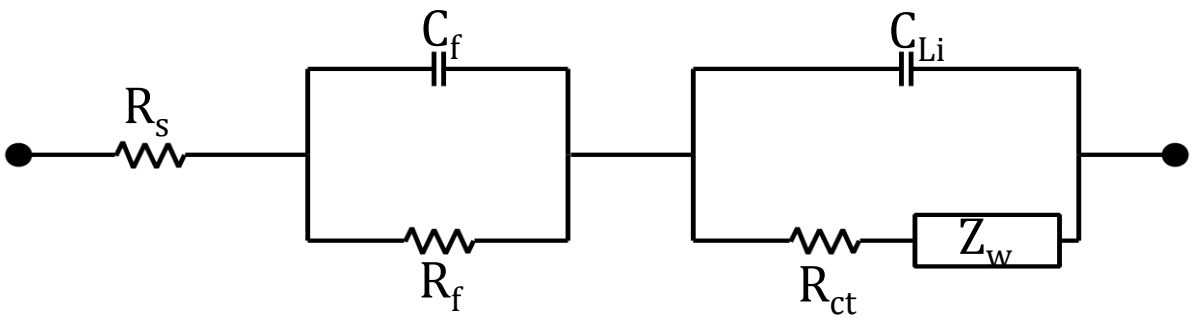

Figure 7.9: The Electrical Equivalent Circuit (EEC) used to fit the experimental EIS data.

A high-frequency semicircle and an intermediate-frequency semicircle composed into one semi-circle, and low frequency tails are observed. Generally, the high frequency semicircle is related to the passivating surface film, the solid-electrolyte interface (SEI). The intermediate frequency semicircle is ascribed to the resistance to charge-transfer process at the electrode/electrolyte interface. The low frequency tail is associated with the Li^+ ion diffusion process in the positive electrode.

The EIS spectra were fitted with an equivalent electrical circuit (EEC) shown in **Figure 7.9**. The fitting parameters involve the solution Ohmic resistance of the electrode system (R_s), solid electrolyte interface (SEI) film resistance (R_f), charge transfer resistance (R_{ct}) due to lithium intercalation/de-intercalation process, the capacitance of the surface film (C_f) and the interfacial capacitance (C_{Li}), and the Warburg element (Z_w) describing the solid state diffusion of lithium ions inside the active particles, signified by the straight sloping line (~45°) at the low frequency region.

The EIS parameters obtained for the LMNC-mic and LMNCA-mic are summarised in **Table 7.3**.

Table 7.3: Summary of EIS parameters extracted from the Nyquist plots

Sample	R_s (Ω)	R_f (Ω)	C_f (μF)	C_{Li} (μF)	R_{ct} (Ω)	Z_w (×10^{-4})
Before cycling						
LMNC-mic	7.0 ± 0.5	22.4 ± 2.2	0.7 ± 0.1	2.4 ± 0.2	152.6 ± 5.4	83.5 ± 4.6
LMNCA-mic	9.0 ± 0.6	31.4 ± 2.7	0.5 ± 0.0	2.2 ± 0.2	191.6 ± 7.2	80.2 ± 13.2
After 50 cycles						
LMNC-mic	16.1±1.3	26.7 ± 2.5	0.4 ± 0.1	2.5 ± 0.2	206.8 ± 9.0	48.7 ± 2.9
LMNCA-mic	8.1 ± 0.5	6.2 ± 1.5	1.9 ± 0.5	2.4 ± 0.2	98.2 ± 3.4	146.5 ± 8.7

The LMNCA-mic shows the same trend as did the LMNCA reported in **Chapter 6**, where the surface film resistance (R_f) and the charge transfer resistance (R_{ct}) decrease with cycling. From the R_{ct} and R_f values it can be deduced that the SEI film covering the electrode surface is destroyed or replaced by redox-active active material with cycling, resulting in the decrease of the whole impedance of the battery cell. It is observed that, although the LMNCA-mic showed the highest impedance (both R_f and R_{ct}) initially, the impedance values dramatically decreased much lower than the corresponding values for the LMNC-mic. For example, the LMNC-mic gave ~ 22 Ω (R_f) and ~ 153 Ω (R_{ct}) for the fresh cell and ~ 27 Ω (R_f) and ~ 207 Ω (R_{ct}) after 50 cycles, while the LMNCA-mic gave ~ 31 Ω (R_f) and ~ 192 Ω (R_{ct}) for the fresh cell and ~ 6 Ω (R_f) and ~ 98 Ω (R_{ct}) after the 50th cycle. It is worth noting that the impedance for the microwaved samples (LMNC-mic and LMNCA-mic) is lower when compared with the un-microwaved samples (LMNC and LMNCA) reported in **Chapter 6**.

The diffusion coefficient (D_{app}) of Lithium ions was calculated by means of **Equation** 6.4 as described in **Chapters 4** and **6**.

$$D_{Li} = \frac{2R^2T^2}{C_{Li}^2 n^4 F^4 A^2 \sigma^2} \quad 7.1$$

Assuming diffusion coefficients of the oxidised and reduced Li species to be equal (D_{ox} = D_{red} = D_{Li}) and equal concentrations (C_{ox} = C_{red} = C_{Li}). D_{Li} is the diffusion coefficient of the lithium ions, R the gas constant, T the absolute temperature, A the geometric surface area of the cathode, F the Faraday constant, n the number of electrons transferred per molecule during oxidation, C_{Li} the lithium concentration in the cathode material and σ is the Warburg factor obtained from the slope of the real impedance (Z') vs. the reciprocal square root of the frequency in the low frequency region ($\omega^{-1/2}$) according to **Equation** 6.5, and as exemplified in **Figure 7.10** for EIS.

$$Z_w = \sigma(1 - j)\omega^{-1/2} \qquad 7.2$$

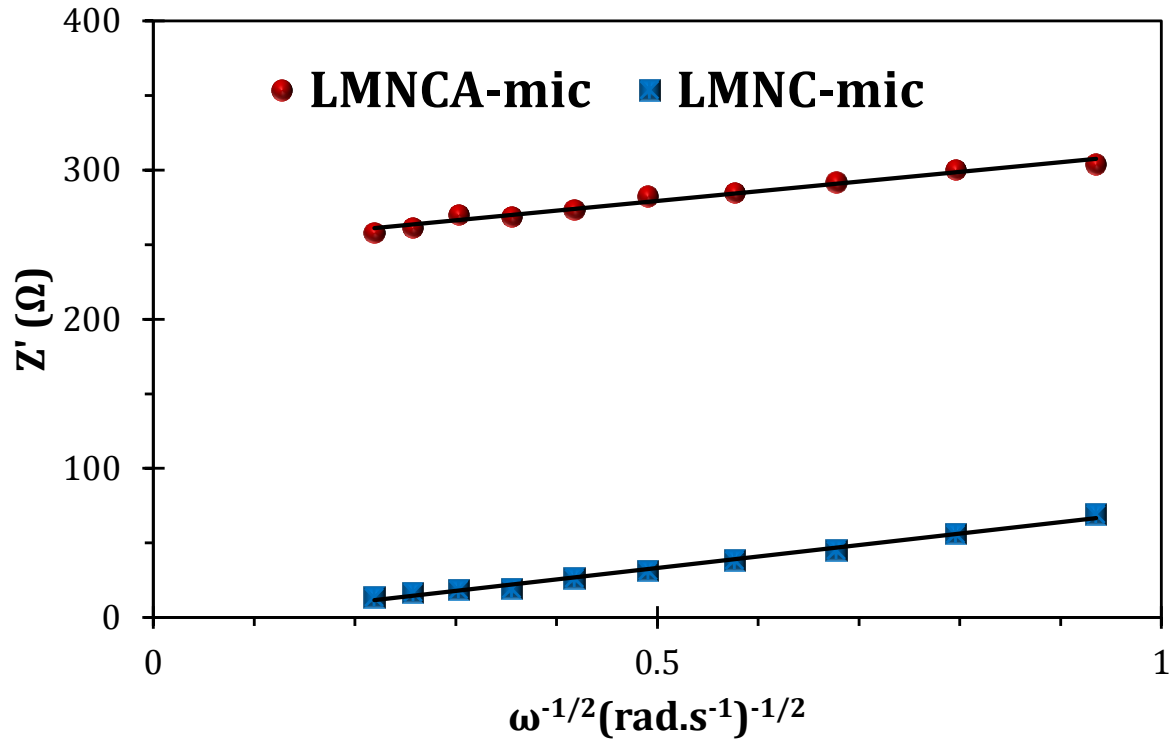

Figure 7.10: Plots of Z' vs $\omega^{-1/2}$ of the LMNC-mic and LMNCA-mic.

As expected the calculated diffusion coefficient value for LMNC-mic of 1.59×10^{-13} $cm^2.s^{-1}$ is inferior to the value for LMNCA-mic of 2.01×10^{-13} $cm^2.s^{-1}$.

7.3 Conclusion on the Impact of Mn^{4+} concentration of $Li_{1.2}Mn_{0.54}Ni_{0.13}Co_{0.13}O_2$ Cathode Material

A green Pechini method was used to produce $Li[Li_{0.2}Mn_{0.54}Ni_{0.13}Co_{0.13}]O_2$ and $Li[Li_{0.2}Mn_{0.52}Ni_{0.13}Co_{0.13}Al_{0.02}]O_2$ after which it was pre-heated, microwaved and then annealed. This synthesis method/procedure showed that the oxidation state of the manganese can be controlled by doping LMNC with Al, thereby increasing the Mn^{3+} concentration, and/or microwaved where the Mn^{4+} concentration would be increased. The results showed that the LMNCA-mic outperforms the LMNC-mic and ultimately is superior compared to all the materials reported in **Chapter 6** and **7**.

References

[1] C.O. Kappe, Chem. Soc. Rev. **37** (2008) 1127.

[2] R. Roy, R. Peelamedu, L. Hurtt, J. Cheng, D. Agrawal, Mater. Res. Innov. **6** (2002) 128.

[3] W. Tu, H. Liu, J. Mater. Chem. **10** (2000) 2207.

[4] S. Balaji, D. Mutharasu, N. Sankara Subramanian, K. Ramanathan, Ionics **15** (2009) 765.

[5] M.M. Thackeray, S. Kang, C.S. Johnson, J.T. Vaughey, R. Benedek, S. Hackney, J. Mater. Chem. **17** (2007) 3112.

[6] H. Deng, I. Belharouak, Y. Sun, K. Amine, J. Mater. Chem. **19** (2009) 4510.

[7] G.M. Koenig Jr., I. Belharouak, H.M. Wu, K. Amine, Electrochim. Acta **56** (2011) 1426.

[8] J.N. Reimers, W. Li, J. Dahn, Phys. Rev. B **47** (1993) 8486.

[9] E. Malicka, J. Krok-Kowalski, J. Warczewski, T. Gron, H. Duda, T. Mydlarz, M. Pawelczyk, A. Pacyna, P. Rduch, G. Wladarz, Acta Phys. Pol. A **116** (2009) 967.

[10] D. Varshney, M. Shaikh, N. Dodiya, I. Mansuri, AIP Conf. Proc. **1349** (2011) 155.

[11] K. Kang, Y.S. Meng, J. Breger, C.P. Grey, G. Ceder, Science **311** (2006) 977.

[12] Y. Choi, S. Pyun, S. Moon, Solid State Ionics **89** (1996) 43.

[13] S. Gopukumar, Y. Jeong, K.B. Kim, Solid State Ionics **159** (2003) 223.

[14] M.S. Whittingham, Chem. Rev. **104** (2004) 4271.

[15] Z. Lu, D. MacNeil, J. Dahn, Electrochem. Solid-State Lett. **4** (2001) A200.

[16] K.M. Shaju, G.V. Subba Rao, B.V.R. Chowdari, Electrochim. Acta **48** (2002) 145.

[17] T. Yi, X. Hu, J. Power Sources **167** (2007) 185.

[18] K.A. Malinger, K. Laubernds, Y.C. Son, S.L. Suib, Chem. Mater. **16** (2004) 4296.

[19] J. Reed, G. Ceder, A. Van Der Ven, Electrochemical Solid State Lett. **4** (2001) A78.

[20] S.H. Yu, T. Yoon, J. Mun, S. jin Park, Y.S. Kang, J.H. Park, S.M. Oh, Y.E. Sung, J. Mater. Chem. A **1** (2013) 2833.

[21] C.J. Jafta, K.I. Ozoemena, M.K. Mathe, W.D. Roos, Electrochim. Acta **85** (2012) 411.

[22] J.D. Wilcox, E.E. Rodriguez, M.M. Doeff, J. Electrochem. Soc. **156** (2009) A1011.

[23] M.E. Orazem, B. Tribollet, Electrochemical impedance spectroscopy, John Wiley & Sons, New Jersey, 2011.

[24] S.A. Mamuru, K.I. Ozoemena, T. Fukuda, N. Kobayashi, J. Mater. Chem. **20** (2010) 10705.

[25] K.I. Ozoemena, N.S. Mathebula, J. Pillay, G. Toschi, J.A. Verschoor, Phys. Chem. Chem. Phys. **12** (2010) 345.

[26] J. Pillay, K.I. Ozoemena, R.T. Tshikhudo, R.M. Moutloali, Langmuir **26** (2010) 9061.

[27] H. Xia, L. Lu, Phys. Scripta **2007** (2007) 43.

[28] K. Shaju, G.S. Rao, B. Chowdari, J. Electrochem. Soc. **151** (2004) A1324.

[29] K. Dokko, M. Mohamedi, M. Umeda, I. Uchida, J. Electrochem. Soc. **150** (2003) A425.

Chapter 8*

Electrolytic Manganese Dioxide Coated with Graphene Oxide or Multi-Walled Carbon Nanotubes Composites Aqueous Asymmetric Electrochemical Capacitors

8.1 Introduction to the Use of Electrolytic Manganese Dioxide in Conjunction with Graphene Oxide or Multi-Walled Carbon Nanotubes as Electrochemical Capacitors

Asymmetric electrochemical capacitors, also known as hybrid supercapacitors, are characterised by Faradaic reactions and charge storage, and have begun to receive immense research interests because of their high energy density, large power density and long lifetime [1]. The use of aqueous electrolytes in asymmetric ECs is important due to several advantages of such systems [2], namely:

I. The simplicity of fabrication and packaging procedures that avoid rigorous environmental controls.

*The following publications resulted from part of the research work presented in this chapter and are not referenced further:
C. J. Jafta, F. Nkosi, L. le Roux, M. Kebede, K. Makgopa, M. K. Mathe, N. Manyala, M. Oyama and K. I. Ozoemena, "Tuning Electrolytic Manganese Dioxide for a High-Voltage Aqueous Asymmetric Electrochemical Capacitor", *ECS Trans.* **50** (2013) 93 – 101
C. J. Jafta, F. Nkosi, L. le Roux, M. K. Mathe, M. Kebede, K. Makgopa, Y. Song, D. Tong, M. Oyama, N. Manyala, S. Chen and K. I. Ozoemena, "Manganese oxide/graphene oxide composites for high-energy aqueous asymmetric electrochemical capacitors", *Electrochim. Acta* **110** (2013) 228 – 233

II. A high degree of safety as compared to the use of organic-based ECs with respect to thermal stability and runaway.

III. The use of low toxicity and low cost electrolytes.

IV. Specific energy that meets or exceeds those of non-aqueous EDLCs.

Toward this end, manganese dioxide (MnO_2) has been regarded as a promising active component for EC electrodes [3, 4]. Electrolytic manganese oxide (EMD), on the other hand, does not show good capacitance. EMD is characterised by small surface areas and composed of a mixture of several crystallographic phases (α, β, γ, δ and λ). Of these, α-MnO_2 gives the best electrochemical capacitance [5]. South Africa has the largest manganese deposit in the world, and remains the major global supplier of EMD. One of the various means of expanding the value chain of its manganese resource would be to find ways of exploiting EMD for energy storage systems. Therefore, there is a need to develop effective protocol whereby commercial EMD may be exploited to generate α-MnO_2 for electrochemical capacitor applications.

In addition, whereas activated carbons have been used extensively in the preparation of electrochemical capacitor electrodes [6-8], graphene and graphene oxide (GO) nanosheets are beginning to be taunted as potential replacement due to their much enhanced energy densities. Theoretically, GO is not suitable for supercapacitor applications [9], but Xu et al. [10] recently showed that GO can exhibit higher capacitance than graphene due to the extra pseudocapacitance effect of the attached oxygen containing functional groups on its basal planes. Thus, in light of its higher capacitance, lower cost and shorter processing time than graphene, GO may become a better choice than graphene in electrochemical capacitor applications. Also, Multi-

Walled Carbaon Nanotubes (MWCNT) with its enhanced electrochemical properties is compared with the GO composites.

It is within such context that this study is carried out. In this chapter the properties of α-MnO_2/GO and α-MnO_2/MWCNT composites as high-energy, high-power asymmetric electrochemical capacitors in neutral aqueous solutions are described. This is the first study on the use of EMD generated α-MnO_2/GO and α-MnO_2/MWCNT hybrids for asymmetric electrochemical capacitors in neutral aqueous electrolytes.

8.2 Results and Discussion

Figure 8.1 shows the FESEM images after certain steps of the synthesis procedure reported in **Chapter 3**.

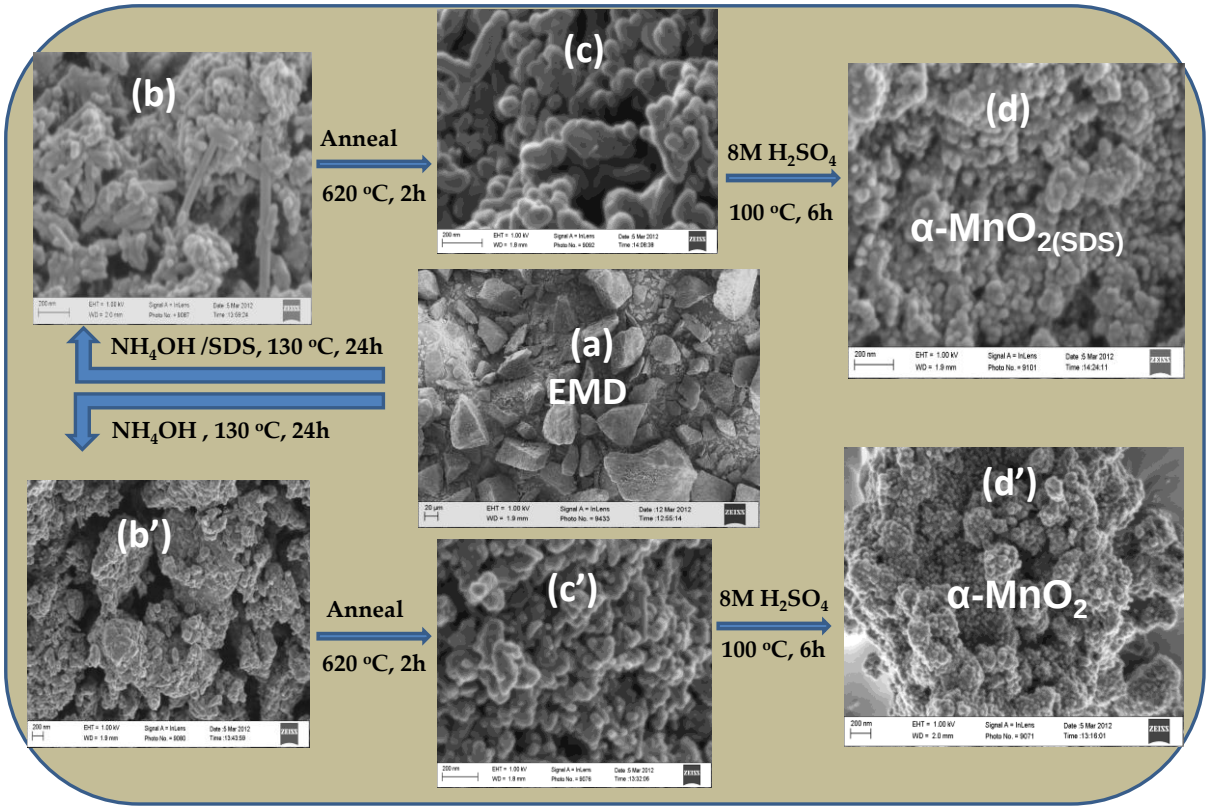

Figure 8.1: FESEM images showing the evolution of the EMD material to nano α-MnO_2 (see text for detail).

As summarised in **Figure 8.1**, the SDS based and SDS free routes show different morphologies of the intermediate products (b/b' and c/c'). While the SDS based intermediates were needle like (b) and rod like (c) nanostructures, their SDS free counterpart (b'and c') were nanoparticles. The final products (d and d') gave essentially similar morphology. The results clearly prove that SDS confers different morphology during the nanostructuring process of the raw EMD. As the EMD and SDS mixture was thoroughly stirred and ultrasonicated for long periods of time prior to hydrothermal treatment, it can be assumed that the distribution of SDS was sufficiently uniform. Considering that the final SDS based product was subjected to high temperature

annealing (620 °C) it means that any 'unreacted SDS' would have been completely burnt off during this heat treatment. Thus, the addition of SDS (an anionic surfactant) during synthesis only served to enhance the disaggregation of the bulky EMD and produced needle like or rod like intermediate nanostructures.

To examine the impact of the SDS on the crystal structures of the final products, XRD analyses were performed.

Figure 8.2 shows the XRD patterns of EMD, α-MnO_2 and α-$MnO_{2(SDS)}$.

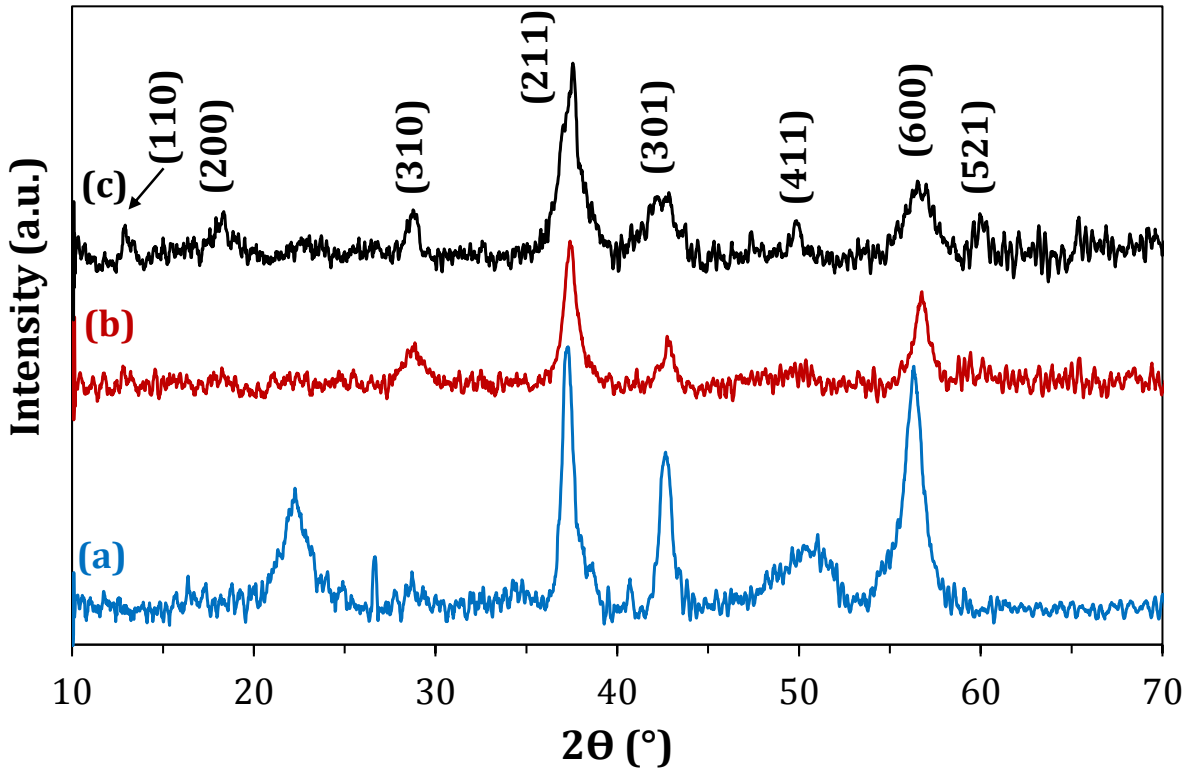

Figure 8.2: X-ray Diffraction patterns of (a) EMD, (b) α-MnO_2 and (c) α-$MnO_{2(SDS)}$.

In contrast to EMD (**Figure 8.2 (a)**), the XRD patterns of the transformed α-MnO_2, both in the absence (**Figure 8.2 (b)**) and presence of the surfactant SDS (**Figure 8.2 (c)**),

show peaks that can be indexed to tetragonal α-MnO_2 (JCPDS 44-0141). Also, the peaks in the former are somewhat broader, signifying the formation of smaller particles.

A graphene oxide sheet obtained by the modified Hummer's method [11] is shown in **Figure 8.3**.

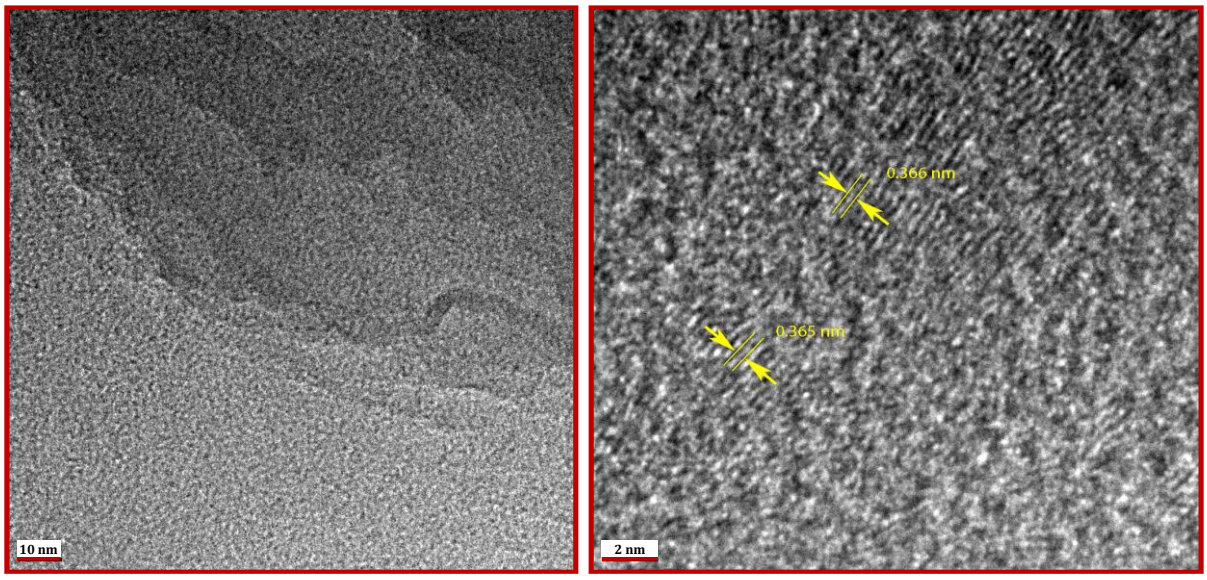

Figure 8.3: Representative HRTEM images of graphene oxide. Scale bars are 10 nm and 2 nm in the left and right panel, respectively.

The smooth sheet may be identified in the micrograph, while the edges tend to fold and roll. Lattice fringes are visible on the edges of graphene oxide sheets due to folds and/or rolls, as can be seen in the HRTEM image in **Figure 8.3**. The separation between neighbouring fringes (**Figure 8.3** inset) was measured to be ~ 0.37 nm and is larger than the inter planar spacing in graphite (0.335 nm) [12], which can be attributed to the presence of oxygen functional groups on the graphene oxide layers.

Cyclic voltammograms recorded for the EMD/MWCNT, α-$MnO_{2(SDS)}$/MWCNT, α-MnO_2/GO and α-$MnO_{2(SDS)}$/GO at a potential sweep rate of 15 mV s^{-1} are presented in **Figure 8.4** for MWCNT coated and **Figure 8.5** for GO coated.

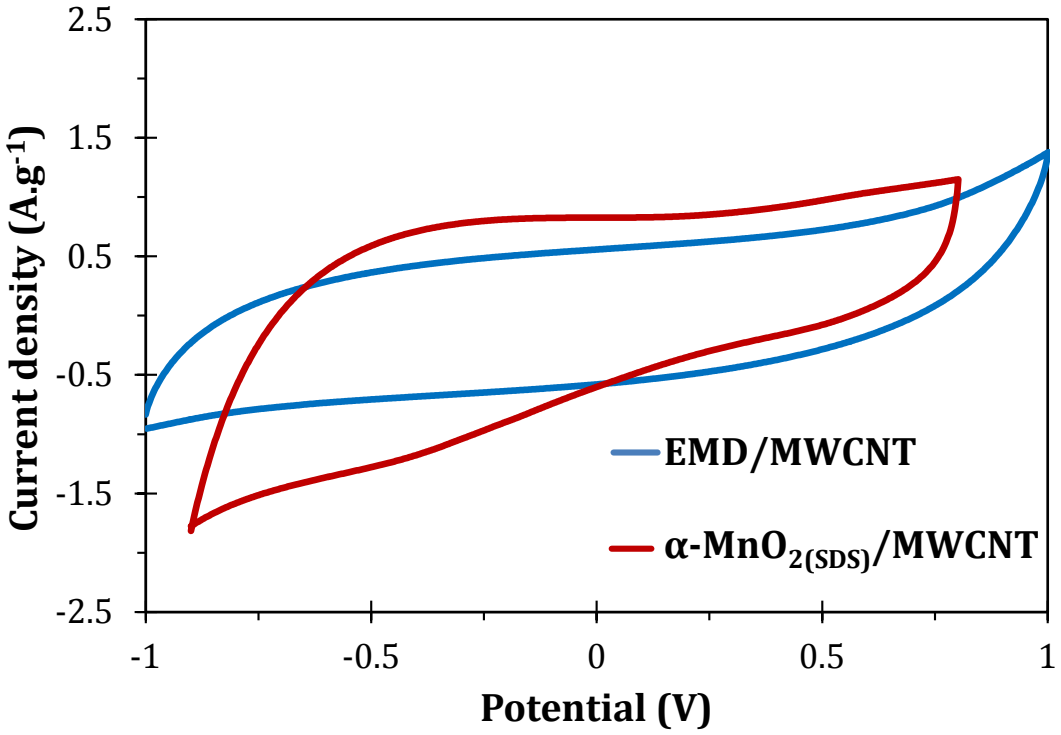

Figure 8.4: Cyclic Voltammograms of EMD/MWCNT and α-$MnO_{2(SDS)}$/MWCNT at a scan rate of 15 mV s^{-1}.

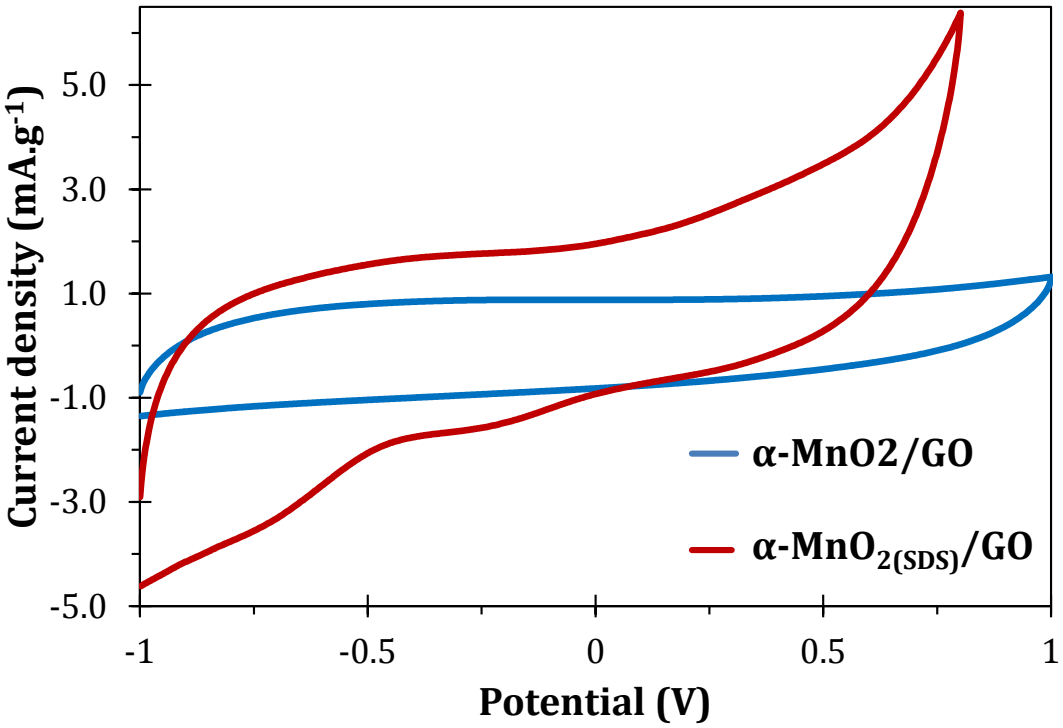

Figure 8.5: Cyclic Voltammograms of α-MnO_2/GO and α-$MnO_{2(SDS)}$/GO at a scan rate of 15 mVs^{-1}.

It is observed that the CV's show almost rectangular shaped voltammograms, which is an indication of capacitive behaviour. In comparison with EMD/MWCNT, the α-$MnO_{2(SDS)}$/MWCNT showed an enhanced current density and α-MnO_2/GO in comparison with the α-$MnO_{2(SDS)}$/GO also showed an enhanced current density which is indicative of enhanced electrochemically active surface area. The α-$MnO_{2(SDS)}$/GO is superior in terms of its current response. This may be ascribed to hydrogen and oxygen evolution, respectively [13]. It seems that the MnO_2 made via SDS route conferred on the MnO_2 catalytic properties for H_2 and O_2 evolution. The current response of the SDS coated samples are superior when compared to the sample without surfactant indicating that the α-$MnO_{2(SDS)}$/GO and α-$MnO_{2(SDS)}$/MWCNT samples have better capacitances. The

addition of SDS (an anionic surfactant) during synthesis should enhance the dispersion / disaggregation of the bulky MnO_2, thus permitting increased surface area of the final product.

The supercapacitive performance properties were evidenced by the galvanostatic charge-discharge experiments, as exemplified in **Figure 8.6** for MWCNT coated and **Figure 8.7** for GO coated.

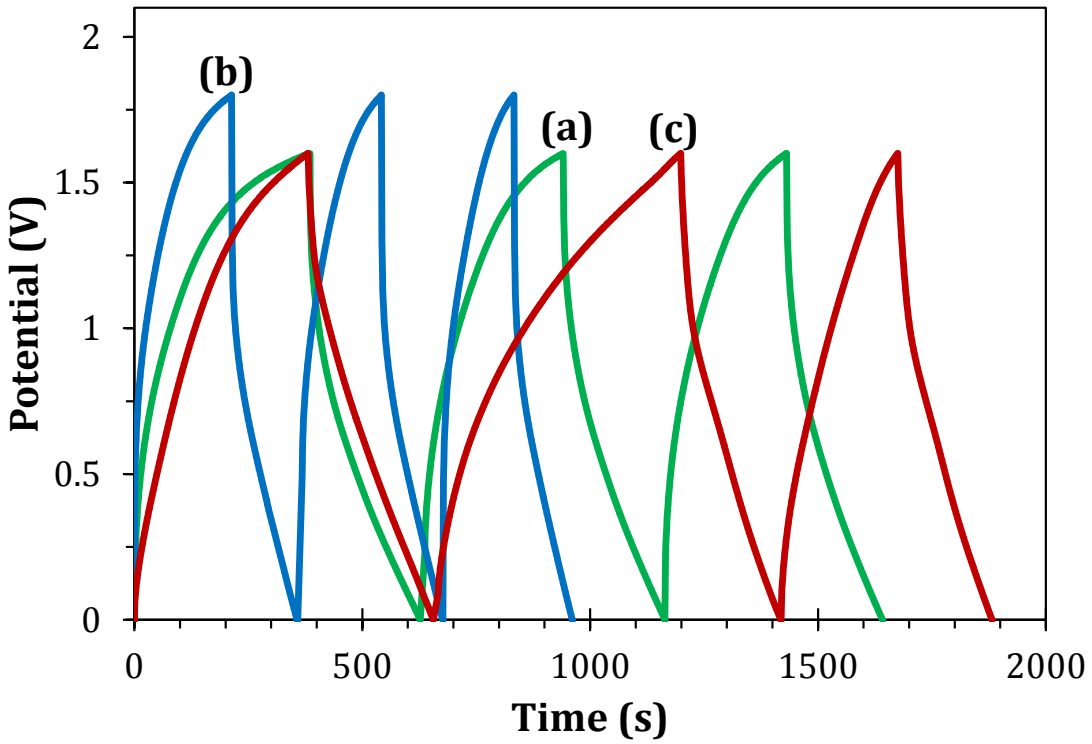

Figure 8.6: Galvanostatic charge-discharge curves at a current density of 0.5 $A.g^{-1}$ of (a) EMD/MWCNT, (b) α-MnO_2/MWCNT and (c) α-$MnO_{2(SDS)}$/ MWCNT.

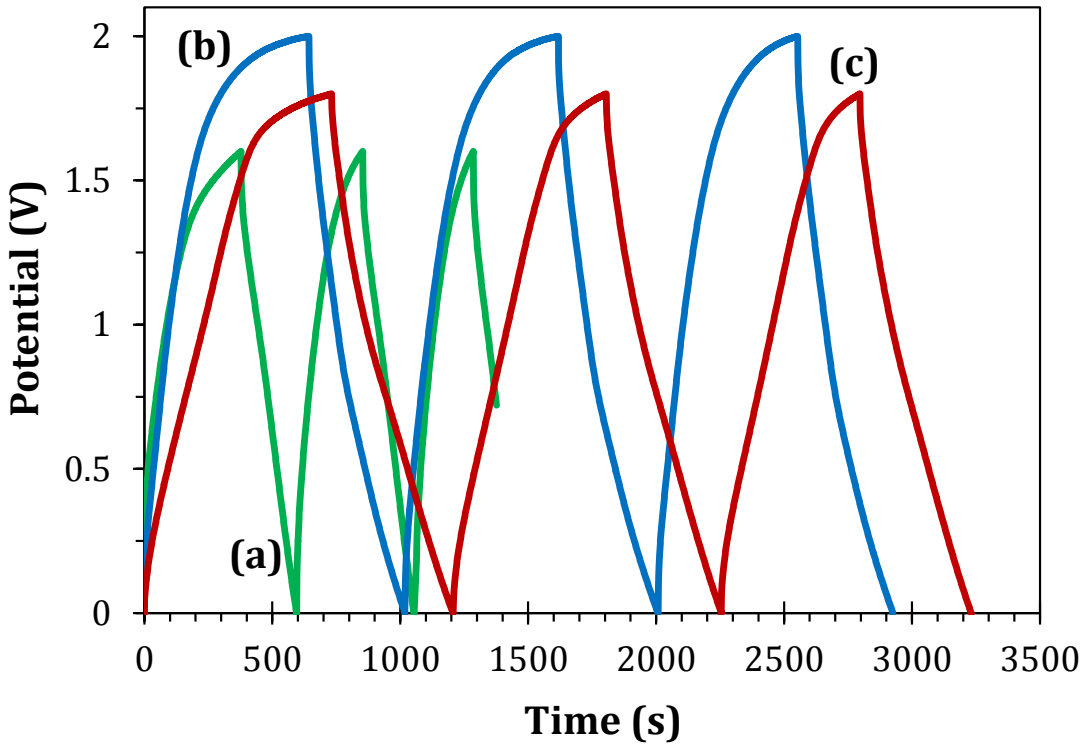

Figure 8.7: Galvanostatic charge-discharge curves at a current density of 0.5 $A.g^{-1}$ of (a) EMD/GO, (b) α-MnO_2/GO and (c) α-$MnO_{2(SDS)}$/GO.

The charge-discharge experiments were conducted for all the samples (EMD/MWCNT, α-MnO_2/MWCNT, α-$MnO_{2(SDS)}$/ MWCNT, EMD/GO, α-MnO_2/GO and α-$MnO_{2(SDS)}$/GO) at different voltage windows as the material permitted. The experimentally determined peak voltages are as follow, EMD/MWCNT at 1.6 V, α-MnO_2/MWCNT at 1.8 V, α-$MnO_{2(SDS)}$/ MWCNT at 1.6 V, EMD/GO at 1.6 V, α-MnO_2/GO at 2.0 V and α-$MnO_{2(SDS)}$/GO at 1.8 V. It is thus seen that the α converted nanoparticulate MnO_2, for both MWCNT and GO coated composites, have the widest voltage windows of 1.8 V and 2.0 V, respectively. It is also observed that with SDS addition the voltage windows narrow to 1.6 V and 1.8 V for the MWCNT and GO coated composites, respectively. The high voltage window (which is greater than the thermodynamic window of water of 1.23 V) may be related to

the evolution of hydrogen at the more negative potential, and oxygen evolution at the more positive potential. The EMD/MWCNT showed the highest voltage drop and α-$MnO_{2(SDS)}$/GO the lowest.

The specific capacitance (C_{sp}), maximum specific power density (P_{max}) and specific energy density (E_{sp}) were determined from the discharge curves using the established **Equations 8.1 – 8.4** for a 2-electrode device [14, 15]:

$$C(F) = \frac{i}{\Delta V/\Delta t} \quad 8.1$$

$$C(F.g^{-1}) = \frac{4C}{m} \quad 8.2$$

$$E_{sp}(Wh.kg^{-1}) = \frac{CV^2}{2m} \quad 8.3$$

$$P_{max}(W.kg^{-1}) = \frac{V^2}{4R_{ir}m} \quad 8.4$$

where i (A) is the applied current, $\Delta V/\Delta t$ (V/s) the slope of the discharge curve after the initial iR drop and m (g) the mass of both electrodes (positive and negative). The mass is considered to be that of only the active material not including the Carbon black and the PVDF binder. V (V) is the maximum voltage obtained during charge and C (F) the calculated capacitance. The internal resistance (R_{ir}) can be calculated from the voltage drop at the beginning of a discharge curve:

$$R_{ir}(\Omega) = \frac{\Delta V_{ir}}{2i} \quad 8.5$$

where ΔV_{ir} is the voltage drop between the first two points from the start of the discharge curve.

For the MWCNT coated composites at current density of 0.5 $A.g^{-1}$, the EMD/MWCNT shows a surprisingly good capacitance of ~ 122 $F.g^{-1}$ for this micron-sized material which beats the uncoated α-MnO_2/MWCNT (~ 75 $F.g^{-1}$) with its nanosized particles. The α-MnO_2/MWCNT only produced the approximately 75 $F.g^{-1}$ for the first few cycles after which the capacitance collapsed and thus no further experiments were performed on this composite. Among the MWCNT the α-$MnO_{2(SDS)}$/MWCNT produced the best capacitance of ~ 127 $F.g^{-1}$.

For the GO coated composites also at a current density of 0.5 $A.g^{-1}$, the first three charge-discharge cycles for EMD/GO show a surprisingly good capacitance of ~ 77 $F\ g^{-1}$, for this micron sized material. However, after the initial three cycles, the capacitance also degenerated rapidly, thus no further experiment was performed with this electrode as well. It is noted that the specific capacitance of the α-MnO_2/GO and α-$MnO_{2(SDS)}$/GO can reach ~ 153 $F.g^{-1}$ and ~ 280 $F.g^{-1}$, respectively, as shown in **Table 8.1**.

Table 8.1: Comparative performance of some manganese oxide based aqueous asymmetric electrochemical capacitors

Electrode	Electrolyte	V_{max} (V)	C_{sp} ($F.g^{-1}$)	E_{sp} ($Wh.kg^{-1}$)	P_{max} ($kW.kg^{-1}$)	Ref
EMD/MWCNT	1 M Li_2SO_4	1.6	122	12.0	1.4	This work
α-MnO_2/MWCNT	1 M Li_2SO_4	1.8	75	9.4	0.9	This work
α-$MnO_{2(SDS)}$/MWCNT	1 M Li_2SO_4	1.6	127	13.8	4.1	This work
EMD/GO	1 M Li_2SO_4	1.6	77	10.4	2.7	This work
α-MnO_2/GO	1 M Li_2SO_4	2.0	153	23.6	4.5	This work
α-$MnO_{2(SDS)}$/GO	1 M Li_2SO_4	1.8	280	35.0	7.2	This work
MnO_2 nw/G	1 M Na_2SO_4	2.0	30	30.4	5	[16]
MnO_2-textile/G	0.5 M Na_2SO_4	1.0	315	12.5	110	[17]
MnO_2/AC	2 M KNO_3	2.0	140	21	123	[13]

Key: G = graphene; nw = nanowire; AC = activated carbon.

To establish the cycling stability of the electrode materials, the four superior ECs were subjected to continuous (1000 cycles) galvanostatic charge-discharge experiments. **Figure 8.8** shows the stability of EMD/MWCNT, α-$MnO_{2(SDS)}$/MWCNT, α-MnO_2/GO and α-$MnO_{2(SDS)}$/GO when cycled at a current density of 1 $A.g^{-1}$ for 1000 cycles.

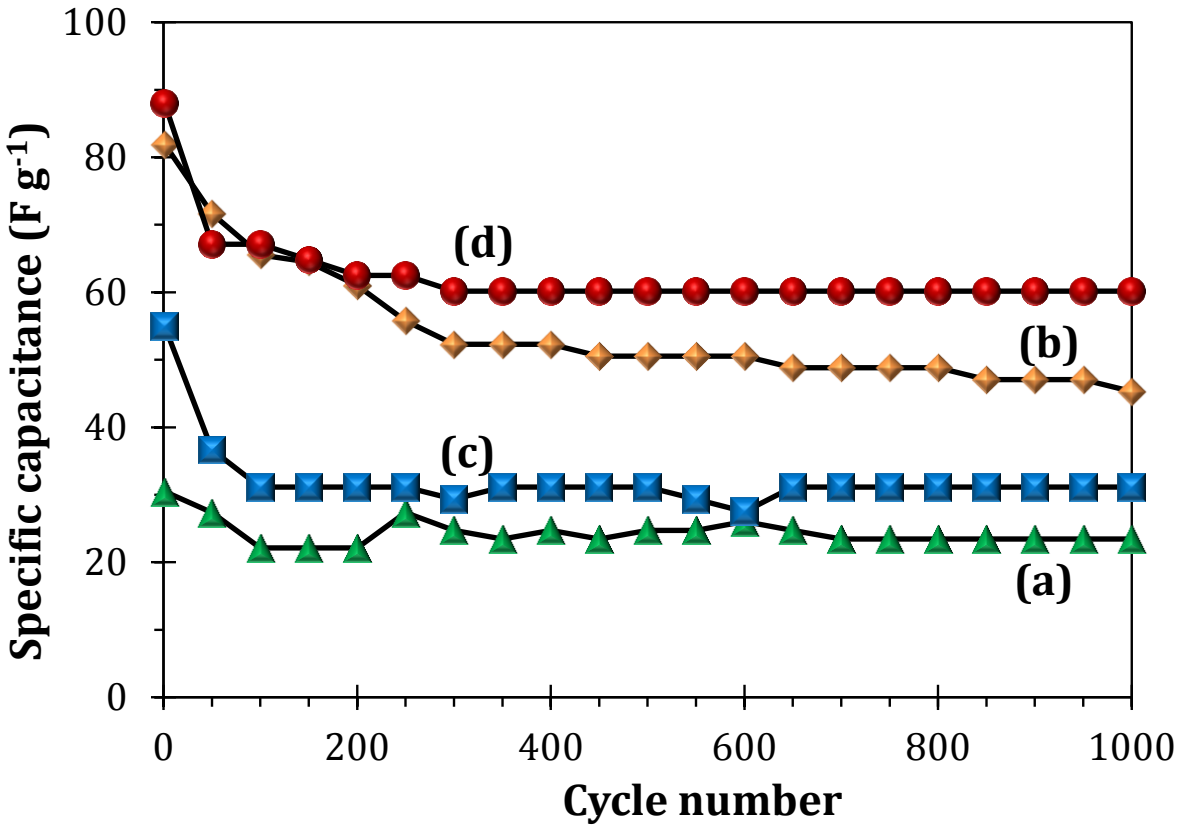

Figure 8.8: The cycle stability of (a) EMD/MWCNT, (b) α-$MnO_{2(SDS)}$/MWCNT, (c) α-MnO_2/GO and (d) α-$MnO_{2(SDS)}$/GO.

The GO coated composites, α-MnO_2/GO and α-$MnO_{2(SDS)}$/GO, showed a 44 % and 30 % decrease in the capacitance within the first 50 cycles after which it started to stabilize at ~ 60 $F.g^{-1}$ and ~ 31 $F.g^{-1}$, respectively. The α-MnO_2/GO and α-$MnO_{2(SDS)}$/GO composites showed a stability of ~ 84 % and ~ 90 %, respectively, between the 50^{th} and 100^{th} cycles. The α-$MnO_{2(SDS)}$/MWCNT composite, however, showed a steadily decrease in capacitance from ~ 83 $F.g^{-1}$ to ~ 45 $F.g^{-1}$, showing a stability of ~ 54 %. The capacitance decrease is related to the equilibration of both electrode potentials, as was also observed Khomenko *et al* [13]. The EMD/MWCNT essentially maintained its capacity of ~ 25 $F\ g^{-1}$.

Figure 8.9 compare the energy and power densities (Ragone plot) of EMD/MWCNT, α-MnO_2/MWCNT, α-$MnO_{2(SDS)}$/MWCNT, EMD/GO, α-MnO_2/GO and α-$MnO_{2(SDS)}$/GO. The energy and power densities of α-$MnO_{2(SDS)}$/GO is apparently higher with a values of 35 $Wh.kg^{-1}$ and 7.2 $kW.kg^{-1}$, respectively. Compared to the references cited α-$MnO_{2(SDS)}$/GO is superior in terms of its energy density.

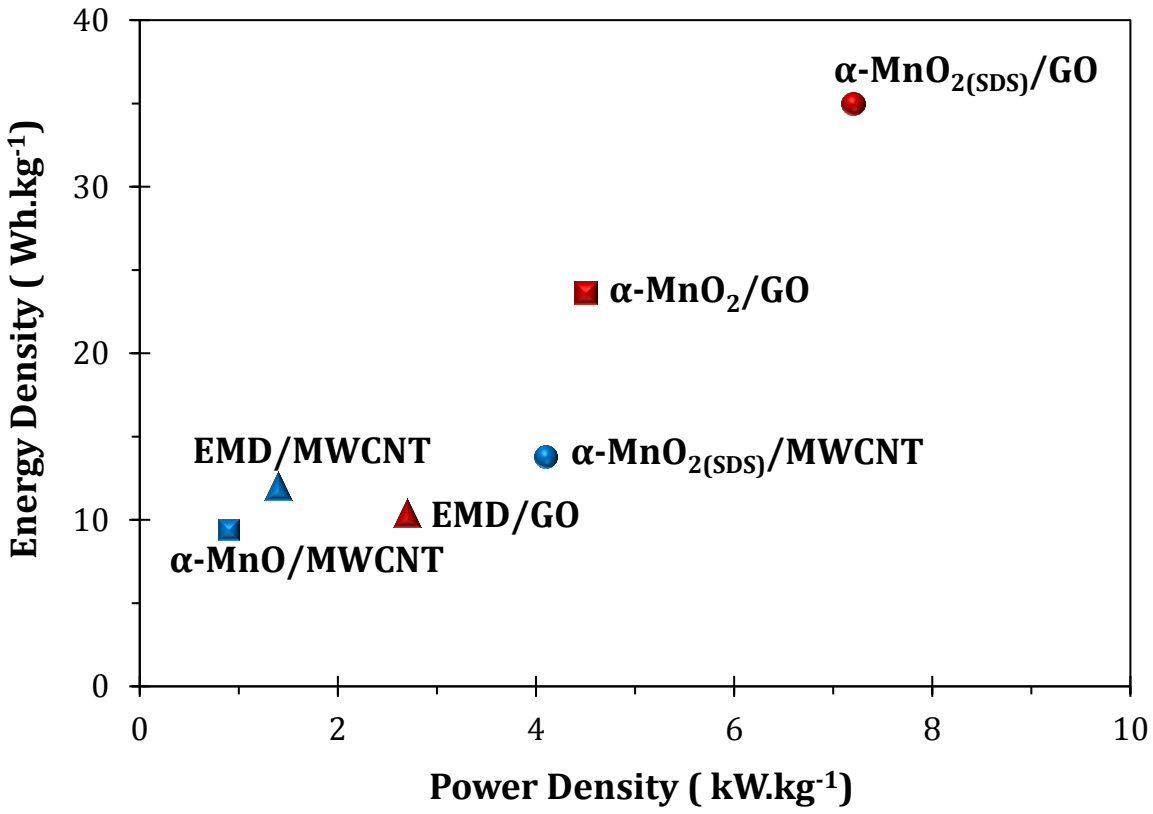

Figure 8.9: Ragone plot comparing the energy and power densities of the EMD/MWCNT, α-MnO_2/MWCNT, α-$MnO_{2(SDS)}$/MWCNT, EMD/GO, α-MnO_2/GO and α-$MnO_{2(SDS)}$/GO.

The enhanced capacitive energy storage properties of the SDS-based α-MnO_2 nanoparticles should perhaps not be surprising since good crystallinity, as expected, should improve the electrochemistry. For example, Ghodbane *et al.* [18] demonstrated

that the crystallographic structure has a significant influence on the capacitive storage behaviour of MnO_2. Mao *et al.* [19] recently showed that a composite of needle like α-MnO_2 and tetrabutylammonium hydroxide stabilized graphene (α-MnO_2/GTR) with good crystallinity showed better capacitive energy storage performance compared with the other two systems with poor crystallinity. Kim *et al*. [20] proved that high crystallinity greatly improved the electrochemistry rapid pseudocapacitive response of Nb_2O_5.

The electrochemical impedance spectra (EIS), for the MWCNT and GO coated composites, before the electrochemical capacitors were cycled (charged and discharged) for stability studies and after they were cycled 1000 times are shown in **Figure 8.10** and **Figure 8.11**, respectively. The equivalent electrical circuits (EEC) for both the MWCNT and GO coated composites are shown in **Figure 8.12**.

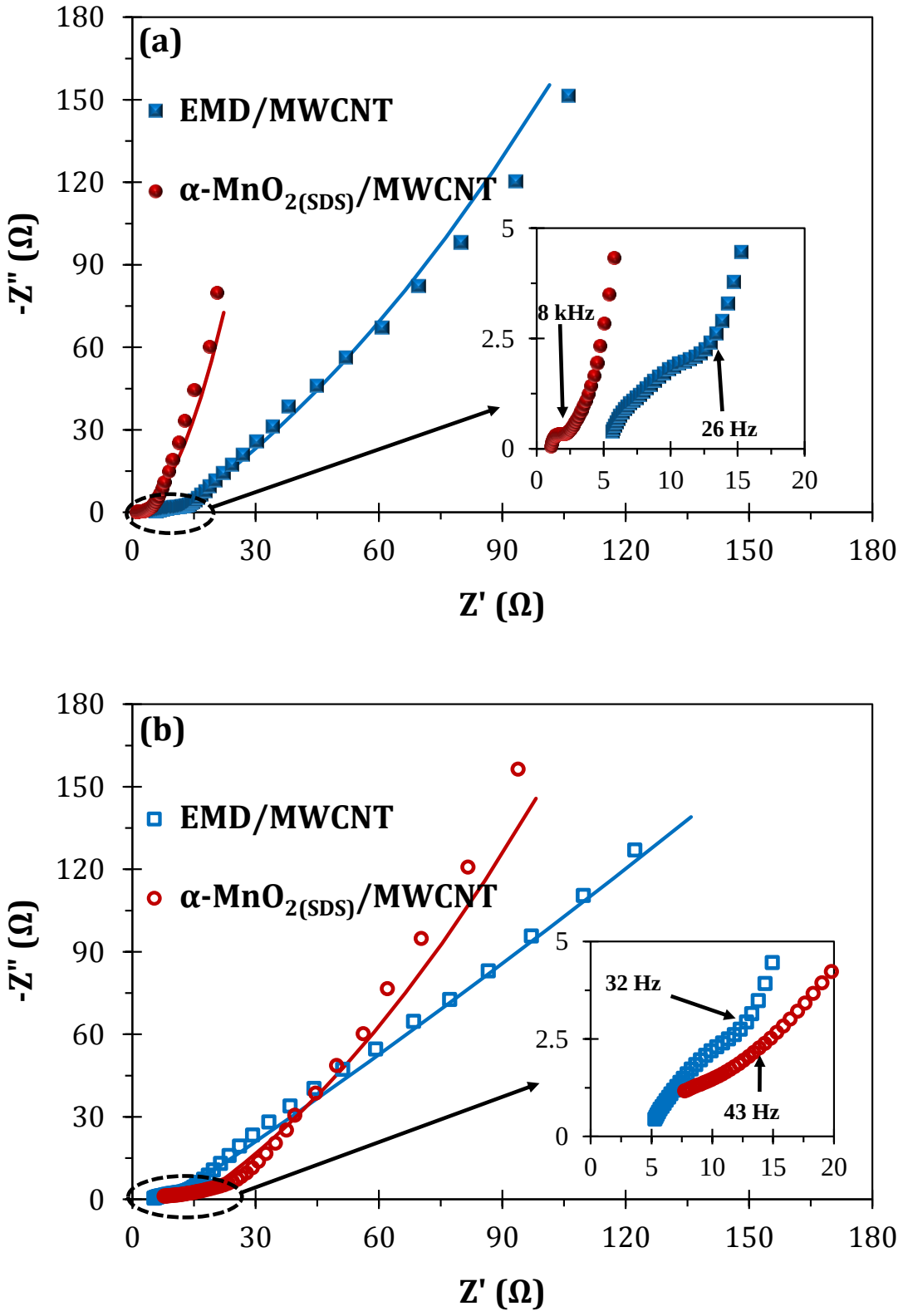

Figure 8.10: Nyquist plots of EMD/MWCNT and α-$MnO_{2(SDS)}$/MWCNT (a) before and (b) after 1000 repetitive cycling. Note that the data points are experimental while solid lines are fitted data.

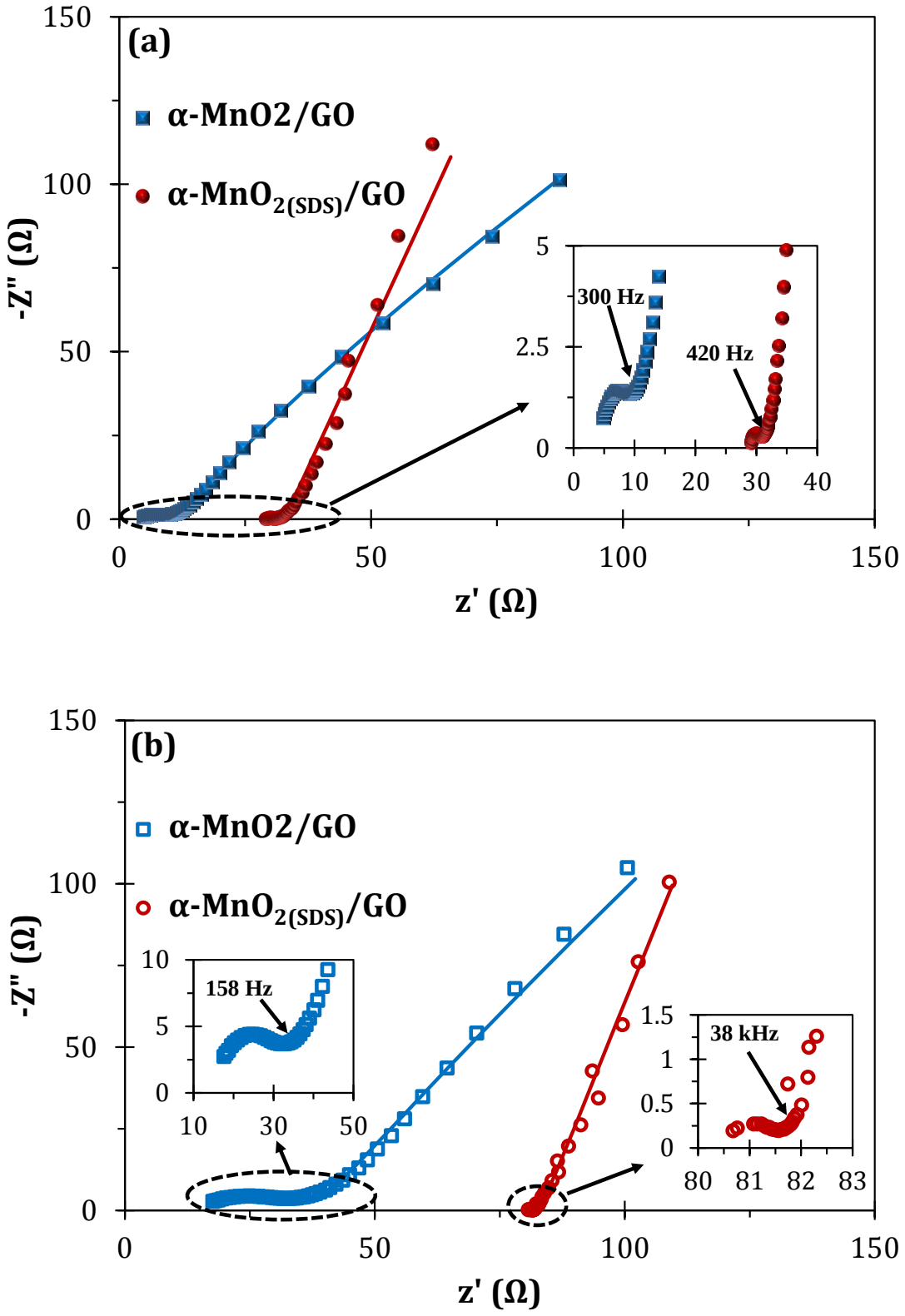

Figure 8.11: Nyquist plots of α-MnO_2/GO and α-$MnO_{2(SDS)}$/GO (a) before and (b) after 1000 repetitive cycling. Note that the data points are experimental while solid lines are fitted data.

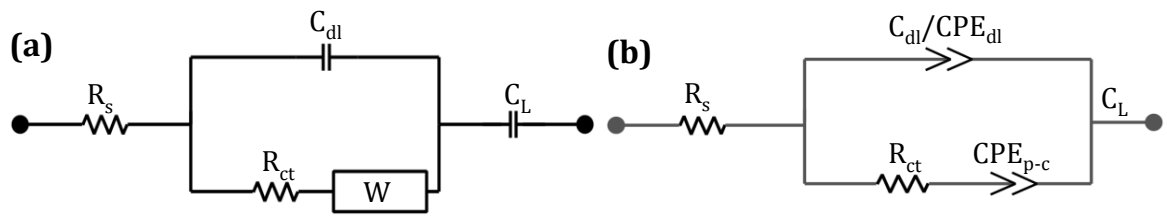

Figure 8.12: The Electrical Equivalent Circuits (EEC) for (a) the MWCNT coated composites and (b) GO coated composites used to fit the experimental EIS data.

The EEC for the MWCNT coated composites (**Figure 8.12 (a)**), which is the Randle EEC consisting of a series resistor R_s attributed to solution ionic resistance, intrinsic resistance of the substrate and contact resistance at the active material/current collector interface, the charge transfer resistance (R_{ct}), the double layer capacitance (C_{dl}) on the grain surfaces, the Warburg resistance (W) due to ion diffusion/transport in the electrolyte, and the limiting capacitance (C_L) [21, 22]. The fitting parameters are listed in **Table 8.2**. The EEC for the GO coated composites (**Figure 8.12 (b)**) consist of a series resistor R_s attributed to solution resistance, intrinsic resistance of the substrate and contact resistance at the active material/current collector interface, in connection with a parallel circuit consisting of a constant phase element (CPE_{dl}) or pure capacitor (C_{dl}) to account for the double layer capacitance and a charge transfer resistance (R_{ct}) in series with a constant phase element ($CPE_{p\text{-}c}$) to account for the pseudo-capacitance by the small amount of redox oxygen containing groups. The fitting parameters are listed in **Table 8.3**.

Table 8.2: Summary of EIS parameters for the MWCNT coated composites

Sample	R_s (Ω)	R_{ct} (Ω)	C_{dl} (μF)	C_L (mF)	$Z_w \times 10^{-4}$
Before cycling					
EMD/MWCNT	6.2	3.7	28.9	249.6	307.9
α-$MnO_{2(SDS)}$/MWCNT	1.2	1.1	42.4	302.4	1412.0
After cycling					
EMD/MWCNT	5.8	3.6	23.4	929.0	189.7
α-$MnO_{2(SDS)}$/MWCNT	9.1	6.3	27.9	253.3	340.5

Table 8.3: Summary of EIS parameters for the GO coated composites

Sample	R_s (Ω)	R_{ct} (Ω)	C_{dl} / CPE_{dl} (mF)	n	$CPE_{p\text{-}c}$ (mF)	n
Before cycling						
α-MnO_2/GO	3.0	10.4	4.0	0.3	15.2	0.7
α-$MnO_{2(SDS)}$/GO	30.2	2.7	1.2	-	82.6	0.8
After cycling						
α-MnO_2/GO	10.2	32.9	1.3	0.3	10.1	0.7
α-$MnO_{2(SDS)}$/GO	81.6	5.2	35.0	-	70.2	0.8

The fitting parameters for EMD/MWCNT and α-$MnO_{2(SDS)}$/MWCNT shown in **Table 8.2** reveals that the double layer capapcitance, Ohmic and charge transfer resistance for EMD/MWCNT is almost constant before and after cycling. This result is consistent with the cycling ability of EMD/MWCNT shown in **Figure 8.8**. However, the charge transfer is much faster, initially, for α-$MnO_{2(SDS)}$/MWCNT (1 Ω) than for EMD/MWCNT (4 Ω). This lower resistance should perhaps not be surprising considering that SDS, used in the hydrothermal process, is known to enhance the electrochemical response of supercapacitors [23]. After 1000 cycles α-$MnO_{2(SDS)}$/MWCNT has an increased charge transfer resistance of 6 Ω. This increase can be attributed to the smaller nanoparticulates. It is also interesting to note that the double layer capacitance of the α-$MnO_{2(SDS)}$/MWCNT is almost double that for the EMD/MWCNT.

Table 8.3 shows the that the R_{ct} values are improved for MnO_2 synthesised in the presence of SDS (α-$MnO_{2(SDS)}$/GO) which is consistent with capacitive performance of this composite. Again, this enhancement should perhaps not be surprising considering that SDS is known to enhance the electrochemical response of supercapacitors [23]. The α-$MnO_{2(SDS)}$/GO shows a diminutive increase in the charge transfer resistance after 1000 cycles whereas the SDS-free electrode (α-MnO_2/GO) showed a sharp increase from 10 Ω to 33 Ω. It is also interesting to note that the double layer capacitance of the sample with α-$MnO_{2(SDS)}$/GO increased from 1 mF to 35 mF after cycling whereas the surfactant-free sample decreased from 4 mF to 1 mF. The pseudo-capacitance from the α-$MnO_{2(SDS)}$/GO sample showed a higher value (83 mF) compared to that of α-MnO_2/GO (15 mF). These values almost stayed constant after 1000 cycles.

From the EIS data, all the electrodes show little or no poisoning of the electrode-electrolyte interface even after several electrochemical cycles.

The response times (t_R) before cycling the cells, determined from the ‘‘knee’’ or ‘‘onset’’ frequencies (f_o), are about 40 ms (26 Hz), 0.1 ms (8 kHz), 3 ms (300 Hz) and 2 ms (420 Hz) for EMD/MWCNT, α-$MnO_{2(SDS)}$/MWCNT, α-MnO_2/GO and α-$MnO_{2(SDS)}$/GO, respectively. The response times after the cells were cycled are about 31 ms (32 Hz), 23 ms (43 Hz), 6 ms (158 Hz) and 26 μs (38 kHz), for EMD/MWCNT, α-$MnO_{2(SDS)}$/MWCNT, α-MnO_2/GO and α-$MnO_{2(SDS)}$/GO, respectively. It is evident from these response times that $MnO_{2(SDS)}$/GO displays the best response time . Note that most commercially available supercapacitors, including those specifically designed for higher power applications operate at frequencies less than 1 Hz [24].

8.3 Conclusion on Manganese Oxide / Graphene Oxide or Multi-Walled Carbon Nanotube Composites as Electrochemical Capacitors

It is shown in this chapter, for the first time, that the South African abundant electrolytic Manganese dioxide consisting of micron sized particles with multi phases can be converted to a nanoparticulate single phased material that is a useful and excellent energy storage material. The electrochemical properties of nanostructured α-MnO_2/graphene oxide and α-MnO_2/multi-walled Carbon nanotubes composites have been reported for application in aqueous asymmetric electrochemical capacitors. The addition of the surfactant (SDS) during the synthesis of α-MnO_2 from a multi phased electrolytic Manganese dioxide led to a significant enhancement on the electrochemical performance of the α-MnO_2/graphene oxide and α-MnO_2/multi-walled Carbon nanotubes nanocomposites. In the electrochemical measurements, the addition of SDS during the synthesis of α-MnO_2 improved the cell conductivity and capacitance. The former is due to the redox-activity of the SDS, while the latter is likely a result of enhanced "effective" surface area. The high energy density, of the superior α-$MnO_{2(SDS)}$/graphene oxide, (35 Wh kg^{-1}) coupled with excellent response time (26 μs after 1000 cycles) and long-term cycling stability, clearly indicate that this nanomaterial may be useful for future development of low cost asymmetric electrochemical capacitor. Also the fact that MnO_2, for energy storage material purposes, was made from commercial and South African abundant EMD rather than from the popular $KMnO_4$ could have a positive outlook on the South African Economy.

References

[1] R. Kötz, M. Carlen, Electrochim. Acta **45** (2000) 2483.

[2] J.W. Long, D. Bélanger, T. Brousse, W. Sugimoto, M.B. Sassin, O. Crosnier, MRS Bull **36** (2011) 513.

[3] V. Subramanian, H. Zhu, B. Wei, J. Power Sources **159** (2006) 361.

[4] W. Wei, X. Cui, W. Chen, D.G. Ivey, Chem. Soc. Rev. **40** (2011) 1697.

[5] S. Devaraj, N. Munichandraiah, J. Phys. Chem. C **112** (2008) 4406.

[6] E. Frackowiak, F. Béguin, Carbon **39** (2001) 937.

[7] E. Frackowiak, F. Béguin, Carbon **40** (2002) 1775.

[8] L.L. Zhang, X. Zhao, Chem. Soc. Rev. **38** (2009) 2520.

[9] Y. Wang, Z. Shi, Y. Huang, Y. Ma, C. Wang, M. Chen, Y. Chen, J. Phys. Chem. C **113** (2009) 13103.

[10] B. Xu, S. Yue, Z. Sui, X. Zhang, S. Hou, G. Cao, Y. Yang, Energy Environ. Sci. **4** (2011) 2826.

[11] W.S. Hummers Jr, R.E. Offeman, J. Am. Chem. Soc. **80** (1958) 1339.

[12] H.P. Boem, Carbon Surface Chemistry in Graphite and Precursors, 1st ed., Gordon and Breach Science Publishers, France, 2001.

[13] V. Khomenko, E. Raymundo-Pinero, F. Béguin, J. Power Sources **153** (2006) 183.

[14] X. Zhao, L. Zhang, S. Murali, M.D. Stoller, Q. Zhang, Y. Zhu, R.S. Ruoff, ACS nano **6** (2012) 5404.

[15] J. Duay, E. Gillette, R. Liu, S.B. Lee, Phys. Chem. Chem. Phys. **14** (2012) 3329.

[16] Z.S. Wu, W. Ren, D.W. Wang, F. Li, B. Liu, H.M. Cheng, ACS nano **4** (2010) 5835.

[17] G. Yu, L. Hu, M. Vosgueritchian, H. Wang, X. Xie, J.R. McDonough, X. Cui, Y. Cui, Z. Bao, Nano letters **11** (2011) 2905.

[18] O. Ghodbane, J. Pascal, F. Favier, ACS Appl. Mater. Interfaces **1** (2009) 1130.

[19] L. Mao, K. Zhang, H.S.O. Chan, J. Wu, J. Mater. Chem. **22** (2012) 1845.

[20] J.W. Kim, V. Augustyn, B. Dunn, Adv. Energy Mater. **2** (2012) 141.

[21] M.S. Wu, C.Y. Huang, K.H. Lin, J. Power Sources **186** (2009) 557.

[22] A. Di Fabio, A. Giorgi, M. Mastragostino, F. Soavi, J. Electrochem. Soc. **148** (2001) A845.

[23] K. Fic, G. Lota, E. Frackowiak, Electrochim. Acta **60** (2012) 206.

[24] C. Du, N. Pan, Nanotechnology **17** (2006) 5314.

Chapter 9

Conclusion and Outlook

9.1 Concluding Remarks

The Lithium Ion Battery cathode materials, $LiMn_{1.5}Ni_{0.5}O_4$ (LMN), $Li_{1.2}Mn_{0.54}Ni_{0.13}Co_{0.13}O_2$ (LMNC) and $Li_{1.2}Mn_{0.52}Ni_{0.13}Co_{0.13}Al_{0.02}O_2$ (LMNCA) were synthesized with a modified, one-step powder forming Pechini method to produce nanoparticulate cathode materials. The modification included the removal of a tedious and time consuming step where after a gel is formed, it is removed from the beaker and pasted on a piece of stainless steel and heated to form the desired powder. With the removal of this step, after the gel is formed it is left to combust forming the desired powder.

The high energy LMN cathode material shows a change, with microwave irradiation, in the morphology and the crystal growth kinetics as seen from the FE-SEM images. With the microwave treatment the spinel cathode loses oxygen creating oxygen vacancies in the lattices. In order to maintain the charge neutrality in the spinel some Mn^{4+} ions are reduced to Mn^{3+} ions. Thus it was successfully shown, with the high energy LMN that with the use of microwave irradiation the Mn^{3+} concentration can be tuned for enhanced electrochemical performance.

It was successfully shown that by substituting Mn with Al, in the solid solution layered cathode material (LMNCA), the *c* lattice increases and cation mixing reduces. This allows for faster Li diffusion due to the decrease in the activation energy of Li hopping and ultimately increases the rate capability of the cathode material as evidenced by the higher rate charge discharge cycles. Due to the fact that Al^{3+} and the Mn^{4+} ions have similar ionic radii, the Al^{3+} occupies the Mn^{4+} sites and increases the Mn^{3+} concentration, as shown by XPS measurements. As the conductivity of the Mn^{3+} ions are superior to the Mn^{4+} ions, the increase in the Mn^{3+} concentration is also partly the result of the increased rate capability. CSAFM measurements also proved that the electrode surface of the LMNCA is more conductive than that of the LMNC electrode surface. The Al dopant, that is redox inactive, also increases the stability of the LMNCA cathode material and thus increases the cycling stability as demonstrated by the continuous galvanostatic charge-discharge experiments. With EIS measurements it is shown that the SEI layer of the LMNCA forms slower compared to that of the LMNC thus improving its cyclability.

Both LMNC and LMNCA cathode materials were treated with microwaves (LMNC-mic and LMNCA-mic). It is proved that the oxidation state of Mn in the layered LMNC and LMNCA cathode materials is increased with microwave treatment. It is thus shown by XPS that with microwave treatment the Mn^{4+} concentration is increased. The galvanostatic charge-discharge experiments (1^{st} discharge capacity) show that the LMNCA-mic, with the redox inactive Al, is superior compared to the LMNC-mic. The LMNCA-mic has a better stability and rate capanility than the LMNC-mic. The EIS results of the LMNC-mic and LMNCA-mic showed the same trend as the LMNC and LMNCA after 50 cycles, with a slower forming SEI layer and thus improved cyclebility for the Al doped cathode material.

With this microwave assisted synthesis method and Al doping of the solid solution layered cathode materials, it is successfully proved that the Mn oxidation state can be controlled. The Mn oxidation state can be increased or decreased by means of microwave treatment or Al doping, respectively. The microwave treated cathode materials (LMNC-mic and LMNCA-mic) is electrochemically superior compared to the un-microwaved cathode materials (LMNC and LMNCA).

South African abundant electrolytic Manganese dioxide (EMD) is successfully converted to a nanoparticulate single phased material that is a useful and excellent energy storage material. The addition of the surfactant (SDS) during the synthesis of α-MnO_2 from EMD proves to enhance the electrochemical performance of the α-MnO_2/graphene oxide and α-MnO_2/multi-walled Carbon nanotubes nanocomposites. It is also shown that by coating the α-MnO_2 with the more cost effective graphene oxide (α-MnO_2/graphene oxide) it delivers an electrochemical capacitor with high energy density (35 $Wh.kg^{-1}$) coupled with excellent response time (26 μs after 1000 cycles) and long-term cycling stability. It is thus successfully proved that the South African abundant EMD can be utilised for energy storage purposes, which can have a positive effect on the South African economy.

In summary, a known synthesis method is modified making it more energy and time efficient. Microwave irradiation is used in order to change the Mn oxidation states of both spinel and layered cathode materials. This ultimately allows for the tuning of the Mn oxidation state in the cathode materials. EMD in conjunction with SDS and graphene oxide is used to make a high energy asymmetric electrochemical capacitor.

9.2 Recommendations for Further Research

- In order to further improve the power density of the high energy $LiMn_{1.5}Ni_{0.5}O_4$ cathode material is to increase its conductivity. Carbon coating is a well-known method to achieve this. A possible alternative method, that can have additional positive effects on the SEI, is to directly deposit a highly conductive Al thin film on the electrode. This deposition of Al was reported, on other electric devices, to have a superior conductivity compared to Ag. The significance of this Al deposition is that the extremely active Al with O and moisture can be decomposed from the Al precursor solution $AlH_3\{O(C_4H_9)_2\}$ to Al, $1.5H_2$ and $O(C_4H_9)_2$. Thus avoiding the insulating Al_2O_3 that so easily forms. The Al deposition can be done on all cathode materials in order to increase the conductivity. Its effect on the SEI can also be studied.

- It is found in this thesis that by doping $Li_{1.2}Mn_{0.54}Ni_{0.13}Co_{0.13}O_2$ with Al it will cause a decrease in the Mn^{3+} concentration. The similar ionic radii of Al^{3+} and Mn^{4+} are the reported reason. The Mg^{2+} ions have a bigger ionic radius compared to Al^{3+}, and the ionic radius of Mn^{3+} is bigger than Mn^{4+}. Thus it is hypothesised that by substituting Mn with Mg, the Mg^{2+} ions will occupy the Mn^{3+} sites and therefore the Mn^{3+} concentration will increase. It is thus suggested that $Li_{1.2}Mn_{0.54}Ni_{0.13}Co_{0.13}O_2$ be doped with both Al and Mg ($Li_{1.2}Mn_{0.54-(x+y)}Ni_{0.13}Co_{0.13}Al_xMg_yO_2$), experimenting with the concentrations and the Mn oxidation state.

- It is found that for both the spinel $LiMn_{1.5}Ni_{0.5}O_4$ and the solid solution layered $Li_{1.2}Mn_{0.54}Ni_{0.13}Co_{0.13}O_2$ cathode materials, prepared by the modified Pechini method, the microwave irradiation increases the electrochemical performance. It

is suggested that other synthesis methods be used to prepare the cathode materials and determine if the microwave irradiation have the same outcome.

- The performance of these LIB electrodes can also be studied at elevated (55 °C) and lower (-10 °C) temperatures.

Appendix A

List of Publications Arising from this Thesis

1. **Jafta CJ**, Mathe MK, Manyala N, Roos WD, Ozoemena KI, "Microwave-assisted synthesis of high-voltage Nanostructured $LiMn_{1.5}Ni_{0.5}O_4$ spinel: Tuning the Mn^{3+} content and electrochemical performance", *ACS Applied Materials & Interfaces* **5** (2013) 7592 – 7598.

2. **Jafta CJ**, Nkosi F, le Roux L, Mathe MK, Kebede M, Makgopa K., Song Y, Tong D, Oyama M, Manyala N, Chen S, Ozoemena KI, "Manganese Oxide/Graphene Oxide Composites for High-Energy Aqueous Asymmetric Electrochemical Capacitors", *Electrochimica Acta* **110** (2013) 228 – 233.

3. **Jafta CJ**, Nkosi F, le Roux L, Mathe MK, Kebede M, Makgopa K, Oyama M, Manyala N, Chen S, Ozoemena KI, "Tuning Electrolytic Manganese Dioxide for a High-Voltage Aqueous Asymmetric Electrochemical Capacitor", *ECS Transactions* **50** (2013) 93 – 101.

4. **Jafta CJ**, Ozoemena KI, Mathe MK and Roos WD, Synthesis, "Characterisation and Electrochemical Intercalation Kinetics of Nanostructured Aluminium-Doped $Li[Li_{0.2}Mn_{0.54}Ni_{0.13}Co_{0.13}]O_2$ Cathode Material for Lithium Ion Battery", *Electrochimica Acta* **85** (2012) 411 – 422.

5. **Jafta CJ**, Mathe MK, Manyala N, Roos WD, Ozoemena KI, "Microwave Irradiation Controls the Manganese Oxidation States of Nanostructured ($Li[Li_{0.2}Mn_{0.52}Ni_{0.13}Co_{0.13}Al_{0.02}]O_2$) Layered Cathode Materials for high-Performance Lithium Ion Batteries", *Submitted* (2014).

Appendix B

Conference Presentations Arising from this Thesis

1. **Jafta CJ**, Ozoemena KI and Mathe MK, "Nanomaterials in Lithium-ion Batteries and Asymmetric Electrochemical Capacitors", The 1st International Conference of Young Researchers on Advanced Materials, Singapore, Singapore 1 – 6 July 2012 (Poster).

2. **Jafta CJ**, Ozoemena KI and Mathe MK, "The Impact of Aluminium-doping on the Structure and Kinetics of the High-capacity $Li[Li_{0.2}Mn_{0.54}Ni_{0.13}Co_{0.13}]O_2$ Cathode Material", The 1st International Conference of Young Researchers on Advanced Materials, Singapore, Singapore 1 – 6 July 2012.

3. **Jafta CJ**, Ozoemena KI and Mathe MK, "Understanding the impact of Al-doping on the electrochemical kinetics of layered lithium-ion battery cathode nanomaterial", The 4th International Conference on Nanoscience and Nanotechnology (NanoAfrica 2012), South Africa, Bloemfontein, 1 – 4 April 2012.

4. **Jafta CJ**, Ozoemena KI, Mathe MK and Roos WD, "Effect of aluminium-doping on the performance of $Li[Li_{0.2}Mn_{0.54}Ni_{0.13}Co_{0.13}]O_2$ cathode material for lithium ion battery annealed at low temperature (700 °C)", The 6th International Conference of the Africa Materials Research Society (AMRS 6), Zimbabwe, Victoria Falls, 11 – 16 December 2011.